THÈSE

Pour l'obtention du Grade de

DOCTEUR DE L'UNIVERSITÉ DE POITIERS

(Faculté des Sciences Fondamentales et Appliquées)
(Diplôme National - Arrêté du 25 mai 2016 modifié)

École Doctorale n°651 :
MIMME – Mathématiques – Informatique – Matériaux – Mécanique - Énergétique

Secteur de Recherche : milieux denses et matériaux

Présentée par :

Mohamed CHARGAOUI

Influence of thickness gradients on buckling-driven delamination in coatings and thin films: a dual experimental and numerical study

Directeurs de Thèse : Christophe COUPEAU et Guillaume PARRY

Soutenue le 26 janvier 2026

Devant la Commission d'Examen

JURY

M. CORDILL	Professeur, Institut Erich Schmid des matériaux, Univ. de Leoben, AUTRICHE	Rapporteure
V. MAUREL	Directeur de recherche, Centre des Matériaux, , Mines ParisTech	Rapporteur
E. BARTHEL	Directeur de recherche, Science et Ingénierie de la Matière Molle, ESPCI PARIS	Examinateur
G. PARRY	Maître de conférences, SIMAP, INP, Univ. Grenoble-Alpes	Examinateur
C. COUPEAU	Professeur des Universités, Institut Pprime, Univ. de Poitiers	Examinateur

Acknowledgements

First and foremost, I thank Allah for granting me strength, patience, and guidance throughout my life and during this PhD journey. Without His will and support, none of this would have been possible. I would like to copy this verse of Quaran that summarize this journey for me:
<<وَمَا بِكُم مِّن نِّعْمَةٍ فَمِنَ ٱللَّهِ>>.

I would like to express my sincere appreciation to my supervisor, Christophe COUPEAU, and my co-supervisor, Guillaume PARRY, for giving me the opportunity to work under your guidance. Your expertise, valuable advice, and constructive feedback have been instrumental in shaping my scientific thinking and developing my research skills. I am truly grateful for all that I have learned from you.

I would also like to acknowledge Bruno LAMONGIE for the design of the mobile shutter, which was essential to the completion of this thesis. I sincerely thank the technical staff for their valuable assistance during the experiments. I am grateful to all the people with whom I worked at the Pprime Laboratory for their support, collaboration, and the stimulating scientific environment. Finally, Finally, I would like to thank Delphine PIERRE for her assistance with administrative procedures related to the doctoral school.

In addition, I wish to acknowledge Vincent MAUREL and Megan CORDILL for taking their expensive time to read this thesis. I am also grateful to Etienne BARTHEL for accepting to attend my thesis defense.

My deepest gratitude goes to my beloved family. To my father Salem, a true soldier, and my mother Fatna, your endless sacrifices, love, and prayers have always been the foundation of my achievements. To my brothers Mouad and Lahcen, and my beloved sisters Layla, Somaya, and Fatimazahra, your encouragement and care gave me the motivation to keep moving forward, even during the most difficult times. I would also like to wish all the success to Mouad and Fati in Finland.

A very special thank you goes to my wife, Hajar Moatassim, for your unwavering support, patience, and belief in me. Your love and constant encouragement gave me the strength to overcome challenges and to believe in myself. I am truly blessed to share this journey with you.

Finally, I would like to thank everyone who has left a positive mark on me throughout this journey: colleagues, friends, and mentors. Your support and encouragement made this path more enriching and meaningful.

Contents

Acknowledgements i
Contents ii
List of figures v
List of tables xvi
List of symbols xvii
Introduction: State of the art 1
1. Buckling-induced delamination of thin films: theoretical approaches 10
1.1. Elastic buckling of thin films 10
1.1.1. Deformation of material 11
1.1.2. Elastic plate theory 13
1.1.3. Föppl-Von Kármán equations 15
1.1.4. Analytical model: straight-sided buckle 16
1.2. Interfacial fracture mechanics 21
1.2.1. Fracture modes 22
1.2.2. Dundurs' parameters 22
1.2.3. Griffith criteria 24
1.2.4. Mode dependence of interfacial fracture 27
1.2.5. Cohesive zone model 30
1.2.6. Mode mixity dependence of the straight sided buckle: Hutchinson and Suo analytical model 35
1.3. Stabilization of the straight sided buckle 37
1.3.1. Steady state propagation of the straight buckle at the front 37
1.3.2. Influence of the elastic contrast on the mode mixity 39
1.4. Secondary buckling 42
1.4.1. Secondary buckling within static approach 43
1.4.2. Secondary buckling within dynamic approach 45
1.5. Conclusion 48
1.6. Résumé en Français 49

2. Experimental techniques and characterization tools for the preparation of controlled well thickness gradient 53
2.1. Thin film deposition: ion beam sputtering 53
2.2. Deposition of nickel films exhibiting well-controlled thickness gradients 56
2.2.1. Nickel target 56
2.2.2. Substrates 57
2.2.3. The deposited samples 58
2.2.4. Stoney curvature's method 59
2.2.5. Interferometric optical microscopy 62
2.2.6. Atomic force microscopy 64
2.2.7. Compression device : Deben 67
2.3. Conclusion 70
2.4. Résumé en Français 71
3. Study of SS and TC buckles in nickel film exhibiting a well-controlled thickness gradient within a static approach 75
3.1. Experimental results 75
3.1.1. SS Buckles parallel to the thickness gradient 75
3.1.2. SS Buckles misaligned with the thickness gradient 83
3.1.3. Telephone cord buckles parallel to the thickness gradient 87
3.1.3.1. In constant width 87
3.1.3.2. In gradient width 89
3.2. FEM modeling within the elastic plate theory 94
3.2.1. FEM details and mechanical model description 94
3.2.2. Model validation: homogeneous plate 98
3.3. FEM results of SS buckles parallel to the thickness gradient 99
3.3.1. FEM simulations versus experiments 99
3.3.2. Influence of thickness gradient intensity on the SS buckles 102
3.3.3. Quantification of the local onset of buckling 104
3.3.4. Influence of thickness gradient on the out-of-plane displacement profile 112
3.4. FEM results of SS buckles perpendicular to the thickness gradient 113
3.5. FEM results of TC buckles parallel to the thickness gradient 118

3.5.1. In constant width 118
3.5.2. In gradient width 122
3.6. FEM results of TC buckles perpendicular to the thickness gradient 128
3.7. Conclusion 134
3.8. Résumé en Français 136
4. Buckling driven delamination in nickel film within a dynamic approach 141
4.1. Spontaneous buckling in homogenous films 141
4.2. Experimental results of SS buckles in films lying parallel to the thickness gradient . 143
4.3. Mechanical numerical modeling 150
4.3.1. Implementation of the numerical model 151
4.3.2. FEM validation against analytical model 154
4.3.3. Impact of substrate compliance 156
4.4. Buckling-driven delamination of SS buckle lying parallel to the thickness gradient . 158
4.4.1. Validity of the mechanical model in case of rigid substrate 158
4.4.2. Identification of interfacial toughness properties 159
4.5. Effect of SS buckles perpendicular to the thickness gradient on the mode mixity angle 163
4.6. Conclusion 166
4.7. Résumé en français 167
I. Synthesis 171
Bibliography 177

List of figures

Fig. 0-1: Various buckling structures. (a) Straight sided buckle [16], (b) circular buckle [21], (c) telephone cord (TC) buckles [27]. 2

Fig. 0-2: (a) Morphological mapping of buckling-driven delamination patterns (symbols) for η=0.95 and ν=0.31. (b) Out-of-plane displacement of telephone-cord buckle branches, as obtained from FEM simulations (top) and experimental measurements (bottom). In the experiment, fracture occurs along the SiO_x/Ag interface, involving 15 nm Ag layer overlaid by 132 nm MoO_x film with residual stress σ_0=1.84 GPa. FEM simulations were performed using parameters G_{IC}/G_0 = 0.34 and σ_0/E^*=6.1×10^{-3}. Adopted from [25]. 4

Fig. 0-3: (a) Buckled configuration of the stripe for ν= 1/3 and $\varepsilon/\varepsilon_1$= 6.25, 7.5, 9.4, 12.5, and 25 (from 1 to 5). The gray (color) represents the out-of-plane displacement of the film, expressed in units of the discretization length l_0. The stripe width corresponds to 1875.l_0/2. (b) Temporal evolution of the delaminated regions for ε=0.09, $k_b/(k_s l_0^2)$= 0.05, $f_{max}/(k_s l_0)$= 0.03, and k_h=k_s. The gray (color) scale ranges from darker to brighter with increasing film height, while non-delaminated areas are shown in white for clarity. The vertical scale is expressed in units of l_0. The four snapshots correspond to dimensionless times τ= 5×10^3, 2×10^4, 3.5×10^4, and 2×10^5. (c) Same as (b), for ε = 0.07 and k_h =k_s/100, shown at τ = 2.4×10^3, 5.4×10^3, 3.5×10^4, and 1×10^5. Adopted from [47]. 5

Fig. 0-4: Optical images (Each image has a size of 200 × 160 μm^2) of the telephone-cord buckles in a wedge-shaped Fe film sample for various thicknesses h. (1) h = 40 nm, (2) h = 70 nm, (3) h = 100 nm, (4) h = 130 nm. Adopted from [49]. 6

Fig. 0-5: The propagation of confined telephone-cord buckles in Y_2O_3 film deposited on GaAs exhibiting a thickness gradient (30-50 nm), deposited on GaAs. Adopted from [50]. 7

Fig. 0-6: Phase diagram of buckling structures as a function of the strain ε_0 and the thickness gradient k_h. The horizontal solid line k_h = 0 highlights a uniform homogenous, constant-thickness film, whereas letters from A to E correspond to symmetric TC buckle, asymmetric TC buckle, symmetric bilateral branched buckle, asymmetric bilateral branched buckle, and unilateral branched buckle, respectively. Adopted from [51]. 8

Fig. 1-1: Schematic of the plate and its coordinate system. 13

Fig. 1-2: Geometry of a one-dimensional SS buckle. Left: unbuckled state; right: buckled state. 16

Fig. 1-3: Representation of the out-of-plane displacement $w(y)$, for buckled film in SS buckle form given by Eq. (1-53), with width 2b and height. 20

Fig. 1-4: Fracture modes for crack propagation, the opening mode (I), the shear mode (II), and the transverse mode (III). 22

Fig. 1-5: Bimaterial Interface crack. 23

Fig. 1-6: Comparison of crack behavior in various bi-material systems presented. Adopted from [59]. The diagram compares earlier bi-material systems reported in [26] (star symbol) with modern bi-material systems (filled circle) depicted in α-β phase. The filled-circle data include examples from multiple sources [60–68]. Abbreviations: BPSG = boro-phosphor-silicate glass, PI = polyimide, TF-MG = thin film metallic glass, FQ = fused quartz and HEA = high entropy alloy. 24

Fig. 1-7: Data from [70] for an epoxy ♯1/glass ♯2 interface. The ψ_1 axis corresponds to l_1 = 12.7 mm, and the ψ_2 axis corresponds to l_2 = 127μm. The solid curves represent $G_c(\psi_2)$ as defined by Eq. (1-80). 28

List of figures

Fig. 1-8: Influence of η on the normalized interfacial toughness $G(\psi)/G_{IC}$ depending on mode mixity ψ from Eq. (1-80). 30

Fig. 1-9: Schematic representation of the successive stages of crack initiation and propagation within the cohesive zone model. 32

Fig. 1-10: Common traction-separation laws used in cohesive zone modeling: (a) cubic polynomial, (b) trapezoidal, (c) smooth trapezoidal, (d)exponential, (e) linear softening, and (f) bilinear softening. Adopted from [81]. 34

Fig. 1-11: Energy release rate for a SS buckle in the case of isotropic stress as function of the normalized internal stress σ_0/σ_c, for various mode mixity parameter η. 36

Fig. 1-12: The phase angle $\omega(\alpha, \beta)$, and the mode mixity angle $\boldsymbol{\psi}$. Adopted from [26]. 37

Fig. 1-13: The steady propagation of the front SS buckle. 38

Fig. 1-14: Influence of the Dundurs' coefficients α_D on the phase angle $\omega(°)$ for $\beta=\alpha_D/4$. Red dashed and black lines represent Hutchinson and Suo model [26] for bi-material combination, and numerical model developed by Zak *et al.* [59], respectively. 40

Fig. 1-15: Mode mixity angle ψ at the sides of the SS buckle as a function of the loading ratio for various film/substrate systems with different elastic contrast. 41

Fig. 1-16: Comparison between analytical solutions and FEM simulations for various values of a_D. (a) Normalized energy release rate, $G/G_0=f(\sigma_0/\sigma_c)$. (b) Mode mixity angle, $\psi=f(\sigma_0/\sigma_c)$. Adopted from [92]. 42

Fig. 1-17: FEM-based stability diagram of buckling morphologies, adapted from [28]. The two nondimensional parameters, β_t, and β_l, are used to map the different buckled states. Four distinct stability domains are identified: planar state, bubbles, straight-sided (SS) buckles, and telephone-cord (TC) buckles. The experimental loadings labelled (a) and (b) in Fig. 1-18 are indicated on the diagram for the two strip widths studied (4 μm and 6 μm). 44

Fig. 1-18: Adapted from [28]. Evolution of a straight-sided (SS) buckle in a 50 nm-thick nickel film under increasing compressive stress, observed by atomic force microscopy (AFM). Image (a) corresponds to a state with higher transverse stress σ_t and lower longitudinal stress σ_l compared to the final configuration in (b). The white contrast highlights the buckling features formed on the film surface during compression. Two morphological transitions are evident: from SS buckles to either periodic bubble-like structures (left side) or telephone-cord (TC) buckles (right side). 45

Fig. 1-19: *In situ* growth and evolutions of buckle modes 1, 2 and 3. The propagation time t for each buckle is indicated in the bottom-right corner of the corresponding image. The zero time corresponds to the first photograph; note that t represents the local propagation time, not the total experimental duration T. (a) Buckle mode 1 (left column), images of sizes 265 × 100 μm^2 captured at 1 min intervals. (b) Buckle mode 2 (middle column), images (340 × 110 μm^2) captured at 6 min intervals. (c) Buckle mode 3 (right column), images (340 × 120 μm^2) captured at 24 min intervals. Black arrows indicate newly formed wave troughs during buckle propagation. Adopted from [33]. 46

Fig. 1-20: Distribution of mode mixity angle along the delamination front for four stages of buckle propagation. As the buckle front advances, local configurational instability generates high mode mixity, effectively pinning the front. A slight shift of the pinning point is observed as the buckle expands around it. Adopted from [30]. 47

List of figures

Fig. 1-21: Modes de rupture pour la propagation des fissures : le mode d'ouverture (I), le mode de cisaillement (II) et le mode de déchirement (III). 51

Fig. 1-22: (a) Diagramme de stabilité morphologique basé sur des simulations par éléments finis (FEM). Les deux paramètres adimensionnels, β_t, and β_l, sont utilisés pour cartographier les différents états de flambage. (b) Distribution de l'angle de mode mixité le long du front de délaminage pour quatre étapes de la propagation de la cloque. 52

Fig. 2-1: Schematic representation of the IBS deposition chamber 54

Fig. 2-2: Schematic of the Nordiko PVD chamber equipped with a custom mobile shutter system. (a) shows an external view from the exit side. (b) Presents an internal exploded view detailing the main components. The system is designed to enable controlled deposition with a thickness gradient by translating a mobile shutter in front of the substrate. Labeled components: (1) Substrate holder, (2) Mobile shutter, (3) Height adjustment system, (4) Shutter rod, (5) Target holder, (6) Position of the nickel target, (7) Argon ion primary gun, (8) DN40CF translator with 150 mm travel, and (9) Ø300 mm mounting flange. 55

Fig. 2-3: IBS deposition machine NORDIKO: view of the inside of the chamber showing the various components. (1) Substrate holder, (2) Argon ion primary gun, (3) Neutralizer, (4) Target shutter, (5) Target holder, (6) Support ion gun, (7) Neutralizer, (8) Mobile shutter. 56

Fig. 2-4: Substrate holder of the NORDIKO machine. The image shows the reference position of the mobile shutter (its starting position), and the blue arrow indicates the direction of its movement during deposition. (1) Silicon wafer substrate (100 µm thickness) placed outside the shutter path and fully exposed to deposition. (2) One of the three polycarbonate (PC) substrates covered by a 100 µm-thick silicon wafer along its length, used to for local thickness measurements. 58

Fig. 2-5: Principal work of the profilometry. (a) Sample holder used on Dektak device. (b) The profiles obtained of the substrate's curvature before and after deposition. Adopted from [115]. 60

Fig. 2-6: White-light interferometric microscope (Talysurf CCI 6000), used for rapid surface topography measurements. 63

Fig. 2-7: Optical and interferometric characterization of sample A. (a) Optical image of the 10 mm × 10 mm nickel film deposited on a PC substrate. The brown region corresponds to the coated area, and the black region highlights the masked (uncoated) area. (b), (c) Corresponding height profiles extracted from the thick and thin sides of the sample, respectively. Red lines represent fits using a bent step function. (d), (e) Interferometric images of the surface morphology on the thick and thin sides of sample A. 64

Fig. 2-8: Schematic diagram of Peak Force Tapping mode. (adapted from [130]). 66

Fig. 2-9: Bruker's Dimension Icon AFM with its main components. (1) Granite stage, (2) Sample stage, (3) Vacuum switch, (4) The SPM head, (5) Screw to release the SPM head, (6) Optics, (7) Photodiode knobs, (8) Laser knobs, (9) LCD display. 67

Fig. 2-10: (a) The microtest-compression (Deben) with its components. (b) Bruker's Dimension Icon AFM with an incorporated straining device (Deben) for sample compression. 68

Fig. 2-11: Stress-strain response of a polycarbonate substrate (10 mm × 10 mm × 2 mm) over five loading cycles. The compression rate was $10^{-3}s^{-1}$. 69

Fig. 2-12 : Schéma de la chambre PVD Nordiko équipée d'un système de volet mobile. (a) Montre une vue externe du côté de la sortie. (b) Présente une vue interne détaillant les composants principaux. Le système est conçu pour permettre un dépôt contrôlé avec un gradient d'épaisseur en déplaçant un volet

mobile devant le substrat. Composants étiquetés : (1) Porte-substrat, (2) Volet mobile, (3) Système de réglage en hauteur, (4) Tige du volet, (5) Porte-cible, (6) Position de la cible de nickel, (7) Canon à ions primaires d'Argon, (8) Translateur DN40CF avec course de 150 mm, et (9) Bride de montage Ø300 mm. 72

Fig. 2-13: Système de micro-compression Deben intégré à l'AFM Bruker Dimension Icon. (a) Vue du dispositif Deben et de ses composants: mâchoires fixe et mobile, capteur de charge et commande motorisée 74

Fig. 3-1 : (a) Optical image of sample A after the first compression cycle. The nickel film was deposited with a continuous thickness gradient along the (*Oy*) direction. A schematic reference bar, shown on the left of the image, illustrates how thickness increases from bottom to top. Several straight-sided buckles (SSBs) are visible, aligned along (*Oy*) and perpendicular to the compression axis (*Ox*). (b) Zoomed-in view of two isolated SSBs, referred to as SSB1 and SSB2 for further analysis..... 77

Fig. 3-2: (a) AFM image of the straight sided buckle SSB1. (b) AFM profiles with respect to local film thickness *h*. 79

Fig. 3-3: (a) Optical image of sample A after the second compression cycle. (b) A zoomed-in view showing that SSB1 became intersected by other buckles, making it unsuitable for analysis. SSB2 remained isolated and was selected for thickness-dependent characterization. 81

Fig. 3-4: Optical and AFM characterization of SSB2. The main image shows an optical image of the SSB2 aligned along (*Oy*) direction. A schematic representation of thickness gradient is shown on the left side. Highlighted dashed boxes show locations where AFM measurements were taken, corresponding to local thicknesses of 177, 183, 190, and 205 nm, respectively. For convenience, two AFM images are shown on the right side. 82

Fig. 3-5: (a) Straight-sided buckle profiles obtained from AFM measurements, with data colored according to their local thickness *h*, with *x* normalized over the half-width *b* (*b* = 3.34 ±0.08 µm). (c) Plot of δ^2 *vs*. h^2, with error bars corresponding to the minimum and maximum values of *h*. 83

Fig. 3-6: Straight-sided buckle lying parallel to the thickness gradient (*Oy*). (a) Optical white-light interferometric image. (b) Height profile along line 1 in (a), showing a thickness gradient along the height step and maximum film thickness of *h* = 198 nm. (c) Buckle profiles extracted from (a) along the oblique lines 2 to 4 (labeled in a), which are oriented at approximately 61° relative to the (*Oy*) axis. The measured edge to peak distances are labelled b_+ and b_-. 85

Fig. 3-7: SSB in sample B " a nickel film on a polycarbonate substrate" lying not parallel (at approximately 40°) to the thickness gradient direction (*Oy*). (a) Optical image of a SSB. (b) AFM (93 × 93 µm^2) image. (c) Buckle profile obtained from AFM measurements corresponding to the oblique (*Ox*') dashed line in (b), with b_- = 15.21 µm and b_+ = 22.31 µm. 86

Fig. 3-8: Telephone cord buckle (TCB) lying approximately parallel to the thickness gradient along the (*Oy*) direction. (a) Optical image of a nickel film on a polycarbonate substrate. Insets show AFM images (93×93µm^2) at two different locations. (b) Step height profile along section line 1 in (a), obtained by white-light interferometric microscopy and fitted with a smoothed bent-step function using Gwyddion software. The local film thickness is measured as *h* = 191 nm. (c) Height profile along section line 2 in (a), also measured by interferometry, illustrating the thickness variation along the gradient. A linear fit confirms its continuous nature. 88

Fig. 3-9: Telephone cord buckling structure of constant width 2*b* = 19.38 µm oriented parallel to the thickness gradient along the (*Oy*) direction. Interferometric optical image of a nickel film on a polycarbonate substrate, with λ_i the local wavelength of the TCB within the thickness gradient..... 89

List of figures

Fig. 3-10: Optical 10 mm × 10 mm image of sample B (nickel-coated polycarbonate substrate), exhibiting a well-controlled thickness gradient along the (*Oy*) direction. (a) Magnified view of the thick edge, showing the nucleation of straight-sided buckles under applied uniaxial compression ($\Delta\sigma_{xx}^{f}$ = 82 MPa and $\Delta\sigma_{yy}^{f}$ = -5.5 MPa). (b) Optical image of the full sample after the complete release of external strain ($\Delta\sigma_{xx}^{f}$ =$\Delta\sigma_{yy}^{f}$=0), revealing the transformation of straight-sided buckles into telephone-cord buckles along the thickness gradient (dashed rectangle). The brown contrast corresponds to the nickel-coated region, whereas the dark areas indicate uncoated PC substrate masked during deposition. The film thickness *h* increases continuously from 0 nm (bottom) to 506 nm (top). A zoomed-in view of the highlighted TCB (dashed rectangle) is shown on the right side. 90

Fig. 3-11: Interferometric optical image of a telephone-cordon buckle in a nickel film on a polycarbonate substrate along a thickness gradient lying along the (*Oy*) direction after the release of the external strain ($\Delta\sigma_{xx}^{f}$ =$\Delta\sigma_{yy}^{f}$ =0). For convenience, only three atomic force microscopy images taken at different *h* positions are presented on the right side. The film thickness *h* varies from 300 nm to 450, as shown on the left side. 92

Fig. 3-12: Morphological parameters of TC buckles in a thickness gradient *h*(*y*): (a) width 2*b* and maximum height δ, (b) normalized maximum height $\delta/2b$ (c) λ (d) normalized wavelength $\lambda/2b$, as a function of *h*(*y*). 93

Fig. 3-13: Finite element modelling and simulation box. The model incorporates a step-by-step thickness gradient simulation along the (a) (O*x*) and (b) (*Oy*) direction. A central delaminated stripe of width 2*b* (shown in white at the middle) is introduced to allow the formation of buckling patterns. (c) Illustration of the thickness gradient along the *i* axis, with *i*=*x* or *y*. A schematic representation of the variation of thickness along the *i* axis, with *i*=*x* or *y*, where the film's thickness decreases step-by-step from h_{max} to $h_{\min}$ across the total length over L_i, which is subdivided into N_i discrete equi-distance sections width $L_k(i)$ for *k* ranging from 1 to N_i. 97

Fig. 3-14: Finite element mesh of the homogeneous plate using S4R shell elements. The nickel film is bonded to a rigid substrate, with a central delaminated stripe (red), where buckling is allowed. The mesh consists of 100 elements along (*Ox*) and 200 along (*Oy*) (total: 20000 elements), with uniform element size 0.6 μm. A zoomed view shows the structured mesh in the stripe region. 98

Fig. 3-15: (a) The normalized height δ/h as a function of the normalized loading σ_{xx}^{0}/σ_c. (b) The normalized out of plane displacement w/h with respect to the normalized in plane coordinate x/b. The blue dashed lines represent the analytical (FvK) solutions. Finite element simulations were performed for a nickel film with Young's modulus E_f = 200 GPa, Poisson's ratio ν_f =0.31, stripe width 2*b* = 6 μm, film's thickness *h* = 20 nm, and uniaxial compressive stress σ_{xx}^{0} varies from 0 to 0.3 GPa and σ_{yy}^{0} =0 GPa. 99

Fig. 3-16: Morphological analysis of a straight-sided buckle lying parallel to the thickness gradient *h*(*y*) along the (*Oy*) direction. (a) Out-of-plane displacement with respect to the local thickness *h* within the gradient. (b) Equilibrium profiles for various thicknesses *h*, with *x* normalized over the half-width *b*. (c) Maximum height δ *vs*. local thickness *h*. Finite element simulations were performed for a nickel film with Young's modulus E_f = 200 GPa, Poisson's ratio ν_f =0.31, stripe width 2*b* = 6.6 μm and uniaxial compressive stress σ_{xx}^{0}= 0.8 GPa and σ_{yy}^{0} =0 GPa. 'Refined elastic' corresponds to FEM simulations taking into account the elasticity of the substrate by correction factors from [37]. 101

Fig. 3-17: Evolution of correction factors (γ_σ, γ_δ) taking into account the elastic contrast α_D of the film/substrate system. α_D=-1 corresponds to the FvK plate theory: (a) γ_σ applied to the critical stress and (b) γ_δ applied to the maximum height δ of the straight-sided buckled, as a function of Dundurs' coefficient α_D. Adopted from [37]. 102

List of figures

Fig. 3-18: Out-of-plane displacements of straight-sided buckles lying parallel to the thickness gradient $h(y)$, for various thickness gradient slopes α and widths $2b$. (a), (e) and (i) correspond to $\alpha = 0.17°$; (b), (f) and (j) to $\alpha = 0.13°$; (c), (g) and (k) to $\alpha = 0.09°$; (d), (h) and (l) to $\alpha = 0.04°$. The stripe width of the initially-debonded zone is $2b = 12$ µm for (a) to (d), $2b = 9.6$ µm for (e) to (h) and $2b = 6$ µm for (i) to (l). In (e) two equilibrium states are separated by dashed lines, the no buckling state (plane) and the straight-sided buckled state. Finite element simulations were performed for a nickel film with Young's modulus $E_f = 200$ GPa, Poisson's ratio $\nu_f = 0.31$, and uniaxial compressive stress $\sigma_{xx}^0 = 0.8$ GPa and $\sigma_{yy}^0 = 0$ GPa. 104

Fig. 3-19: FEM numerical results of a straight-sided buckle lying parallel to the thickness gradient $h(y)$ along the (Oy) direction. Maximum height δ of a straight-sided buckle *vs*. internal stress σ_{xx}^0, for various normalized local thickness $h(y)/h_{min}$ and gradient slope α for: (a) $\alpha = 0.17°$ and $h_{min} = 40$ nm, (b) $\alpha = 0.13°$ and $h_{min} = 30$ nm, (c) $\alpha = 0.09°$ and $h_{min} = 20$ nm, (d) $\alpha = 0.04°$ and $h_{min} = 10$ nm. h_{min} is the minimum thickness of the considered. Finite element simulations were performed for a nickel film with Young's modulus $E_f = 200$ GPa, Poisson's ratio $\nu_f = 0.31$, stripe width $2b = 6$ µm, and uniaxial compressive stress $\sigma_{xx}^0 = 0.8$ GPa and $\sigma_{yy}^0 = 0$ GPa. 106

Fig. 3-20: Same as in Fig. 3-19 for various stripe widths (a) $2b = 9.6$ µm, (b) $2b = 12$ µm. Finite element simulations were performed for a nickel film with Young's modulus $E_f = 200$ GPa, Poisson's ratio $\nu_f = 0.31$ and uniaxial compressive stress $\sigma_{xx}^0 = 0.8$ GPa and $\sigma_{yy}^0 = 0$ GPa. 108

Fig. 3-21: FEM numerical results of a straight-sided buckle lying parallel to the thickness gradient $h(y)$ along the (Oy) direction. Maximum height δ of a straight-sided buckle *vs*. the applied stress σ_{xx}^0 for various stripe widths and with the same gradient slope for α, and local thickness h: (a) $h = 37$ nm, (b) $h = 74$ nm, (c) $h = 111$ nm, (d) $h = 148$ nm. Finite element simulations were performed for a nickel film with Young's modulus $E_f = 200$ GPa, Poisson's ratio $\nu_f = 0.31$, and uniaxial compressive stress $\sigma_{xx}^0 = 0.8$ GPa and $\sigma_{yy}^0 = 0$ GPa. 110

Fig. 3-22: The dependence of onset of buckling σ_c^{TG} *versus* the local film thickness h for various gradient slopes α, and two stripe widths (a) $2b = 6$ µm and (b) 12 µm (b). Color points represent FEM data for various α. Dashed black line corresponds to the analytical FvK for a homogenous plate, with Eq. (3-4). The inset zoom highlighting the deviations between FEM results and the analytical FvK. Finite element simulations were performed for a nickel film with Young's modulus $E_f = 200$ GPa, Poisson's ratio $\nu_f = 0.31$, and uniaxial compressive stress $\sigma_{xx}^0 = 0.8$ GPa and $\sigma_{yy}^0 = 0$ GPa. 111

Fig. 3-23: The dependence of onset of buckling σ_c^{TG} *versus* $(h/b)^2$ for various gradient slopes α for two stripe widths $2b = 6$ µm, and 12 µm. Color points represent FEM data for various α, while cercle symbol (data for $2b = 6$ µm) and square (data for $2b = 12$ µm). Dashed black line corresponds to the analytical FvK for a homogenous plate, with $\sigma_c = \pi^2 E_f/(1-\nu_f^2).(h/b)^2$. Finite element simulations were performed for a nickel film with Young's modulus $E_f = 200$ GPa, Poisson's ratio $\nu_f = 0.31$, and uniaxial compressive stress $\sigma_{xx}^0 = 0.8$ GPa and $\sigma_{yy}^0 = 0$ GPa. 112

Fig. 3-24: The locally normalized out-of-plane displacement w/h of a straight-sided buckle lying parallel to the thickness gradient $h(y)$ along the (Oy) direction with respect to the normalized x position to the half-width x/b for various normalized local thickness $h(y)/h_{min}$ and gradient slope α for : (a) $\alpha = 0.13°$ and $h_{min} = 30$ nm, (b) $\alpha = 0.17°$ and $h_{min} = 40$ nm. Finite element simulations were performed for a nickel film with Young's modulus $E_f = 200$ GPa, Poisson's ratio $\nu_f = 0.31$, stripe width $2b = 12$ µm, and uniaxial compressive stress $\sigma_{xx}^0 = 0.8$ GPa and $\sigma_{yy}^0 = 0$ GPa. 113

Fig. 3-25: Influence of a thickness gradient $h(x)$ perpendicular to a straight-sided buckle lying along the (Ox) direction. (a) Out-of-plane displacements with respect to the different thickness gradients (h_{max}/h_{min}) with their associated asymmetry b_+/b. (b) Mapping of equilibrium profiles of the SS buckle with respect to h_{max}/h_{min}. Finite element simulations were performed for a nickel film with Young's

modulus E_f = 200 GPa, Poisson's ratio ν_f =0.31, maximum thickness h_{max} = 150 nm, stripe width 2b = 36 µm, and uniaxial compressive stress σ_{xx}^0= 0.8 GPa and σ_{yy}^0 =0 GPa. The number of sections N_x along the width is considered to be 60. 115

Fig. 3-26: (a) Normalized asymmetry ratio b_+/b_- *versus* h_{max}/h_{min} for various width 2b. (b) Zoom on the region of small value h_{max}/h_{min}. Finite element simulations were performed for a nickel film with Young's modulus E_f = 200 GPa, Poisson's ratio ν_f =0.31, stripe width 2b = 36 µm (blue squares), 2b = 12 µm (red squares), and uniaxial compressive stress σ_{xx}^0= 0.8 GPa and σ_{yy}^0 =0 GPa. The number of sections N_x along the width is considered to be 60 and 40 for 2b = 36 µm and 12 µm, respectively. 116

Fig. 3-27: Influence of a thickness gradient $h(x)$ perpendicular to a straight-sided buckle on the onset of buckling. Maximum height δ of a straight-sided buckle *vs*. internal stress σ_{xx}^0, for two thickness gradients h_{max}/h_{min}. Finite element simulations were performed for a nickel film with Young's modulus E_f = 200 GPa, Poisson's ratio ν_f =0.31, h_{max} = 150 nm, stripe width 2b = 36 µm, and uniaxial compressive stress σ_{xx}^0= 0.8 GPa and σ_{yy}^0 =0 GPa. The number of sections N_x along the width is considered to be 60. 117

Fig. 3-28: Out-of-plane displacements of buckles lying parallel to the thickness gradient $h(y)$, for various thickness gradient slopes α and widths 2b. (a), (e) and (i) correspond to α = 0.17°; (b), (f) and (j) to α = 0.13°; (c), (g) and (k) to α = 0.09°; (d), (h) and (l) to α = 0.04°. The stripe width of the initially-debonded zone is 2b = 12 µm for (a) to (d), 2b = 9.6 µm for (e) to (h) and 2b = 6 µm for (i) to (l). In (e), three equilibrium states are separated by dashed lines, the no buckling state (plane) and the buckled states characterized by straight-sided (SSB) and telephone-cord (TCB) buckles. Finite element simulations were performed for a nickel film with Young's modulus E_f = 200 GPa, Poisson's ratio ν_f =0.31, and isotropic compressive stress $\sigma_{xx}^0 = \sigma_{yy}^0$ = 0.8 GPa. 119

Fig. 3-29: Critical stress for the straight-sided to the telephone cord transition in a thickness gradient $\sigma_{SS\text{-}TC}$ *vs*. (a) thickness h and (b) width 2b. Finite element simulations were performed for a nickel film with Young's modulus E_f = 200 GPa, Poisson's ratio ν_f =0.31 and isotropic compressive stress $\sigma_{xx}^0 = \sigma_{yy}^0$ = 0.8 GPa. 120

Fig. 3-30 : Critical stress for the straight-sided to the telephone cord transition in a thickness gradient, $\sigma_{SS\text{-}TC}$ *vs.* σ_c. Finite element simulations were performed for a nickel film with Young's modulus E_f = 200 GPa, Poisson's ratio ν_f =0.31 and isotropic compressive stress $\sigma_{xx}^0 = \sigma_{yy}^0$ = 0.8 GPa. 121

Fig. 3-31: Wavelength of a telephone-cord buckle λ vs. local thickness $h(y)$ for various half-width b and gradient intensity α. Finite element simulations were performed for a nickel film with Young's modulus E_f = 200 GPa, Poisson's ratio ν_f =0.31 and isotropic compressive stress $\sigma_{xx}^0 = \sigma_{yy}^0$ =0.8 GPa. 122

Fig. 3-32: FEM mechanical modelling and boundary conditions of the simulation box. A delaminated area is located at the middle part with a tapered strip width 2$b(y)$ (see white areas). The film's thickness decreases from 450 nm at y = 0 to 300 nm at $y = L_y$, with the distance L_y divided into N discrete, equidistant sections width L_y/N. 123

Fig. 3-33: Simulated telephone cordon buckles presented in Fig. 3-12 (Out-of-plane displacement) aligned parallel to the thickness (*resp.* width) gradient $\boldsymbol{h(y)}$ (*resp.* 2$b(y)$), under various internal stresses σ_0. (a), (b), (c), and (d) correspond to 0.6, 0.7, 0.8, 0.9 and 1 GPa, respectively. Finite element simulations were performed for a nickel film with Young's modulus E_f = 200 GPa, Poisson's ratio ν_f =0.31... 124

Fig. 3-34: Experimental and FEM morphological parameters of TCB in a film with both thickness and width gradients. (a) Buckle width 2b (black; left side) and maximum height δ (red; right side) as a function of the local film thickness h. (b) Normalized maximum height $\delta/2b$ *vs*. h. (c) Computed ratio

of local heights $\delta_{FEMelastic}/\delta_{FEMrigid}$ *vs*. h. FEM simulations corresponding to a nickel film (E_f = 200 GPa, v_f = 0.31) on a polycarbonate substrate (E_s = 2.5 GPa, v_s = 0.37). 126

Fig. 3-35: Experimental and FEM evolution of (a) the local wavelength λ and (b) the normalized wavelength $\lambda/2b$ of TCB as a function of the local film thickness h, for various internal stresses σ_0. FEM simulations were performed for a nickel film (E_f = 200 GPa, v_f = 0.31). 128

Fig. 3-36: Influence of a thickness gradient $h(x)$ lying along the (Ox) direction and perpendicular to a telephone cord buckle. Out-of-plane displacements with respect to the various thickness gradients (h_{max}/h_{min}). Finite element simulations were performed for a nickel film with Young's modulus E_f = 200 GPa, Poisson's ratio v_f =0.31, stripe width $2b$ = 12 µm and isotropic compressive stress σ_0 = 3.0 GPa. The number of sections N along the width is considered to be 40. h_{max} is fixed to 150 nm and h_{min} ranges 150 to 40 nm. 129

Fig. 3-37: Out-of-plane displacement profiles w *vs*. normalized x to the width $x/2b$ of the TCB in (a) a uniform film and (b) a film exhibiting a thickness gradient of h_{max}/h_{min} =2.03. Finite element simulations were performed for a nickel film with Young's modulus E_f = 200 GPa, Poisson's ratio v_f =0.31, stripe width $2b$ = 12 µm, h_{max} = 150 nm and isotropic compressive stress σ_0 = 3.0 GPa. The number of sections N along the width is considered to be 40. 130

Fig. 3-38: Influence of a thickness gradient $h(x)$ perpendicular to a TCB lying along the (Oy) direction for various h_{max}/h_{min} and σ_0. (a) Dependence of the normalized edge-to-peak distance ratio b_-/b_+ along line A and B, with respect to the thickness gradient h_{max}/h_{min}. (b) Degree of asymmetry γ of the TCB along sections A and B, defined as $\gamma = (b_+/b_-)_A/(b_+/b_-)_B$, with respect to the thickness gradient. Finite element simulations were performed for a nickel film with Young's modulus E_f = 200 GPa, Poisson's ratio v_f =0.31, stripe width $2b$ = 12 µm, h_{max} = 150 nm. The number of sections N along the width is considered to be 40. 131

Fig. 3-39: Influence of a thickness gradient $h(x)$ perpendicular to a telephone cord buckle lying along the (Oy) direction. Relative height difference Δ with respect to the thickness gradient h_{max}/h_{min} for various σ_0. Finite element simulations were performed for a nickel film with Young's modulus E_f = 200 GPa, Poisson's ratio v_f =0.31, stripe width $2b$ = 12 µm, h_{max} = 150 nm. The number of sections N along the width is considered to be 40. 132

Fig. 3-40: (a) Relative height difference Δ and (b) degree of asymmetry γ of the TC buckle, with respect to the thickness gradient h_{max}/h_{min}.. Finite element simulations were performed for a nickel film with Young's modulus E_f = 200 GPa, Poisson's ratio v_f =0.31, h_{max} = 150 nm and isotropic compressive stress σ_0 = 1 GPa. The number of sections N along the width are considered to be 40, 60 and 120 for $2b$ = 12, 18 and 36 µm, respectively. 133

Fig. 3-41: (a) Caractérisation optique et AFM du film de nickel SSB2 présentant un gradient d'épaisseur. (b) Hauteur maximale de la ride (δ) en fonction de l'épaisseur locale (h). Les résultats expérimentaux et les simulations FEM confirment que δ diminue lorsque h augmente. La prise en compte de l'élasticité du substrat améliore l'accord avec l'expérience..... 137

Fig. 3-42: L'évolution de la hauteur maximale δ d'une ride droite en fonction de la contrainte interne σ_{xx}^0, pour différentes épaisseurs locales normalisées $h(y)/h_{min}$..... 137

Fig. 3-43: (a) Caractérisation optique et AFM d'une ride droite présentant un gradient d'épaisseur. (b) Profil de déplacement hors plan w le long de l'axe x', mesuré à un angle de 40° par rapport à la direction du gradient (Ox). (c) Déplacement hors plan schématisé en fonction du gradient d'épaisseur. Ce diagramme représente la variation du déplacement hors plan en fonction du profil d'épaisseur. (d) Profils d'équilibre de la ride (SS buckle), montrant la variation du déplacement ($w(x, y) + h(x)$) en fonction du rapport de gradient h_{max}/h_{min}. 138

List of figures

Fig. 3-44: (a) Structure de flambage en cordon téléphonique (*Telephone cord buckling*) de largeur constante $2b$ = 19.38 µm orientée parallèlement au gradient d'épaisseur le long de la direction (Oy). (b) Déplacement hors plan schématisé en fonction du gradient d'épaisseur. (c) Longueur d'onde (λ) d'une cloque en cordon téléphonique en fonction de l'épaisseur locale $h(y)$ pour différentes demi-largeurs b et différentes pentes de gradient α. (d) Contrainte critique pour la transition de la cloque à rides droits au cordon téléphonique dans un gradient d'épaisseur, $\sigma_{SS\text{-}TC}$ en fonction de σ_c. 139

Fig. 3-45: (a) Différence de hauteur relative (Δ) et (b) degré d'asymétrie (γ) de la cloque en cordon téléphonique (TCB), en fonction du gradient d'épaisseur h_{max}/h_{min}. 140

Fig. 4-1: Optical image of spontaneous buckles in Ni (940 nm)/PC. (a) Three days and (b) six months after deposition. 142

Fig. 4-2: Optical image of spontaneous buckles, mainly TCBs in Mo (300nm)/Si(100µm), taken shortly after few days of deposition. 143

Fig. 4-3: Optical images of sample C. (a) as deposited and (b) after final loading. The thickness gradient is shown on the left side, with h varying from 10 to 580nm along the (Oy) direction. 144

Fig. 4-4: Stress-strain curve of the PC substrate. S_i represents the loading step i (i varies from 1 to 6), reporting in table 4-1. 145

Fig. 4-5: Straight-sided buckle in a nickel film deposited on a polycarbonate substrate propagating along a thickness gradient lying along the (Oy) direction. The optical image in the middle was obtained at the final loading stage. The thickness gradient is shown on the left side, ranging from the thicker upper part down to the thinner lower. Six loading increments were performed by uniaxial compression of the substrate along the (Ox) axis. The critical thickness of arrest of the buckle is reported for each loading step S_i as horizontal color lines. For convenience, only the atomic force microscopy investigations of the loading steps S_1 and S_4 are presented on the right side. 147

Fig. 4-6: Morphological parameters of the straight-sided buckle extracted from AFM investigation (table 4-1). The front width $2b_{front}$ is plotted on the left and the front height δ_{front} on the right, as a function of the elastic strain energy stored in the unbuckled plate per unit area G_0..... 148

Fig. 4-7: Straight-sided buckle in a nickel film deposited on a polycarbonate substrate propagating along a thickness gradient lying along the (Oy) direction. The optical image in the middle was obtained at the final loading stage. The thickness gradient is shown on the left side, ranging from the thicker upper part down to the thinner lower. Seven loading increments were performed by uniaxial compression of the substrate along the (Ox) axis. The critical thickness of arrest of the buckle is reported for each loading step S_i as horizontal color lines. For convenience, only the atomic force microscopy investigations of the loading steps S_1 and S_5 are presented on the right side. 149

Fig. 4-8: (a) Schematic illustration of the 3D geometrical model illustrating the variation of thickness of the Ni film along the Oy direction. (b) Bilinear traction-separation law used for modeling interfacial damage between the film and substrate. (c) Mode-mixity dependent interfacial toughness $G_c(\psi)$, representing the total energy required for interface fracture. 153

Fig. 4-9: Comparison of the SS buckle evolution for interfacial toughness G_{IC} (a) = 0.8 J/m² and G_{IC} (b) = 0.3 J/m². An initial defect of square geometry of length l_x = 12 µm is highlighted by a square white dashed line. Out-of-plane displacement w, scalar damage variable d, elastic energy stored in the element G^*(J/m²) and mode mixity angle $\psi(°)$ obtained for a Ni film on a rigid substrate (h_f = 200 nm, E_f = 200 GPa, ν_f = 0.31, σ_{xx}^f = 1.213 GPa, σ_{yy}^f = 0 GPa, T_n^0 = 18 MPa, T_t^0 = 39 MPa, η = 0.9, t_i = 0.002 s, t_f = 0.008 s). The time evolution is shown in each row, from the initial time t_i, where σ_o is initially reached up to t_f, the end of the simulation. 155

List of figures

Fig. 4-10: Comparison of the SS buckle evolution for interfacial toughness G_{IC} (a) = 0.8 J/m² and G_{IC} (b) = 0.3 J/m². An initial defect of square geometry of length l_x = 12 µm is highlighted by a square white dashed line. Out-of-plane displacement w, scalar damage variable d, elastic energy stored in the element G^*(J/m²), and mode mixity angle $\psi(°)$ obtained for a Ni film on PC substrate (h_f = 200 nm, h_s = 12 µm E_f = 200 GPa, ν_f = 0.31, E_s = 2.5 GPa, ν_s = 0.37, σ_{xx}^f = 1.213 GPa, σ_{yy}^f = 0 GPa, T_n^0 = 18 MPa, T_t^0 = 39 MPa, η = 0.9, t_i = 0.002 s, t_f = 0.08 s). The time evolution is shown on each row, from the initial time t_i, where σ_o is initially reached up to t_f , the end of the simulation..... 157

Fig. 4-11: FEM simulations of a straight-sided buckle propagating in a thickness gradient $h(y)$ lying along the (Oy) direction. (a) Out-of-plane displacements w on the right side and mode mixity angle ψ on the left side. FEM/CZM simulations for a nickel film deposited on a rigid substrate (E_f = 200GPa, ν_f = 0.31, h_{max} = 200 nm, h_{min} = 10 nm, σ_{xx}^f = 1.31 GPa, σ_{yy}^f = 0.88 GPa, T_n^0 = 18 MPa, T_t^0 =39 MPa, η = 0.9, G_{IC} = 0.52 J/m²)..... 159

Fig. 4-12: Numerical simulations of a straight-sided buckle propagating in a thickness at three different loading steps S_1, S_3 and S_6. (a) Out-of-plane displacements. The thickness gradient $h(y)$ is lying along the (Oy) direction, as shown on the left side. (b) Mode mixity angle ψ. FEM/CZM simulations for a nickel film deposited on polycarbonate substrate (E_f=200 GPa, ν_f= 0.31, E_s=2.5 GPa, ν_s= 0.37, h_{max}=200 nm, h_{min}=10 nm, T_n^0 = 18 MPa, T_t^0 =39 MPa, η = 0.9, G_{IC} = 1.6 J/m²)..... 161

Fig. 4-13: FEM interfacial toughness characteristics. (a) Critical thickness of arrest of the buckle h^* *versus* G_{IC} for four loading steps from S_1 to S_4, for η =0.9. The loading state (σ_{xx}^f,σ_{yy}^f) given in Table 1 for each S_i is recalled in the legend, the experimental values of h^* as horizontal color lines as well. (b) Numerical interfacial toughness (G_{IC}, η) combination for the four loading step S_i allowing to mimic the experimental arresting buckle thicknesses h^*_i. FEM/CZM simulations for a nickel film deposited on polycarbonate substrate (E_f=200 GPa, ν_f= 0.31, E_s=2.5 GPa, ν_s= 0.37, h_{max}=200 nm, h_{min}=10 nm, T_n^0 = 18 MPa, T_t^0 =39 MPa)..... 163

Fig. 4-14: FEM configuration with cohesive zone model. Film is considered to be elastic film with E_f = 200 GPa and ν_f = 0.31 and the substrate rigid. Internal stress: σ_0 = 0.8 GPa. Width 2b = 12 µm. Thickness gradient: h_{max} = 170 nm, h_{min} = 60 nm. Cohesive zone parameters: normal loading T_n^0 = 18 MPa, shear loading T_s^0 = 39 MPa. Interfacial toughness of the film/substrate: G_{IC} = 0.36 J/m² and η = 0.9..... 164

Fig. 4-15: (a) Out-of-plane displacement w. (b) The damage variable d. (c) ψ angle (see the color bar on the right) along the two sides of an asymmetrical straight-sided buckle. FEM simulations with parameters given in Figure 3-15. FEM/CZM simulations for a nickel film deposited on a rigid substrate (E_f = 200GPa, ν_f = 0.31, h_{max} = 170 nm, h_{max} = 60 nm, 2b = 12 µm, T_n^0 = 18 MPa, T_t^0 =39 MPa, η = 0.9, G_{IC} = 0.36 J/m², σ_0 = 0.78 GPa)..... 165

Fig. 4-16: Image optique de flambages spontanés dans (a) Ni (940 nm) / PC, observés (a) trois jours et (b) six mois après le dépôt. (c) Flambages en cordons de téléphone (TCBs) spontanés dans un film de Mo (300 nm) sur Si (100 µm) observés peu après le dépôt. 167

Fig. 4-17: (a) Courbe contrainte-déformation du substrat PC et étape de chargement. (b) Image optique et AFM illustrant la propagation et l'arrêt des SSBs dans le gradient..... 168

Fig. 4-18: Caractéristiques de la ténacité interfaciale FEM. (a) Déplacements hors-plan w et 5 (b) angle de mode mixité (ψ) simulés pour les étapes S_1, S_3 et S_6. (b) Épaisseur critique d'arrêt h_i^* simulée en fonction de G_{IC} pour quatre paliers de chargement. (c) Combinaisons numériques de ténacité interfaciale (G_{IC}, η) permettant de reproduire les épaisseurs d'arrêt expérimentales h_i^*..... 169

Fig. 4-19: (a) Déplacement hors plan w. (b) Variable d'endommagement d. (c) Angle ψ (voir l'échelle de couleurs à droite) le long des deux flancs d'une cloque à flancs droits asymétrique..... 170

List of figures

Fig. I-1: (a) AFM observations of confined TCBs propagating in Y_2O_3 film on GaAs substrate exhibiting thickness gradient of 50 to 30nm, adopted from [50]. Numerical simulations of a TCB propagating in various thickness gradient (h_{max}/h_{min}) along the (Oy) direction, shown on the left side. Each column presents various thickness gradient, represented as h_{max}/h_{min}. (b) Out-of-plane displacement w. (c) Mode mixity angle ψ. FEM/CZM simulations for a film deposited on a rigid substrate (E_f = 200GPa, ν_f = 0.31, h_{max} = 200 nm, l = 12 µm, T_n^0 = 18 MPa, T_t^0 =117 MPa, η = 0.9, G_{IC} = 0.9 J/m², σ_{xx}^f = 2.0 GPa, σ_{yy}^f = 1.76 GPa. 176

List of tables

Table 2-1: Summary of the deposited samples, deposition directions, shutter speeds, and residual stress (σ_0) for nickel films on PC substrates. 59

Table 2-2: Résumé des échantillons déposés, directions/vitesses du volet, et contrainte résiduelle (σ_0) pour les films de nickel sur substrats PC. 73

Table 3-1: Experimental morphological characteristics of the straight-sided buckle profile extracted misaligned to the thickness gradient. 87

Table 4-1: Experimental morphological and mechanical characteristics of the straight-sided buckle propagating in the thickness gradient direction shown in Fig. 4-5. The internal stress in the film σ_0=0.91 GPa. 146

Table 4-2: Experimental morphological and mechanical characteristics of the straight-sided buckle propagating in the thickness gradient shown in Fig. 4-7. The internal stress in the film σ_0=0.81±0.1 GPa. 150

List of symbols

u, v : In-plane displacements

w : Out-of-plane displacement

δ : Height

σ : Stress

σ_c : Critical buckling stress

σ_0 : Internal stress

ϵ : Strain

E : Young's modulus

ν : Poisson's ratio

h : Thickness

α : Thickness gradient slope

G : Energy release rate

U : The total elastic energy stored in the plate

K : Cohesive stiffness

ω : Phase angle

$2b$: Stripe width

β_t, β_l and η : Dimensionless parameters

λ : Wavelength

G_C : Interfacial toughness

G_{IC} and G_{IIC} : Mode I and II interfacial toughness, respectively

ψ : Mode mixity angle

G_0 : Elastic strain energy stored in the film by unit surface in the unbuckled film

G^* : Stored elastic energy per unit surface

α_D and β : Dundurs' coefficients

Introduction: State of the art

Thin films and coatings play a crucial role in a wide range of technological applications, such as microfluidics, microelectronics, optical devices and thermal barrier systems [1,2]. These films are commonly produced by chemical vapor deposition (CVD) [1] or physical vapor deposition (PVD) techniques [3–5] and often exhibit large intrinsic stresses, either compressive or tensile, sometimes reaching several gigapascals (GPa) [6,7]. Such intrinsic stresses can induced various types of damage, substantially affecting the performance and reliability of the films/substrate systems [8,9]. Common sources of stress in films include mismatches in thermal expansion coefficients and lattice parameters between the film and substrate [6,9]. Under compressive stress, thin films frequently undergo delamination, accompanied by the formation of various buckling patterns. Buckling phenomena are multi-scale, ranging from macro to micro-scale, and even down to atomic scale in the case of two-dimensional materials such as graphene [10] or MoS_2 [11]. The buckling patterns are widely observed using optical (OM) and atomic force microscopy (AFM). Various buckling morphologies have been characterized in compressed films, including straight-sided (SSB) buckles [12–16], circular buckles (CB) [17–21] or telephone cord (TCB) buckles [16,22–25], which have been documented in details in [26], and illustrated in Fig. 1.

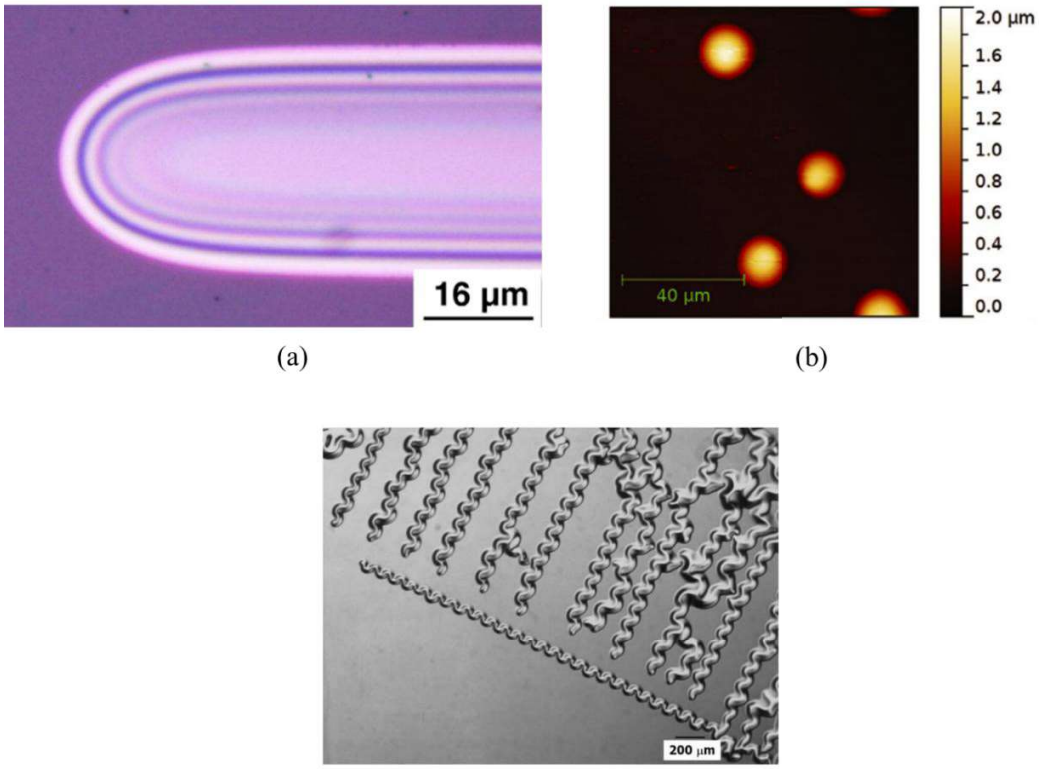

(a) (b)

(c)

Fig. 0-1: Various buckling structures. (a) Straight sided buckle [16], (b) circular buckle [21], (c) telephone cord (TC) buckles [27].

By far, the most commonly observed buckling morphologies are TC buckles, primary due to the isotropic stress often present in coatings and thin films [24,28–30]. These TC buckles can originate either result from instabilities at the delamination crack front [30,31] or from the secondary buckling of SS buckles as they evolve further [16,24,26,28,32,33].

Even though, the SSB and CB are well understood for homogenous films on rigid substrates within the framework of the elastic plate theory [26]. Experimental results for those buckles in hard films on compliant substrates show that their critical stress for buckling and the maximal heights differ from the predicted critical stress from the theoretical ones. Zhao *et al.* [34] extended the Föppl–von Kármán (Fvk) nonlinear plate theory to include substrate compliance and studied its effect on circular buckles. They showed that softer substrates significantly reduce the critical buckling stress and increase buckle height. Additionally, the energy release rate increases for shorter radius of the circular delaminated film. The critical stress for the SSB is affected by the compliant substrate similarly to the CB. One can cite the work of by B. Cotterell and Z. Chen [35],

and later by Hutchinson and Suo [36], the later studied and analyzed the SSB delamination with more focus on the effects of substrate compliance, in particular the critical buckling, the energy release rate at the mode mixity of the interface delamination crack as a function of the elastic mismatch between the film and substrate. They found that, the more compliant the substrate, the easier for the film to buckle and the higher the energy release rate. Later, Parry *et al.* [37] investigated in details, the effects of compliant substrate on the straight sided buckles for various film/substrate systems using finite element method simulations. They showed that the critical stress for buckling decreases, as well as the increase in the maximal height with increasing the elastic mismatch between the film and substrate. Additionally, the profile of the straight sided buckle differs from the analytical profile of the elastic plate theory. The effect of substrate compliance was also observed in the work of Piet C.P. Bouten *et al.*[38] and O. van der Sluis *et al*. [39]. The substrate compliance not only influence the critical stress, and maximal height but also causes small depression at edges of the straight sided buckle, one can cite the work of Yin Zhang *et al.* [40]. Later Boijoux *et al.* [41], developed numerical model which analyses the depression of this buckle with respect to the elastic mismatch, and shows that the elastic mismatch can be determined from analyzing the height of straight sided buckle profile and its depression along the edges. Using the elastic mismatch, mechanical properties can be directly assessed such as Young's modulus of the film/substrate system. Although often considered undesirable, the buckling of films can offer valuable insights about the mechanical properties of the associated materials, such as film/substrate Young's moduli, internal stress or toughness [22,23,38,39,42,43]. For instance, Coupeau *el al*. [42,43] , shows that the Young's modulus of the film/substrate system can be determined. This method of using buckling morphologies was successfully applied to stainless steel 600 nm thick film deposited on silicon wafers. Determining the interfacial adhesion using the SS and CB of the hard film/rigid system is well explored analytically by Hutchinson and Suo [26]. However, assessing the interfacial toughness from complex buckling structures such as telephone cord buckles remains an open subject. Nevertheless, numerical models using finite element simulation provides deep understanding of assessing the interfacial toughness, for instance the work of Faou *et al.* [22], where they demonstrated that the interfacial adhesion of mode I can be directly determined from the wavelength of telephone cord buckles, the wavelength was used to determine the interfacial adhesion for a series of films with identical SiO_2/Ag interface. Cordill *et al.* [23] assessed interfacial adhesion from telephone cord buckles in tungsten films on SiO_2 substrates with various film thickness. They found that using inflection points of the TC buckle profile gave interfacial adhesion within 15% of the values calculated by approximating those buckles as SS buckles. Finally, the finite element method (FEM) has played a crucial role in advancing the understanding of buckling phenomena [16,22,26,28,29,44–46]. Finite element method incorporated with a cohesive zone model approach is utilized in investigating the propagation of buckles. In this context, Faou *et al.* [25,30] were able for the first time to model the TC buckle, and shows that mode mixity was the responsible of TC buckles undulation. A phase diagram of delamination morphologies was developed, and shown in Fig. 2 based on the two normalized parameters of mode I toughness interface of the film/substrate and energy and the

elastic strain energy per unit surface stored in the film *vs.* the normalized residual stress and the bulk young's modulus. The aforementioned phase diagram includes the boundary for no delamination of the film/substrate, to TC buckles and its branches, and finally to complete delamination when the elastic strain energy per unit surface stored in the film becomes important.

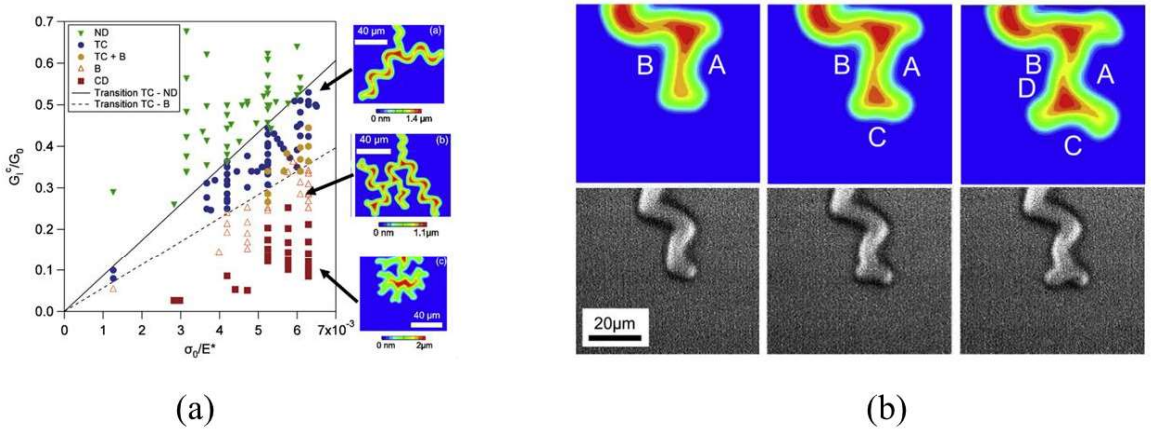

Fig. 0-2: (a) Morphological mapping of buckling-driven delamination patterns (symbols) for η=0.95 and ν=0.31. (b) Out-of-plane displacement of telephone-cord buckle branches, as obtained from FEM simulations (top) and experimental measurements (bottom). In the experiment, fracture occurs along the SiO_x/Ag interface, involving 15 nm Ag layer overlaid by 132 nm MoO_x film with residual stress σ_0=1.84 GPa. FEM simulations were performed using parameters G_{IC}/G_0 = 0.34 and σ_0/E^*=6.1×10^{-3}. Adopted from [25].

Jagla [47] proposed a finite element-like approach using a two dimensional triangular mesh as a thin film elastically attached to a rigid substrate to model buckling and delamination. Unlike FEM methods, the nodes in the mesh interact with their neighbors through defined elastic constants, which include the stretching constant, the bending constant, and an additional constant that accounts for the Poisson ratio of the material. Using this model, several buckling structures and delamination of thin films found in experiments, are modeled and are shown in Fig. 3

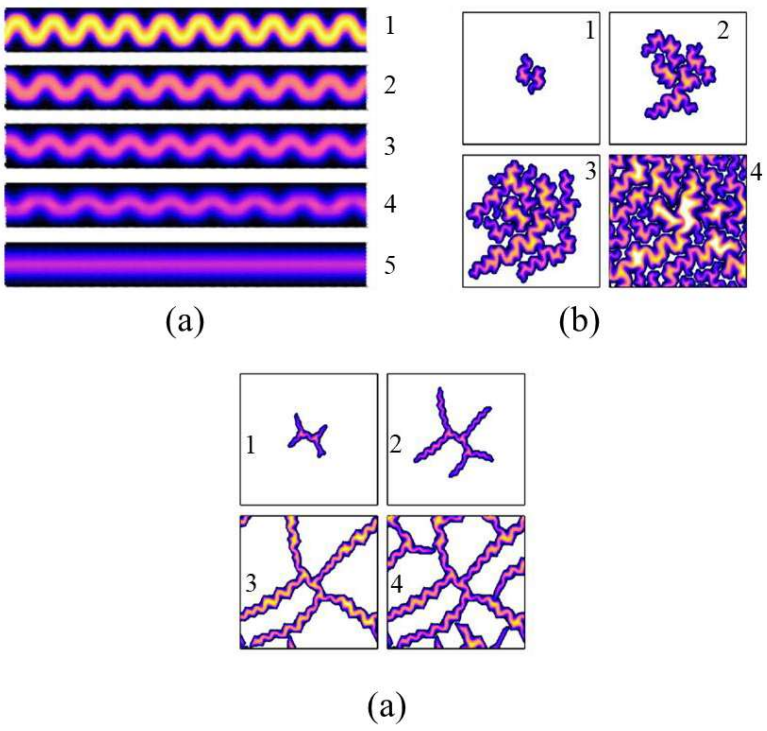

Fig. 0-3: (a) Buckled configuration of the stripe for ν= 1/3 and $\varepsilon/\varepsilon_1$= 6.25, 7.5, 9.4, 12.5, and 25 (from 1 to 5). The gray (color) represents the out-of-plane displacement of the film, expressed in units of the discretization length l_0. The stripe width corresponds to 1875.l_0/2. (b) Temporal evolution of the delaminated regions for ε=0.09, $k_b/(k_s l_0^2)$= 0.05, $f_{max}/(k_s l_0)$= 0.03, and k_h=k_s. The gray (color) scale ranges from darker to brighter with increasing film height, while non-delaminated areas are shown in white for clarity. The vertical scale is expressed in units of l_0. The four snapshots correspond to dimensionless times τ= 5×10^3, 2×10^4, 3.5×10^4, and 2×10^5. (c) Same as (b), for ε = 0.07 and k_h =k_s/100, shown at τ = 2.4×10^3, 5.4×10^3, 3.5×10^4, and 1×10^5. Adopted from [47].

The influence of film thickness on buckling behavior has been investigated experimentally. In particular, Zhang *et al*. [48] and Yu. *et al*. [49] studied buckling in thin films with varying thicknesses. Their results demonstrated that thicker regions tend to show pronounced TC buckles and its branches, while thinner regions exhibit smaller buckling heights, as illustrated in Fig. 4. Furthermore, they observed that beyond a certain thickness, the film undergoes complete delamination from the substrate. This behavior is attributed to the increase in elastic energy stored as the film thickness increases.

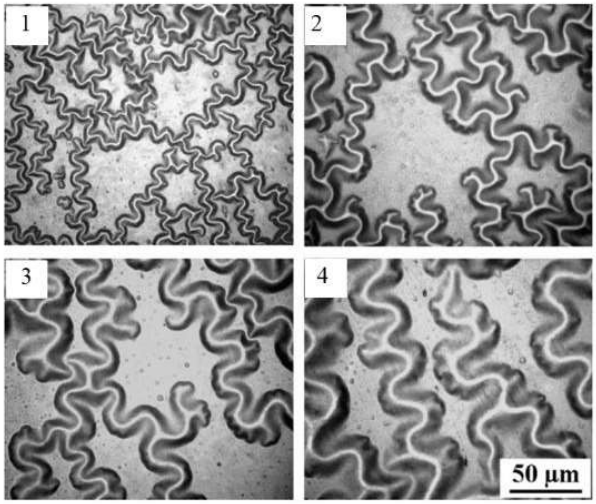

Fig. 0-4: Optical images (Each image has a size of 200 × 160 μm^2) of the telephone-cord buckles in a wedge-shaped Fe film sample for various thicknesses h. (1) h = 40 nm, (2) h = 70 nm, (3) h = 100 nm, (4) h = 130 nm. Adopted from [49].

Most of these studies focus on homogeneous films, where the thickness is assumed to be constant. However, Paumier *et al.* [50] experimentally investigated buckling in thin films with a thickness gradient induced by a shadowing effect during the deposition. Although the thickness gradient or variation was not controlled, their results showed that thicker regions tend to develop more pronounced buckling, while thinner regions exhibit reduced TC buckling heights, as shown in Fig. 5. Moreover, they observed that when the film thickness falls below a critical threshold, the formation of TCBs can be entirely confined and suppressed (Fig. 5).

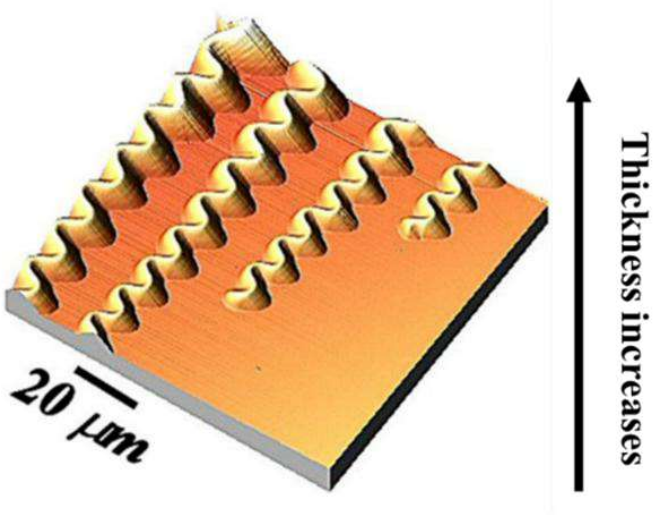

Fig. 0-5: The propagation of confined telephone-cord buckles in Y_2O_3 film deposited on GaAs exhibiting a thickness gradient (30-50 nm), deposited on GaAs. Adopted from [50].

Additionally, Yang *et al.* [51] studied the symmetry breaking in the telephone-cord buckle morphologies for films exhibiting thickness and strain gradients. They showed that the degree of asymmetry increases with thickness and strain gradients. Their work focused on understanding how these gradients influence TCB formation. A phase diagram of buckle morphologies as a function of the applied strain ε_0 (horizontal axis) and thickness gradient k_h (vertical axis) is presented in Fig. 6. The diagram is divided into five distinct regions: symmetric TCB (A region), asymmetric TCB (B region), symmetric bilateral branched buckle (C region), asymmetric bilateral branched buckle (D region) and unilateral branched buckle (E region). A symmetric TCB is expected for the case of uniform film thickness is represented as black horizontal line $k_h = 0$. Additionally, as ε_0 increases, the symmetric TCB transforms into symmetric bilateral branched buckle (C region). However, as k_h increases three regions (B, D and E) are expected depending on ε_0.

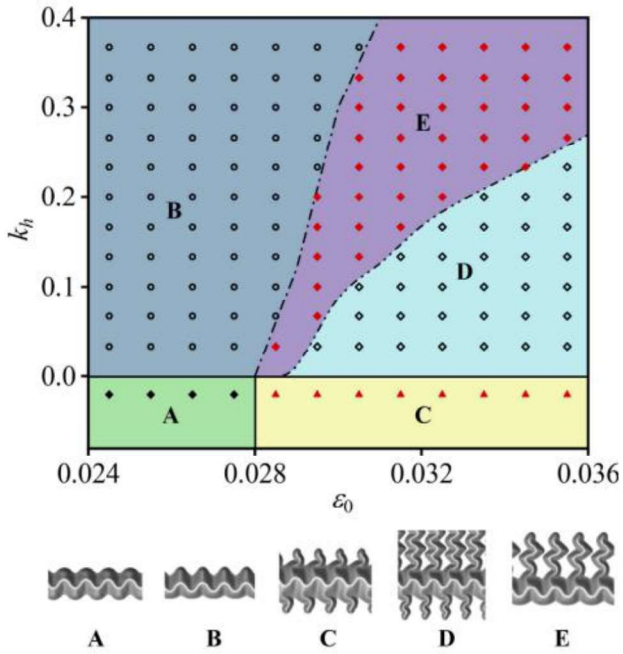

Fig. 0-6: Phase diagram of buckling structures as a function of the strain ε_0 and the thickness gradient k_h. The horizontal solid line $k_h = 0$ highlights a uniform homogenous, constant-thickness film, whereas letters from A to E correspond to symmetric TC buckle, asymmetric TC buckle, symmetric bilateral branched buckle, asymmetric bilateral branched buckle, and unilateral branched buckle, respectively. Adopted from [51].

Despite these advancements, the influence of thickness gradients on buckling, particularly SS and TC buckles remains an open question. In this context, this thesis aims to investigate the effect on nickel thin films with well-controlled thickness gradients deposited on polycarbonate substrates. The primary objectives are:

- To study experimentally the buckling structures in nickel thin films with controlled thickness gradients and characterize their morphology and mechanical properties.
- To study experimentally how various thickness gradients influence buckling behavior, in particularly on the SS and TC buckles.
- To develop a mechanical model to study the buckling structures in films with thickness gradient on rigid and elastic substrates
- To investigate the buckling driven-delamination of ductile thin films deposited on rigid and elastic substrates, and study the effects of thickness gradient on the response of the film in the case of SS and TC buckles.
- To study the conditions leading to buckling-driven delamination and identify parameters that match observed experimental results through finite element simulations.

- Explore how thickness gradient in films influences the mechanics of buckles propagation

This research has allowed collaboration between the "Surface Interfaces et Matériaux sous Contrainte" group at the P' Institute in Poitiers and the "Physique du Métal" group at the SIMaP laboratory in Grenoble, combining expertise in experimental and numerical modeling.

The thesis is structured into four chapters:

- Chapter 1: Provides background on the research context and reviews the application of Föppl–Von Kármán (FvK) plate theory in understanding buckling in films. It introduces the concept of fracture mechanics, followed by theoretical survey on the effect of mode mixity on the SS buckle. Finally, the phenomenon of secondary buckling is discussed and linked to the mode mixity dependence.
- Chapter 2: Describes the experimental setup, sample preparation and methodology for elaborating thin films with controlled thickness gradients.
- Chapter 3: The experimental and numerical investigation of various buckles, mainly the SS and TC buckles will be explored. The experimental results will be compared to FEM results within a static approach and will be discussed in detail.
- Chapter 4: Examines buckling-driven delamination, implementing a cohesive zone model in FEM to study the SS and TC buckle propagation in thin films with controlled thickness gradients. Particular attention is given to the influence of interface toughness and thickness gradients on delamination behavior.

Chapter 1

1. Buckling-induced delamination of thin films: theoretical approaches

This chapter aims to provide a comprehensive overview of elastic plate theory, fracture mechanics, and buckling of thin films. It begins with the fundamentals of plate and shell mechanics within the Föppl–Von Kármán (FvK) plate theory and progresses to the mechanics of interfacial fracture. This is followed by an introduction to the cohesive zone model, which is then incorporated in simulations using the phenomenological empirical law proposed by Hutchinson and Suo [26] in order to express mixed-mode dependence of fracture. Additionally, the chapter presents the theoretical background on the mixed-mode dependence of various buckling structures, with a particular focus on straight-sided and telephone cord buckles. Overall, this chapter provides the theoretical foundation for the buckling phenomena that will be explored through finite element simulations and experimental investigations.

1.1. Elastic buckling of thin films

The study of how materials deform elastically goes back to the early 20th century, with one of the earliest and most fundamental description given by Hook's law [52]. Elasticity is generally defined as a material's ability to return to its original shape and size once the applied forces are removed. This is known as perfect elasticity, in such conditions, materials that exhibit such elasticity behaviors can be described by a linear relationship between the stress and strain [52,53]. That said, nonlinearity often comes into play, especially when materials are subjected to large displacements or forces. In these cases, the nonlinearity does not come from the material's itself, but rather from the changes in its geometry. This is geometric nonlinearity is at the heart of phenomena like thin film buckling [26].

The thin film buckling is commonly studied within the framework of the elastic plate theory, first developed by A. Föppl [54] and later by T. Von Kármán [55]. Together, their work led to the well-established Föppl-Von Karman (FvK) plate theory, which provides a theoretical framework to understand the non linear mechanics of thin films. Building on this theory, J. W. Hutchinson and Z. Suo [26] introduced a model for buckling-driven delamination, linking the plate theory with interfacial fracture mechanics.

1.1.1. Deformation of material

To describe the elastic deformation of a material, let's think of a body with no external or internal force apply on it with material points defined in a cartesian coordinate system as $\vec{X}(x, y, z)$. Under deformation within the elastic regime, a point in the body is displaced to ($x+u$, $y+v$, $z+w$), where $\vec{U}(u, v, w)$ is the displacement vector, and u, v, and w its components.

We can define the strain as the relative change in length, given by:

$$\epsilon = \frac{dl' - dl}{dl}, \tag{1-1}$$

where dl and dl' are the initial and final lengths, respectively. Therefore, we can express the squared lengths in the undeformed and deformed states as:

$$dl^2 = dx^2 + dy^2 + dz^2, \tag{1-2}$$

$$dl'^2 = (dx + du)^2 + (dy + dv)^2 + (dz + dw)^2. \tag{1-3}$$

Expanding Eq. (1-3), we obtain:

$$dl'^2 = dl^2 + 2\sum_k dX_k dU_k + \sum_k (dU_k)^2. \tag{1-4}$$

Here X_k=x, y, z and U_k=u, v, w. The term $\sum_k 2dX_k dU_k + \sum_k dU_k{}^2$ represents the induced element length by the elastic deformation. The differential dU_k can be expressed using partial derivatives:

$$dU_k = \sum_{m=x}^{z} \frac{\partial U_k}{\partial X_m} dX_m, \tag{1-5}$$

and the quadratic term becomes:

$$(dU_k)^2 = \left(\sum_{m=x}^{z} \frac{\partial U_k}{\partial X_m} dX_m\right)\left(\sum_{n=x}^{z} \frac{\partial U_k}{\partial X_n} dX_n\right) = \sum_{m,n=x}^{z} \frac{\partial U_k}{\partial X_m}\frac{\partial U_k}{\partial X_n} dX_m dX_n. \tag{1-6}$$

Similarly, summing over all k, the cross term becomes:

$$2\sum_k dX_k dU_k = 2\sum_{k,m}\left(\frac{\partial U_k}{\partial X_m}+\frac{\partial U_k}{\partial X_m}\right)dX_k dX_m. \tag{1-7}$$

Inserting Eq. (1-6) and (1-7) into (1-4), we find:

$$dl'^2 = dl^2 + \sum_{i,j}\left(\sum_k \frac{\partial U_k}{\partial X_i}\frac{\partial U_k}{\partial X_j}+\frac{\partial U_i}{\partial X_j}+\frac{\partial U_j}{\partial X_i}\right)dX_i dX_j. \tag{1-8}$$

This can be expressed in the form:

$$dl'^2 = dl^2 + 2\sum_{i,j}\epsilon_{ij} dX_i dX_j. \tag{1-9}$$

From Eqs. (1-8) and (1-9) we can define the Green-Lagrange strain tensor:

$$\varepsilon_{ij} = \frac{1}{2}\left(\frac{\partial U_i}{\partial X_j}+\frac{\partial U_j}{\partial X_i}+\sum_k \frac{\partial U_k}{\partial X_i}\frac{\partial U_k}{\partial X_j}\right). \tag{1-10}$$

The deformation tensors which relate the deformations and displacements, commonly named as Green-Lagrange strain components can be given as:

$$\varepsilon_{xx} = \frac{\partial u}{\partial x}+\frac{1}{2}\left(\frac{\partial u}{\partial x}^2+\frac{\partial v}{\partial x}^2+\frac{\partial w}{\partial x}^2\right), \tag{1-11}$$

$$\varepsilon_{yy} = \frac{\partial v}{\partial x}+\frac{1}{2}\left(\frac{\partial u}{\partial y}^2+\frac{\partial v}{\partial y}^2+\frac{\partial w}{\partial y}^2\right), \tag{1-12}$$

$$\varepsilon_{zz} = \frac{\partial w}{\partial z}+\frac{1}{2}\left(\frac{\partial u}{\partial z}^2+\frac{\partial v}{\partial z}^2+\frac{\partial w}{\partial z}^2\right), \tag{1-13}$$

$$2\varepsilon_{xy} = 2\varepsilon_{yx} = \frac{\partial v}{\partial x}+\frac{\partial u}{\partial y}+\frac{\partial u}{\partial x}\frac{\partial u}{\partial y}+\frac{\partial v}{\partial x}\frac{\partial v}{\partial y}+\frac{\partial w}{\partial x}\frac{\partial w}{\partial y}, \tag{1-14}$$

$$2\varepsilon_{xz} = 2\varepsilon_{zx} = \frac{\partial w}{\partial x}+\frac{\partial u}{\partial z}+\frac{\partial u}{\partial x}\frac{\partial u}{\partial z}+\frac{\partial v}{\partial x}\frac{\partial v}{\partial z}+\frac{\partial w}{\partial x}\frac{\partial w}{\partial z}, \tag{1-15}$$

$$2\varepsilon_{yz} = 2\varepsilon_{zy} = \frac{\partial w}{\partial y}+\frac{\partial u}{\partial z}+\frac{\partial u}{\partial y}\frac{\partial u}{\partial z}+\frac{\partial v}{\partial y}\frac{\partial v}{\partial z}+\frac{\partial w}{\partial y}\frac{\partial w}{\partial z}. \tag{1-16}$$

1.1.2. Elastic plate theory

We begin by adopting the Kirchhoff assumptions: the plate is considered homogenous, isotropic, linearly elastic and very thin. It consists of two parallel surfaces separated by a thickness h along (Oz) direction, as shown in Fig. 1-1. The two surfaces are separated by the mid-surface or the median plane. All deformations, stresses and displacements are represented with respect to this median plane. Since the thickness h of the plate is assumed to be small compared to the in-plane dimensions along the (Oxy) plane, the problem can be treated under the thin plate approximation.

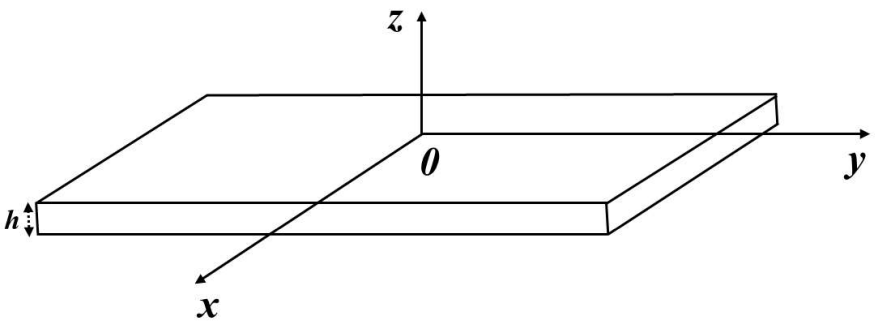

Fig. 1-1: Schematic of the plate and its coordinate system.

In the buckled state, the plate undergoes large out-of-plane displacement $w(x, y)$ along the z-axis. This displacement is very high compared to the displacement in the in plane (Oxy). As a result, the Green-Lagrange tensors can be simplified. Von-Karman proposed that the quadratic terms in the in-plane displacement, for instance $(\partial U_i/\partial x_i)^2$, can be neglected, except for the quadratic terms in the out-of-plane displacement $(\partial w/\partial x)^2$ and $(\partial w/\partial y)^2$, which represents the rotations about the (Ox) and (Oy) direction, respectively.

By simplifying the strain tensors expression (Eqs. 1-11 to 1-16), the components of the strain tensors become:

$$\varepsilon_{xx} = \frac{\partial u}{\partial x} + \frac{1}{2}\left(\frac{\partial w}{\partial x}\right)^2 ; \ \varepsilon_{yy} = \frac{\partial v}{\partial x} + \frac{1}{2}\left(\frac{\partial w}{\partial y}\right)^2 ; \ \varepsilon_{zz} = \frac{\partial w}{\partial z}, \tag{1-17}$$

$$2\varepsilon_{xy} = \frac{\partial v}{\partial x} + \frac{\partial u}{\partial y} + \frac{\partial w}{\partial x}\frac{\partial w}{\partial y} \quad ; \quad 2\varepsilon_{xz} = \frac{\partial w}{\partial x} + \frac{\partial u}{\partial z} ; \quad 2\varepsilon_{yz} = \frac{\partial w}{\partial y} + \frac{\partial v}{\partial z}. \tag{1-18}$$

Given the small thickness of the plate, the strains and stresses associated with the z-direction are negligible. We therefore assume:

$$\varepsilon_{zz} = \varepsilon_{xz} = \varepsilon_{yz} = 0, \text{ and } \sigma_{zz} = \sigma_{xz} = \sigma_{yz} = 0. \tag{1-19}$$

Using these assumptions, the displacement components across the plate thickness are expressed in terms of the median plane displacements $\bar{u}$, $\bar{v}$, $\bar{w}$ as:

$$u = \bar{u} - z\frac{\partial w}{\partial x};\ \ v = \bar{v} - z\frac{\partial w}{\partial y}\ ;\ w = \bar{w}, \tag{1-20}$$

The corresponding in-plane strain components become:

$$e_{xx} = \frac{\partial \bar{u}}{\partial x} + \frac{1}{2}\left(\frac{\partial w}{\partial x}\right)^2, \tag{1-21}$$

$$e_{yy} = \frac{\partial \bar{v}}{\partial y} + \frac{1}{2}\left(\frac{\partial w}{\partial y}\right)^2, \tag{1-22}$$

$$2e_{xy} = \frac{\partial \bar{v}}{\partial x} + \frac{\partial \bar{u}}{\partial x} + \frac{\partial w}{\partial x}\frac{\partial w}{\partial x}. \tag{1-23}$$

The stress strain relationship for isotropic linear elasticity is given by Hooke's law:

$$\sigma_{ij} = 2\mu\varepsilon_{ij} + \lambda\varepsilon_{kk}\delta_{ij}, \tag{1-24}$$

with δ_{ij} is the Kronecker symbol, and (μ, λ) are Lamé coefficients, given as:

$$\mu = \frac{E_f}{2(1+\nu_f)} \text{ and } \lambda = \frac{\nu_f E_f}{(1+\nu_f)(1-2\nu_f)}, \tag{1-25}$$

with E_f and ν_f are the young's modulus and Poisson's ratio of the film, respectively. In plane stress conditions, the out-of-plane stress is neglected which gives:

$$\sigma_{zz} = 0 \xrightarrow{yields} \epsilon_{zz} = \frac{-\lambda}{2\mu+\lambda}\left(\varepsilon_{xx} + \varepsilon_{yy}\right). \tag{1-26}$$

Substituting into Hooke's law, we obtain:

$$\sigma_{xx} = \frac{E_f}{1-\nu_f^2}\left(\epsilon_{xx} + \nu_f \epsilon_{yy}\right), \tag{1-27}$$

$$\sigma_{yy} = \frac{E_f}{1-\nu_f^2}\left(\epsilon_{yy} + \nu_f \epsilon_{xx}\right), \tag{1-28}$$

$$\sigma_{xy} = \frac{E_f}{1+\nu_f}\epsilon_{xy}. \tag{1-29}$$

1.1.3. Föppl-Von Kármán equations

The Föppl-Von Kármán (FvK) plate theory was developed in the late of the 19th century, building upon the classical Kirchhoff–Love plate theory [56], itself an extension of the Euler-Bernoulli beam theory. The FvK theory is formulated within the framework of elasticity and is particularly suited for describing the nonlinear behavior of thin plates and films undergoing moderate to large out-of-plane displacements. The FvK equations are given as partial differential equations. Here, for simplicity, we only give the expressions:

$$D\nabla^2\nabla^2 w = N_{xx}\frac{\partial^2 w}{\partial x^2} + N_{yy}\frac{\partial^2 w}{\partial y^2} + 2N_{xy}\frac{\partial^2 w}{\partial x \partial y}, \tag{1-30}$$

$$\frac{\partial N_{xx}}{\partial x} + \frac{\partial N_{xy}}{\partial y} = 0\,;\ \frac{\partial N_{yx}}{\partial x} + \frac{\partial N_{yy}}{\partial y} = 0, \tag{1-31}$$

where $w(x,y)$ is the out-of-plane displacement, and D is the flexural rigidity of the plate, defined as:

$$D = \frac{E_f h^3}{12(1-\nu_f^2)}. \tag{1-32}$$

The operator $\nabla^2\nabla^2$ is the biharmonic (double Laplacian) operator. The components N_{ij} are the internal forces acting on rectangular element of the plate along the median plane, obtained by integrating the stress components through the plate thickness:

$$N_{ij} = \int_{-h/2}^{h/2} \sigma_{ij}\, dz. \tag{1-33}$$

The first FvK equation (1-30) expresses the balance of transverse (out-of-plane) forces and includes the coupling with in-plane stresses. The second Eq. (1-31) represents the equilibrium of in-plane forces (membrane equilibrium), ensuring force balance in the plane of the plate. These coupled nonlinear equations are central to the analysis of buckling, post-buckling, and large deflections in thin elastic plates. They serve as the foundation for understanding the interplay between geometry, material properties, and stress in problems such as wrinkling, buckling, and buckling-driven delamination in thin film and coatings.

1.1.4. Analytical model: straight-sided buckle

To derive the analytical model of the SS buckle, we consider an isotropic, elastic thin films of a constant-thickness h, deposited on a rigid substrate. The coordinate system is defined by the orthonormal axes (Ox, Oy), with the film's Young's modulus E_f and Poisson's ratio ν_f, as shown in Fig. 1-2. Under the assumptions of thin plate theory ($h<<b$), the film is modeled as a wide, clamped Euler column of width $2b$, where buckling occurs in the out-of-plane (Oz) direction, perpendicular to the film plane (Oxy). Initially, we suppose that there is no adhesion[1] between the film and the substrate. The film is clamped at its lateral edges located in $y=\pm b$. The reference surface is taken as the median plane, where the displacements, stresses, and strains are represented.

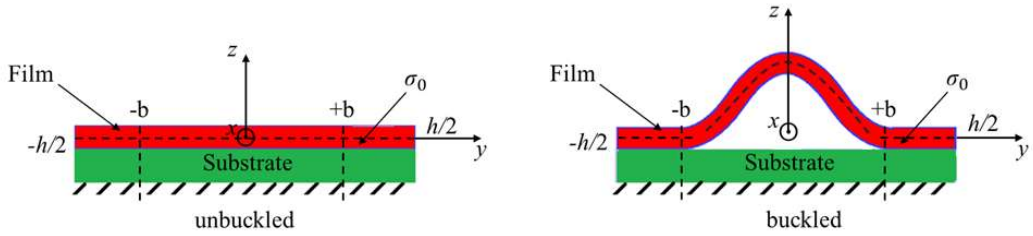

Fig. 1-2: Geometry of a one-dimensional SS buckle. Left: unbuckled state; right: buckled state.

Given the system is invariant along the (Ox) direction, we will not consider any displacements along this axis. Therefore, the problem can be solved as a two-dimensional. Consequently:

$$\frac{\partial N_{xx}}{\partial x} = \frac{\partial N_{xy}}{\partial y} = 0 \xrightarrow{yields} \frac{\partial N_{yy}}{\partial y} = 0. \tag{1-34}$$

[1] In the contrary, elastic energy is needed to break the interfacial toughness

As result we have $N_{yy} = cte.$ Under these conditions, the first FvK simplifies to:

$$D\frac{\partial^4 w}{\partial y^4} - N_{yy}\frac{\partial^2 w}{\partial y^2} = 0, \tag{1-35}$$

During buckling process, the changes in the resultant stresses (i.e. the stress integrated in the thickness of the film) in plane (O, x, y) are defined as $\Delta N_{xx} = N_{xx} + \sigma_0 h$ and $\Delta N_{yy} = N_{yy} + \sigma_0 h$ where N_{xx} and N_{yy} are their associated resultant stresses. At the unbuckled state, the film is subjected to an isotropic internal stress in compression $\sigma_{xx}^0 = \sigma_{yy}^0 = -\sigma_0$. The internal stress is considered positive, i.e, $\sigma_0 > 0$, corresponding to compression. This sign convention is adopted to simplify the equations and analyses presented throughout the thesis. Thus, the FvK equation can be furthered simplified to:

$$\frac{\partial^4 w}{\partial y^4} + \chi^2\frac{\partial^2 w}{\partial y^2} = 0, \text{ with } \chi^2 = \frac{h(\sigma_0 - \Delta\sigma_{yy})}{D}, \tag{1-36}$$

In the case of tensile stress where $\sigma_{yy} < 0$, we have $h(\Delta\sigma_{yy} - \sigma_0) < 0$, leading to $\chi^2 > 0$. In this case, only one physically admissible solution exists, a plane equation $w(y)=0$, under the assumption of rigid substrate (*i.e*, $w \geq 0$). In the case of compressive stress $\sigma_{yy} > 0$ (i.e, $\chi^2 < 0$), the general solution of the simplified FvK equation can be given as:

$$w(y) = c_1\, sin(\chi y) + c_2\, cos(\chi y) + c_3 y + c_4. \tag{1-37}$$

The clamped boundary conditions at $y=\pm b$ are:

$$w(\pm b) = 0,\ \frac{\partial w(\pm b)}{\partial y} = 0. \tag{1-38}$$

Replacing Eq. (1-37) into Eq. (1-38) yields in four equations:

$$c_1\, sin(\chi b) + c_2\, cos(\chi b) + c_3 b + c_4 = 0, \tag{1-39}$$

$$-c_1\, sin(\chi b) + c_2\, cos(\chi b) - c_3 b + c_4 = 0, \tag{1-40}$$

$$c_1\chi\, cos(\chi b) - c_2\chi\, sin(\chi b) + c_3 = 0, \tag{1-41}$$

$$c_1\chi\, cos(\chi b) + c_2\chi\, sin(\chi b) + c_3 = 0. \tag{1-42}$$

Adding and subtracting Eqs. (1-39) and (1-40) gives:

$$2c_2\, cos(\chi b) + 2c_4 = 0 \xrightarrow{yields} c_4 = -c_2\, cos(\chi b). \tag{1-43}$$

$$2c_1\, sin(\chi b) + 2c_3 b = 0 \xrightarrow{yields} c_1\, sin(\chi b) = -c_3 b. \tag{1-44}$$

Adding and subtracting Eqs. (1-41) and (1-42) gives:

$$2c_1\chi\, cos(\chi b) + 2c_3 = 0 \xrightarrow{yields} c_3 = -c_1\chi\, cos(\chi b). \tag{1-45}$$

$$2c_2\chi\, sin(\chi b) = 0 \xrightarrow{yields} c_2\, sin(\chi b) = 0. \tag{1-46}$$

The solution of Euler column can be determined by examining the relationships between the four constants c_i. In particular, the expected solution of the Euler column must be symmetric about the centerline y=0, with maximum height at that point.

From Eq. (1-46), two possibilities arise:

Firstly, if c_2=0, then Eq. (1-43) implies c_4=0, and the solution becomes:

$$w(y) = c_1\, sin(\chi y) + c_3 y. \tag{1-47}$$

This solution does not satisfy the imposed symmetry and exhibits a maximum height at the centerline. Secondly, if sin(χb)=0, then $\chi b = n\pi$, with $n \in N^*$. In this case, Eqs. (1-44) and (1-45) yield $c_1 = c_3 = 0$, and the solution reduces to:

$$w(y) = c_2\, cos(\chi y) + c_4. \tag{1-48}$$

From Eq. (1-43), we obtain:

$$c_4 = -c_2\, cos(n\pi) = (-1)^{n+1} c_2. \tag{1-49}$$

The solution can be rewritten as:

$$w(y) = c_2(cos(\chi y) - (-1)^n). \tag{1-50}$$

The maximum height occurs at the center *y=0*:

$$w(0) = c_2(1 - (-1)^n). \tag{1-51}$$

For *n*=1, corresponding to the lowest buckling mode, $w(0) = \delta = 2c_2$. Therefore, the physical solutions are:

$$w_0(y) = 0, \tag{1-52}$$

$$w(y)_{euler} = \frac{\delta}{2}\left(1 + \cos\frac{\pi}{b}y\right). \tag{1-53}$$

The first solution corresponds to the plane state, while the second describes the SS buckle known as Euler column. Eq. (1-53) is symmetric with respect to the centerline. For *n*>1, higher harmonic modes such as secondary, tertiary and so on. A graphical representation of the analytical Euler column given in Eq. (1-53) is shown in Fig. 1-3, with δ the maximal height. Finally, substituting $\chi = n\pi/b$ in Eq. (1-36) gives the critical buckling stress

$$\sigma_c = \sigma_0 - \Delta\sigma_{yy} = \frac{D}{h}\left(\frac{n\pi}{b}\right)^2 = \frac{\pi^2}{12}\frac{E_f}{1-\nu_f^2}\left(\frac{h}{b}\right)^2. \tag{1-54}$$

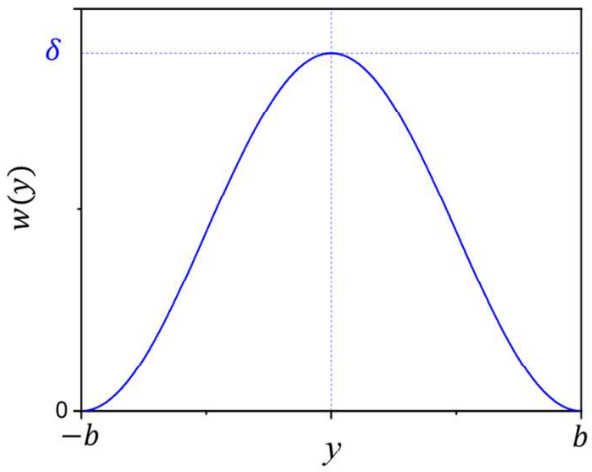

Fig. 1-3: Representation of the out-of-plane displacement $w(y)$, for buckled film in SS buckle form given by Eq. (1-53), with width $2b$ and height.

The maximal height δ can be obtained as function of σ_c. We previously expressed the deformations tensors in the median plane with respect to the displacement in Eqs. (1-21) to (1.23). In the buckled state, we can express the strain tensors as:

$$e_{xx} = \frac{1}{E_f}\left(\bar{\sigma}_{xx} - v_f\bar{\sigma}_{yy}\right) = \frac{\partial\bar{u}}{\partial x} = \frac{\partial\bar{u}_0}{\partial x}, \tag{1-55}$$

$$e_{yy} = \frac{1}{E_f}\left(\bar{\sigma}_{yy} - v_f\bar{\sigma}_{xx}\right) = \frac{\partial\bar{v}}{\partial x} + \frac{1}{2}\left(\frac{\partial w}{\partial y}\right)^2. \tag{1-56}$$

While at the plane state those Eqs. (1-55) and (1-56) can be expressed as:

$$e^0_{xx} = \frac{1}{E_f}\left(\bar{\sigma}^0_{xx} - v_f\bar{\sigma}^0_{yy}\right) = -\frac{1-v_f}{E_f}\sigma_0 = \frac{\partial\bar{u}_0}{\partial x}, \tag{1-57}$$

$$e^0_{yy} = \frac{1}{E_f}\left(\bar{\sigma}^0_{yy} - v_f\bar{\sigma}^0_{xx}\right) = -\frac{1-v_f}{E_f}\sigma_0 = \frac{\partial\bar{v}_0}{\partial y}. \tag{1-58}$$

Using displacement components across the plate thickness previously given in Eq. (1-20) expressed in terms of the median plane displacements $\bar{u}$, $\bar{v}$, $\bar{w}$, Eqs. (1-55) and (1-56) becomes:

$$e_{xx} = \frac{1}{E_f}\left(\bar{\sigma}_{xx} - v_f\bar{\sigma}_{yy}\right) = -\frac{1-v_f}{E_f}\sigma_0, \tag{1-59}$$

$$e_{yy} = \frac{1}{E_f}\left(\bar{\sigma}_{yy} - v_f\bar{\sigma}_{xx}\right) = -\frac{1-v_f}{E_f}\sigma_0 + \frac{\partial\Delta\bar{v}}{\partial x} + \frac{1}{2}\left(\frac{\partial w}{\partial y}\right)^2. \tag{1-60}$$

Eq. (1-55) gives:

$$\bar{\sigma}_{xx} = -\left(1 - v_f\right)\sigma_0 + v_f\bar{\sigma}_{yy}. \tag{1-61}$$

Inserting Eq. (1-61) into Eq. (1-60) gives:

$$\frac{1-v_f}{E_f}\left(\bar{\sigma}_{yy} + \sigma_0\right) = \frac{\partial\Delta\bar{v}}{\partial x} + \frac{1}{2}\left(\frac{\partial w}{\partial y}\right)^2. \tag{1-62}$$

Whatever the internal stress σ_0, the in-plane stress in the buckled part of the plate is given by $\bar{\sigma}_{yy} = -\sigma_c$, by integrating the Eq. (1-62) between $\pm b$, we can express the maximal height as:

$$\delta = h\sqrt{\frac{4}{3}\left(\frac{\sigma_0}{\sigma_c} - 1\right)}. \tag{1-63}$$

The height δ shown in Eq. (1-63) increases with square root of the normalized stress σ_0/σ_c. The analytical model discussed in this section assumes constant thickness. In the third chapter, we will investigate the validity of the FvK theory to films with thickness gradients, using both finite element simulations and experimental results.

1.2. Interfacial fracture mechanics

This section focuses on the mechanics of cracks that propagate along the interface between two bonded materials. Such interfacial cracks are key fundamentals in understanding the buckling and buckling-driven delamination phenomena in thin films and coatings. Starting by considering two materials subjected to a force which tends to separate them, this force can lead to a crack that may either open or slide relative to each other, or even a crack that may propagate or kink out of the interface when the force reaches a critical level. In the following, we present an overview of interfacial fracture to support the development of a numerical model aimed at exploring the buckling-driven delamination in thin films throughout the course of this study.

1.2.1. Fracture modes

Let's suppose that we have two dissimilar materials bonded to each other with a crack in the interface. Depending on the applied stresses, the crack propagation can occur under three classical modes failure, or more commonly under mixed mode fracture [26]. Mode I is the opening mode, where the crack faces separate perpendicular to the crack plane due to tensile stress. Mode II is the sliding or shear mode, in which the crack faces slide over each other in the crack plane and perpendicular to the crack front. Mode III is the tearing; where the crack faces slide relative to each other parallel the crack front (Fig. 1-4).

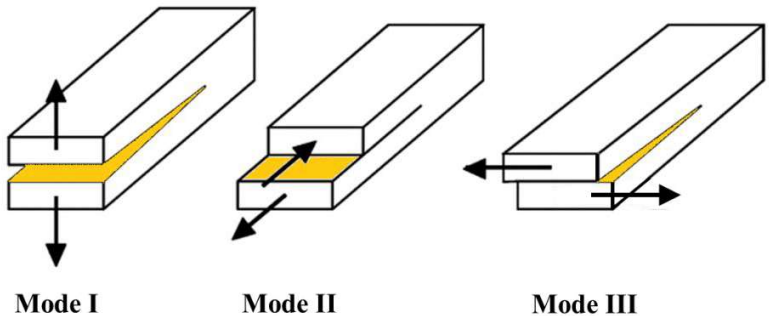

Fig. 1-4: Fracture modes for crack propagation, the opening mode (I), the shear mode (II), and the transverse mode (III).

In the case of homogenous, isotropic elastic materials, cracks often kink out of their original plane when they reach a critical stress and tend to propagate in pure mode I near the crack tip. However, for cracks in bimaterial interface, the situation is more complex. When the crack reaches critical condition, the crack extends along the interface as long as the interfacial toughness is weak compared to the energy release rate. In these cases, crack propagation generally occurs in mixed mode, involving both modes I and II.

1.2.2. Dundurs' parameters

The elastic contrast between two bonded materials (see Fig 1-5) are widely characterized by Dundurs' coefficients introduced by John Dundurs [57]. They play a crucial role in interfacial fracture mechanics. Those coefficients are dimensionless parameters that depend on the mechanical properties of the bonded material, as illustrated in Fig. 1-5 for materials 1 and 2, characterized by Young's modulus E_1, E_2 and Poisson's rations ν_1, ν_2, respectively.

The two Dundurs' coefficients, α_D and β, are defined as [26,58]:

$$\alpha_D = \frac{\overline{E}_1 - \overline{E}_2}{\overline{E}_1 + \overline{E}_2}, \tag{1-64}$$

$$\beta = \frac{1}{2}\frac{\overline{E}_1(1-\overline{v}_2{}^2) - \overline{E}_2(1-\overline{v}_1{}^2)}{\overline{E}_1 + \overline{E}_2}, \tag{1-65}$$

where $\overline{E}_1 = \frac{E_1}{1-v_1^2}$ (*resp.* $\overline{v}_1 = \frac{v_1}{1-v_1}$) and $\overline{E}_2 = \frac{E_2}{1-v_2^2}$ (*resp.* $\overline{v}_2 = \frac{v_2}{1-v_2}$) represent the reduced Young's modulus (*resp.* reduced Poisson's ratio) of materials 1 and 2, respectively under plane strain conditions. A value of a_D =-1 refers to a soft material on a hard material, whereas a_D =+1 corresponds to a hard material on a soft material. While, for no elastic mismatch between the two materials α_D=0.

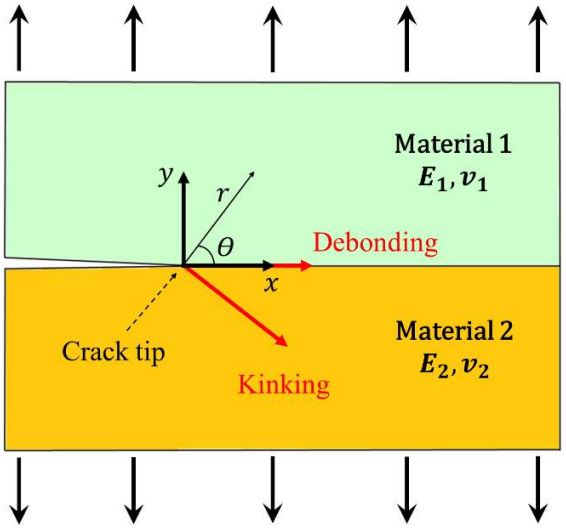

Fig. 1-5: Bimaterial Interface crack.

There are many possible combinations of α_D and β for biomaterial systems under the plane conditions, for instance it is well documented that the values of α_D and β lie within the parallelogram defined by $\alpha_D = \pm 1$ and $\alpha_D - 4\beta = \pm 1$ [58], as shown in Fig. 1-6 for biomaterial systems in filled star symbols. However recent study by Zak *et al.* [59] demonstrates that the assumption of real bi material systems being in the region of the parallelogram is not valid anymore, instead there are plenty of modern materials which have value of $\beta > \alpha_D/4$, as shown in Fig. 1-6. Graphene film on SiO_2 shows values of α_D=0.89 and β =0.37.

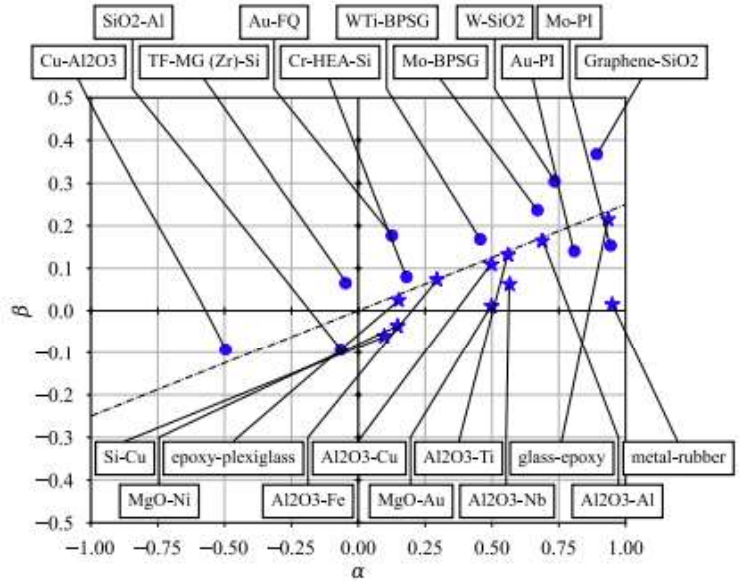

Fig. 1-6: Comparison of crack behavior in various bi-material systems presented. Adopted from [59]. The diagram compares earlier bi-material systems reported in [26] (star symbol) with modern bi-material systems (filled circle) depicted in α-β phase. The filled-circle data include examples from multiple sources [60–68]. Abbreviations: BPSG = boro-phosphor-silicate glass, PI = polyimide, TF-MG = thin film metallic glass, FQ = fused quartz and HEA = high entropy alloy.

1.2.3. Griffith criteria

In 1920, inspired by Inglis's linear elastic for stresses around an elliptical hole, Alan Arnold Griffith proposed a critical energy based criterion for the propagation of the cracks in brittle materials [69]. This was considered to be the birth and origin of fracture mechanics [69]. The energy-based criterion proposed by A.A Griffith was able to explain why cracks may not propagate under load despite their presence in materials. The theory demonstrated that a crack would only propagate when the energy released during the crack growth exceeds the energy required to create new crack surfaces; this becomes the core of fracture mechanics and remains widely used today.

To understand Griffith's criteria, we begin by introducing the fundamentals of work, energy, and strain energy density.

The work done (W) by an applied force is defined as:

$$W = \int_0^L F.dx \tag{1-66}$$

However, it is more convenient to express work in terms of stress and strain rather than force F and displacement dx. By multiplying Eq. (1-66) by volume V and dividing by area A and length L, we get:

$$W = \int_0^L \frac{F}{A}.\frac{dx}{L}.V. \tag{1-67}$$

Now, the work can be expressed as a function of stress σ and strain ϵ:

$$W = \int_0^\epsilon \sigma.d\epsilon.V = U'.V, \tag{1-68}$$

where, U' is the strain energy density, and it can be expressed as:

$$U' = \int_0^\epsilon \sigma.d\epsilon = \int_0^\epsilon E\epsilon d\epsilon = \frac{1}{2}E\epsilon^2 = \frac{\sigma\epsilon}{2}. \tag{1-69}$$

The elastic energy stored in the plate per unit volume U' can derived from the stress σ_{ij}, and deformation tensors ϵ_{ij}:

$$U' = \frac{1}{2}\sum_{i,j}\sigma_{ij}\epsilon_{ij}. \tag{1-70}$$

Under plane conditions Eq. (1-70) becomes:

$$U' = \frac{1}{2\mathrm{E}}\left[\sigma_{xx}^2 + \sigma_{yy}^2 - 2v\sigma_{xx}\sigma_{yy} + 2(1+v)\sigma_{xy}^2\right]. \tag{1-71}$$

The total elastic energy stored in the plate can derived from the integration of U' (Eq. 1-71) over the entire volume $dxdydz$:

$$U = \iiint U'\,dxdydz. \tag{1-72}$$

We can express the elastic energy stored in the plate as a function of stress or strain tensors. The total elastic energy can be decomposed to the sum of two parts:

$$U = U_c + U_f, \tag{1-73}$$

with:

$U_c = \frac{E_f h}{2\left(1-v_f^2\right)} \iint \left[\epsilon_{xx}^2 + \epsilon_{yy}^2 - 2v\epsilon_{xx}\epsilon_{yy} + \left(1-v_f\right)\epsilon_{xy}^2\right] dxdy$, the Membrane (in-plane) strain energy, (1-74)

and

$U_f = \frac{Eh^3}{2\left(1-v_f^2\right)} \iint \left[\left(\frac{\partial^2 w}{\partial x^2}\right)^2 + \left(\frac{\partial^2 w}{\partial y^2}\right)^2 + 2v\frac{\partial^2 w}{\partial x^2}\frac{\partial^2 w}{\partial y^2} + 2(1-v)\left(\frac{\partial^2 w}{\partial x \partial y}\right)^2\right] dxdy$, the bending (out-of-plane) energy, (1-75)

where E, v, h are the Young's modulus, Poisson's ratio and thickness of the plate.

When an external load is applied to a material containing a crack, the system or the material tends to release built-up elastic energy in the region surrounding the crack. As the crack propagates, it creates new surfaces, which result in an increase of the system's surface energy and decrease in the elastic strain energy. In order that the crack continues propagating, the reduced elastic strain energy of the system must be greater or equal to the energy that is required to create new crack surfaces. In other words, the energy released by the system as the crack grows and expands have to be sufficient to compensate the increase in the energy required to create new crack surfaces.

From a thermodynamic perspective, crack growth is controlled by the principle of decreasing total free energy. If the elastic energy released exceeds the surface energy required for crack propagating, the crack will propagate. Conversely, if the energy released is insufficient, the crack remains stable or may even heal.

The Griffith theory can be summarized as follows:

- If cracks pre-exist in brittle materials such as glass, they will act as stress concentrators.
- The concentrated stress near or at the crack tip breaks atomic bonds one by one.
- As the crack advances, new surfaces are created, increasing the surface energy, while the stored elastic energy in the material or body decreases.

- The crack continues to propagate only if the total energy is reduced during the process.

The energy release rate G, can be defined as the decrease rate of the elastic energy U (the variation of the elastic energy spent during the crack propagation of surface dS) with respect to the crack surface S, and is given as:

$$G = -\frac{dU}{dS}. \tag{1-76}$$

The crack propagation would occur if the energy release rate G is higher than the interfacial toughness G_C, it would remain stable in the contrary ($G < G_C$). This energy-based criterion forms the foundation of linear elastic fracture mechanics (LFEM), which will be explored in Chapter 4 for the buckling delamination of thin films.

1.2.4. Mode dependence of interfacial fracture

The mode mixity of interfacial fracture is a fundamental aspect in understanding crack propagation behavior. In most materials, regardless of the elastic mismatch, crack propagation is rarely observed in pure mode I (opening) or pure mode II (shearing) or mode III (tearing). Instead, it usually occurs as a combination of various modes, known as mixed mode fracture. In the present work, the analysis is restricted to mixed-mode conditions involving modes I and II.

The mixed mode fracture is quantified by the mode mixity angle ψ, defined as the ratio of the stress intensity factors (K_I, K_{II}) or local stress components near the crack tip. The mode mixity angle is given by [26]:

$$\tan(\psi) = \left(\frac{K_I}{K_{II}}\right)_{(r=l,\theta=0°)} \; or \; \tan(\psi) = \left(\frac{\sigma_{xy}}{\sigma_{yy}}\right)_{(r=l,\theta=0°)}, \tag{1-77}$$

where σ_{xy} ($r = l$, $\theta = 0°$) and σ_{yy} ($r = l$, $\theta = 0°$) are the shear and normal stress components at the crack tip, respectively, and l is the reference length dependent on specimen geometry. The angle $\psi = 0°$ corresponds to pure mode I, and $\psi = 90°$ corresponds to pure mode II.

The total energy release rate in mixed mode scenario under plane strain conditions, is expressed as:

$$G = G_I + G_{II}, \tag{1-78}$$

or equivalently,

$$G = \frac{K_I^2}{\bar{E}} + \frac{K_{II}^2}{\bar{E}}, \tag{1-79}$$

where $\overline{E} = \frac{E}{(1-\nu^2)}$ is the reduced Young's modulus under plane strain, G_I and G_{II} are the contribution of modes I and II to the total energy release rate, respectively.

Several experimental studies confirmed that the interfacial toughness G_C depends on the mode mixity. One can cite the work by Liechti and Chai [70], where they developed an experimental setup to investigate crack propagation at a glass/epoxy interface. The setup enabled precise control of loading conditions or mode mixity, and various combinations of positive or negative shear loads to assess the interfacial toughness G_C across these conditions. In their setup, the specimen length was much larger than the epoxy thickness, and the bottom layer was constrained to a rigid grip. The elastic mismatch was characterized by Dundurs' parameters: α_D=-0.935, β = -0.188. Fig. 1-7 shows the values of mode mixity angles, ψ_1 and ψ_2, corresponding to references lengths l_1 = 12.7 mm and l_2 = 127 μm, respectively, with l_1=100×l_2. The choice of reference length depends on the in-plane length of the specimen geometry, such as crack length, and the size of the fracture process zone or a plastic zone at fracture. Here the choices are based on specimen geometry. A slight small shift of about 15° is observed between ψ_1 and ψ_2. They demonstrate that the interfacial toughness is slightly dependent on the sign of the shear component (see Fig. 1-7). Pure mode I is observed when G_C reaches its minimum around ψ = 0°, and pure mode II when mode mixity ψ = 90°. For 0°< ψ <45°, the interfacial toughness is relatively independent to the mode mixity. In other words, the interfacial toughness consists of a strong contribution of mode I criteria of crack initiation required a constant interfacial toughness. Additionally, as ψ, so does G_c.

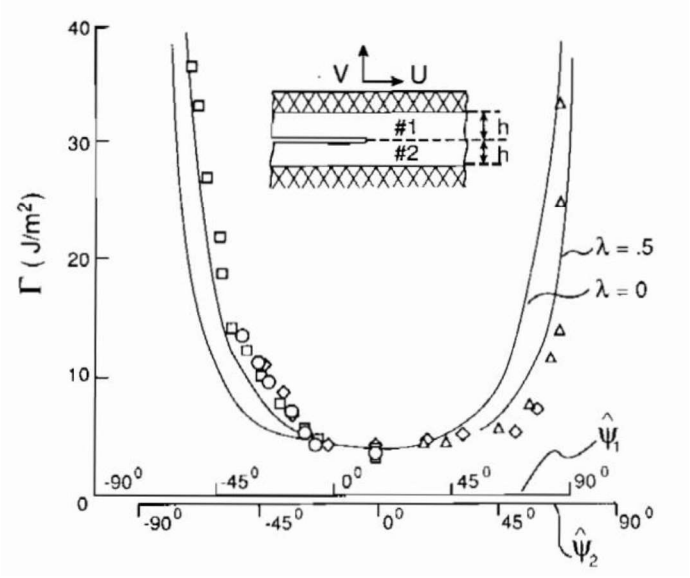

Fig. 1-7: Data from [70] for an epoxy ♯1/glass ♯2 interface. The ψ_1 axis corresponds to l_1 = 12.7 mm, and the ψ_2 axis corresponds to l_2 = 127μm. The solid curves represent $G_c(\psi_2)$ as defined by Eq. (1-80).

Building on these experimental results, Hutchinson and Suo developed a phenomenological model for the mode mixity dependence of interfacial fracture toughness. This model is widely used to study interfacial crack propagation in adhesive joints and composite systems, especially when the mode mixity dominates [70,71]. The model assumes symmetrical toughness with respect to the mode mixity angle ψ and is expressed as [26]:

$$G_C(\psi) = G_{IC}\left(1 + tan^2(\eta.\psi)\right) = G_{IC}f(\psi), \tag{1-80}$$

where G_{IC} is the mode I critical toughness and η a dimensionless parameter used to tune the contribution of mode I and II to the critical interfacial toughness G_C. The parameter η typically ranges from 0 to 1, with η=0 and η=1 represent pure mode I and pure mode II contributions, respectively. The normalized interfacial toughness $G_C(\psi)$ to mode I toughness for various values of η is reported in Fig. 1-8. When η = 0 the interface has a brittle-like behavior, with no mixed mode dependence. As η rises and is close to 1, a strong mixed mode dependence is observed.

In the context of buckling in thin films, mode mixity plays a crucial role in understanding the buckling-driven delamination, which involves significant contributions from both opening and shearing modes. Accurate modeling of the interfacial toughness with respect to the mode mixity dependence is therefore essential in predicting failure in thin films or even optimizing the lifetime of film/substrate systems in various industrial applications.

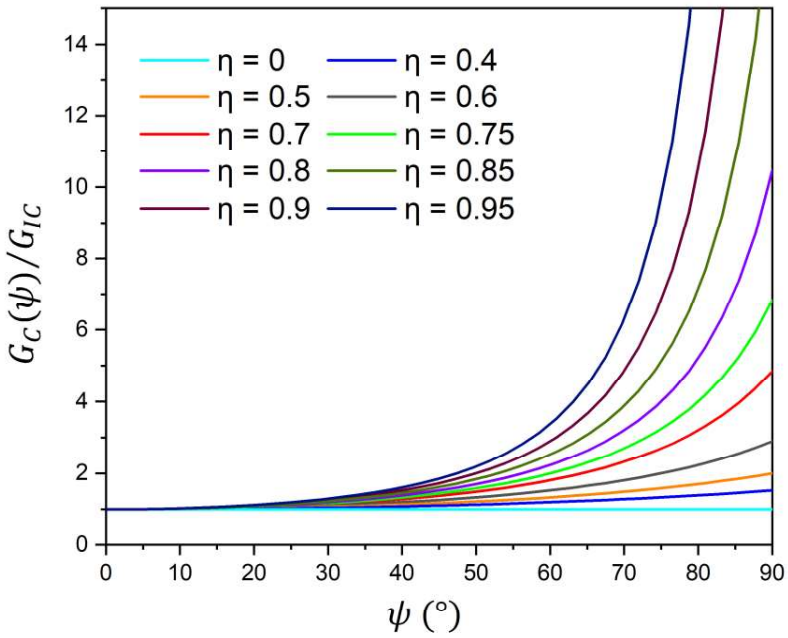

Fig. 1-8: Influence of η on the normalized interfacial toughness $G(\psi)/G_{IC}$ depending on mode mixity ψ from Eq. (1-80).

1.2.5. Cohesive zone model

The cohesive zone model (CZM) was developed to address the drawback of classical linear fracture mechanics, particularly in describing the crack propagation within gradual debonding through a traction separation law between two surfaces before reaching complete separation, rather than abrupt failure. Originally introduced by Dugdale [72] and Barenblatt [73] in the context of the ductile materials. This concept was later extended to interfacial fracture mechanics, such as applications involving buckling of thin films, composites and layered structures.

The traction separation law relates the traction vector $\vec{T} = (T_n, T_t)$ acting across the interface and the separation displacement or opening vector $\vec{\delta} = (\delta_n, \delta_t)$, which includes both normal and tangential components:

$$\vec{T} = K\vec{\delta}, \tag{1-81}$$

where K is the cohesive stiffness, typically chosen large enough to avoid artificial elastic deformation before damage initiation. This linear relationship holds until a critical traction is reached. Various damage initiation criterions are used, as for example a quadratic criterion (as used in our studies):

$$\left(T_n/T_n^0\right)^2 + \left(T_t/T_t^0\right)^2 = 1, \tag{1-82}$$

with T_n^0 and T_n^0 are the maximum tractions in normal and shear directions, respectively.

The mode mixity angle ψ can be expressed as the ratio of shear to normal traction components:

$$\tan\psi = \frac{T_t}{T_n}. \tag{1-83}$$

The evolution of traction with separation follows three main stages, illustrated schematically in Fig. 1-9.

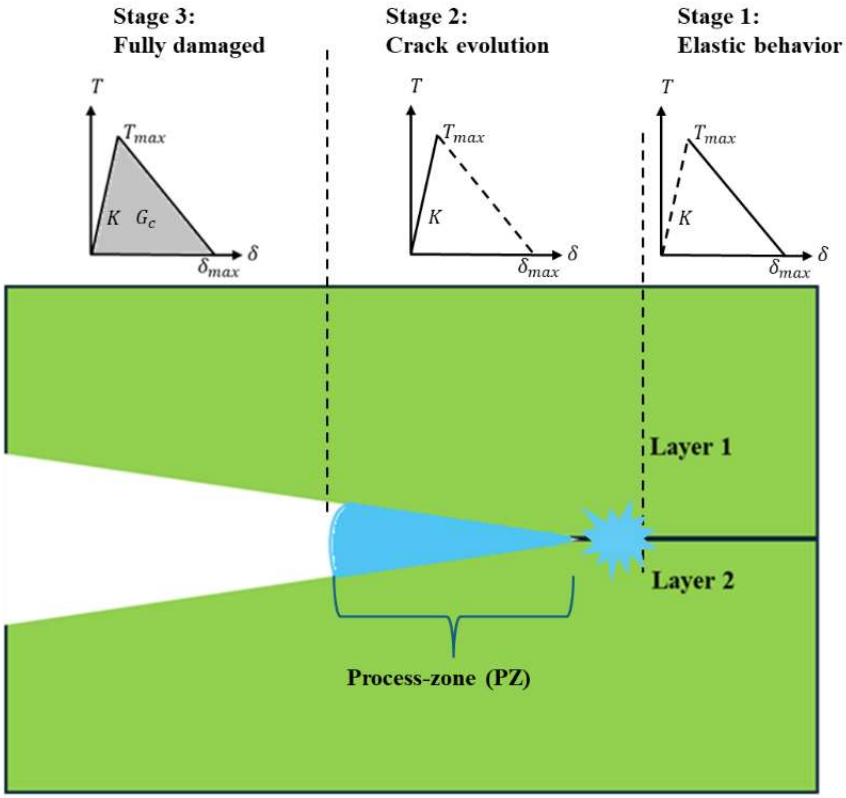

Fig. 1-9: Schematic representation of the successive stages of crack initiation and propagation within the cohesive zone model.

The stages of the traction separation law can be expressed as follows:

- Stage 1: Elastic behavior; for small separations, the interface between surfaces 1 and 2 behaves elastically, and the traction increases linearly with separation displacement.
- Stage 2: Damage initiation when the traction reaches a critical value depending on the (T_n^0, T_t^0) components, beyond which cohesive strength begins to degrade.
- Stage 3: Traction decreases irreversibly to zero as the interface undergoes full separation at $\delta = \delta_{max}$[2].

When the condition of damage is met, the damage or the crack begins to grow and expands followed by a decrease in the traction force (softening) and eventually reduces to zero when the maximal separation displacement is completed. During the softening (irreversible process), the

[2] Note that reversible cohesive laws can also be implemented (potential based models)

cohesive stiffness decreases by a factor (1-d) where d represents the scalar damage variable. For d=1, the interface is at complete separation. For $0 < d < 1$, the damage is expanding, while for d=0 the interface is still intact.

The cohesive stiffness decreases with damage according to:

$$T = (1 - d)K\delta. \tag{1-84}$$

The fracture energy G_c, which quantifies the work required to completely break the interface, is described as the area under the traction-separation curve as follows:

$$G_C = \int_0^{\delta_{max}} T d\delta, \tag{1-85}$$

Several constitutive shapes of the traction–separation law have been proposed. We cite, for instance linear softening [74], bilinear softening [75,76], exponential [77], trapezoidal [78], smoothed trapezoidal [79] and cubic polynomial law [80]. Fig. 1-10 taken from [81] depicts descriptions of those laws, representing the normalized traction $T/T_{\max}$ as a function of the normalized opening displacement δ/δ_{max}. Although computational stability often influence the choice of these models with linear and bilinear laws being frequently adopted in finite element modeling (FEM) because of their robustness and simplicity [82,83], while smoother exponential or polynomial shapes can improve convergence in unstable propagation regimes [84,85], the selection of a cohesive law is not driven solely by numerical aspects. Studies in the literatures [86–88] showed that the shape of the traction–separation curve should also reflect the underlying micromechanical mechanisms occurring within the crack tip (process zone). In particular, Tvergaard and Hutchinson [86] showed that cohesive laws can be physically motivated by decohesion at interfaces in the presence of plastic deformation, providing more realistic smooth transitions at the interface.

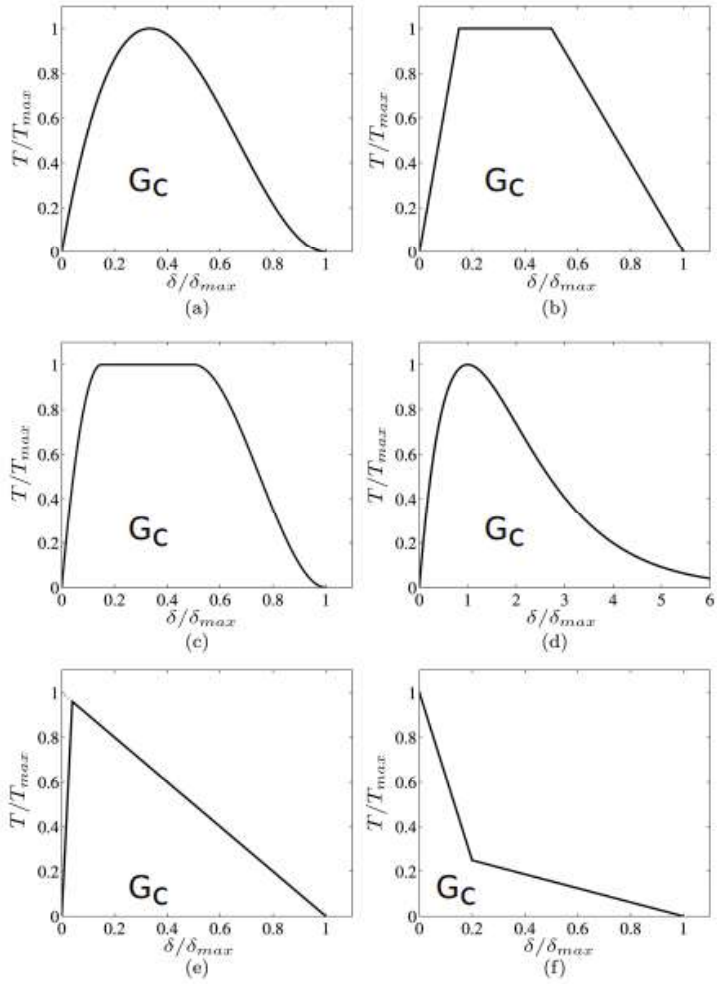

Fig. 1-10: Common traction-separation laws used in cohesive zone modeling: (a) cubic polynomial, (b) trapezoidal, (c) smooth trapezoidal, (d) exponential, (e) linear softening, and (f) bilinear softening. Adopted from [81].

The critical energy (Eq. 1-76) corresponds to the triangle area, an energy effectively spent by the system when a complete separation is achieved, it is a function of the mode mixity angle ψ, and can be simplified in the case linear softening traction separation law in Fig. 1-10(e) to:

$$G_C(\psi) = \frac{1}{2} T^i \delta^f, \tag{1-86}$$

where T^i represents the peak and maximum traction, and δ^f corresponds to the opening at the maximum traction.

1.2.6. Mode mixity dependence of the straight sided buckle: Hutchinson and Suo analytical model

In the case of SS buckles, the normalized energy release rate G/G_0 can be expressed as a function of the internal stress σ_0 and the critical buckling stress σ_c, given by Hutchinson and Suo [26]:

$$\frac{G}{G_0} = \left(1 - \frac{\sigma_c}{\sigma_0}\right)\left(1 + \frac{3\sigma_c}{\sigma_0}\right), \tag{1-87}$$

with G_0 the elastic strain energy per unit area available to be released under plane strain condition [26]. For an isotropic internal stress σ_0, this energy can be expressed as:

$$G_0 = \frac{(1-\nu)h\sigma_0^2}{E}. \tag{1-88}$$

When the stress is anisotropic with different stress components σ_{xx} and σ_{yy}, the expression in Eq. (1-88) becomes:

$$G_0 = \frac{h(\sigma_{xx}^2+\sigma_{yy}^2-2\nu\sigma_{xx}\sigma_{yy})}{2E}. \tag{1-89}$$

Fig. 1-11 presents the normalized energy release rate $G/[G_0.f(\psi)]$ versus the loading ratio σ_0/σ_c, for various η. For $\eta=0$ (no mode mixity dependence), as the ratio σ_0/σ_c increases, the energy release rate G asymptotically approaches $G = \frac{4G_0}{3}$ (see Fig. 1-11), while upon buckling ($\sigma_0=\sigma_c$), G vanishes.

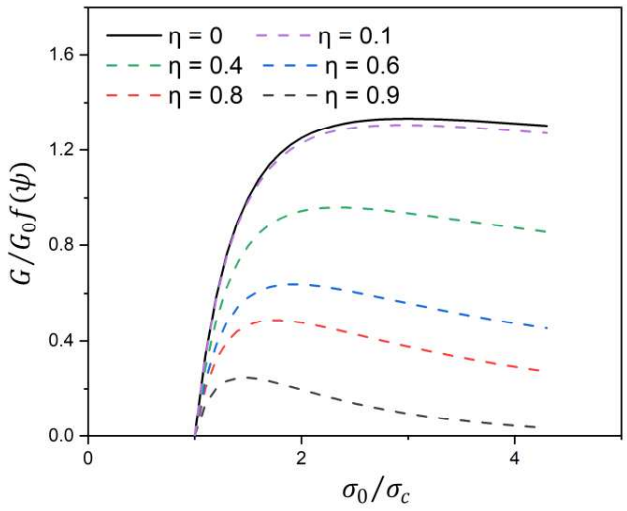

Fig. 1-11: Energy release rate for a SS buckle in the case of isotropic stress as function of the normalized internal stress σ_0/σ_c, for various mode mixity parameter η.

From a fracture mechanics point of view, a crack will propagate if the energy release rate exceeds the interfacial toughness, as result the crack growth would continue unstably leading to complete separation. for example, in the case of $\eta=0$ as shown in Fig. 1-11, the crack is expected to propagate until complete separation. However, this prediction does not fully align with experimental observations. In practice, crack fronts often propagate in a stable manner, particularly in the case of buckle-driven delamination. This discrepancy has been addressed by considering mode mixity, which plays a critical role in controlling crack stability. Both experimental [26,59] and theoretical [26,89] studies have shown that mode mixity plays a critical role in stabilizing the propagation of SS buckles, especially along their lateral edges.

Hutchinson and Suo [26] developed an analytical model to understand how the mode mixity vary with respect to σ_0/σ_c, in both CB and SS buckles. The mode mixity angle ψ can be expressed as:

$$\tan\psi = \frac{4\cos(\omega)+\sqrt{3}\delta/h\sin(\omega)}{-4\sin(\omega)+\sqrt{3}\delta/h\cos(\omega)}, \tag{1-90}$$

with ω, the phase angle that depends on the Dundurs' parameters α_D and β, as shown in Fig. 1-12a. For simplicity, many studies focus on the case where there is no elastic mismatch where $\alpha_D=0$ and $\beta=0$, giving a phase angle of ω=52.1°. Fig. 1-12b illustrates how the mode mixity angle ψ varies with respect to σ_0/σ_c for various values of α_D.

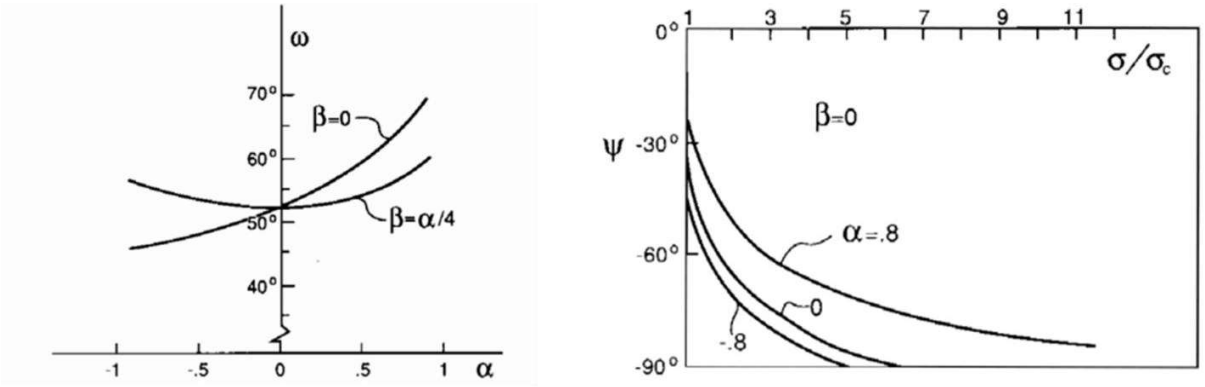

(a) (b)

Fig. 1-12: The phase angle $\omega(\alpha, \beta)$, and the mode mixity angle ψ. Adopted from [26].

One key factor influencing the stabilization of SS buckles is the evolution of mode mixity during the buckle growth. For instance, for low elastic contrast α_D=-0.8 as shown in Fig. 1-12b, significant contributions from both mode I (opening mode) and mode II (shearing mode) at low load σ_0/σ_c. Let's for instance suppose that σ_0 is constant, if the sides of the SS buckle expand, σ_c decreases as result σ_0/σ_c increases, the mode mixity angle ψ increases in absolute value as shown in Fig. 1-12, therefore the interfacial toughness $G_C(\psi)$ increases strongly with ψ, as previously shown in Fig. 1-8, all of this will lead to buckle arrest phenomena. The transition from mode I to II affects the SS buckle growth behavior significantly. Mode II generally encounters greater resistance to propagation due to high interfacial toughness. As a result, even if the energy release rate remains high, but the mode mixity increases the interfacial toughness, leading to stable lateral crack fronts. This explains why the sides of SS buckles often stabilized, resulting in a finite width that remains constant even as the buckle height increases.

1.3. Stabilization of the straight sided buckle

1.3.1. Steady state propagation of the straight buckle at the front

As previously discussed, SS buckles tend to expand laterally along the transverse direction, driven by compressive stress until the interfacial toughness exceeds the energy release rate. However, experimental observations reveal that once the buckles are formed, they can propagate longitudinally in steady state. In order, to understand the steady state propagation of the SS buckle, Hutchinson and Suo [36] developed an approach where they approximate the front of the SS buckle by a spherical shape with radius $R=b$. This model allows the evaluation of the energy release rate

at SS buckle the front. Fig. 1-13 illustrates the propagation mechanisms of the SS buckles, as well as their typical morphology.

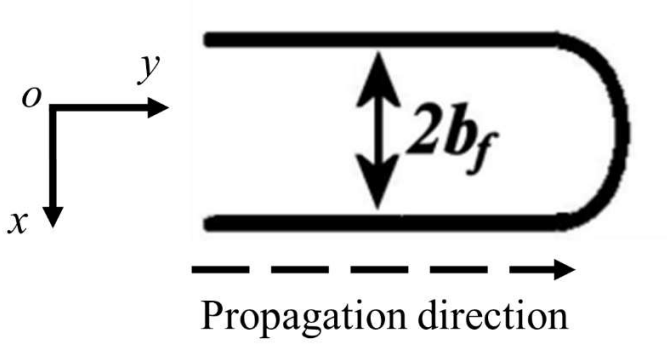

Fig. 1-13: The steady propagation of the front SS buckle.

The average energy release rate at the front of the SS buckle [26], is given as:

$$G_{ss} = \frac{1}{b}\int_{b_0}^{b} G db, \tag{1-91}$$

where G is the energy release rate of a circular buckle, with radius increasing from b_0 to b. Using the expression of G (see Eq. (1-87)) given previously, Eq. (1-91) can be simplified to:

$$G_{ss} = G_0\left(1 - \frac{\sigma_c^*}{\sigma_0}\right)^2, \tag{1-92}$$

where G_0 is the elastic strain energy stored in the film by unit surface and $\sigma_c{}^*$ the critical stress for a circular buckle, defined as:

$$\sigma_c^* = 1.2235\frac{E_f}{1-\nu_f^2}\left(\frac{h}{R}\right)^2. \tag{1-93}$$

For the demonstration of the mode mixity angle ψ^* at the SS buckle front, one can refer to the work of Hutchinson and Suo [26]. Here, we only give the corresponding mode mixity angle ψ^*, given as [26,36]:

$$\tan\psi^* = \frac{\cos(\omega)+0.2486(1-\nu_f)\delta/h\sin(\omega)}{-\sin(\omega)+0.2486(1-\nu_f)\delta/h\cos(\omega)}. \quad (1\text{-}94)$$

This expression is quite similar to the Eq. (1-90). The mode mixity angle ψ^* at the front depends on the phase angle, the out-of-plane displacement, the film thickness h and on the geometrical parameters of the front SS buckle.

Steady state propagation requires that the energy release rate at the front of the SS buckle must exceed the interfacial toughness under the mode mixity dependence, as described by Hutchinson and Suo [26]:

$$G_{ss} \geq G_C(\psi^*). \quad (1\text{-}95)$$

Therefore, the knowledge of the distribution of the mode mixity angle ψ^*across the front of the SS buckle is required to understand the steady state propagation of the SS buckle. Comparing this to the sides of the SS buckle, the normalized energy release rate $G/[G_0.f(\psi)]$ is higher than at the front $G_{ss}/[G_0 f(\psi^*)]$. This difference gives an idea on why the sides of the SS buckle often expand faster than the front, leading to the characteristic striped morphology of the SS buckles.

1.3.2. Influence of the elastic contrast on the mode mixity

The mode mixity angle ψ is influenced by the elastic contrast of the bi-material system, through the phase angle $\omega(\alpha_D, \beta)$ [26]. This dependency is illustrated in Fig 1-14. In particular Hutchinson *et al.* [26] showed that when $\beta = \alpha_D/4$, the phase angle ω is insensitive to elastic contrast, with α_D varying within the range of $-0.8 \leq \alpha_D \leq 0.8$. However, for a precise interpretation of mode mixity angle in general systems, it is necessary to account for the elastic contrast [36,59], since recent studies [59] demonstrated that modern bi-material exhibits a broad range of phase angles $\omega(\alpha_D, \beta)$. Zak *et al.* [59,90] developed numerical model which accounts for various elastic contrast in the film/substrate system. Using his model, the phase angle $\omega(\alpha_D, \beta)$ can be expressed as:

$$\omega(\alpha_D,\beta) = 52.466 + 10.510.\alpha_D - 1.403.{\alpha_D}^3 + 9.477.{\alpha_D}^4 + 10.298.{\alpha_D}^5 - 48.786.\beta - 6.444.\beta^3 + 5.943.\alpha_D.\beta. \quad (1\text{-}96)$$

We plotted the phase angle (Eq. 1-96) over a wide range of values of α_D, considering $\beta = \alpha_D/4$, and compared the results with the classical Hutchinson and Suo model [26]. As shown in Fig. 1-14, it is clearly observed that incorporating the elastic contrast α_D is essential for accurate phase angle evaluation.

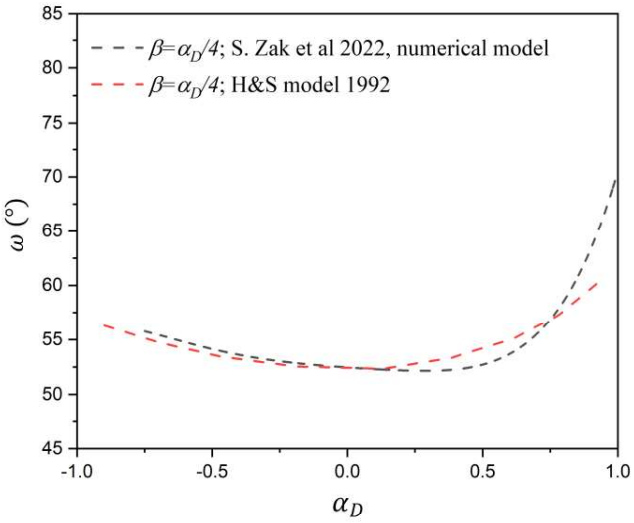

Fig. 1-14: Influence of the Dundurs' coefficients α_D on the phase angle $\omega(°)$ for $\beta=\alpha_D/4$. Red dashed and black lines represent Hutchinson and Suo model [26] for bi-material combination, and numerical model developed by Zak *et al.* [59], respectively.

To illustrate how ω influences ψ, Fig. 1-15 presents ψ at the sides of the SS buckle as a function of σ_0/σ_c for various (α_D, β). The evolution of mode mixity angle with loading and elastic mismatch plays a critical role in the propagation behavior of the SS buckles, as shown in Fig. 1-15. For instance, in the case of an elastic film on a rigid substrate, where the Dundurs' coefficients are (α_D, β) = (-1, 0), the initial mode mixity at the onset buckling ($\sigma_c=\sigma_0$) is ψ=47°. Pure mode II (ψ=90°) is reached just at a small loading ratio of σ_0/σ_c = 4.3. In contrast, in the case of no elastic mismatch (α_D=0, β=0), the mode mixity angle is ψ=37° at σ_0/σ_c = 1, indicating a more mode I dominated. As the load increases, pure mode II (ψ=90°) is achieved only at σ_0/σ_c=7.7. To further understand the role of elastic contrast, a third system was considered: Ni film with E_f =200 GPa and ν_f=0.31 on a substrate with E_s=25 GPa and ν_s=0.37, yielding to α_D=0.75 and β = 0.15. At the buckling stress $\sigma_0=\sigma_c$, the corresponding mode mixity angles are ψ=31° for β= 0.15, and ψ=33° for $\beta= \alpha_D/4$. Pure mode II reached at loading ratios of σ_0/σ_c=12 and σ_0/σ_c=10.8 for β= 0.15 and $\beta= \alpha_D/4$, respectively. In the case of nickel (Ni) films on a compliant polycarbonate (PC) substrate (The core material system that will be used in the course of this PhD work), results in an elastic contrast of α_D=0.975 and β= 0.2, consistent with the values reported by Monetto *et al.* [91]. At $\sigma_0=\sigma_c$, the mode mixity angle is relatively low and shows negligible effect of β as well, for instance ψ=19° for β= 0.2 and ψ=22° for $\beta= \alpha_D/4$, respectively, indicating significant contribution of mode I. However, the evolution of ψ shows strong dependence on β, particularly in pure mode II that is attained at σ_0/σ_c=32 and σ_0/σ_c=25 for $\beta= \alpha_D/4$ and β= 0.2, respectively.

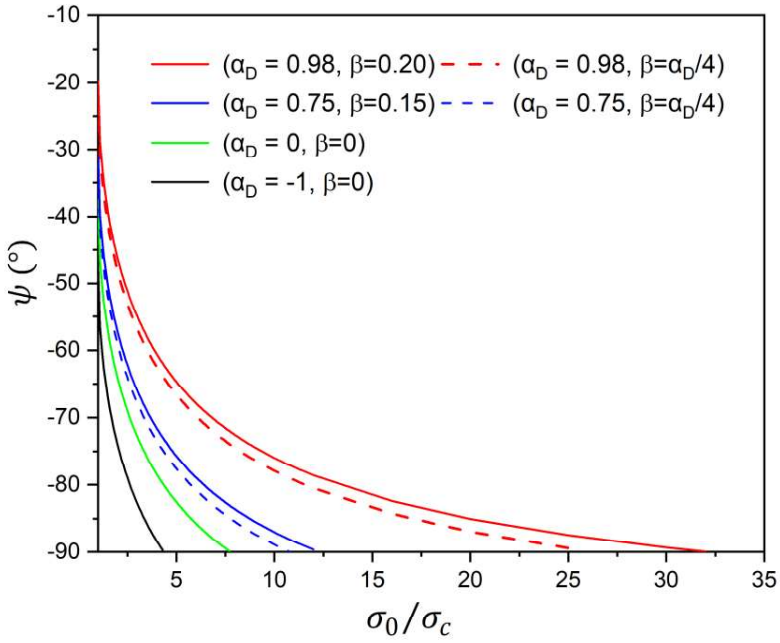

Fig. 1-15: Mode mixity angle ψ at the sides of the SS buckle as a function of the loading ratio for various film/substrate systems with different elastic contrast.

One can cite the work of Boijoux *et al.*[92], where the authors investigates experimentally and FEM simulations incorporated cohesive zone model the SS buckle in elastic films on a various substrates from rigid to compliant substrates with $\beta = \alpha_D/4$. They demonstrated the influence of Dundurs' coefficient α_D on the mode mixity, the results are presented in Fig. 1-16b, it shows that the higher α_D the lower mode mixity dependence, in good agreement with results of Zak *et al.* [59,90]. The effect α_D on the energy release rate G is studied, and it is shown in Fig. 1-16a, the results demonstrated for values α_D of between -1 and 0, the energy release rate G seem to be unaffected. Beyond these regions the energy release rate is significantly increased, for instance for α_D=0.82 it increased by 68%. The increase in the energy release rate due to the elastic contrast is studied as well by Cotterell *et al.* [35].

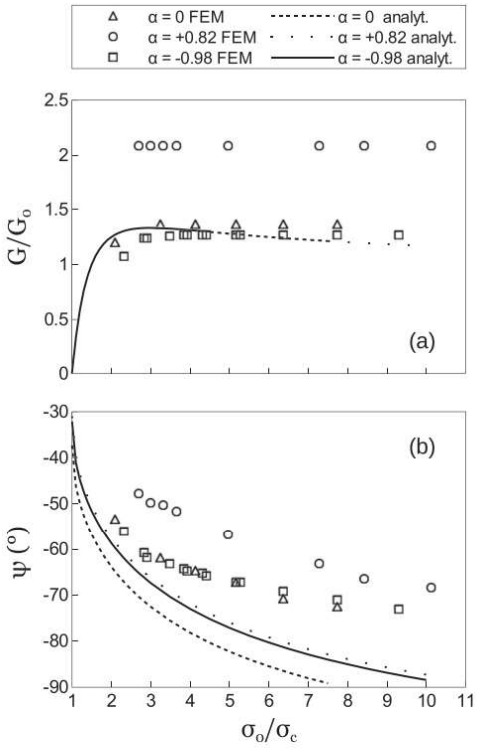

Fig. 1-16: Comparison between analytical solutions and FEM simulations for various values of a_D. (a) Normalized energy release rate, $G/G_0=f(\sigma_0/\sigma_c)$. (b) Mode mixity angle, $\psi=f(\sigma_0/\sigma_c)$. Adopted from [92].

These comparisons clearly demonstrate that the elastic mismatch has a significant influence on the mode mixity. Systems with higher α_D tend to exhibit lower initial mode mixity angles upon buckling, favoring a greater contribution from mode I. This condition promotes the growth of buckles and enhances the buckling delamination by effectively lowering the interfacial toughness. All those results guide us to ask for a fundamental question: how does the local interfacial toughness at the SS buckle front depend on the mode mixity? This will be the main focus that will be addressed in detail in Chapter 4.

1.4. Secondary buckling

Although we previously discussed the stability of SS buckles in the context of mode mixity, the destabilization of the SS buckles has been extensively investigated through experimental and finite element studies done by several authors [12,14,16,24–26,28,32,44,45,51]. From a mechanical stability point of view, the growth of a SS buckle cannot be sustained at high isotropic compressive stresses. Under such conditions, the buckles seek to minimize its length or total energy, which leads to a secondary buckling known as the telephone cord buckles. As mentioned in the

introduction of this thesis, SS buckles are rarely observed experimentally; instead, TC buckles are commonly observed in various stressed thin films on various substrates. This secondary buckling can either evolve from the instability of SS buckles [24,26,28] or from the instability of the crack front during delamination [30,31] within two approaches: a static approach and a dynamic approach. Despite numerous studies, no analytical model currently exists to predict the critical buckling stress and maximum height for TC buckles, in contrast to the SS and circular (C) buckles that are fully described in the framework of the FvK plate theory [26]. To address this gap, Ni *et al.* [24] developed an analytical framework describing the three-dimensional post-equilibrium of TC buckles by solving the FvK equations [55]. However, this model is only valid in the limit where the normalized amplitude of the wavy centerline relative to the wavelength remains very small.

1.4.1. Secondary buckling within static approach

The transition from SS buckles into either C buckles or TC buckles was studied through combined experimental and numerical studies by Parry *et al.* [28]. The authors developed a phase diagram of buckling morphologies, based on FEM simulations. In their simulations, an elastic homogenous film of thickness h and stripe width $2b$, on rigid substrate, are considered. The phase diagram in Fig. 1-17 provides a clear overview of the morphological transitions with respect to stress anisotropy and geometrical properties of the buckles. β_t and β_l are two dimensionless parameters, defined as:

$$\beta_t = \frac{(1-\nu_f^2)\sigma_t^0}{E_f}\left(\frac{2b}{h}\right)^2, and\ \beta_l = \frac{(1-\nu_f^2)\sigma_l^0}{E_f}\left(\frac{2b}{h}\right)^2. \quad (1\text{-}97)$$

σ_t^0 and σ_l^0 represent the transverse and longitudinal residual stresses, respectively. E_f is the Young's modulus, ν_f is the Poisson's ratio of the film, $2b$ is the stripe width and h is the film thickness. Depending on the ratio between β_t and β_l, different morphologies are expected: For instance, when compressive stresses, either intrinsic or externally applied, exceed the critical buckling stress predicted by the elastic plate theory [28], buckling occurs. If the longitudinal stress is significantly larger than transvers stress, circular buckles are expected. In contrast, when the transverse stress is higher, SS buckles will be formed. However, under high and nearly isotropic compressive stress, SS buckles become unstable and evolve into TC buckles as shown in Fig. 1-17.

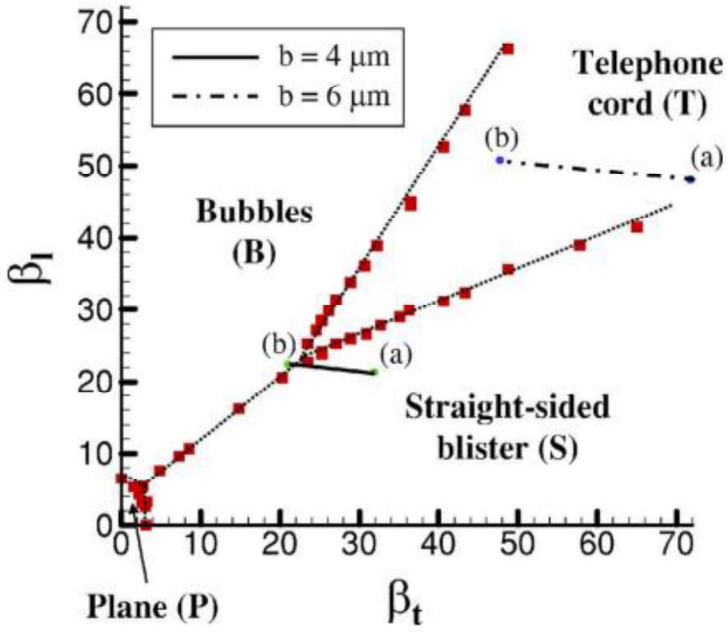

Fig. 1-17: FEM-based stability diagram of buckling morphologies, adapted from [28]. The two nondimensional parameters, β_t, and β_l, are used to map the different buckled states. Four distinct stability domains are identified: planar state, bubbles, straight-sided (SS) buckles, and telephone-cord (TC) buckles. The experimental loadings labelled (a) and (b) in Fig. 1-18 are indicated on the diagram for the two strip widths studied (4 μm and 6 μm).

Experimental observations by Parry *et al.* [28] that validate the phase diagram are presented in Fig. 1-18, showing atomic force microscopy images of various buckling structures. In this experiment, a 50 nm thick nickel film was subjected to high transverse compressive stress, leading initially to the formation of SS buckles. Depending on the stress anisotropy, the SS buckles evolve into periodic bubbles or TC buckles. The bright white contrasts in the AFM images correspond to buckling structures. Thus, both numerical simulations and experimental observations consistently demonstrate that SS buckles become unstable under high isotropic compressive stress and tends to evolve towards more energetically favorable buckles.

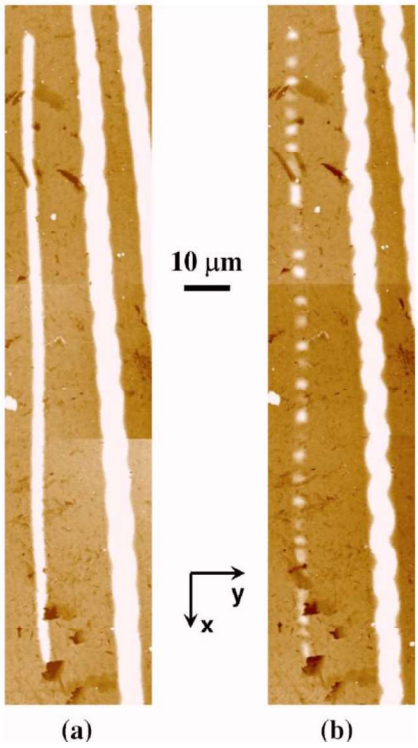

Fig. 1-18: Adapted from [28]. Evolution of a straight-sided (SS) buckle in a 50 nm-thick nickel film under increasing compressive stress, observed by atomic force microscopy (AFM). Image (a) corresponds to a state with higher transverse stress σ_t and lower longitudinal stress σ_l compared to the final configuration in (b). The white contrast highlights the buckling features formed on the film surface during compression. Two morphological transitions are evident: from SS buckles to either periodic bubble-like structures (left side) or telephone-cord (TC) buckles (right side).

Meanwhile, the transition from SS to TC buckles in homogenous stressed films has been widely documented [29,45-47]. Moon *et al.* [45] studied SS buckles confined within stripes of varying widths and showed that SS buckles evolve to TC buckles at sufficiently large widths. A similar transition was experimentally observed by Yu *et al.* during the propagation of buckles in $SiAlN_x$ films [16,33]. Jia *et al.* further explored this SS-TC transition in strained aluminum films [32], numerically demonstrating that the critical for secondary buckling decreases as the buckle width increases.

1.4.2. Secondary buckling within dynamic approach

A detailed analysis of the transition from the SS to TC buckles within a dynamic framework was carried out by observing optical microscopy images taking at different time intervals [33]. For instance, considering buckle “mode 1” shown in Fig. 1-19, the SS buckle front head initially

propagates gradually with well-defined and uniform front at t=0 and up to 1 min. However, from t=2min onward, the SS buckle starts to destabilize and evolves into TC buckle. The destabilization continues with time. When attending 5 min, a fully developed TC buckle is observed with well defined wavelength λ. Different behaviors were observed for "mode 2". In this case, although the buckle head seem to have morphology of the SS buckle, nevertheless the length of the SS segment is very small (less than wavelength). In contrast, mode 3 exhibits a completely different phenomenon: it starts as a pure TC buckle, with the buckle front showing sagging-in behavior [30]. As the TC buckle advances, it repeats cycles of pinning and undulation, ultimately leading to the formation of a well-defined wavelength.

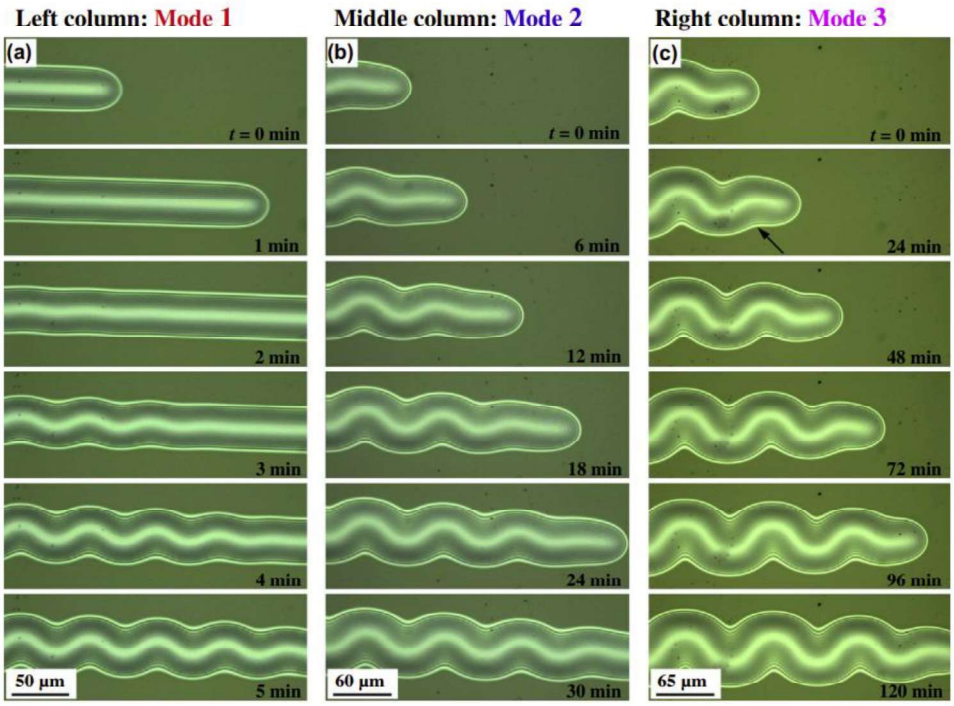

Fig. 1-19: *In situ* growth and evolutions of buckle modes 1, 2 and 3. The propagation time t for each buckle is indicated in the bottom-right corner of the corresponding image. The zero time corresponds to the first photograph; note that t represents the local propagation time, not the total experimental duration T. (a) Buckle mode 1 (left column), images of sizes 265 × 100 µm^2 captured at 1 min intervals. (b) Buckle mode 2 (middle column), images (340 × 110 µm^2) captured at 6 min intervals. (c) Buckle mode 3 (right column), images (340 × 120 µm^2) captured at 24 min intervals. Black arrows indicate newly formed wave troughs during buckle propagation. Adopted from [33].

To understand the dynamic behavior of mode 3 shown in Fig. 1-19, we refer to the study of Faou *el al.* [30]. For the first time, they incorporated FEM simulations with cohesive zone model using the phenomenological law developed by Hutchinson and Suo [26] to explain the dynamic

nature of the TC buckle. First, they shown that circular buckle destabilizes into a sag due to configurational instability [31]. Their results demonstrate that mode mixity angle ψ at the interface is a key factor controlling the undulation and governs the evolution of the TC buckle. These findings are illustrated in Fig. 1-20, which presents mapping of the mode mixity angle during the growth of a TC buckle over time. The mode mixity angle is shown to increase from a median value of ψ=72° to nearly ψ=90°, leading to the formation of a pinning point, where the interfacial toughness corresponds to pure mode II conditions. The TC buckle grows by branching around such pinning points; this branching process repeats, giving rise to a well-defined wavelength.

Such dynamic behaviors not only influence the buckling morphology but also impact the functionality of film/substrate systems. However, mechanical properties such as interfacial toughness of the film/substrate system can be assessed from the TC buckle geometry [22,23]. In this context, Faou *et al.* [22] established a direct relationship between the wavelength of a TC buckle and the associated interfacial adhesion.

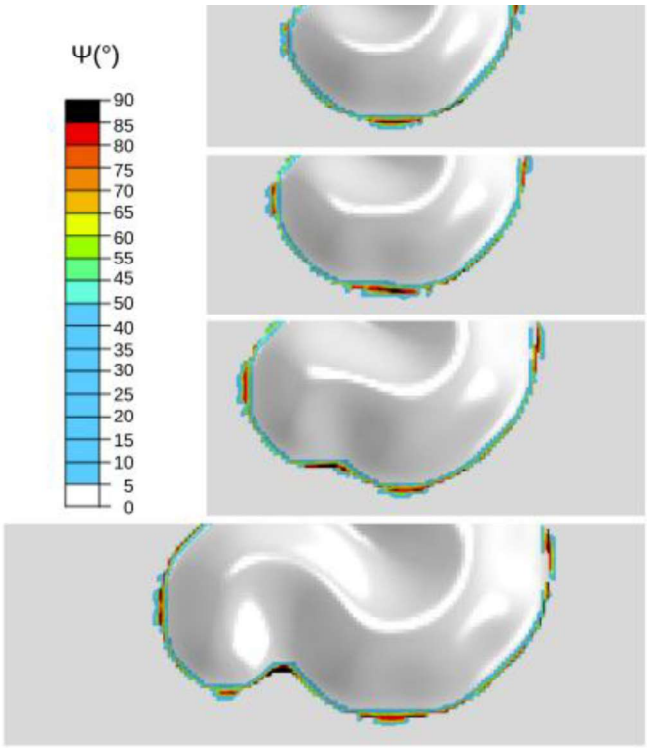

Fig. 1-20: Distribution of mode mixity angle along the delamination front for four stages of buckle propagation. As the buckle front advances, local configurational instability generates high mode mixity, effectively pinning the front. A slight shift of the pinning point is observed as the buckle expands around it. Adopted from [30].

1.5. Conclusion

In this chapter, we developed a comprehensive theoretical framework to analyze buckling phenomena in thin films. Starting from the Föppl–Von Kármán equations, we derived the elastic foundations necessary to describe the large out-of-plane deformations, or nonlinear behavior, that characterize buckling phenomena in compressed thin films. Following, a complete analysis of the straight-sided buckle within the elastic plate theory was shown. We then introduced a detailed overview on the fracture mechanics, including energy release rate and mixed-mode angle, to describe the crack growth along an interface. To capture the complex interplay between interfacial toughness and buckling, we described in detail the cohesive zone modeling, with traction-separation laws allowing for a gradual separation between bonded materials. This approach allows us to understand the bucking phenomena observed in practice in a more realistic representation of interfacial behavior. Using the Hutchinson–Suo model and incorporating Dundurs' parameters, we discussed how elastic mismatch affects the interfacial toughness through its influence on the mode mixity parameter ψ. Special attention was given to the instability transitions that occur during delamination propagation. In particular, we examined the transition of the straight-sided buckle morphologies to undulated telephone-cord structures, interpreting this particular shape either as a secondary buckling, or as shaped by the propagation with alternate pining points on the left and on the right of the front. Overall, this chapter establishes the theoretical foundation necessary for analyzing and interpreting complex delamination patterns in thin film systems. The framework developed here provides a basis for both numerical implementation and experimental validation, which will be pursued within a static and dynamic approaches that will be the core objective of chapters 3 and 4, respectively.

1.6. Résumé en Français

Ce chapitre a pour objectif de fournir les fondations théoriques essentielles à l'étude du flambage des films minces. Il introduit d'abord la théorie des plaques élastiques et des cloques, en se concentrant sur les équations non linéaires de Föppl–Von Kármán (FvK). Le cadre théorique passe ensuite à la mécanique de la fracture interfaciale, y compris le Modèle de Zone Cohésive (CZM) et la loi empirique d'Hutchinson et Suo qui intègre la dépendance en mode mixte de la ténacité. Une attention particulière est portée aux structures de flambage comme les cloques à rides droites (SSB) et les flambages en cordon de téléphone (TCB). Dans l'ensemble, ce chapitre établit les bases théoriques qui seront exploitées par les simulations des éléments finis et les investigations expérimentales ultérieures.

I. Flambage Élastique des Films Minces

L'étude du flambage des films minces s'inscrit dans le cadre de la théorie des plaques élastiques, où la non-linéarité provient des changements de géométrie et des grands déplacements.

- **Fondements et Tenseur de Déformation**

La déformation d'un matériau est décrite par le vecteur déplacement $\vec{U}(u,v,w)$. Le comportement non linéaire est capturé par le tenseur de déformation de Green-Lagrange :

$$\varepsilon_{ij} = \frac{1}{2}\left(\frac{\partial U_i}{\partial X_j} + \frac{\partial U_j}{\partial X_i} + \sum_k \frac{\partial U_k}{\partial X_i}\frac{\partial U_k}{\partial X_j}\right). \quad (1\text{-}98)$$

- **Théorie des plaques élastiques et hypothèses de Kirchhoff-Von Kármán**

La théorie des plaques suppose que la plaque est homogène, isotrope, élastique et très mince (épaisseur *h* petite par rapport aux dimensions dans le plan *Oxy*). En commençons par les hypothèses de Kirchhoff: Les contraintes et déformations associées à la direction *z* sont négligeables, d'où $\varepsilon_{zz}= \varepsilon_{xz} = \varepsilon_{yz} =0$ et $\sigma_{zz}= \sigma_{xz} = \sigma_{yz} =0$. On utilisons ces hypothèses, et la loi de Hooke, on peut exprimer les contraintes en fonction des deformations :

$$\sigma_{xx} = \frac{E_f}{1-v_f^2}\left(\epsilon_{xx} + v_f\epsilon_{yy}\right), \quad \sigma_{yy} = \frac{E_f}{1-v_f^2}(\epsilon_{yy} + v_f\epsilon_{xx}), \quad \sigma_{xy} = \frac{E_f}{1+v_f}\epsilon_{xy}. \quad (1\text{-}99)$$

Von Kármán propose que les termes quadratiques des déplacements dans le plan (*Oxy*) peuvent être négligés, mais les termes quadratiques du déplacement hors-plan $(\partial w\backslash\partial x)^2$ et $(\partial w\backslash\partial y)^2$ doivent être conservés. La théorie FvK permet de décrire le comportement non linéaire des plaques minces sous des déplacements modérés à grands. Les équations sont couplées et représentent :

$$\begin{cases} D\nabla^2\nabla^2 w = N_{xx}\frac{\partial^2 w}{\partial x^2} + N_{yy}\frac{\partial^2 w}{\partial y^2} + 2N_{xy}\frac{\partial^2 w}{\partial x \partial y} \\ \frac{\partial N_{xx}}{\partial x} + \frac{\partial N_{xy}}{\partial y} = 0\,;\ \frac{\partial N_{yx}}{\partial x} + \frac{\partial N_{yy}}{\partial y} = 0 \end{cases} \quad (1\text{-}100)$$

Où D est la rigidité de flexion de la plaque : $D = E_f h^3/\ (12.\ (1\text{-}\nu_f^2)$. Les composantes N_{ij} sont les efforts résultants dans le plan, obtenus par intégration des contraintes σ_{ij} dans l'épaisseur.

- **Modèle analytique du flambage ride droit (Straight-sided, SS buckle)**

Le modèle analytique est dérivé pour un film d'épaisseur constante h, sous une contrainte de compression isotrope $\sigma_{xx}^0 = \sigma_{yy}^0 =$- σ_0 (σ_0 >0 pour la compression), sur un substrat rigide. En résoudrons Eq. (1-100), on peut obtenir la contraint critique σ_c pour une transition de plan à ride droite avec une hauteur maximale δ, ce contraint est défini comme celui-ci:

$$\begin{cases} \sigma c\ = \frac{\pi^2}{12}.\frac{E_f}{1-\nu_f^2}.\left(\frac{h}{b}\right)^2 \\ \delta = h\sqrt{\frac{4}{3}\left(\frac{\sigma_0}{\sigma_c} - 1\right)} \end{cases} \quad (1\text{-}101)$$

II. Mécanique de la rupture interfaciale

La propagation des fissures à l'interface se fait généralement sous trois modes classiques (voir Fig.): Mode I (ouverture) : Séparation perpendiculaire au plan de fissure (traction), mode II (cisaillement/glissement) : Glissement des faces de la fissure dans le plan et perpendiculaire au front de fissure, mode III (Déchirement) : Glissement des faces de la fissure parallèlement au front de fissure.

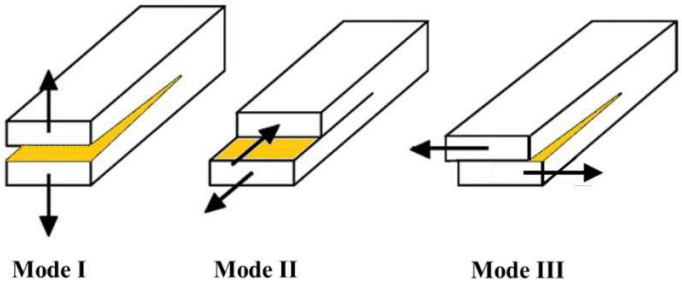

Fig. 1-21: Modes de rupture pour la propagation des fissures : le mode d'ouverture (I), le mode de cisaillement (II) et le mode de déchirement (III).

- **Critère de Griffith et taux de libération d'énergie (*G*)**

Le critère de Griffith stipule qu'une fissure se propage uniquement si l'énergie élastique libérée pendant la croissance de la fissure (G) est supérieure ou égale à l'énergie requise pour créer de nouvelles surfaces (ténacité interfaciale G_C).

- **Dépendance au mode mixte**

La rupture interfaciale se produit généralement en mode mixte (combinaison de Mode I et II), quantifiée par l'angle de mode mixité (ψ). Le modèle phénoménologique de Hutchinson et Suo décrit la dépendance de G_C par rapport à l'angle de mode mixité (ψ) : $G_C(\psi)=G_{IC}.(1+tan^2(\eta.\psi))=G_{IC}.f(\psi)$, Où η est un paramètre sans dimension qui module la contribution du Mode I (G_{IC}) et du Mode II (G_{IIC}) à la ténacité critique.

- **La dépendance de mode mixity: Cas d'une ride droite**

Le taux de libération d'énergie normalisé (G/G_0) pour des rides droits est donné par le modèle du Hutchinson et Suo:

$$\frac{G}{G_0} = \left(1 - \frac{\sigma_c}{\sigma_0}\right)\left(1 + \frac{3\sigma_c}{\sigma_0}\right), \tag{1-102}$$

- **Modélisation du Délaminage**

Le Modèle de zone cohésive (CZM) a été développé pour décrire la propagation de fissure non pas comme une rupture abrupte (contrairement à la mécanique de la rupture élastique linéaire, LFEM), mais comme un délaminage graduel régi par une loi de traction-séparation. Cette loi fondamentale relie le vecteur de traction T= (T_n, T_t) au vecteur de séparation δ= (δ_n, δ_t). Le processus de rupture se déploie en plusieurs étapes : un comportement initial purement élastique

(traction linéaire $T=K\delta$), suivi par l'initiation du dommage lorsque la traction atteint une valeur critique (T_{max}), et enfin par l'évolution du dommage (adoucissement) menant à la séparation complète à δ_{max}. L'énergie de rupture (G_C) est définie comme l'aire totale sous cette courbe de traction-séparation, représentant le travail total requis pour rompre complètement l'interface.

III. Flambage Secondaire (Cloques en Cordon de Téléphone)

Sous des contraintes compressives élevées et quasi isotropes, less rides droites (SSB) deviennent instables et évoluent vers des structures à énergie plus faible, comme les cloques en cordon de téléphone (TC, Telephone Cord).

- **Diagramme de stabilité (Fig. 1-22a) :** Les simulations par éléments finis (FEM) ont permis d'établir un diagramme de stabilité morphologique en fonction des paramètres adimensionnels de contrainte ($\beta_t=(1-\nu_f^2)/E_f.(2b/h)^2.\sigma_t^0$, $\beta_l=(1-\nu_f^2)/E_f.(2b/h)^2.\sigma_l^0$), montrant la transition entre l'état plan, les bulles, les cloques SS et TC.

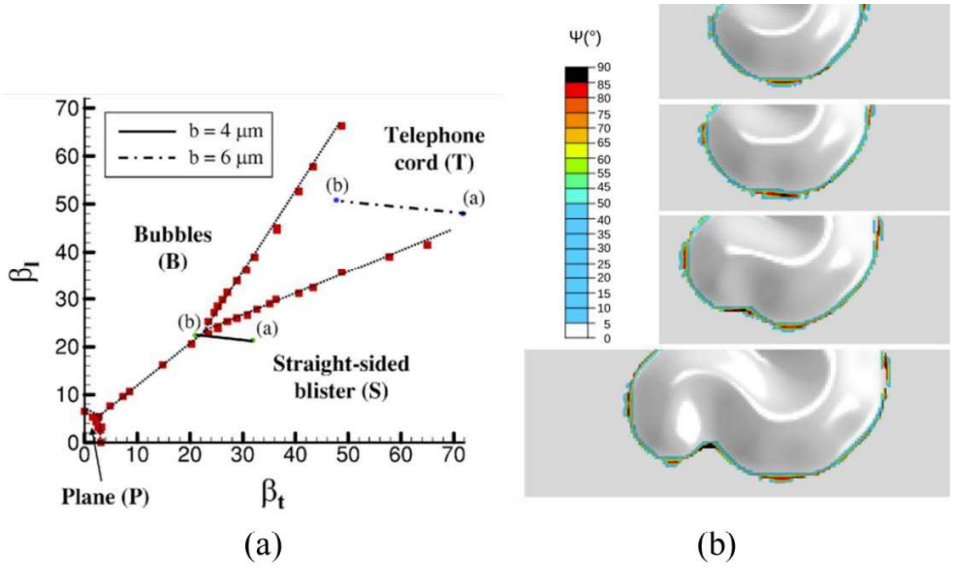

Fig. 1-22: (a) Diagramme de stabilité morphologique basé sur des simulations par éléments finis (FEM). Les deux paramètres adimensionnels, β_t, and β_l, sont utilisés pour cartographier les différents états de flambage. (b) Distribution de l'angle de mode mixité le long du front de délaminage pour quatre étapes de la propagation de la cloque.

- **Comportement Dynamique :** Des études dynamiques (Fig. 1-22b) ont montré que le cloquage de type cordons (TCB) résulte de l'instabilité du front, où l'angle de mode mixité (ψ) augmente localement jusqu'à 90° (Mode II pur) créant des points d'ancrage (pinning points) autour desquels la cloque se propage par ramification, générant l'ondulation caractéristique.

Chapter 2

2. Experimental techniques and characterization tools for the preparation of controlled well thickness gradient

This chapter focuses on the experimental techniques and custom setups developed throughout this thesis. The main objective was to elaborate and characterize nickel thin films with well-controlled thickness gradients. The deposition of nickel films was carried out using a modified ion beam sputtering (IBS) system (Nordiko), equipped with a motorized mobile shutter designed to generate well-defined thickness gradients. Mechanical testing experiments were conducted *in situ* using a Deben micro-compression device, integrated into a Bruker Dimension Icon atomic force microscope (AFM), allowing real time measurements of surface deformation under controlled strain rate. The surface deformation and thickness gradients were then characterized using complementary techniques, including optical microscopy and white-light interferometric profilometry (Talysurf CCI 6000), providing precise surface and thickness measurements. The internal stress in the films prior deposition is estimated using the Stoney's curvature method, for that Stulys profilometry was used. The following chapter is dedicated to the description of the experimental protocols used throughout the thesis, analysis and interpretations of results are presented in the later chapters.

2.1. Thin film deposition: ion beam sputtering

Thin films are commonly elaborated using chemical vapor depositions (CVD) and physical vapor deposition (PVD) techniques such as magnetron sputtering [4–6] and ion beam sputtering (IBS) [93]. Developed in the late 1960s, IBS has since become a widely adopted method for depositing thin films due to its ability to produce films on various substrates, such as on rigid and flexible substrates, with high stoichiometry control, strong adhesion, material versality and uniformity [94]. In contrast to CVD, which relies on chemical reactions, IBS uses an ion source to generate a focused beam of ions. To generate ions, a high electric field, typically in the range 2-10kV, is applied. This high-voltage creates an electrostatic field that confines electrons in the center of the source [95]. Once the argon gas is injected into the ion gun, the high electric field ionizes the argon, creating a plasma inside the source ions, as shown in Fig. 2-1. Ar^+ ions are then accelerated toward a target under high-voltage and sputters target material through momentum

transfer. These ejected atoms travel through the vacuum chamber in plasma and condense onto the surface of the substrate.

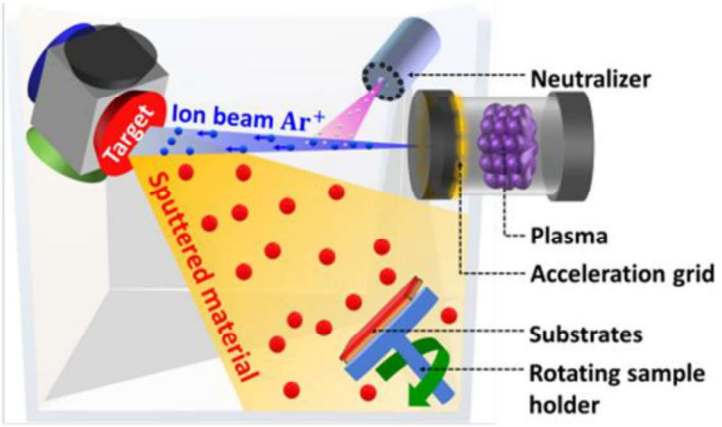

Fig. 2-1: Schematic representation of the IBS deposition chamber

In our study, the goal was to produce thin films with a well-controlled thickness gradient. For this purpose, a custom-designed mobile shutter was developed by Ing. Bruno Lamongie and integrated into a Nordiko IBS machine. An external and internal view of the IBS deposition chamber with the integrated mobile shutter is shown in Fig. 2-2a. The main components of the custom shutter system are illustrated in Fig. 2-2(b). The mobile shutter, labeled (2), and is motorized and programmed via a LabView interface to move at variable speeds ranging from 5 mm/s to 30 nm/s. It is mechanically supported and actuated via a rod (4) and mounted on a DN40CF translator (8) with 150 mm travel. Its vertical position can be adjusted using the height control system (3), allowing alignment with respect to the substrate holder (1). The Nordiko IBS chamber is equipped with four targets positions, represented by the target holder (5). The target corresponds to the material to be sputtered, for instance, a nickel target (6) is mounted in the holder, as schematically shown in Fig. 2-2(b). The argon ion gun (7) generates the primary ion beam used to sputter atoms from the target, which then condense onto the substrate mounted on the substrate holder (1). The internal components of the custom-designed mobile shutter are mounted on a Ø300 mm flange (9), which seals the front access port of the chamber.

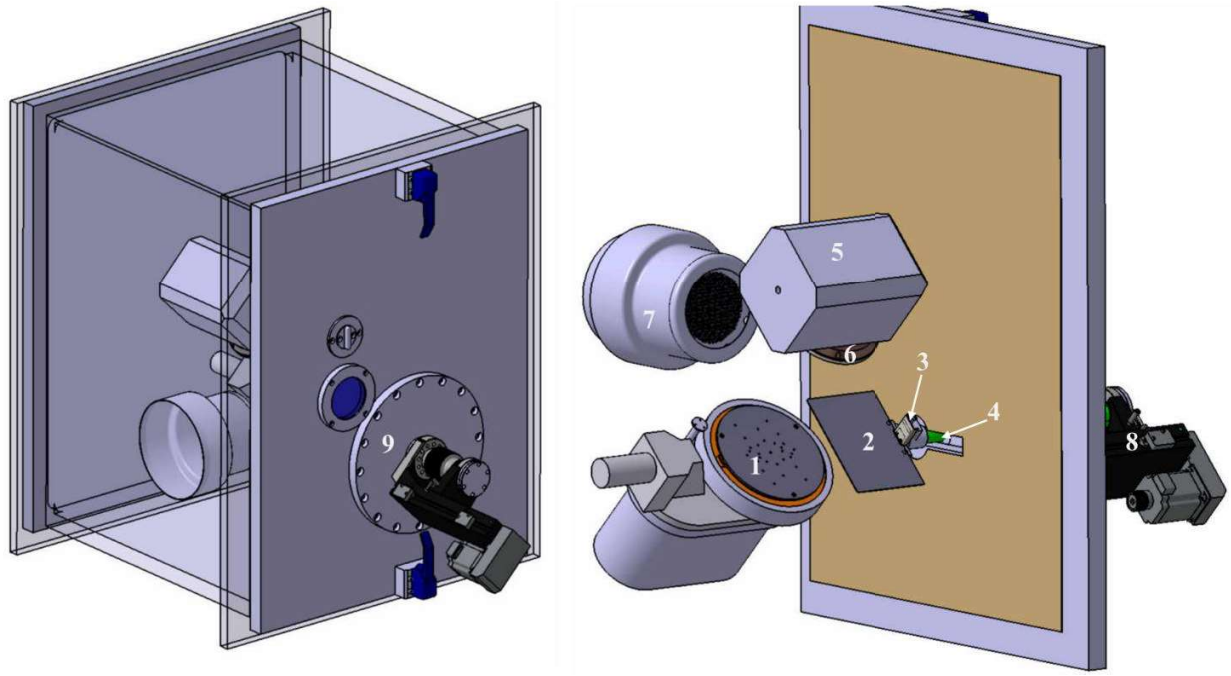

(a) (b)

Fig. 2-2: Schematic of the Nordiko PVD chamber equipped with a custom mobile shutter system. (a) shows an external view from the exit side. (b) Presents an internal exploded view detailing the main components. The system is designed to enable controlled deposition with a thickness gradient by translating a mobile shutter in front of the substrate. Labeled components: (1) Substrate holder, (2) Mobile shutter, (3) Height adjustment system, (4) Shutter rod, (5) Target holder, (6) Position of the nickel target, (7) Argon ion primary gun, (8) DN40CF translator with 150 mm travel, and (9) Ø300 mm mounting flange.

Fig. 2-3 presents the actual interior of the Nordiko IBS chamber, showing the integrated components in their assembly configuration. The substrate holder (1) can be rotated during deposition to ensure uniformity in thickness, however, this feature was intentionally disabled in our experiments to produce thin films with a well-controlled thickness gradient. Due to mechanical constraints of the chamber, the mobile shutter can only travel up to the center of the substrate holder. The substrate is positioned at a 45° tilt using alpha motor controller. This inclination allows the mobile shutter to pass safely above the substrate holder without collision, as the clearance distance between them is very small and approximately 1.5 mm. The 45° tilt angle also contributes to achieving homogeneity and good quality of the deposited thin films.



Fig. 2-3: IBS deposition machine NORDIKO: view of the inside of the chamber showing the various components. (1) Substrate holder, (2) Argon ion primary gun, (3) Neutralizer, (4) Target shutter, (5) Target holder, (6) Support ion gun, (7) Neutralizer, (8) Mobile shutter.

2.2. Deposition of nickel films exhibiting well-controlled thickness gradients

2.2.1. Nickel target

The choice of the target material was critical to ensure thin films that will be used in studying the buckling structures within the framework of elastic plate theory. For this purpose, a high purity nickel target was selected. The nickel target was purchased from société CRYO TECHNIQUES ET COUCHES MINCES [96], with a stated purity of 99.99% and dimensions of 152.4 mm in diameter and 6.35 mm in thickness. It was mounted inside the Nordiko IBS system described in the previous section. Nickel was chosen for its well-known mechanical properties and its compatibility with physical vapor deposition processes. Compared to softer metals such as gold or copper, nickel exhibits relatively high strength and low ductility [19]. It is widely used in various

applications, especially in microelectromechanical systems (MEMS) [97], which benefit from its mechanical robustness and ease of fabrication. MEMS components such as pressure sensors, thermal actuators, micro-coils, micromotors, and other nickel-based microstructures have been extensively studied [97–99]. Nickel has a Young's modulus in the range of 200 to 220 GPa and a Poisson's ratio of approximately 0.31 [12,37,100]. Its yield strength varies from around 59 MPa to 320 MPa [100], and can significantly higher when the material exhibits nanoscale grain sizes [101,102].

2.2.2. Substrates

- ***Silicon substrate***

Silicon (Si) is a semiconductor which are widely used in various applications, practically found in all electronic devices that enrich our lives [103,104]. A silicon wafer is a thin slice of crystalline semiconductor, commonly made in circular shape [105]. They heavily used in the manufacture of semiconductor devices [106]. The silicon wafers are very flat and thin with thickness ranges from hundred nm to hundred μm , allowing for precise surface characterization of the thin films such as thickness, roughness, and microstructure analysis [107,108]. Because it is flat and thin, it offers precise measurements of the internal stress in the films that are deposited on silicon [109,110]. In our study, monocrystalline silicon wafers oriented (100) with thickness 100 μm, 150 μm, 200 μm are used for our deposition. The deposition on silicon allows us to study the microstructural properties of nickel films. To prepare silicon substrates, the procedure was to cut and cleave rectangles with length of 1 mm and width of 0.5 mm. The procedure is to cleave those rectangles by mechanical cleavage using diamond by pressing the border of the wafer along the cleavage direction, then the Si substrates are easily cleaved along the whole length [111].

- ***Polycarbonate substrate***

An appropriate substrate has to be selected for the deposition of the nickel thin films. Polycarbonate (PC) was chosen for its excellent mechanical properties, dimensional stability and compatibility with surface preparation steps. Polycarbonate is an amorphous thermoplastic known for its high optical transparency, resistance to mechanical deformation, durability and relatively low sensitivity to moisture. It also absorbs very little moisture and has a high heat deflection temperature. These properties make it particularly suitable for cleaning, deposition and mechanical testing under ambient conditions. It exhibits a Young's modulus in the range of 2.0–2.5 GPa and a Poisson's ratio of approximately 0.37 [112]. Its combined mechanical stability and surface smoothness made it an appropriate choice for the experimental setups used in this work. The PC substrates were purchased from goodfellow [112] and cut into pieces of 10×10 mm^2 squares with a thickness of 2 mm.

2.2.3. The deposited samples

The next step was to establish a reliable deposition procedure for producing nickel thin films with well-controlled thickness gradients. All films were deposited using the modified NORDIKO ion beam sputtering (IBS) system. Before each deposition, the polycarbonate (PC) and silicon (Si) wafer substrates were cleaned in an ultrasonic bath with isopropanol for 15 minutes, followed in demineralized water to remove surface impurities. The cleaned PC substrates were mounted on the sample holder near the reference position of the mobile shutter, as shown in Fig. 2-4. To enable local thickness measurements after deposition, a 100 µm-thick silicon wafer was placed along the full 10 mm length of each PC sample to act as a partial mask, creating a distinct step between the coated and uncoated regions. In addition to this masking, a separate silicon wafer was mounted at position "1" outside the range of the shutter's motion, where it remained fully exposed throughout the deposition process. This configuration resulted in a film of uniform thickness on the Si wafer, without any gradient. As detailed in the next section, this homogeneous in thickness coated sample was used to support complementary stress characterization of nickel films.

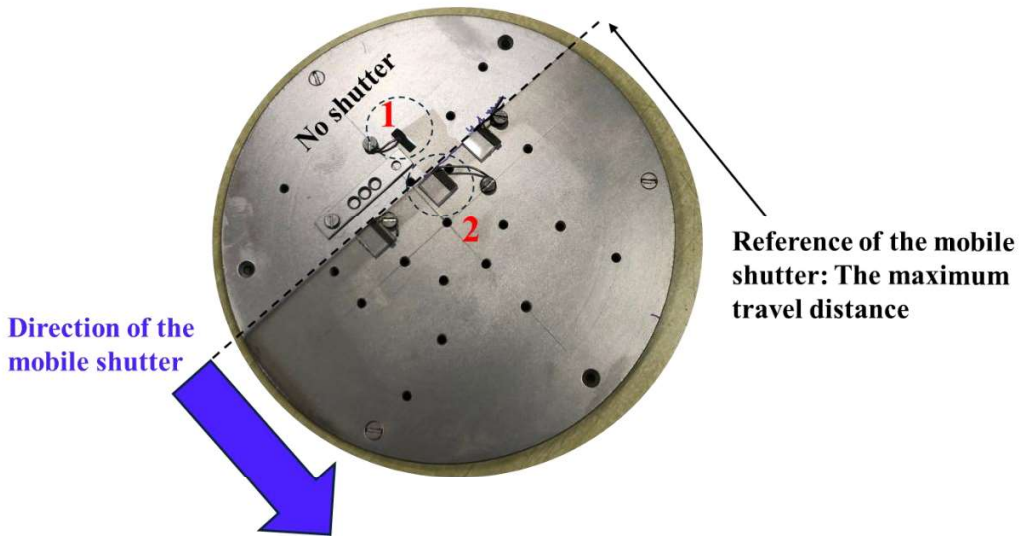

Fig. 2-4: Substrate holder of the NORDIKO machine. The image shows the reference position of the mobile shutter (its starting position), and the blue arrow indicates the direction of its movement during deposition. (1) Silicon wafer substrate (100 µm thickness) placed outside the shutter path and fully exposed to deposition. (2) One of the three polycarbonate (PC) substrates covered by a 100 µm-thick silicon wafer along its length, used to for local thickness measurements.

The motorized shutter was programmed to move across the 10 mm length of the PC substrates either in a single pass or in repeated back-and-forth motions. As defined in Fig. 2-4, the backward

motion refers to the shutter moving from the closed to the open position (blue arrow), while the forward motion corresponds to the return from open to closed (opposite of the blue arrow direction). Each direction could be assigned an independent speed, enabling precise control over the film's thickness gradient. For example, a slower backward pass followed by a faster forward return results in an asymmetric gradient across the substrate. Shutter speeds ranged from 5 mm/s down to 30 nm/s, with a nominal travel range of up to 110 mm. However, due to mechanical limitations of the NORDIKO machine, only a restricted portion of this range was usable in practice. Samples were therefore positioned near the reference position to ensure consistent and reproducible deposition conditions.

All films were deposited under the same base operating conditions:

- The base starting pressure:10-6 Pa
- The working pressure: 0.012 Pa
- Power on target: 160 W
- Depositions temperature: Room temperature (RT)
- Deposition rate: 0.08-0.07 nm/s

The main differences between samples lay in the shutter motion sequence, speed, and number of passes. These parameters, along with the measured residual stress and thickness variations across each film, are summarized in Table 2-1. The experimental procedures used to evaluate these quantities are described in the following sections.

Sample	Direction (Fr: Forward, Bc: Backward)	Speed (µm/s)	σ_0 (GPa)	*hmax*/*hmin* (nm/nm)
A: Ni018	Bc	3	0.8±0.08	300/15
B: Ni027	Bc	2	0.78±0.01	506/0
C: Ni028	Bc/ Fr/ Bc	2.5/20/10	0.91±0.1	580/10
D: Ni029	Bc/ Fr/ Bc	2.5/33/10	0.81±0.02	470/10
E: Ni030	Bc/ Fr/ Bc/Fr/Bc/Fr	5/20/10/5000/10/5000	1.02±0.03	530/30

Table 2-1: Summary of the deposited samples, deposition directions, shutter speeds, and residual stress (σ_0) for nickel films on PC substrates.

2.2.4. Stoney curvature's method

Thin films and coatings deposited by physical vapor deposition methods often exhibit high residual stresses, reaching sometimes the order of gigapascals (GPa) [6,7]. Therefore, evaluating the internal stress within the deposited nickel films was important part of the experimental procedure. In this work, residual stress was estimated using the classical Stoney's curvature

method [113] or similar method used by K. Roll [114], which accounts for the elastic properties of the film. The measurements were performed using a Dektak stylus profilometer, as illustrated in Fig. 2-5. Profilometry scans were carried out on the silicon wafer (see Fig. 2-4), which has a uniform nickel film.

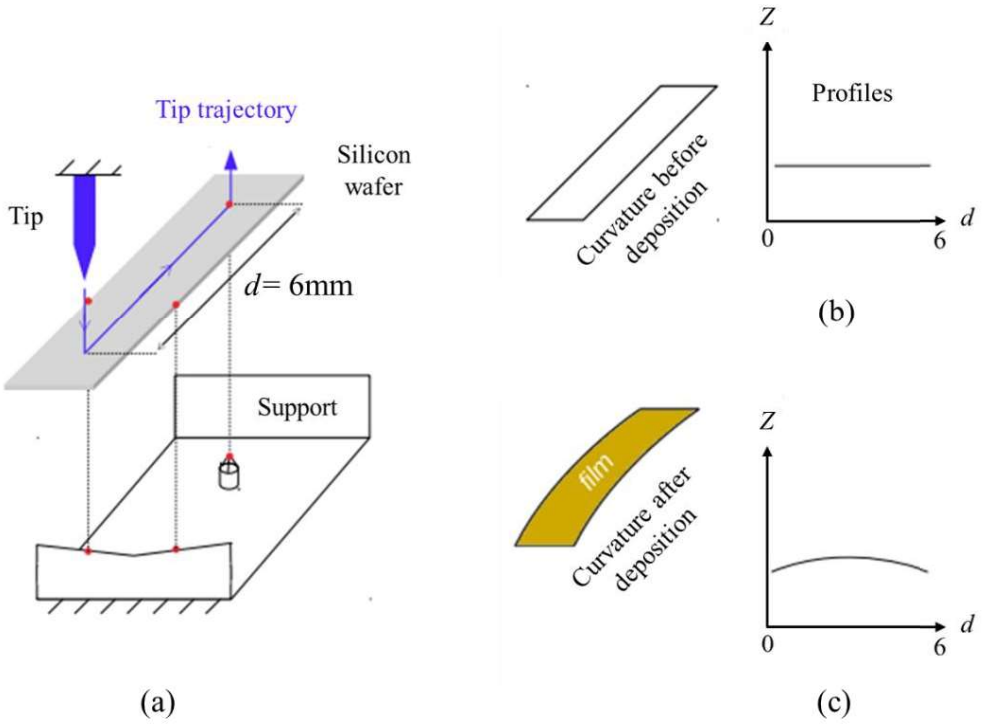

Fig. 2-5: Principal work of the profilometry. (a) Sample holder used on Dektak device. (b) The profiles obtained of the substrate's curvature before and after deposition. Adopted from [115].

The Stylus profilometry tip applied a small normal force and traces the profile of the sample surface over the length of 6 mm. In order to ensure the accuracy of the measurements, multiple scans were performed before and after deposition. The difference in the curvature before after deposition was used to estimate the macroscopic stress in the films.

To apply Stoney's curvature method correctly, the following assumption must be hold [116,117]:

- The lateral dimensions of the substrate are much larger than the film and substrate thickness.
- The film thickness is much smaller than the substrate thickness.
- Both film and substrate are homogenous, isotropic and elastic.
- Curvature is uniform in all in-plane directions (spherical deformation).

The macroscopic stress σ_0 in the film is considered to have mainly two components: the thermal stress σ_{th}, which arises from thermal expansion mismatch between film and substrate and the intrinsic stress σ_i, which depends on the deposition conditions, and the film growth [118]:

$$\sigma_0 = \sigma_{th} + \sigma_i. \tag{2-1}$$

The thermal stress can be expressed as:

$$\sigma_{th} = E_f(\alpha_s - \alpha_f)(T_D - T_{RT}), \tag{2-2}$$

where E_f is the Young's modulus of the film, α_f and α_s are the thermal expansion coefficients of the film and substrate, and T_D, and T_{RT} are the substrate temperature during deposition, and at room temperature, respectively. Since all the depositions were carried out at room temperature, thermal stresses were neglected. The macroscopic stress can be simplified and calculated using the Stoney equation:

$$\sigma_0 = \frac{E_S}{6(1-v_s^2)}\frac{h_s^2}{h_f}\left(\frac{1}{R_f} - \frac{1}{R_i}\right), \tag{2-3}$$

with E_s, v_s, and h_s are the Young's modulus, Poisson's ratio, and thickness of the silicon substrate; h_f is the thickness of the nickel film; and R_i and R_f are the curvature radii of the substrate before and after deposition. The curvature radius is given by [118]:

$$R_{i\ or\ f} = \frac{d^2}{8f_{i\ or\ f}}, \tag{2-4}$$

where d is the scan length, f_i and f_f are the vertical deflections of the substrate before and after deposition, respectively.

The macroscopic stress calculated for each sample using Eqs. (2–3) and (2–4) is reported in table 2-1. In addition, *in situ* stress evolution during film growth was monitored using the PUMA magnetron sputtering system (with Prof. Gregory Abadias, Institut Pprime) not shown here. These measurements were used to examine how deposition pressure influences the development of internal stress in nickel films.

2.2.5. Interferometric optical microscopy

Optical interferometry has been used for precise surface metrology, dating back to the early 20th century, with instruments such as the Michelson and Twyman–Green interferometers. While early systems were sensitive to environmental disturbances, the technique has since evolved into a robust and non-contact method for high-resolution topography measurement [119] [120]. It is now widely used in determining film thickness, surface roughness and morphological features, offering sub-nanometer vertical resolution. In this work, surface characterizations were performed using a white-light interferometric microscope (Talysurf CCI 6000, Taylor Hobson). Fig. 2-6 shows the Talysurf CCI 6000, Taylor Hobson system with its main elements. The Talysurf CCI is supported on an antivibration table used to isolate the instrument from external noise and vibration sources. The CCI has a motorized stage, which allows controlled movement along the X, Y and Z axes using the movement controller. The tilt adjustment around X and Y axes can be made from the translating table. The tilt adjustment is one of the first procedures to be done prior to measurement. The systems consist of an objective lens with Mirau interferometer connected to an optical measuring head component. The CCI system uses white light that is generated by an external source. This light is split into two parallel beams: one reflects off the sample surface and the other off a reference mirror. When the beams recombine, the resulting interference carries information about height variations on the sample surface [121]. Modern systems capture this data across a two-dimensional field to reconstruct the 3D topography of the sample. This machine provides high-resolution in the vertical axis, ranging from 0.01 nm to 0.5 nm, and lateral resolution between 0.5 µm to 7 µm. Therefore, this instrument was critical for characterizing thickness gradients and buckle profiles in the nickel films.

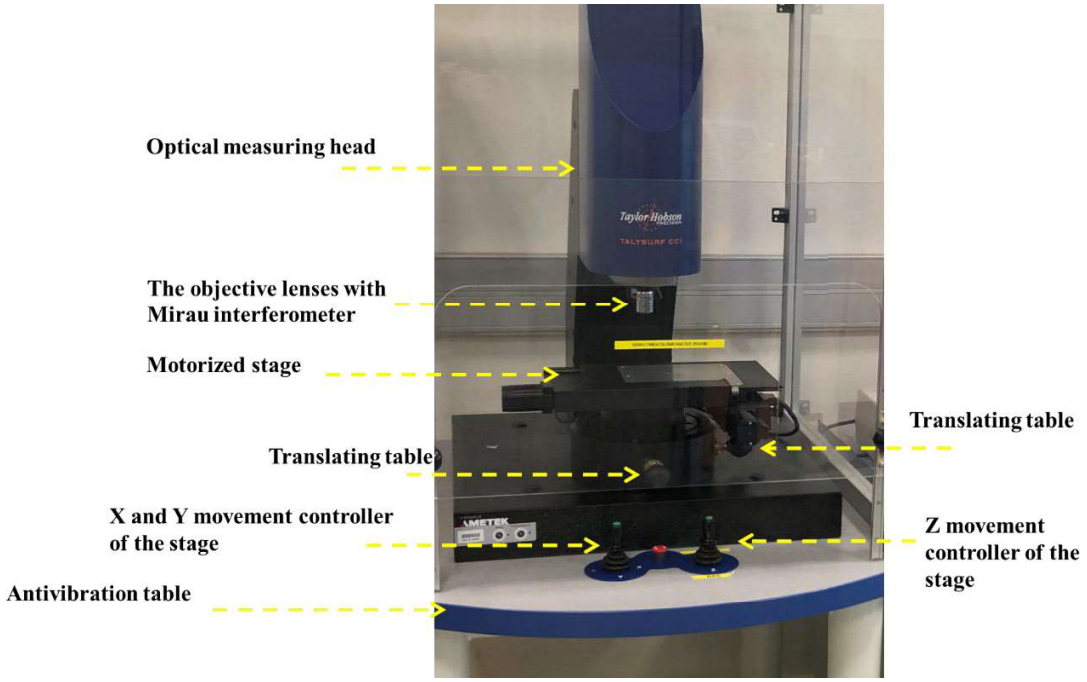

Fig. 2-6: White-light interferometric microscope (Talysurf CCI 6000), used for rapid surface topography measurements.

Thickness gradient measurements were carried out on each deposited sample. As an example, Fig. 2-7 shows the characterization of sample A. Fig. 2-7(a) presents an optical image of the full 10 mm × 10 mm polycarbonate substrate after deposition. The brown region corresponds to the nickel-coated area, while the dark region is the masked zone, where a 100 µm-thick silicon wafer was placed to create a step for thickness measurement. Interferometric scans were performed on both thick and thin sides of the gradient. Insets (d) and (e) in Fig. 2-7 show two selected regions: (d) from the thicker side and (e) from the thinner side. The red lines indicate where the height profiles were extracted. These profiles are shown in (b) and (c), respectively, and were fitted using a smoothed bent step function in Gwyddion software. The measured thicknesses were approximately h=286±10nm for the thick region and h=20±6nm for the thin, the error in thickness originated from the fitted step function. In this case, the results demonstrate that sample is deposited with continuous thickness gradient across the length (Oy) of the sample. Thickness measurements for other samples were performed in the same manner. The maximum and minimum thickness, denoted h_{max} and h_{min}, are listed table 2.1.

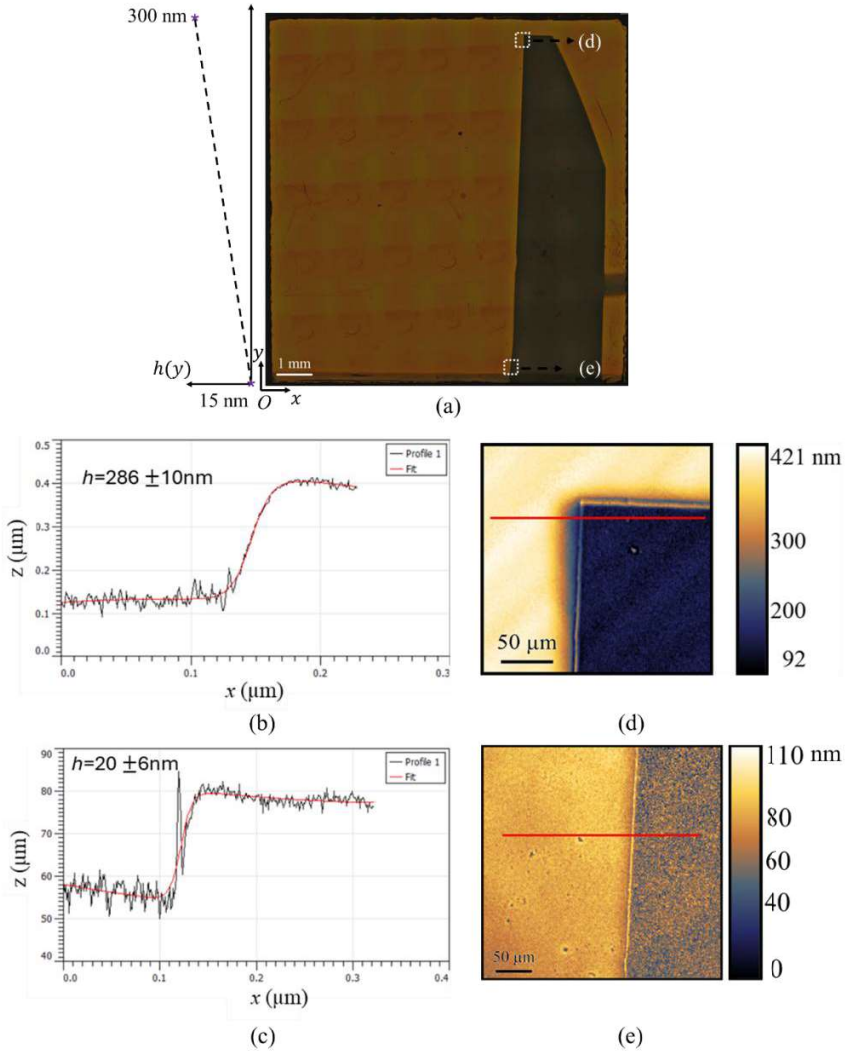

Fig. 2-7: Optical and interferometric characterization of sample A. (a) Optical image of the 10 mm × 10 mm nickel film deposited on a PC substrate. The brown region corresponds to the coated area, and the black region highlights the masked (uncoated) area. (b), (c) Corresponding height profiles extracted from the thick and thin sides of the sample, respectively. Red lines represent fits using a bent step function. (d), (e) Interferometric images of the surface morphology on the thick and thin sides of sample A.

2.2.6. Atomic force microscopy

While optical interferometry allowed for large area thickness and buckle profile measurements, higher resolution imaging was needed to investigate fine scale surface features and buckles in the nickel film. For this purpose, atomic force microscopy was used. AFM is a high resolution surface

characterization technique that provides a three dimensional information about surfaces at the nanoscale. Developed by Binning, Quate and Geber in 1986 [122], AFM has become a cornerstone tool in material and nanoscience. Unlike optical or electron microscopy, AFM operates by mechanically scanning a sharp probe across the sample surface. Interactions between the tip and surface generate topographic data. The cantilever deflection is tracked by a laser beam reflected onto a position-sensitive photodetector, allowing high precision monitoring of the tip and sample interaction. Several operating modes are available depending on the nature of the sample and the desired information. In contact mode, the tip remains in continuous contact with the surface, providing high-resolution imaging [123,124], though this can induce lateral forces that may damage soft samples. Tapping mode reduces this risk by oscillating the cantilever near its resonance frequency, allowing intermittent contact [125,126]. In non-contact mode, the tip remains very close to the surface without touching it and detects weak attractive forces. This is particularly suitable for imaging very soft samples [127].

Peak force tapping (PFT) is the most significant breakthrough in AFM technology since the introduction of tapping mode, developed by Pittenger *et al.* [128]. It provides improved control tip-sample interaction, enables the lower available imaging forces and high resolution imaging. Unlike traditional tapping mode, PFT operates far below the cantilever's resonance frequency, and the tip taps the sample periodically with a peak to peak amplitude of about 300 nm in air [129]. During this procedure the pN-level interaction forces are measured directly by the deflection of the cantilever. The feedback loop controls and keeps the peak force down to 10 pN at actuation rates up to 8 kHz, in air and fluid. The PFT mode requires tunning the cantilever, and controlling the forces to protect the tip and the sample surface while collecting high resolution images. The-tip sample interaction forces are recorded as a function of time during each scan cycle. For instance, Fig. 2-8 presents a schematic of the PFT working principle and shows the tip-sample interaction within a single scan cycle. Initially, when the tip is far from the surface, no force acts on the cantilever. As the tip approaches the surface, attractive forces between the tip and sample become significant. Once these forces overcome the stiffness of the cantilever, deflection occurs, referred to as snap-in and the tip makes contact with surface. The force then increases and reaches its maximum value, known as the peak force. A feedback loop maintains this peak force constant during scanning. After reaching the peak, the tip begins to retract from the surface, and the force decreases to a minimum value, referred to as the pull-off point. Once the tip separates from the surface, it is affected by long-range forces, which are very small or negligible. The cycle then repeats. The total duration of a single complete cycle can be as short as 0.5 ms [128].

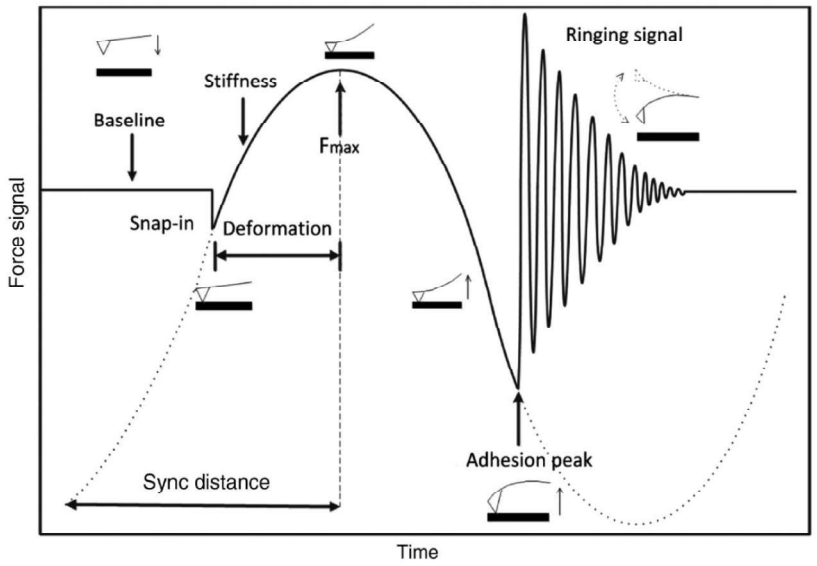

Fig. 2-8: Schematic diagram of Peak Force Tapping mode. (adapted from [130]).

The AFM system used throughout this study is a Bruker Dimension Icon, shown in Fig. 2-9, which displays its main components. The system is mounted on anti-vibration block to isolate it from external noise and mechanical disturbances. The granite stage (1) provides a stable support platform for the entire AFM system. The sample stage (2), designed to hold the specimen during scanning, is mounted directly on the granite stage. The vacuum switch (3) controls the vacuum hold used to fix the sample in place on the stage. The SPM head (4) is the main component of the Bruker Dimension Icon system. It can be detached easily using the screw release (5). The optics system (6) is critical part of the SPM head that enables precise laser alignment. The photodiode alignment knobs (7) are used to align the reflected laser beam onto the center of the quadrant photodetector, while the laser alignment knobs (8) adjust the laser position on the back of the cantilever. The operational status of the laser and photodiode alignment can be monitored through the LCD display (9).

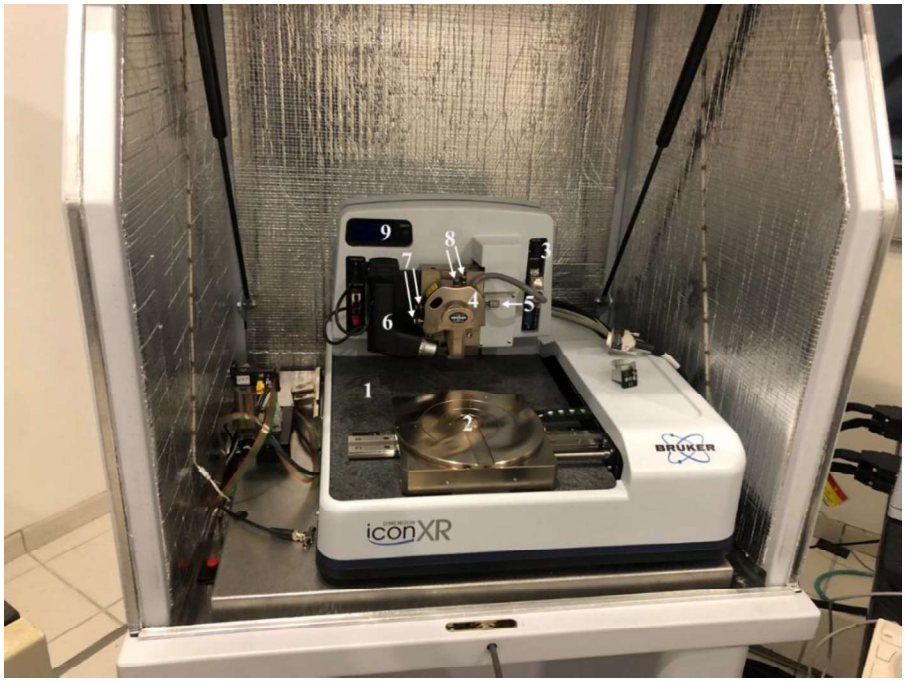

Fig. 2-9: Bruker's Dimension Icon AFM with its main components. (1) Granite stage, (2) Sample stage, (3) Vacuum switch, (4) The SPM head, (5) Screw to release the SPM head, (6) Optics, (7) Photodiode knobs, (8) Laser knobs, (9) LCD display.

All AFM measurements were performed using Bruker Scan Assist tips (nominal resonance frequency f~70 kHz, spring constant k ~ 0.4 N/m). Scanning was performed over areas ranging from 0.5×0.5 μm^2 to 94×94 μm^2, with a resolution of 512×512 and 256×256 pixels. Data acquisition was controlled using Nanoscope software, which includes the ScanAsyst module. Using this module the scanning parameters can adjusted, such as set-point force and feedback gain in real-time to ensure high resolution images with minimal tip–sample force.

2.2.7. Compression device : Deben

To study the mechanical behavior of the nickel thin films under uniaxial compression, an automated micro-compression device (Microtest, Deben UK Ltd), shown in Fig. 2-10a, was used. This compact, motorized system is specifically designed for in situ mechanical testing and is fully compatible with the Icon AFM microscope, due its fitted size and precise displacement control. The Deben stage operates under ambient conditions and can be configured in either tension or compression modes using an integrated 5kN load cell (labeled in Fig. 2-10a). The applied displacement is automatically controlled via a Deben software installed on computer and connected via an interface cable and plug (visible at the top right of Fig. 2-10a), allowing precise displacement of the movable jaw. The sample is mounted between a fixed stainless-steel jaw and

a mobile clamp. The software enables automated displacement control, real time feedback, and data logging. Displacement rates ranging from 0.05 mm/min to 0.3 mm/min are achievable, enabling quasi-static experiments. The system also includes optical encoders for accurate displacement tracking. The Deben stage used throughout thesis is shown in Fig. 2-10a, illustrating its main components. The sample is mounted between two jaws: a fixed stainless-steel block and a movable block connected to a rectangular sliding frame. Displacement is applied by turning the ratchet, which advances the mobile jaw. The setup is mounted on a ceramic base and is equipped with an optical fiber system to track displacement during loading.

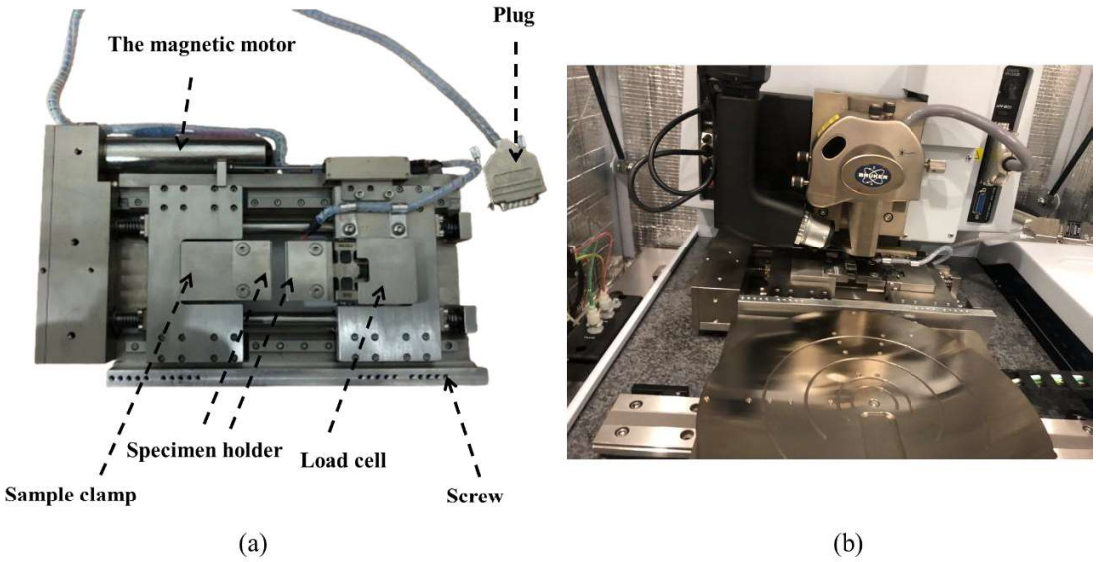

Fig. 2-10: (a) The microtest-compression (Deben) with its components. (b) Bruker's Dimension Icon AFM with an incorporated straining device (Deben) for sample compression.

Prior to testing the nickel-coated samples, the mechanical behavior of the bare polycarbonate (PC) substrates was characterized. Substrates with dimensions of 10 × 10 mm² and a thickness of 2 mm were subjected to five cycles of uniaxial loading and unloading at a strain rate of 10^{-3} s^{-1}. The applied strain reached up to 4.4%. The resulting stress–strain curves, presented in Fig. 2-11, display the expected hysteresis behavior typical of polymers, due to internal damping and viscoelasticity [131]. The curves show full elastic recovery with no residual strain or plastic deformation at the end of each cycle. Since the deformation remained entirely in the elastic regime, the stress–strain data were treated as engineering values, which are a reliable approximation of true stress and strain within this strain range. This confirmed that the PC substrate would not interfere with deformation measurements in the coated samples, validating its use as a mechanically passive support during buckling experiments.

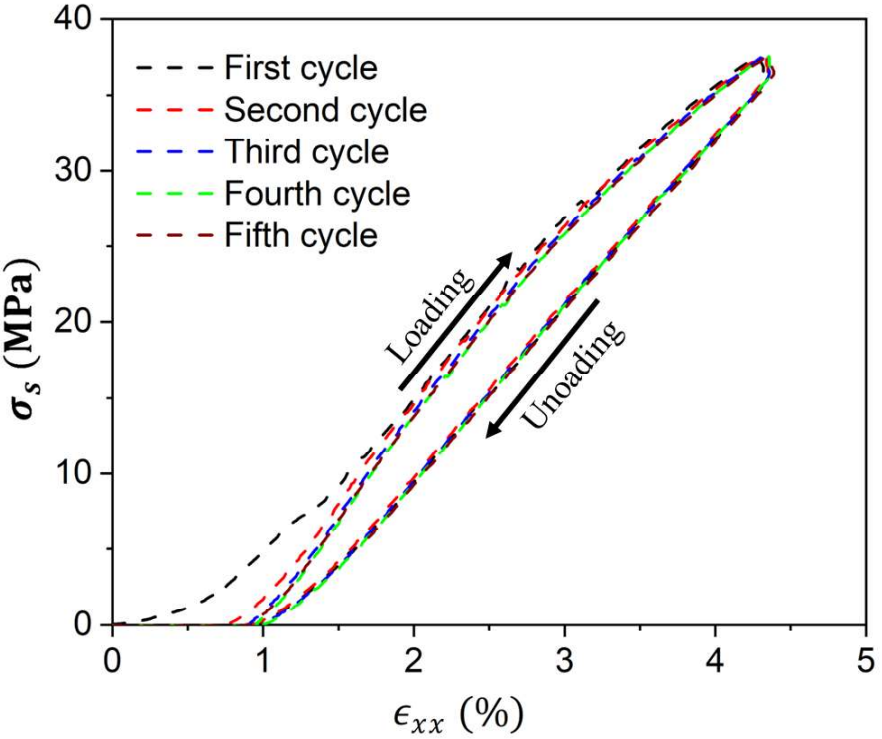

Fig. 2-11: Stress-strain response of a polycarbonate substrate (10 mm × 10 mm × 2 mm) over five loading cycles. The compression rate was $10^{-3}s^{-1}$.

For *in situ* observation during compression, the Deben stage was mounted inside the Bruker Dimension Icon AFM system (Fig. 2-10b). The setup enables simultaneous topographical imaging and mechanical loading. During the test, the AFM tip remained centered on the region of interest while uniaxial displacement was applied incrementally, enabling real-time observation of the morphological evolution under controlled mechanical strain.

2.3. Conclusion

This chapter presented the experimental protocols developed and used to produce and characterize nickel thin films with well-controlled thickness gradients. The process began with the selection of suitable materials: nickel was chosen as the film elastic material for its mechanical strength and compatibility with physical vapor deposition, while polycarbonate was selected as a flexible substrate to support post-deposition mechanical testing. To create thickness gradients across the films, a designed-custom mobile shutter was integrated into the NORDIKO IBS-PVD system. This setup allows us to precisely control the thickness gradients by varying the shutter speeds and passes, leading to smooth, continuous gradients along the length of the sample. Once the films were deposited, their internal stress was first assessed using Stoney's method based on profilometry scans. Thickness gradients were then measured using white-light interferometry, which provided local film thickness across the sample. AFM imaging was used to investigate surface features such as roughness, buckling, and delamination, both before and after compression. The AFM was coupled with a Deben micro-compression stage, allowing in situ imaging during uniaxial loading. Altogether, this experimental framework provided the tools needed to fabricate, characterize and mechanically test thin films exhibiting well-controlled thickness gradient at multiple scales. The results of these methods form the basis for the mechanical and morphological analyses presented in the following chapters.

2.4. Résumé en Français

Ce chapitre décrit les techniques et dispositifs expérimentaux fondamentaux développés pour élaborer et caractériser des films minces de nickel présentant des gradients d'épaisseur contrôlés. L'élaboration des films a été réalisée par pulvérisation par faisceau d'ions (IBS) avec un système Nordiko modifié intégrant un obturateur mobile motorisé pour générer ces gradients. La caractérisation précise de l'épaisseur et de la surface a mobilisé la profilomètre interférométrique à lumière blanche (Talysurf CCI 6000), complétée par la méthode de courbure de Stoney pour estimer les contraintes internes des films. Les tests mécaniques *in situ* ont été effectués sous compression uniaxiale grâce au dispositif Deben intégré au microscope à force atomique (AFM) Bruker Dimension Icon, permettant des mesures en temps réel des déformations. Ce cadre expérimental complet est le socle des analyses mécaniques et morphologiques détaillées dans les chapitres ultérieurs.

I. Dépôt des films minces de nickel par faisceau d'ions

L'élaboration des films a été réalisée par pulvérisation par faisceau d'ions (IBS), une technique de dépôt physique en phase vapeur (PVD) privilégiée pour sa capacité à produire des films uniformes, bien adhérents, avec un contrôle élevé de la stœchiométrie. L'IBS utilise une source d'ions pour générer un faisceau focalisé d'ions. Un champ électrique intense (2-10 kV) est appliqué pour confiner les électrons. L'injection d'argon gazeux provoque son ionisation, créant un plasma au sein du canon à ions. Les ions Ar^+ sont accélérés vers une cible et la pulvérisent par transfert de moment, projetant des atomes qui se condensent ensuite sur le substrat.

Afin de produire des film minces avec des gradients d'épaisseur bien défini, un volet mobile motorisé (conçu par Eng. B. Lamongie) a été intégré au système IBS Nordiko (Fig. 2-2). Le volet mobile (2) est motorisé et programmé via LabView pour se déplacer à des vitesses variables (de 5mm/s à 30 nm/s). Il est monté sur un translateur DN40CF avec course de 150 mm. La rotation de porte substrat (1) a été désactivée pour produire le gradient. Le substrat est positionné à une inclinaison de 45° pour permettre au volet mobile de passer au-dessus du porte-substrat sans collision.

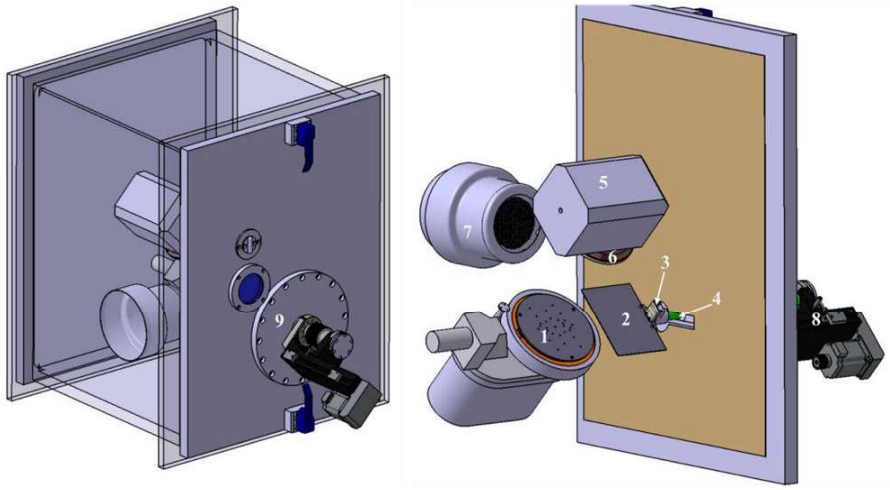

Fig. 2-12 : Schéma de la chambre PVD Nordiko équipée d'un système de volet mobile. (a) Montre une vue externe du côté de la sortie. (b) Présente une vue interne détaillant les composants principaux. Le système est conçu pour permettre un dépôt contrôlé avec un gradient d'épaisseur en déplaçant un volet mobile devant le substrat. Composants étiquetés : (1) Porte-substrat, (2) Volet mobile, (3) Système de réglage en hauteur, (4) Tige du volet, (5) Porte-cible, (6) Position de la cible de nickel, (7) Canon à ions primaires d'Argon, (8) Translateur DN40CF avec course de 150 mm, et (9) Bride de montage Ø300 mm.

II. Matériaux et protocole de dépôt

- **Matériaux cible et substrats**

Les matériaux cibles et les substrats ont été sélectionnés en fonction de leurs rôles spécifiques dans l'étude. Le Nickel (Ni), utilisé comme cible, est la source des films élastiques et présente une pureté de 99.99%. Ses propriétés mécaniques sont bien définies: un module d'Young E_f compris entre 200 et 220 GPa et un coefficient de Poisson v_f = 0 .31. Le Silicium (Si) monocristallin (100) a été choisi comme substrat pour l'étude de la microstructure et pour la mesure de la contrainte interne, avec des épaisseurs allant de 100 à 200 µm. Enfin, le Polycarbonate (PC), un thermoplastique amorphe, a servi de substrat pour les tests mécaniques. Il se caractérise par un module d'Young E_s de 2.0 à 2.5 GPa et un coefficient de Poisson v_s = 0.37.

Les substrats PC et Si ont été préparés par nettoyage ultrasonique (isopropanol, puis eau déminéralisée) avant montage sur le porte-substrat. Un masquage partiel par une plaquette de Si (100 µm) pour créer une marche pour les mesures d'épaisseur locale après dépôt.

Les conditions de dépôt sont listés: Pression de travail, 0.012 Pa, avec une puissance sur la cible de nickel de 160 W, a une température ambiante (RT). Les vitesses et séquences de déplacement du volet déterminent le profil d'épaisseur, comme résumé dans le tableau 2-1.

Échantillon	Direction (Fr: Forward, Bc: Backward)	Speed (µm/s)	σ_0 (GPa)	*hmax*/*hmin* (nm/nm)
A: Ni018	Bc	3	0.8±0.08	300/15
B: Ni027	Bc	2	0.78±0.01	506/0
C: Ni028	Bc/ Fr/ Bc	2.5/20/10	0.91±0.1	580/10
D: Ni029	Bc/ Fr/ Bc	2.5/33/10	0.81±0.02	470/10

Table 2-2: Résumé des échantillons déposés, directions/vitesses du volet, et contrainte résiduelle (σ_0) pour les films de nickel sur substrats PC.

III. Outils de caractérisation

- **Méthode de Stoney**

Les contraintes interne σ_0 (souvent de l'ordre du GPa) sont estimées en mesurant le rayon du courbure du substrat Si avant et après (R_f) le dépôt (R_f) à l'aide d'un profilomètre Dektak par l'utilisation de l'équation de Stoney : $\sigma_0=E_s h_s^2/(6.(1- v_s^2).(1/R_f -1/R_i)$.

- **Interférométrie Optique**

Pour la mesure des épaisseurs locales sur la longueur de nos échantillons, nous avons utilisé le profilomètre interférométrique à lumière blanche (Talysurf CCI 6000, Taylor Hobson), capable de fournir des mesures précises de la surface et de l'épaisseur.

- **Tests Mécaniques *In Situ* avec microscopie à force atomique (AFM): Dispositif deben**

Microscopie à force atomique (AFM) a été utilisée pour l'imagerie nanométrique à haute résolution des surfaces des films de nickel. Le mode peak force tapping (PFT) a été privilégié pour contrôler l'interaction pointe-échantillon à un niveau de force très faible (jusqu'à 10 pN), assurant une imagerie de haute qualité sans endommager l'échantillon. L'étude mécanique a été menée *in situ* en intégrant le dispositif de micro-compression motorisé Deben (Microtest) au système AFM Bruker Dimension Icon. Ce dispositif compact permet d'appliquer une déformation uniaxiale contrôlée (0.05 à 0.3 mm/min) tout en observant en temps réel les déformations de surface et le flambage. Les tests préliminaires sur le substrat en polycarbonate ont validé son comportement purement élastique sous ces contraintes, confirmant son rôle de support passif lors des expériences.

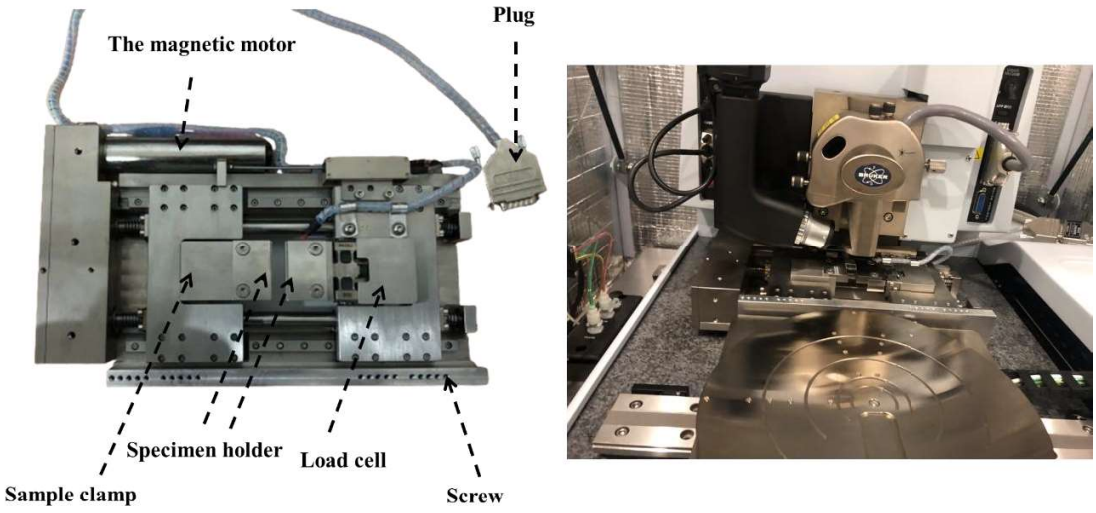

Fig. 2-13: Système de micro-compression Deben intégré à l'AFM Bruker Dimension Icon. (a) Vue du dispositif Deben et de ses composants: mâchoires fixe et mobile, capteur de charge et commande motorisée

Chapter 3

3. Study of SS and TC buckles in nickel film exhibiting a well-controlled thickness gradient within a static approach

This chapter explores the influence of well-controlled thickness gradients on the buckling morphologies in nickel films deposited on polycarbonate (PC) substrates, focusing on both straight-sided (SS) and telephone cord (TC) buckles. The nickel films were subjected to uniaxial compression using a Deben microtest stage, which induced a variety of buckling morphologies, mainly SS and TC buckles. After release of the external strain applied to the substrate, the resulting morphologies were characterized using optical microscopy, white-light interferometry and atomic force microscopy. To systematically explore the influence of various thickness gradients on buckling structures, finite elements method (FEM) simulations were performed. The numerical results are presented, compared to the experimental observations and discussed in detail. The results of this chapter were the origin of three papers, one published in "Thin solid films" [132], and the two others submitted [133,134].

3.1. Experimental results

3.1.1. SS Buckles parallel to the thickness gradient

The as-deposited sample A previously cited in sub-section 2.2.5 (Fig. 2-7) was used for this study. The residual stress was estimated as σ_0 = 0.8 GPa using Stoney's curvature method [113]. No buckles on the as-deposited nickel films using an optical microscopy were observed.

To induce buckling, the PC substrate of the as-deposited sample was subjected to uniaxial compressive strain along the (*Ox*) direction using a Deben microtest stage equipped with a 5kN load cell. Assuming optimal transfer of the strain through the interface and using stress–strain relations giving in Eqs. 1-27 and 1-28 in section 1.1.2, the in-plane stress components transmitted to the film, $\Delta\sigma_{xx}^f$ and $\Delta\sigma_{yy}^f$, are calculated using the expression given by [135]:

$$\Delta\sigma_{xx}^f = \frac{E_f}{E_s}\frac{1-\nu_f\nu_s}{1-\nu_f^2}\sigma_a^s \text{ and } \Delta\sigma_{yy}^f = \frac{E_f}{E_s}\frac{\nu_f-\nu_s}{1-\nu_f^2}\sigma_a^s, \quad (3\text{-}1)$$

where E_f, ν_f (*respectively* E_s, ν_s) are the Young's modulus and Poisson's ratio of the film (*respectively* the substrate) and σ_a^s is the applied stress to the substrate.

The substrate was strained up to 0.65% at room temperature and atmospheric conditions, using a constant displacement rate of 0.05 mm/min, which gives in-plane stress components of $\Delta\sigma_{xx}^f$ = 336 MPa and $\Delta\sigma_{yy}^f$ =-22 MPa.

Fig. 3-1a shows the nickel film deposited on a PC substrate (sample A) after the release of the external strain. The film thickness h varies linearly from approximately 15 nm at the thinnest edge to 300 nm at the thickest region, across the 10 mm length along the (Oy) direction, as depicted on the left side.

After loading, several SSBs were formed in the nickel film (Fig. 3-1a). These buckles are mainly lying along the (Oy) direction, roughly perpendicular to the compression axis (Ox), which is consistent with the mechanics of buckling in compressively stressed thin films on compliant substrates [135–137]. While most buckles are well aligned with the gradient direction, some exhibit irregular orientations, likely due to film/substrate interface, free surface defects, sample boundaries or even buckle-buckle interactions. Since our focus here is on SSBs aligned parallel to the thickness gradient, two isolated and nearly parallel buckles, located near the central region of the sample highlighted by the dashed rectangle, referred to as zone A in the following, were selected for detailed analysis. These two buckles are labeled SSB1 and SSB2, in Fig. 3-1b. Both buckles appear to have nucleated from visible surface defects, highlighted by dashed cercles.

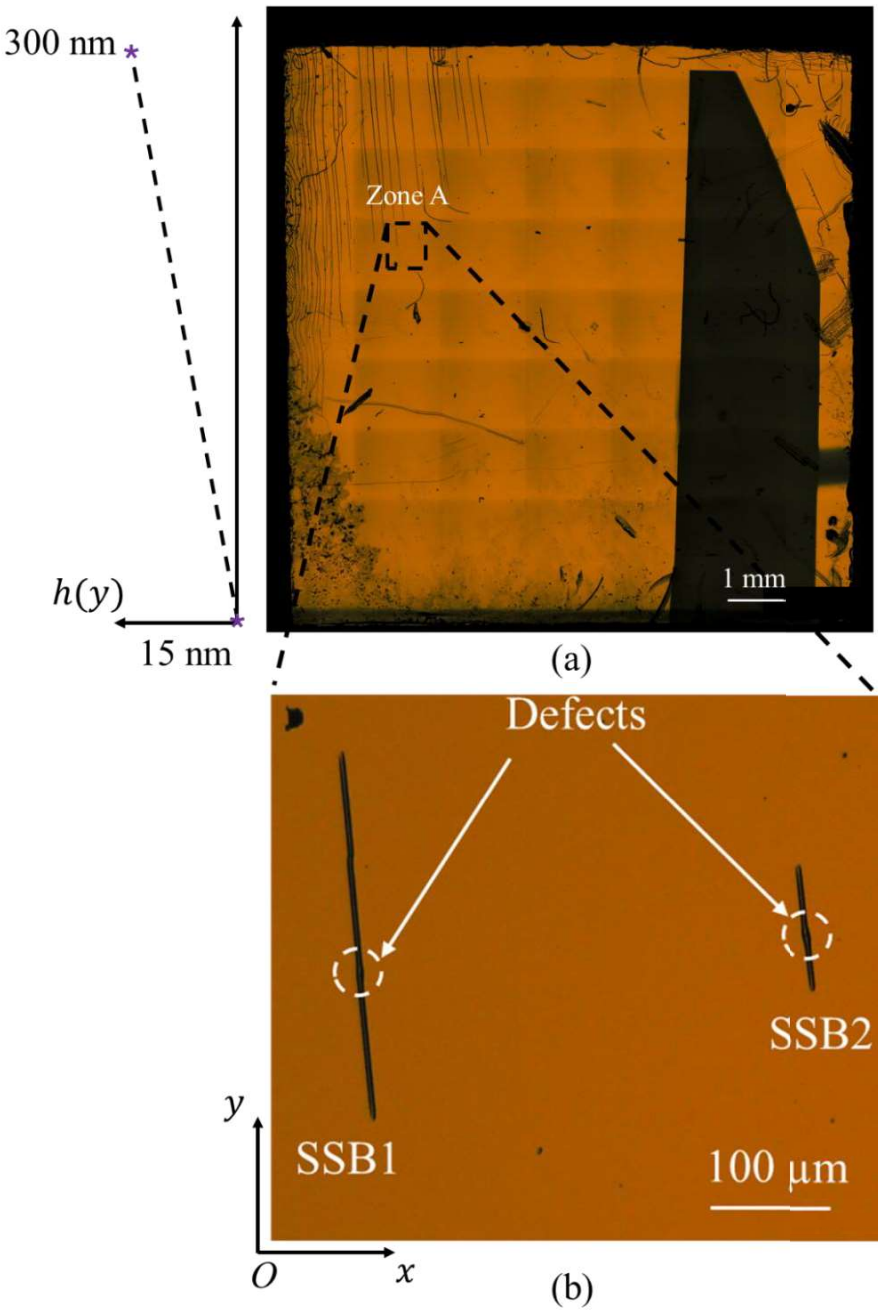

Fig. 3-1 : (a) Optical image of sample A after the first compression cycle. The nickel film was deposited with a continuous thickness gradient along the (*Oy*) direction. A schematic reference bar, shown on the left of the image, illustrates how thickness increases from bottom to top. Several straight-sided buckles (SSBs) are visible, aligned along (*Oy*) and perpendicular to the compression axis (*Ox*). (b) Zoomed-in view of two isolated SSBs, referred to as SSB1 and SSB2 for further analysis.

Study of SS and TC buckles in nickel film exhibiting a well-controlled thickness gradient within a static approach

We first focus on the upper part of the SSB1, which was analyzed by atomic force microscopy (AFM). All AFM measurements reported in this section were performed after complete unloading of the external strain. Fig. 3-2a shows the AFM image (80×80 μm^2) corresponding to this part. A surface defect can be clearly seen in the top-left corner, and was served as a reference for local thickness measurements. The film thickness h was determined from the height difference between the defect and flat reference regions located at the same lateral (x) position but sufficiently far from the buckle to avoid interference. Using this method, the film thickness h was found to decrease from approximately 200 nm at the top (near the defect) to 173 nm at the bottom, as shown on the left side in Fig. 3-2a. Additionally, AFM analysis reveals that the buckle width $2b$ remains constant behind the front, with an average value of $2b$ = 7.1 μm. Two horizonal cross-sections along the SSB1, corresponding to local thicknesses of h = 173 nm (red) and h = 184 nm (violet) were selected to be analyzed. The out-of-plane displacement profiles w, corresponding to those local thicknesses with their respective colors, are shown in Fig. 3-2b. It is well known that the equilibrium profile of an elastic straight-sided buckled in the case of a homogeneous, constant-thickness film follows a symmetric sinusoidal shape within the framework of the Foppl-Von Karman (Fvk) elastic plate theory given by [26]:

$$w(x,y) = \frac{\delta}{2}\left(1 + cos\left(\frac{\pi x}{b}\right)\right). \tag{3-2}$$

The maximum height δ is given by [26]:

$$\delta = \frac{4}{\pi}\sqrt{\left(\frac{\sigma_0(1-\nu_f^2)}{E_f}b^2 - \frac{\pi^2}{12}h^2\right)}. \tag{3-3}$$

Fig. 3-2b demonstrates that the profiles can be well fitted by a sinusoidal shapes function, with δ decreasing with increasing film thickness h, in agreement with Eq. (3-3).

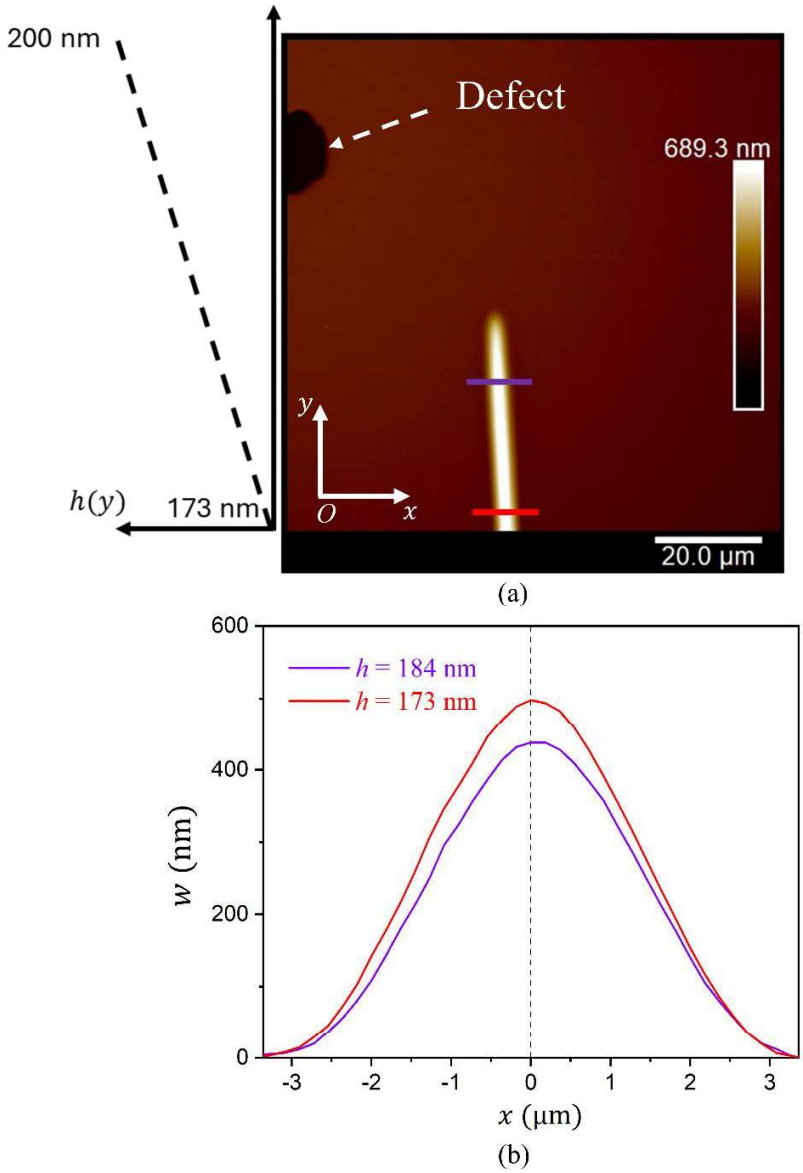

Fig. 3-2: (a) AFM image of the straight sided buckle SSB1. (b) AFM profiles with respect to local film thickness h.

The sample A was subjected to a second uniaxial compression cycle along the (Ox) axis. The transferred in-plane stress in the film was estimated to be approximately $\Delta\sigma_{xx}^{f}$ = 812 MPa, corresponding to an elastic substrate strain of 1.38%. This additional compression led to the nucleation of new buckles, as shown in Fig. 3-3a. A magnified view of zone A highlighted by the dashed box in (a) is presented in Fig. 3-3b. The same buckles SSB1 and SSB2 were followed. After the second compression, both SSB1 and SSB2 shown to extend from the thinner to thicker part (upward) of the film along the (Oy) direction. This can be observed by comparing their lengths

to their initial states shown in Fig. 3-1b. However, the SSB1 became intersected by another buckles, making it challenging for further analysis. In contrast, SSB2 remained clearly isolated and distinguishable and unaffected by interactions with other buckles; it was therefore selected for further analysis.

The upward propagation of SSB2 along the (*Oy*) directions can be well explained within the framework of the elastic plate theory (FvK), where the critical buckling stress σ_c can be expressed as [26]:

$$\sigma_c = \frac{\pi^2}{12}\frac{E_f}{1-\nu_f^2}\left(\frac{h}{b}\right)^2. \tag{3-4}$$

According to Eq. (3-4), for a constant width (2*b*), as the film thickness *h* increases (*resp*. decreases), the critical stress σ_c increases (*resp*. decreases). Therefore, the observation of SSB2 propagation towards higher values of *h* comes from the increase of the loading stress ($\Delta\sigma_{xx}^f + \sigma_0$) (external and internal stress in the film) being higher than σ_c. However, as *h* decreases, the propagation downward is energetically favorable and no buckle arrest is expected, nevertheless the buckle did not propagate, this strongly suggests that the increase of the loading stress did not compensate for the elastic energy stored in the film, being lower than the interfacial toughness. This behavior is of particular interest and will be explored in detail in Chapter 4.

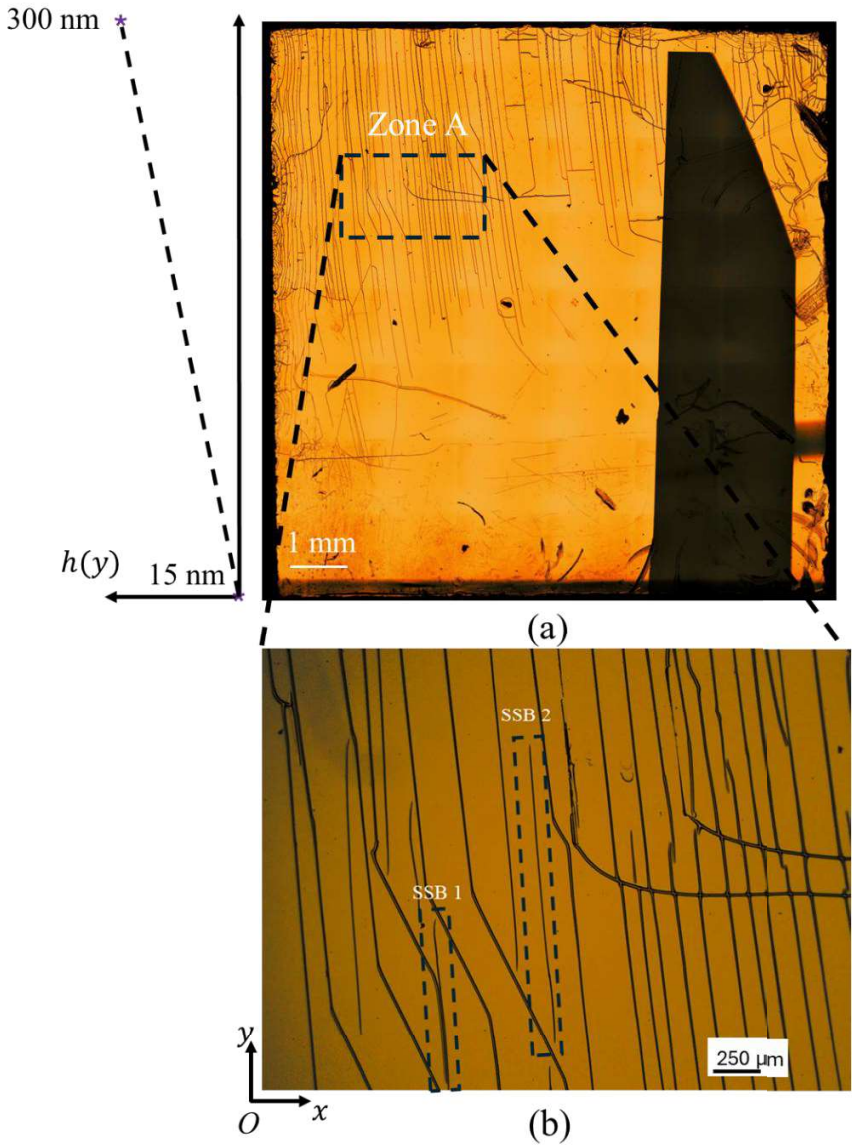

Fig. 3-3: (a) Optical image of sample A after the second compression cycle. (b) A zoomed-in view showing that SSB1 became intersected by other buckles, making it unsuitable for analysis. SSB2 remained isolated and was selected for thickness-dependent characterization.

Fig. 3-4 presents an optical image of SSB2, where each colored tick is associated with its local thickness shown on the left side. AFM measurements were performed at various distinct locations along the (*Oy*) directions, corresponding to local thicknesses *h* of 177 nm, 183 nm, 190 nm and 205 nm, respectively. These positions are highlighted by dashed boxes in the optical image. For convenience, only two AFM images are shown for *h* of 177 and 205 nm, respectively, and are presented on the right side.

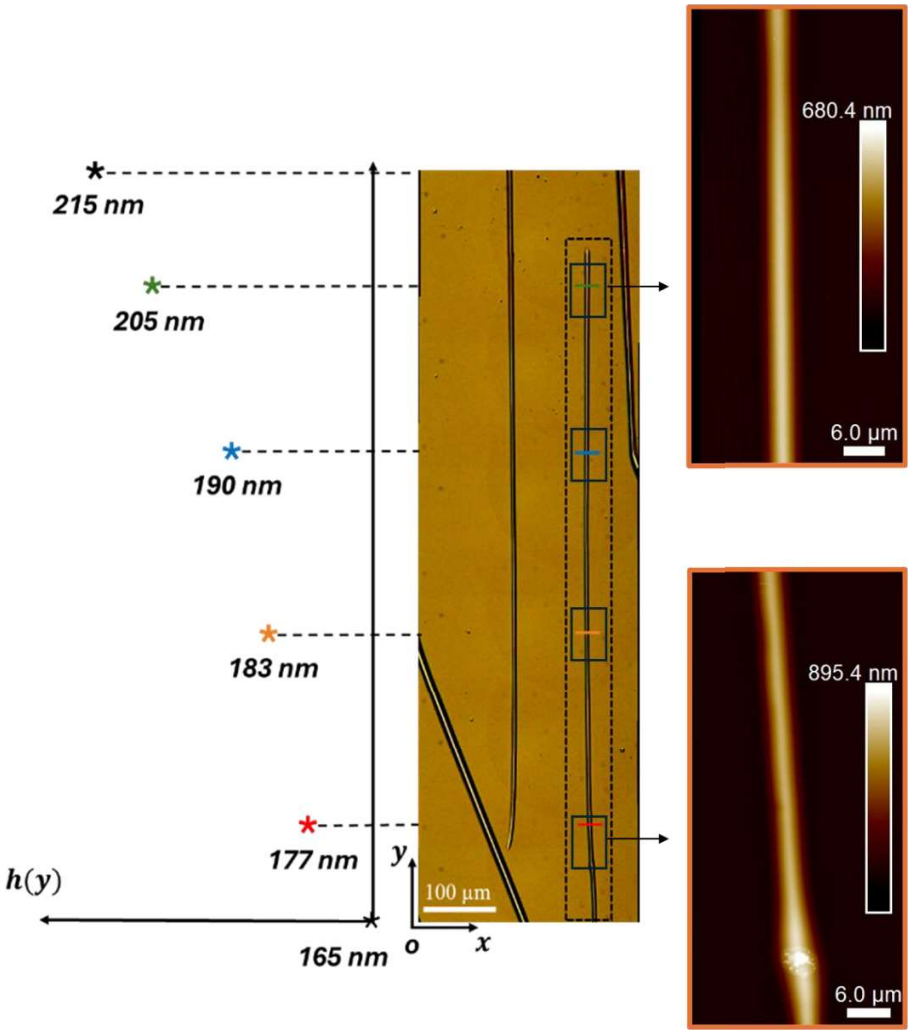

Fig. 3-4: Optical and AFM characterization of SSB2. The main image shows an optical image of the SSB2 aligned along (*Oy*) direction. A schematic representation of thickness gradient is shown on the left side. Highlighted dashed boxes show locations where AFM measurements were taken, corresponding to local thicknesses of 177, 183, 190, and 205 nm, respectively. For convenience, two AFM images are shown on the right side.

AFM measurements reveal that the buckle width $2b$ remains nearly constant along the entire length of SSB2, with an average value of $2b = 6.68 \pm 0.16$ µm despite the variation in local thicknesses h. The out-of-plane displacement w profiles at various h locations with the horizontal position x normalized over the half-width b of the buckle ($b = 3.34 \pm 0.08$ µm) are shown in Fig. 3-5a. Those profiles show symmetrical sinusoidal shapes at their centerline marked as vertical dashed line at $x = 0$, in accordance with FvK equations (Eq. (3-2)) [26]. Furthermore, the height of the buckle, δ, is presented with respect to the film thickness h in Fig. 3-5b. The experimental values are represented by stars symbols and the calculated values from the FvK (Eq. (3-3)) are

shown as circular dots. The results demonstrate that δ^2 continuously decreases as h^2 increases, while the width of the SS buckle remains approximately constant. These results are similar (linear trend) to what is expected in the case of a homogeneous, constant-thickness film, described in the framework of the elastic theory [26] (see Eq. (3-3)). However, the experimental values (stars symbols) are systematically higher to what is expected in this theoretical framework (circular dots). This mismatch may be attributed to either the elastic compliance of the substrate [37] or plastic events taking place in the films [20,138–140]. One can also not exclude any subtle effect of the thickness gradient itself.

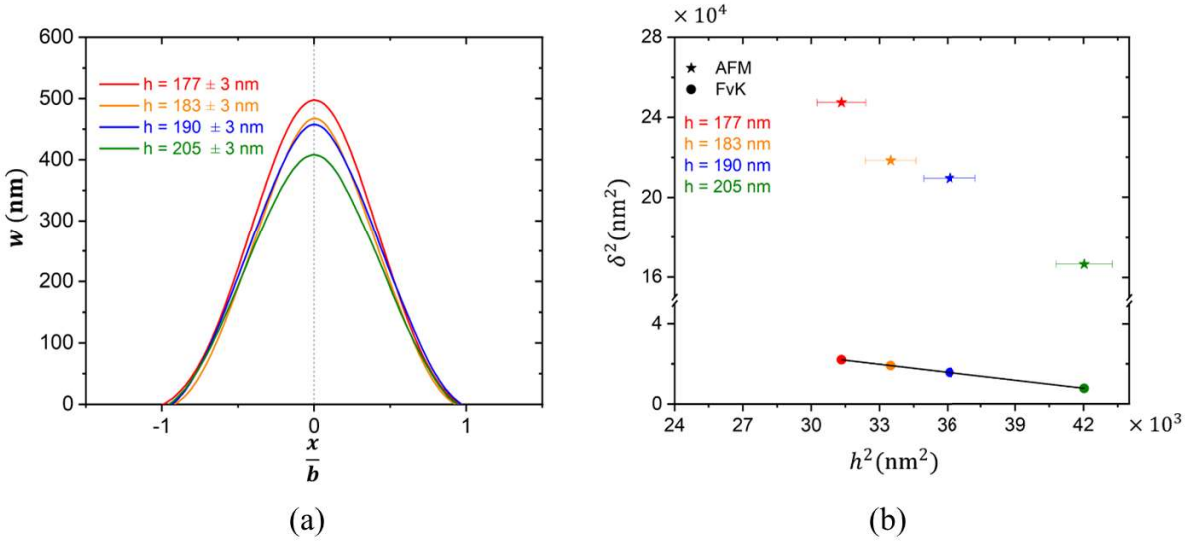

Fig. 3-5: (a) Straight-sided buckle profiles obtained from AFM measurements, with data colored according to their local thickness h, with x normalized over the half-width b (b = 3.34 ±0.08 µm). (c) Plot of δ^2 *vs.* h^2, with error bars corresponding to the minimum and maximum values of h.

3.1.2. SS Buckles misaligned with the thickness gradient

Up to this point, we examined SSBs that are aligned parallel to the thickness gradient, focusing on profiles extracted along the (Ox) direction. Ideally, we would also investigate SSBs that are progressively misaligned with the gradient up to the limiting case where the buckle becomes perpendicular to it in order to directly characterize how thickness gradients influence buckle profiles. Because such configurations are not available in our experimental data, we instead analyze SSB profiles measured along directions that are not parallel to the gradient. This approach allows us to evaluate how the relative orientation between the thickness gradient and the buckle axis affects the resulting buckle shape.

Figure 3-6a shows a white-light interferometric image of an SSB oriented toward the height step. The thickness gradient is visible on the left side. Because the buckle is nearly parallel to the

gradient direction, we can directly evaluate how the local film thickness influences both the out-of-plane displacement w and the buckle half-width b. Four cross sections marked by white solid lines and labeled 1 to 4 in Fig. 3-6a were analyzed.

Section 1 highlights the thickness gradient along the (Oy) direction. The maximum thickness is h = 198 nm at a distance of 35 µm from the height step; beyond this point the thickness becomes uniform. Three additional cross sections (2 to 4) oriented obliquely along (Ox') at approximately 61° relative to (Oy), present the out-of-plane displacement including local thickness contributions $[w(x',y')+h(y)]$ along x'.

Profile 2 was taken in a region with no thickness gradient and remains symmetric as expected, with identical half-widths b = 10.65 µm. Profile 3 corresponds to an area with a slight thickness variation, from 198 nm to 180 nm, which produces a mild asymmetry: b_- = 10.29 µm and b_+ = 10.65 µm. Profile 4, where the thickness varies more strongly (198 nm to 150 nm), shows a more pronounced asymmetry, with b_- = 9 µm and b_+ = 11 µm. In both cases, the maximum height shifts toward the thinner region.

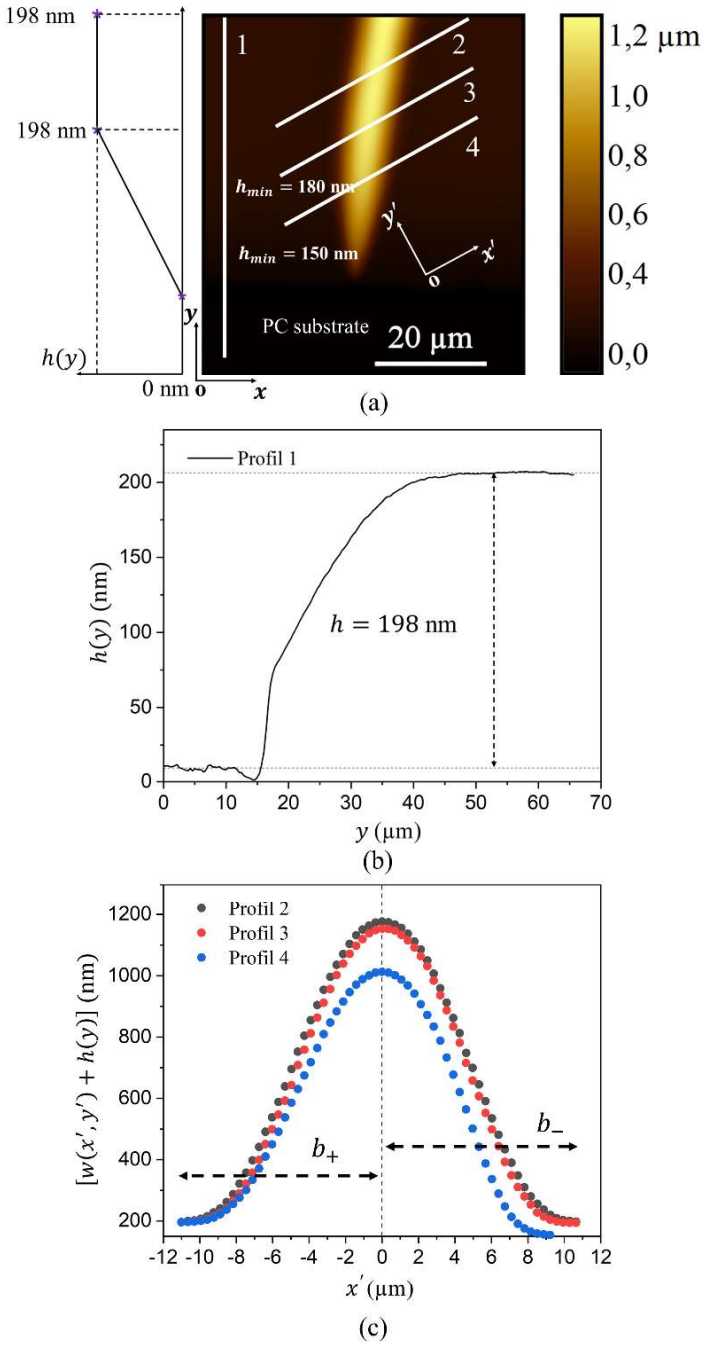

Fig. 3-6: Straight-sided buckle lying parallel to the thickness gradient (*Oy*). (a) Optical white-light interferometric image. (b) Height profile along line 1 in (a), showing a thickness gradient along the height step and maximum film thickness of h = 198 nm. (c) Buckle profiles extracted from (a) along the oblique lines 2 to 4 (labeled in a), which are oriented at approximately 61° relative to the (*Oy*) axis. The measured edge to peak distances are labelled b_+ and b_-.

Figure 3-7 presents another SSB from sample B, where the buckle lies at ~ 40° relative to the gradient. Residual stress in the film was estimated as $\sigma_0 \approx 0.8$ GPa. Local film thicknesses were measured as 490 nm on the main surface and 327 nm on the step. A cross section extracted along an oblique direction reveals a strongly asymmetric profile, with $b_- = 15.21$ µm and $b_+ = 22.31$ µm, as previously discussed.

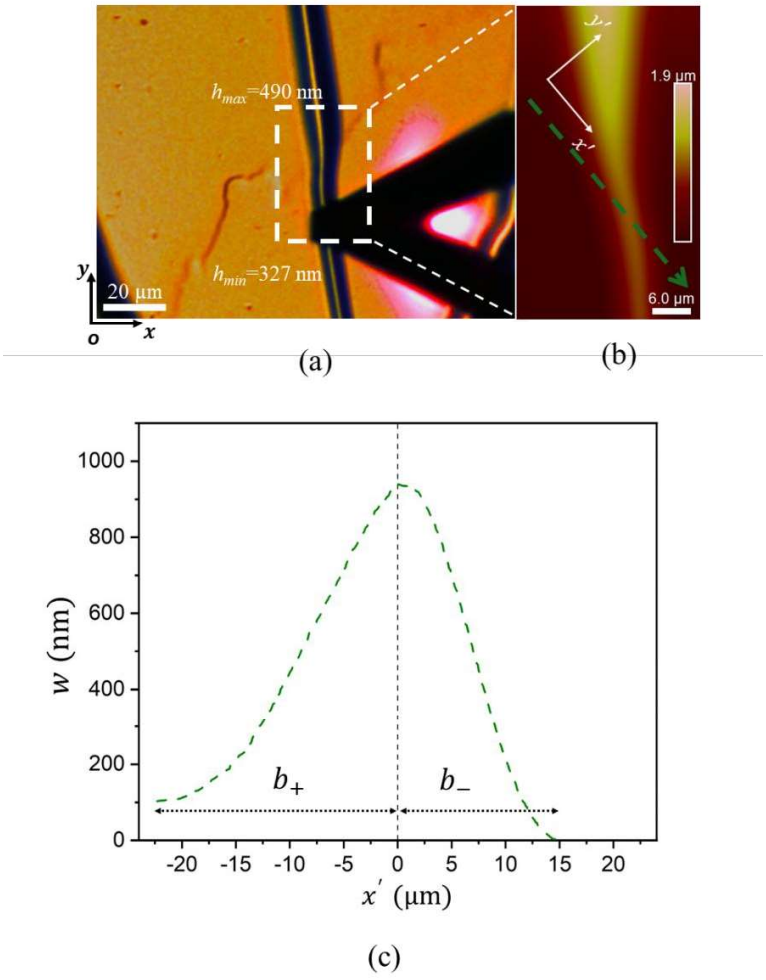

Fig. 3-7: SSB in sample B " a nickel film on a polycarbonate substrate" lying not parallel (at approximately 40°) to the thickness gradient direction (*Oy*). (a) Optical image of a SSB. (b) AFM (93 × 93 µm^2) image. (c) Buckle profile obtained from AFM measurements corresponding to the oblique (*Ox*') dashed line in (b), with $b_- = 15.21$ µm and $b_+ = 22.31$ µm.

To quantify SSB asymmetry under different gradients, the dimensionless ratios h_{max}/h_{min} and b_+/b_- are used. Experimental results show that larger thickness ratios lead to greater asymmetry.

The thickness ratio, however, provides only qualitative information about the gradient and does not imply linear variation. Such asymmetry may be characteristic of SSBs not perfectly aligned with the gradient.

Thickest edge h_{max} (nm)	*Thinnest edge* h_{min} (nm)	*Edge-to-peak distance,* b_+, b_- (µm)	*Thickness ratio,* h_{max}/h_{min}	*Edge-to-peak ratio,* b_+/b_-
147	118	18.94, 16.26	1.24	1.16
198	150	11.0, 9.0	1.32	1.22
490	327	22.31, 15.21	1.49	1.47

Table 3-1: Experimental morphological characteristics of the straight-sided buckle profile extracted misaligned to the thickness gradient.

3.1.3. Telephone cord buckles parallel to the thickness gradient

3.1.3.1. In constant width

Fig. 3-8a presents an optical image of a TCB in a nickel film deposited on a PC substrate (sample A), oriented approximately parallel to the thickness gradient. A reference height step without coating (PC substrate) is visible as a dark contrast, serving as a reference for thickness measurements using white-light interferometry. To characterize the variation of thickness along the (*Oy*) direction, two sections labeled 1 and 2 (red arrow in Fig. 3-8a) were analyzed. The corresponding interferometric height profiles are shown in Figs. 3-8b and 3-8c. Section 1 provides a maximum thickness of h = 191 nm, while section 2 reveals a continuous, approximately linear variation of height along (*Oy*), confirming the presence of a well-thickness gradient. The variation of h along the (*Oy*) direction is schematically represented on the left side in Fig. 3-8a, with h varies from 191 nm to 144 nm. Two AFM images ($93\times93\mu m^2$) capturing the morphology of TCB in different positions are also shown as insets on the right, with their respective locations marked by arrows.

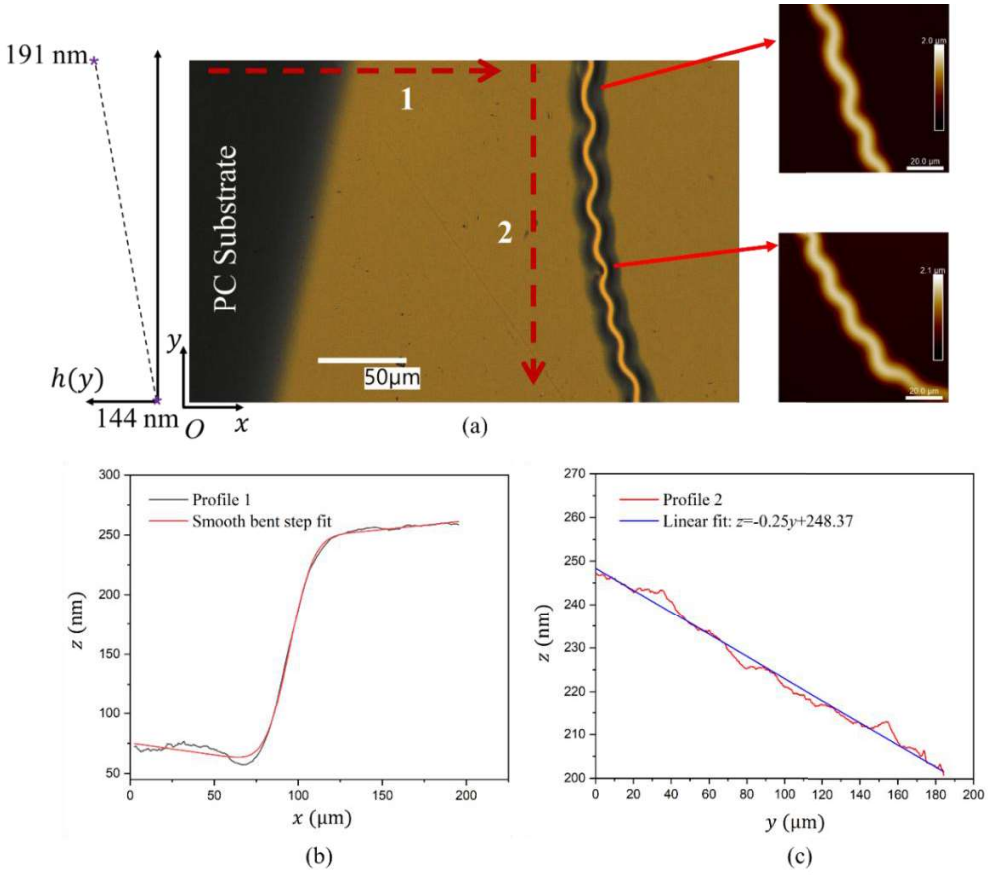

Fig. 3-8: Telephone cord buckle (TCB) lying approximately parallel to the thickness gradient along the (*Oy*) direction. (a) Optical image of a nickel film on a polycarbonate substrate. Insets show AFM images ($93\times93\mu m^2$) at two different locations. (b) Step height profile along section line 1 in (a), obtained by white-light interferometric microscopy and fitted with a smoothed bent-step function using Gwyddion software. The local film thickness is measured as h = 191 nm. (c) Height profile along section line 2 in (a), also measured by interferometry, illustrating the thickness variation along the gradient. A linear fit confirms its continuous nature.

The first four successive wavelengths from Fig. 3-8a, were analyzed by a white interferometric microscopy and presented in Fig. 3-9. The thickness gradient is shown on the left, with h varying from 191 nm to 161 nm. One of the most important geometrical parameter that characterize the TCBs is its wavelength λ. Studies [22,23] have shown that the film/substrate interfacial adhesion can be directly assessed form λ. Additionally, It is well reported that, in homogenous, constant-thickness films, TCBs exhibit a uniform wavelength λ at constant width $2b$ [45,51]. Notably, the width $2b$ of the TCB remains here approximately the same, of about 19.38 µm. Meanwhile, the TCB lying along the thickness gradient clearly shows that the wavelength λ decreases with

decreasing film thickness h, with $\lambda_1 = 32$ µm, $\lambda_2 = 30$ µm, $\lambda_3 = 24$ µm and $\lambda_4 = 21$ µm, respectively. As reported by Moon *et al.* [141], an increase in film thickness leads to a higher strain energy in the film, which in turn results in larger wavelengths of the TCBs. This trend observed in homogeneous films [141] aligns well with our observations in the case of a thickness gradient.

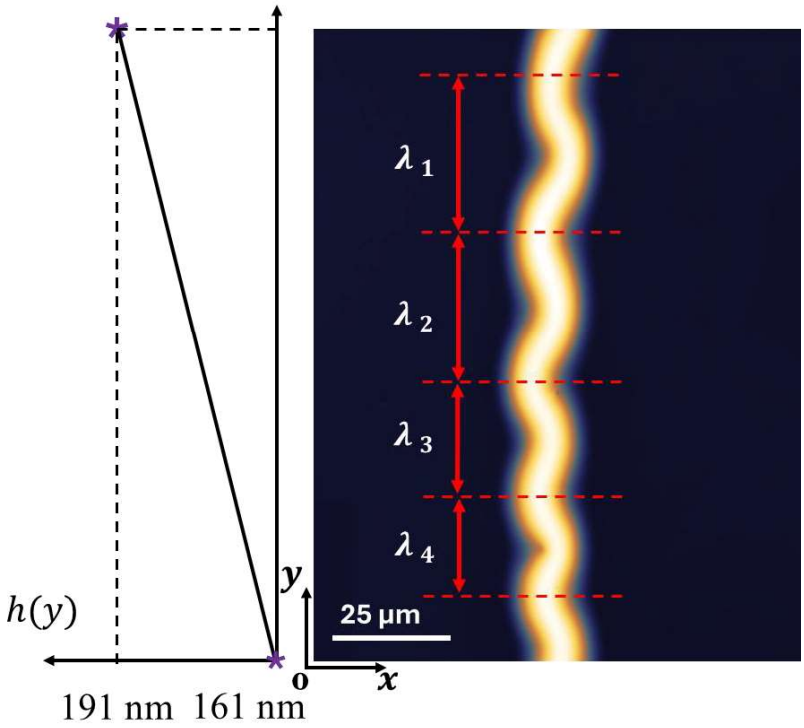

Fig. 3-9: Telephone cord buckling structure of constant width $2b$ = 19.38 µm oriented parallel to the thickness gradient along the (Oy) direction. Interferometric optical image of a nickel film on a polycarbonate substrate, with λ_i the local wavelength of the TCB within the thickness gradient.

3.1.3.2. In gradient width

Fig. 3-10a presents the thicker edge region of the compressed sample B, which shows two induced SSBs. The sample was subjected to further uniaxial compression up to $\Delta\sigma_{xx}^f = 1.224$ GPa, resulting in several SSBs that propagated downward through the thickness gradient (along the (Oy) axis), including the highlighted SSB in Fig. 3-10a. Fig. 3-10b shows an optical image of the full 10 mm×10 mm nickel-coated PC substrate (sample B) after the release of the external strain ($\Delta\sigma_{xx}^f = \Delta\sigma_{yy}^f = 0$). The brown contrast corresponds to the nickel coated region, while the dark areas indicated uncoated regions masked during deposition. The film thickness h along the (Oy) direction varies from 0 nm to 506 nm, as shown on the left side. After the release of the external

strain, the SSB highlighted by white arrow in Fig. 3-10a evolves into a TCB, as shown on the right side in Fig. 3-10b (A zoomed-in view of the highlighted rectangle in (b)), a phenomenon known as secondary buckling [16,28]. Unless otherwise specified, all results discussed here were conducted after unloading, for which the film was only subjected to its residual stress σ_0.

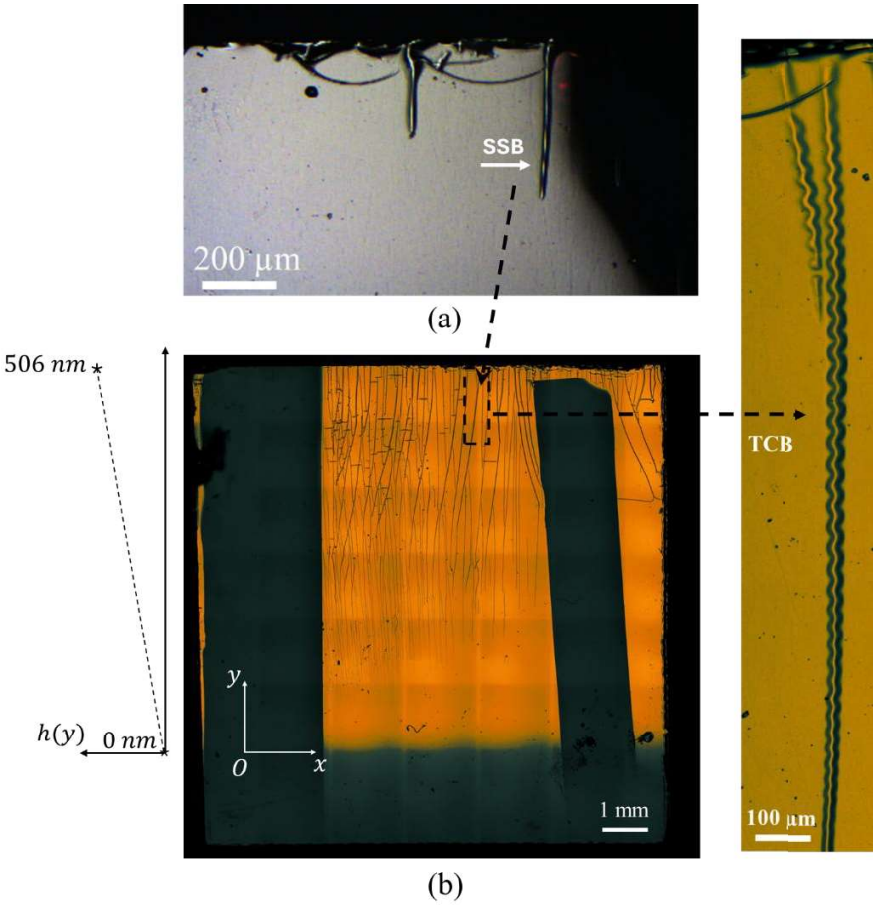

Fig. 3-10: Optical 10 mm × 10 mm image of sample B (nickel-coated polycarbonate substrate), exhibiting a well-controlled thickness gradient along the (*Oy*) direction. (a) Magnified view of the thick edge, showing the nucleation of straight-sided buckles under applied uniaxial compression ($\Delta\sigma_{xx}^f$ = 82 MPa and $\Delta\sigma_{yy}^f$ = -5.5 MPa). (b) Optical image of the full sample after the complete release of external strain ($\Delta\sigma_{xx}^f$ =$\Delta\sigma_{yy}^f$=0), revealing the transformation of straight-sided buckles into telephone-cord buckles along the thickness gradient (dashed rectangle). The brown contrast corresponds to the nickel-coated region, whereas the dark areas indicate uncoated PC substrate masked during deposition. The film thickness *h* increases continuously from 0 nm (bottom) to 506 nm (top). A zoomed-in view of the highlighted TCB (dashed rectangle) is shown on the right side.

Fig. 3-11 presents a white-light interferometric image of the highlighted TCB in Fig. 3-10b. This TCB lies parallel to the thickness gradient along the (*Oy*) direction. The gradient is shown on the left, where the film thickness $h(y)$ decreases from 450 nm to 300 nm over a length of 1.22 mm. The buckle was analyzed locally by AFM all along its length. However, for convenience, only three representative AFM images corresponding to the regions marked by colored dashed rectangles are shown on the right. The first two AFM images correspond to the TCB, located in thicker and intermediate regions, respectively, while the last one shows a SSB at the thinner region. These AFM scans clearly reveal that the wavelength λ and the delaminated buckle width $2b$ decrease with decreasing thickness, associated with a reduction in out-of-plane displacement. The TCB clearly exhibits a continuous gradient in its stripe width $2b(y)$, which increase with h, consistent with studies on uniform films [49,142,143], thicker regions leading to larger delaminated widths due to higher stored elastic energy. The delaminated widths gradient is attributed to the initial SSB propagation through the thickness gradient. A critical thickness (or critical width) exists below which no transition to a TCB is observed. For the present experimental case, this critical thickness corresponds to h^*=333 nm and $2b^*$ = 28 µm.

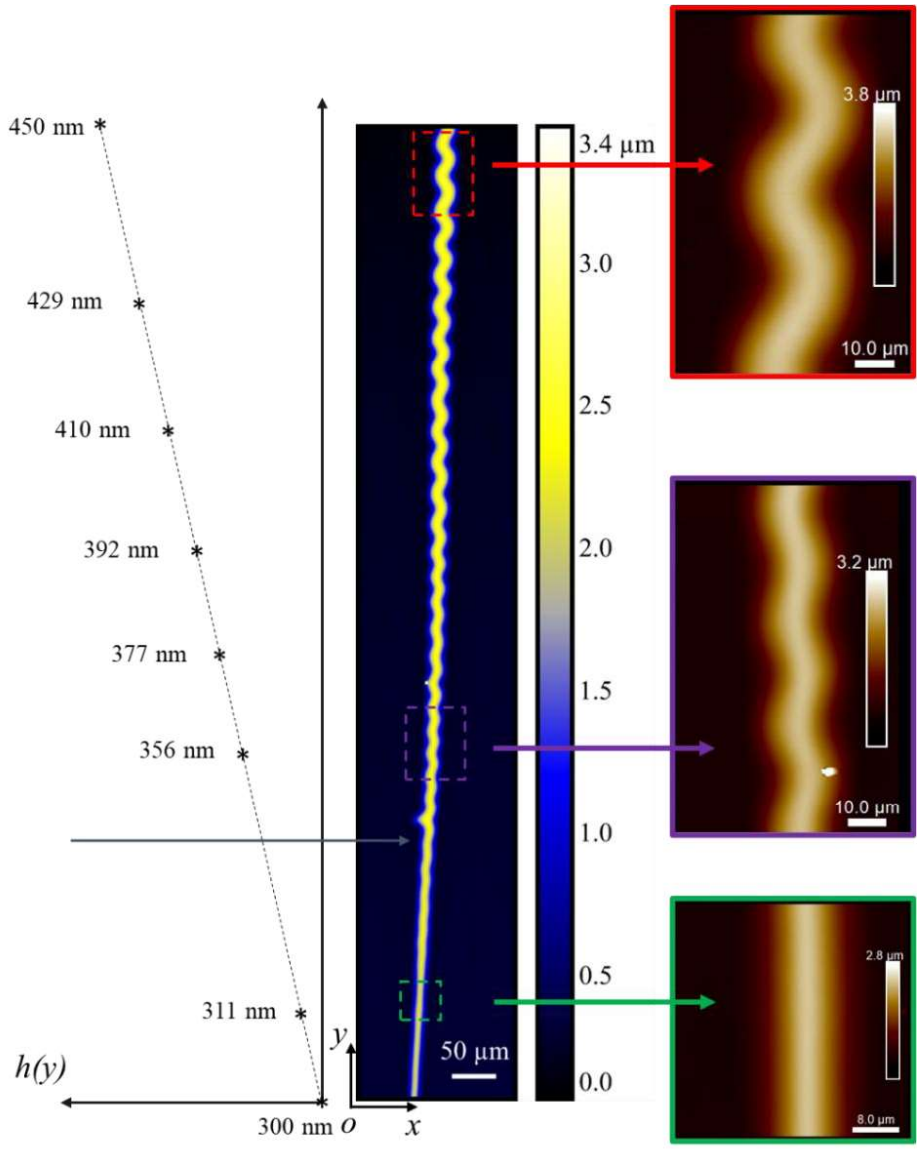

Fig. 3-11: Interferometric optical image of a telephone-cordon buckle in a nickel film on a polycarbonate substrate along a thickness gradient lying along the (*Oy*) direction after the release of the external strain ($\Delta\sigma_{xx}^{f}=\Delta\sigma_{yy}^{f}=0$). For convenience, only three atomic force microscopy images taken at different *h* positions are presented on the right side. The film thickness *h* varies from 300 nm to 450, as shown on the left side.

Fig. 3-12 presents the morphological analysis of the TCB structure across the thickness gradient and tapered width. Both $2b$ and δ increase with $h(y)$ (see Fig. 3-12a). However, $2b$ grows more rapidly than δ, leading to a decrease in the normalized height $\delta/2b$ with increasing $h(y)$, as illustrated in Fig. 3-12b. Finally, the variations of wavelength λ of the TC buckle with respect to

local $h(y)$ are presented in Fig. 3-12c. The normalized wavelength, expressed as $\lambda/2b$, is also presented in Fig. 3-12d. The wavelength λ at each position y was determined as the distance between two consecutive points having the same phase (e.g., from crest to crest). The half-width $2b$ was measured at the point located halfway between two consecutive crests. λ is shown to decrease with the decreasing film thickness $h(y)$, similarly to what can be observed in the case of homogeneous, constant thickness films [49,143]. The $\lambda/2b$ values are ranging from approximately 0.9 to 1.1, in good agreement with those reported in the literature between 0.8 to 1.6, again for homogeneous films [22,45,51,144].

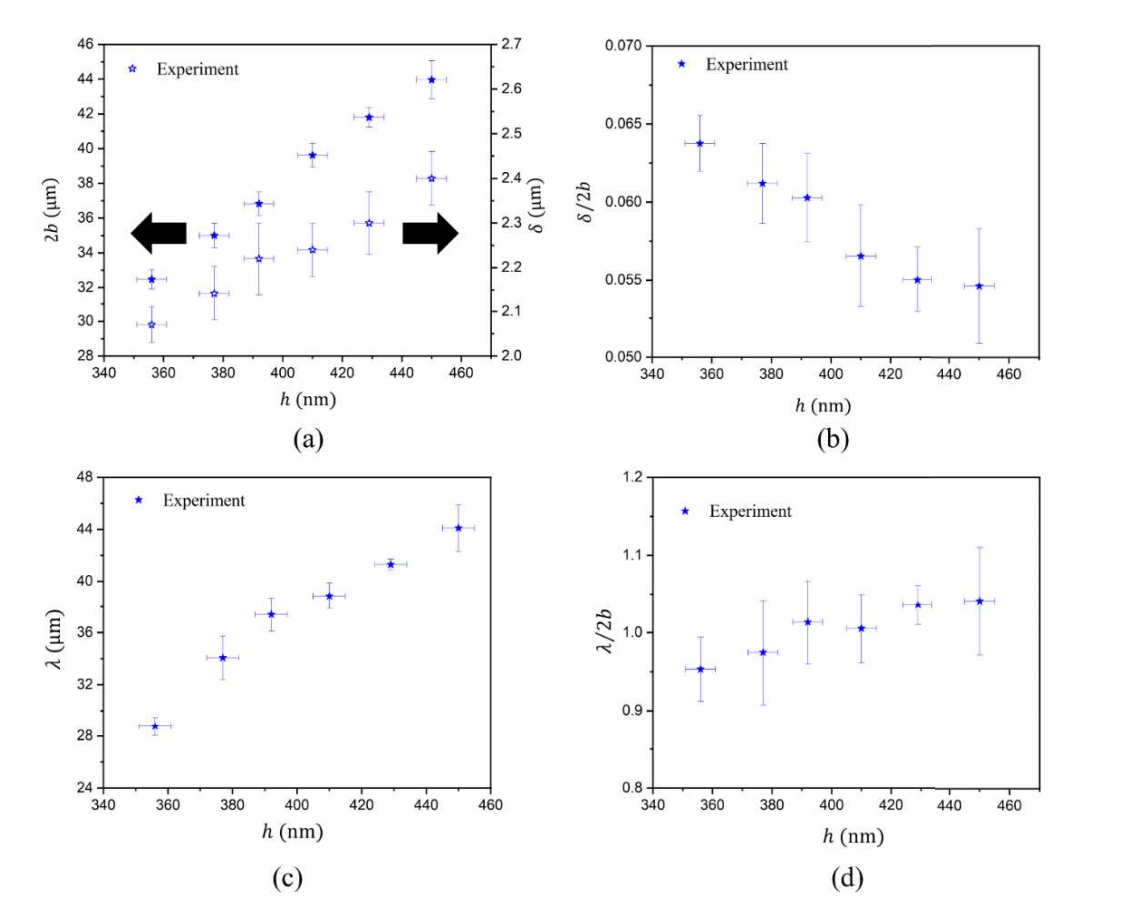

Fig. 3-12: Morphological parameters of TC buckles in a thickness gradient $h(y)$: (a) width $2b$ and maximum height δ, (b) normalized maximum height $\delta/2b$ (c) λ (d) normalized wavelength $\lambda/2b$, as a function of $h(y)$.

3.2. FEM modeling within the elastic plate theory

3.2.1. FEM details and mechanical model description

In order to explain the experimental observations, thin films exhibiting a thickness gradient were modeled using FEM in the ABAQUS software [145]. The analysis was performed with the ABAQUS/Standard solver in a static framework. Four-node plane strain elements with reduced integration (S4R) were employed to balance the computational costs with solution accuracy. The mechanical model, illustrated in Fig. 3-13 has a parallelepipedal geometry with dimensions L_x = 60 µm and L_y = 120 µm, along the (O*x)* and (O*y*) axis, respectively, with element thickness varying as $h_k(i)$ (where $i = x$ or y*)*. Geometrical nonlinearities were considered using the Green-Lagrange strain tensor. The model consists of two components, a nickel film and its associated rigid substrate. The film is treated as a 2D elastic plate with a Young's modulus of E_f = 200 GPa and a Poisson's ratio ν_f = 0.31 [12,37,146], while the substrate is assumed to be an infinitely rigid body, unless otherwise specified.

The film's underlying thickness gradient is defined by the following expressions:

$$h_k(i) = h_{max} - \left(\frac{k-1}{N_i-1}\right)\Delta h, \tag{3-5}$$

and

$$tan\ \alpha = \frac{\Delta h}{L_i}, \tag{3-6}$$

where $h_k(i)$ represents the thickness of the element along the (O*i*) axis (where i=x or y), h_{max} is the maximum thickness, and $\Delta h = h_{max}$-h_{min} denotes the thickness variation. The index k ranges from 1 to N_i, with N_i corresponding to the number of sections. In the simulations, N_i is typically set to 100 for $h_k(x)$ and 200 for $h_k(y)$, unless otherwise specified. The thickness gradient is further characterized by its slope, denoted α. Note that, since a plate model is used for the film, the thickness h is entered as a parameter, the plate being constituted of flat elements.

The interface between the film and the substrate is modeled as frictionless, with hard contact to prevent the film from penetrating into the substrate. The boundary conditions used in the simulation, as given in Fig. 3-13, are described in detail below:

- The film is fully constrained at all nodes except within the rectangular stripe corresponding to the initially debonded zone, where the film is free to buckle. In the constrained regions, the displacements are set to $u = v = w = 0$ for all nodes.

- Nodes at $x = 0$ and $x = L_x$ (*resp.* at $y = 0$ and $y = L_y$) are constrained with $u = 0$, $\theta_y = 0$ and $\theta_z = 0$ (*resp.* $v = 0$, $\theta_x = 0$ and $\theta_z = 0$), where θ_i is a rotation about i axis.

- The substrate is fully constrained, with all nodal displacements set to $u = v = w = 0$.

As defined by these boundary conditions, all in-plane displacements of the film in the bonded regions are fully constrained. This implies that the total in-plane strain components vanish:

$$\epsilon_{xx}^{tot} = \epsilon_{yy}^{tot} = 0. \tag{3-7}$$

In the framework of the small-strain assumption in thermo-elasticity [147], the total strain can be written as the sum of the mechanical (elastic) and thermal strains:

$$\epsilon_{ij}^{tot} = \epsilon_{ij}^{el} + \epsilon_{ij}^{th}, \text{ with } \epsilon_{ij}^{th} = \alpha_{ij}\Delta T. \tag{3-8}$$

Using Eqs. (3-7) and (3-8), the elastic strain in the bonded regions becomes:

$$\epsilon_{ij}^{el} = -\alpha_{ij}\Delta T. \tag{3-9}$$

Substituting Eq. (3-9) into Eqs. (1-27) to (1-29) defined previously in sub-section 1.1.2 1eads to [46]:

$$\sigma_{xx}^{0} = -\frac{E_f}{1-v_f^2}\left(\alpha_{xx} + v_f\alpha_{yy}\right)\Delta T, \tag{3-10}$$

$$\sigma_{yy}^{0} = -\frac{E_f}{1-v_f^2}\left(\alpha_{yy} + v_f\alpha_{xx}\right)\Delta T, \tag{3-11}$$

$$\text{and } \sigma_{xy}^{0} = 0. \tag{3-12}$$

These expressions are used to mimic the compressive residual stresses observed in the experiments. Anisotropic thermal expansion is assigned to the film through two thermal expansion coefficients, α_{xx} and α_{yy}, corresponding to the (Ox) and (Oy) directions, respectively. For simplicity, the temperature difference is set to $\Delta T = 1$.

Finally, to initiate buckling in the delaminated zone, an imperfection is introduced to trigger the buckling response in the form of Euler modes, as well as symmetric and antisymmetric bumps with respect to the (*Ox*) direction [29], defined as follows:

$$w\ (x,y) = v_E cos^2\left(\frac{\pi x}{2b}\right) + v_+ \sin\left(\frac{\pi x}{b}\right)\sin(k_+ y), \tag{3-13}$$

Here, v_E and v_+ represent the amplitudes of the Euler and symmetric bump modes, respectively. The wavenumber of the symmetric bump is given by $k_+ = 2\pi/\lambda_+$, with λ_+ is its wavelength. In the simulations, the following values are used: $\lambda_+ = 2b$, $v_E = 10^{-3} \times h_{max}$ and $v_+ = v_E/30$. It is worth noting that those imperfections are very small and do not influence the post-critical buckling shape.

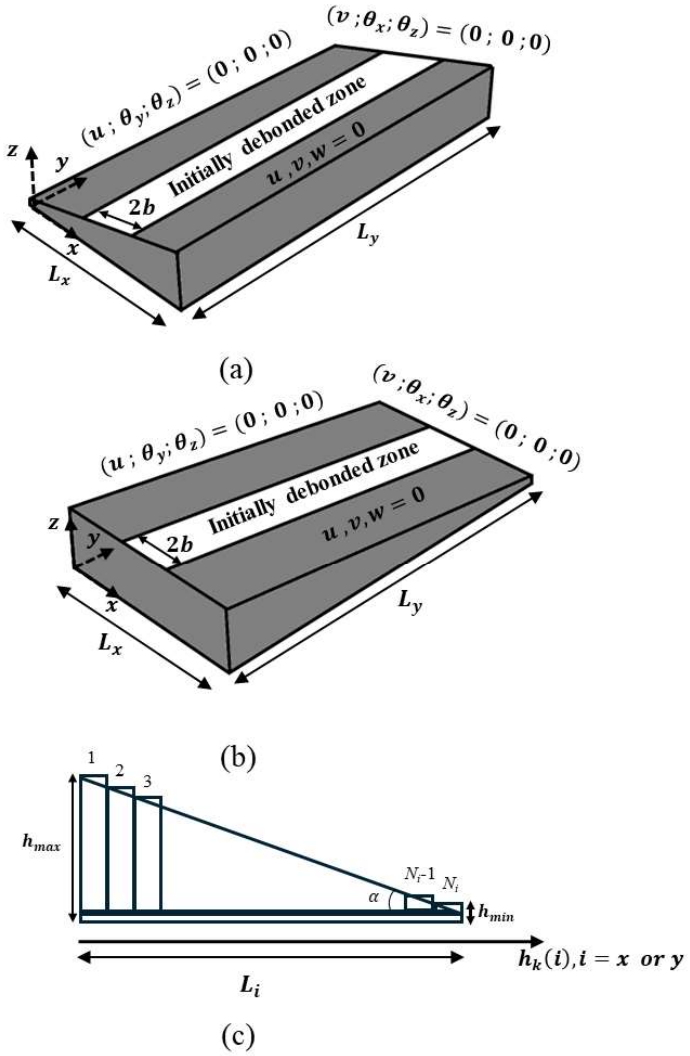

Fig. 3-13: Finite element modelling and simulation box. The model incorporates a step-by-step thickness gradient simulation along the (a) (O*x*) and (b) (*Oy*) direction. A central delaminated stripe of width 2*b* (shown in white at the middle) is introduced to allow the formation of buckling patterns. (c) Illustration of the thickness gradient along the *i* axis, with *i*=*x* or *y*. A schematic representation of the variation of thickness along the *i* axis, with *i*=*x* or *y*, where the film's thickness decreases step-by-step from h_{max} to $h_{\min}$ across the total length over L_i, which is subdivided into N_i discrete equi-distance sections width $L_k(i)$ for *k* ranging from 1 to N_i.

3.2.2. Model validation: homogeneous plate

We now proceed the validation of the FE mechanical model in the framework of the FvK plate theory for a homogenous, constant-thickness films h [26]. This is necessary to ensure the accuracy and reliability of the mechanical model, mesh quality and boundary conditions before applying it to more complex thickness gradient systems. Fig. 3-14 shows a well and uniform structured mesh that consists of square elements (aspect ratio = 1) with a size of 0.6 µm. The zoom in view of the mesh is shown at the top marked by dashed circle. The number of elements is set to $N_x = 100$ along the (Ox) and $N_y = 200$ along the (Oy), resulting in a total of 20000 elements. The initially delaminated region is highlighted in red.

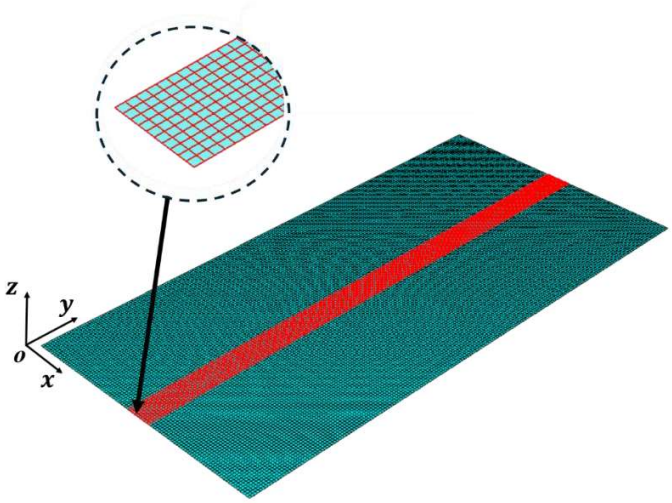

Fig. 3-14: Finite element mesh of the homogeneous plate using S4R shell elements. The nickel film is bonded to a rigid substrate, with a central delaminated stripe (red), where buckling is allowed. The mesh consists of 100 elements along (Ox) and 200 along (Oy) (total: 20000 elements), with uniform element size 0.6 µm. A zoomed view shows the structured mesh in the stripe region.

We consider a nickel film with a thickness h = 20 nm, subjected to an internal compressive stress, with σ_{xx}^0 varies from 0 to 0.3 GPa and $\sigma_{yy}^0 = 0$ GPa. The delaminated width is arbitrary fixed to $2b$ = 6 µm. Fig. 3-15 shows FEM results as solid red lines, while the FvK solutions as blue dashed lines. Fig. 3-15a depicts the evolution of normalized out-of-plane height δ/h as a function of normalized stress σ_{xx}^0/σ_c, where σ_c is the critical stress for buckling given by Eq. (3-4). It is shown that δ/h follows a square root function of σ_{xx}^0/σ_c, consistent with the FvK plate theory. Fig. 3-15b presents the normalized out-of-plane displacement profile w/h with respect to normalized coordinate x/b, where the FEM results accurately reproduce the expected sinusoidal shape of a

SSB predicted by Eq. (3-2). These results confirm that the FEM simulations can reproduce the analytical model for a SSB. A parametric study was also conducted to study the sensitivity of the initial imperfection (see Eq. 3-13); a small imperfection amplitude of the order of h/1000 was sufficient to produce the FvK solutions.

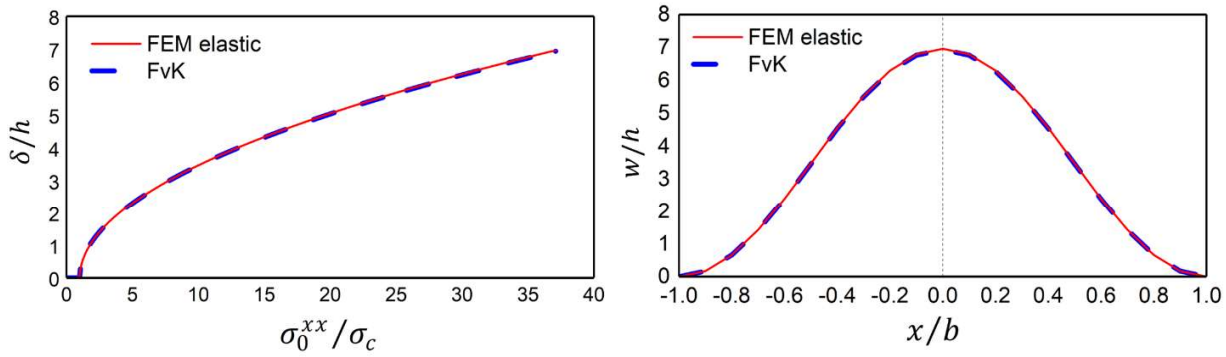

(a) (b)

Fig. 3-15: (a) The normalized height δ/h as a function of the normalized loading $\sigma_{xx}{}^0/\sigma_c$. (b) The normalized out of plane displacement w/h with respect to the normalized in plane coordinate x/b. The blue dashed lines represent the analytical (FvK) solutions. Finite element simulations were performed for a nickel film with Young's modulus E_f = 200 GPa, Poisson's ratio ν_f =0.31, stripe width $2b$ = 6 µm, film's thickness h = 20 nm, and uniaxial compressive stress $\sigma_{xx}{}^0$ varies from 0 to 0.3 GPa and $\sigma_{yy}{}^0$ =0 GPa.

3.3. FEM results of SS buckles parallel to the thickness gradient

3.3.1. FEM simulations versus experiments

The FEM simulation follows the model described earlier, with the film thickness h varies step-by-step from h_{min} = 177 nm to h_{max} = 205 nm along the (Oy) direction (experimental case of Fig. 3-4). The compressive stresses were set similarly to the experiment, $\sigma_{xx}{}^0 = \sigma_{yy}{}^0$ = 0.8 GPa. Fig. 3-16a presents the impact of thickness gradient on the out-of-plane displacement $w(x)$. A schematic representation of the local thickness h variation is shown on the left side. Displacement profiles $w(x)$ are extracted along the (Ox) direction at different local h values and depicted in Fig. 3-16b. The FEM elastic profiles are represented as solid lines "FEM elastic", colored according to their respective value of h. It is shown that the equilibrium shape of the SSB is well described by a sinusoidal profile as expected by Eq. (3-2) [26]. Additionally, it is observed that w increases as h decreases, consistent with predictions from elasticity theory for a homogeneous constant-thickness film [26]. A direct comparison between the numerical FEM elastic and experimental height δ values is shown in Fig. 3-16c. The FEM elastic results (circular dots) follow the same trend as experiments, with δ increasing as h decreases. However, they systematically underestimate the

experimental values (reported here as stars). This discrepancy may be attributed to the elastic contrast between the film and its substrate. Note that plasticity could also increase the maximum height; this effect was recently investigated for gold films both experimentally and numerically by FEM simulations [20,138]. However, nickel is not known to be extremely ductile, so that we can exclude such an explanation.

To account for the elastic contrast between the film and its substrate, we refined our FEM results using a numerical model that was developed by Parry *et al*. [37]. In their work, they have shown that both σ_c and δ are influenced by the substrate elasticity. Parry *et al*. [37] introduced two correction factors, defined as $\gamma_\sigma(\alpha_D)$ and $\gamma_\delta(\alpha_D)$, for both σ_c and δ, respectively, where the elastic contrast is characterized by the Dundurs' coefficient α_D, given by :

$$\alpha_D = \frac{E_f(1-\nu_s^2)-E_s(1-\nu_f^2)}{E_f(1-\nu_s^2)+E_s(1-\nu_f^2)}, \tag{3-14}$$

α_D =-1 refers to a soft film on a hard substrate; on the other hand, α_D =+1 corresponds to a hard film on a soft substrate. In Parry *et al*. numerical model, the refined critical stress σ_c^r and maximum height δ^r are thus expressed by [37]:

$$\sigma_c^r = \gamma_\sigma(\alpha_D).\sigma_c \quad \text{and} \quad \delta^r = \gamma_\delta(\alpha_D).h\sqrt{\frac{4}{3}\left(\frac{\sigma_0}{\sigma_c^r}-1\right)}. \tag{3-15}$$

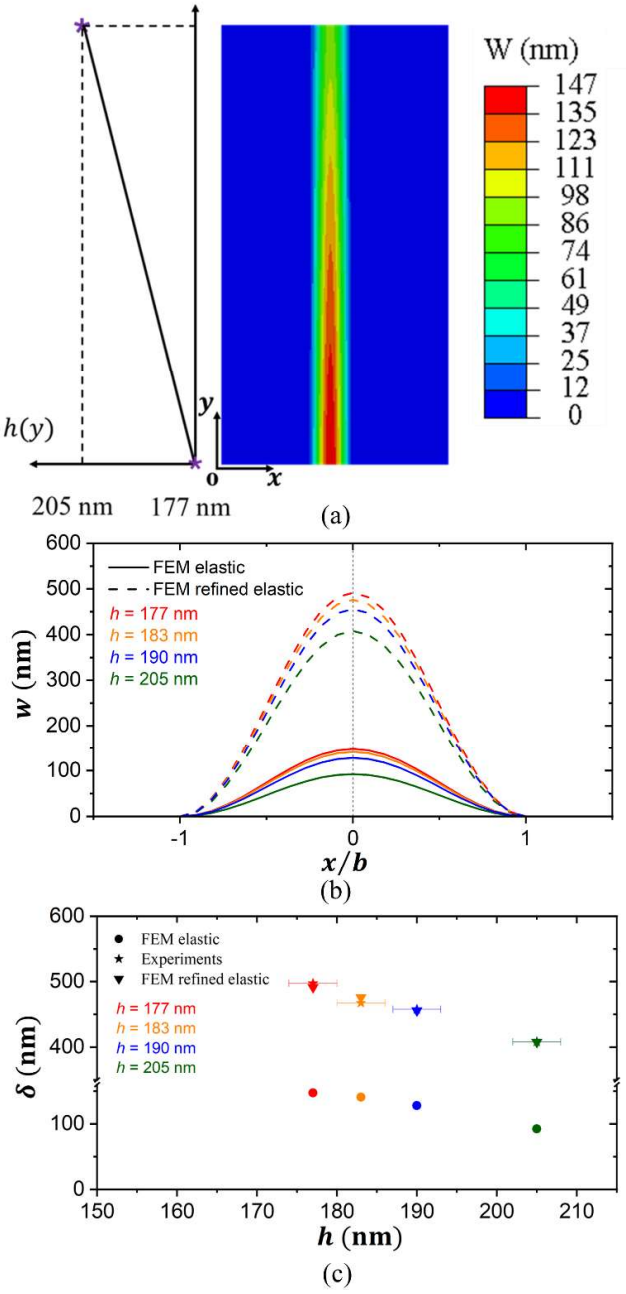

Fig. 3-16: Morphological analysis of a straight-sided buckle lying parallel to the thickness gradient $h(y)$ along the (Oy) direction. (a) Out-of-plane displacement with respect to the local thickness h within the gradient. (b) Equilibrium profiles for various thicknesses h, with x normalized over the half-width b. (c) Maximum height δ *vs*. local thickness h. Finite element simulations were performed for a nickel film with Young's modulus E_f = 200 GPa, Poisson's ratio ν_f =0.31, stripe width $2b$ = 6.6 µm and uniaxial compressive stress σ_{xx}^0= 0.8 GPa and σ_{yy}^0 =0 GPa. 'Refined elastic' corresponds to FEM simulations taking into account the elasticity of the substrate by correction factors from [37].

Fig. 3-17 illustrates the dependence of the correction factors $\gamma_\sigma(\alpha_D)$ and $\gamma_\delta(\alpha_D)$ with the elastic contrast α_D. It is observed that γ_σ decreases while γ_δ increases with α_D, whereas both factors approach 1 for $\alpha_D = -1$.

In our experimental case, E_s = 2.5 GPa and ν_s = 0.37 [37], it leads to α_D= 0.97, which gives correction factors of γ_σ =0.73 on the critical stress and γ_δ =2.3 on the maximum height. The numerical 'FEM refined elastic' results reported in Fig. 3-16 (dashes lines in (b); triangular dots in (c)) thus correspond to the expected maximum height that accounts for the elasticity of the substrate, by correcting the previous FEM results. As expected, the height is strongly enhanced and shows a much better agreement with the experimental data. Note that the shape of the corrected buckles presented in Fig. 3-16b was assumed to be a sinusoidal function as the equilibrium one expected in the framework of the FvK equations.

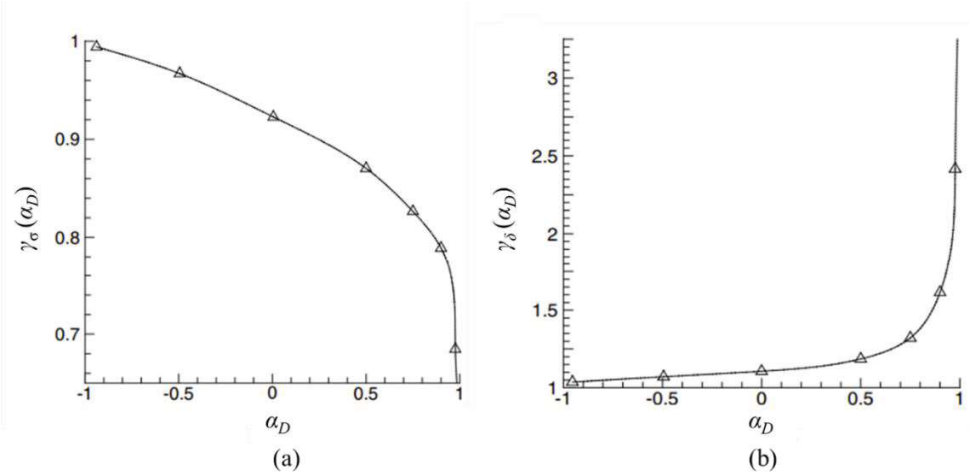

Fig. 3-17: Evolution of correction factors (γ_σ, γ_δ) taking into account the elastic contrast α_D of the film/substrate system. α_D=-1 corresponds to the FvK plate theory: (a) γ_σ applied to the critical stress and (b) γ_δ applied to the maximum height δ of the straight-sided buckled, as a function of Dundurs' coefficient α_D. Adopted from [37].

3.3.2. Influence of thickness gradient intensity on the SS buckles

We now extend the analysis to explore the influence of key geometric parameters: the thickness gradient slope α and stripe width $2b$ on the formation and morphology of SSBs. The objective is to study the geometric conditions under which buckling occurs and how the morphology evolves as a function of local thickness. FEM simulations were performed for various α and $2b$, for a nickel

film, under uniaxial compressive stress of σ_{xx}^0 = 0.8 GPa and σ_{yy}^0 = 0 GPa. The uniaxial stress components were chosen to ensure that buckling only occurs in the form of SSB [28].

Fig. 3-18 summarizes the out-of-plane displacement $w(x,y)$ obtained from FEM simulations for various combinations of α and $2b$. Each row (resp. each column) corresponds to a width (resp. a thickness gradient slope α) ranging from 6 to 12 µm (resp. from 0.04° to 0.17°).

For the wider $2b$ = 12 µm, it is shown that the out-of-plane displacement w decreases as α increases. Additionally, for a given α, w decreases with increasing h along the (Oy) direction (see Fig. 3-18a). Similar behaviors are observed for $2b$=9.6 µm, except that a transition from a SSB to a plane state occurs for α =0.17°, as shown in Fig. 3-18e, where the two regions are labelled. Reducing $2b$ to 6 µm results in the same transition from a SSB to a plane state even at lower h values, for both α =0.13° and α =0.17°. Additionally, a gentle (*i.e.*, small slope) thickness gradient behaves like a homogenous film while a steep thickness gradient significantly modifies the local maximum height δ. Finally, it is observed that either increasing h or decreasing $2b$ allows for reaching the transition threshold from the SSB to the plane state. This can be explained within the framework of FvK plate theory; as the thickness $h(y)$ increases, σ_c is increased up to the internal stress σ_{xx}^0 for which the buckling becomes energetically unfavorable. Similarly, decreasing the width 2b leads to the shift of the buckling threshold towards lower $h(y)$ values.

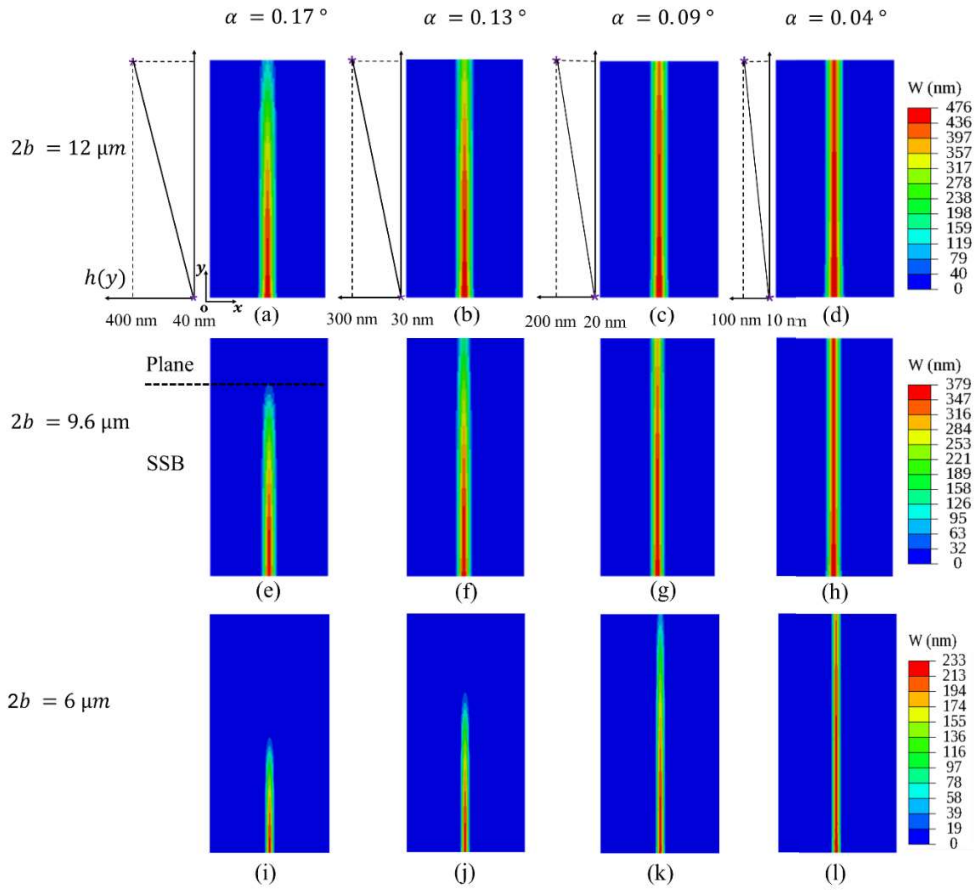

Fig. 3-18: Out-of-plane displacements of straight-sided buckles lying parallel to the thickness gradient $h(y)$, for various thickness gradient slopes α and widths $2b$. (a), (e) and (i) correspond to $\alpha = 0.17°$; (b), (f) and (j) to $\alpha = 0.13°$; (c), (g) and (k) to $\alpha = 0.09°$; (d), (h) and (l) to $\alpha = 0.04°$. The stripe width of the initially-debonded zone is $2b = 12$ µm for (a) to (d), $2b = 9.6$ µm for (e) to (h) and $2b = 6$ µm for (i) to (l). In (e) two equilibrium states are separated by dashed lines, the no buckling state (plane) and the straight-sided buckled state. Finite element simulations were performed for a nickel film with Young's modulus $E_f = 200$ GPa, Poisson's ratio $\nu_f = 0.31$, and uniaxial compressive stress $\sigma_{xx}^0 = 0.8$ GPa and $\sigma_{yy}^0 = 0$ GPa.

3.3.3. Quantification of the local onset of buckling

For each y position along the gradient, δ was extracted at the middle of the SSB (maximum height) while incrementally increasing σ_{xx}^0 from 0 up to the target value of 0.8 GPa. Fig. 3-19 presents the evolution of the maximum height δ as a function of the internal stress σ_{xx}^0, for a fixed width of $2b = 6$ µm and for various gradient slopes α. The color bar on the right highlights the local thicknesses $h(y)/h_{min}$, where h_{min} corresponds to the minimum thickness of the gradient. Four

gradient slopes are studied: (a) α = 0.04°, (b) 0.09°, (c) 0.13° and (d) 0.17°, with h_{min} = 10, 20, 30 and 40 nm, respectively. The solid lines depicts FEM results extracted at various $h(y)$ positions along the gradient, whereas the dashed lines represents the FvK predictions in the case of a homogenous, constant-thickness film [26]. Additionally, a zoom-in near the onset buckling highlighting the transition threshold from a plane state to a SSB is provided in insets. In the following, we label the critical stress in gradient obtained by FEM as σ_c^{TG} and the analytical critical stress by FvK as σ_c, as shown by black arrows in Fig. 3-19a.

For α = 0.04° (see (a)), near the critical threshold, FEM results for small h (blue curves) agree well with FvK predictions. However, as h increases (toward red curves), we can observe that the numerical height δ of the SSB shows disparity with the expected FvK one. Note that far from the critical threshold, this disparity disappears and the computed δ is shown to well follow the Fvk solutions regardless of the local h within the gradient. The shift of σ_c^{TG} with respect to σ_c increases as h increases, particularly at higher values of h (green curves). As it is shown in Fig. 3-19a, the shift is almost negligible for $h(y)/h_{min}$ = 1.45 (dark blue), while it reaches almost one half of the initial threshold for $h(y)/h_{min}$ = 4.6 (green). Additionally, it can be clearly seen that for $h(y)/h_{min}$ between 5.06 and 5.95, the transition from a plane state to a SSB occurs, although the FvK plate theory predicts no buckling ($\sigma_c > \sigma_{xx}^0$). Near the critical threshold, it is shown that δ does not follow anymore the square root function dependence, and this becomes more pronounced as h increases within the gradient. This behavior is seen for the other gradient slopes α, where the effect becomes less pronounced as α decreases, as shown in Figs. 3-19b-d. This earlier buckling becomes more pronounced with steeper gradients. This explains the previous observation in Fig. 3-18 increasing α (*resp*. h) allows the transition threshold from the SSB to the plane state to appear. These findings highlight that the thickness gradient strongly affects not only σ_c, but also δ near the threshold, with the effect becoming more pronounced as α increases.

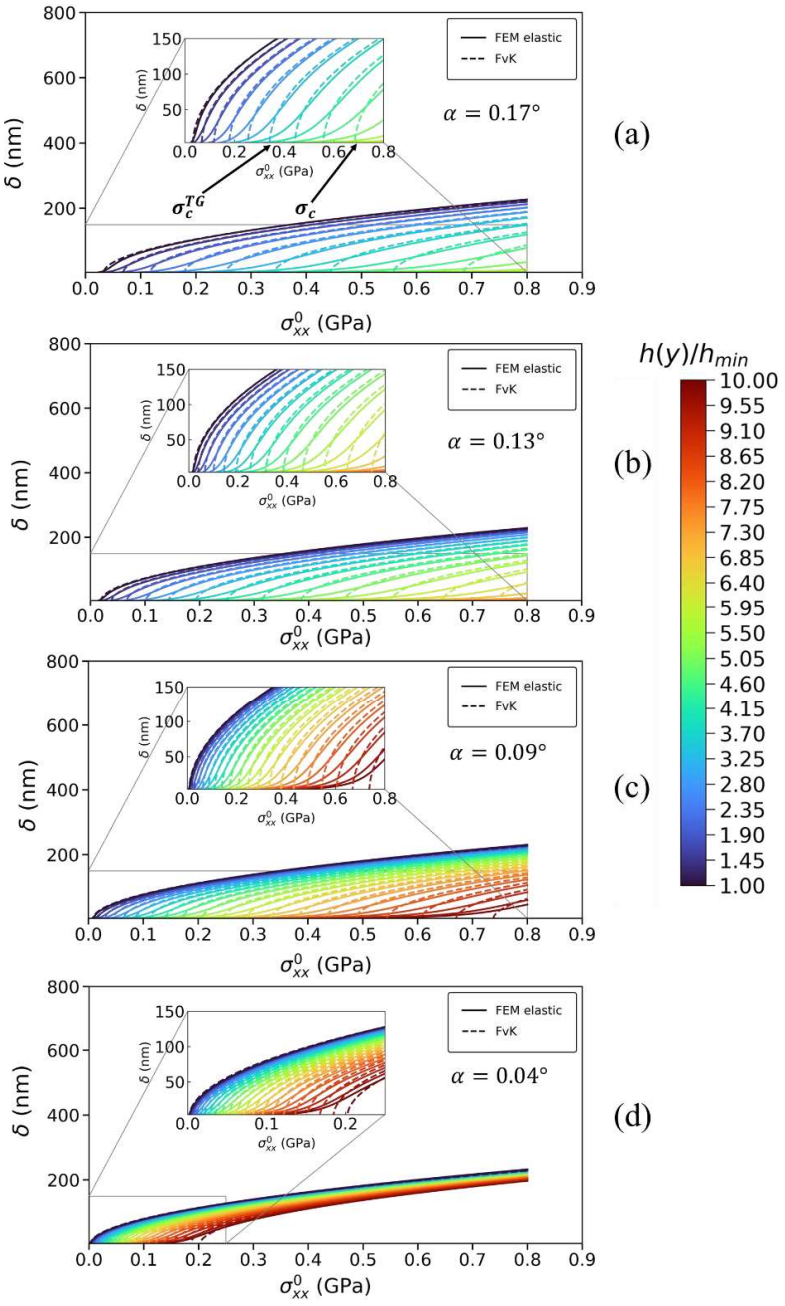

Fig. 3-19: FEM numerical results of a straight-sided buckle lying parallel to the thickness gradient $h(y)$ along the (Oy) direction. Maximum height δ of a straight-sided buckle *vs.* internal stress σ_{xx}^0, for various normalized local thickness $h(y)/h_{min}$ and gradient slope α for: (a) $\alpha = 0.17°$ and $h_{min} = 40$ nm, (b) $\alpha = 0.13°$ and $h_{min} = 30$ nm, (c) $\alpha = 0.09°$ and $h_{min} = 20$ nm, (d) $\alpha = 0.04°$ and $h_{min} = 10$ nm. h_{min} is the minimum thickness of the considered. Finite element simulations were performed for a nickel film with Young's modulus $E_f = 200$ GPa, Poisson's ratio $\nu_f = 0.31$, stripe width $2b = 6$ µm, and uniaxial compressive stress $\sigma_{xx}^0 = 0.8$ GPa and $\sigma_{yy}^0 = 0$ GPa.

Fig. 3-20 shows the corresponding FEM results for the same gradients as in Fig. 3-19, but for wider stripes of $2b$=9.6 µm (a) and 12 µm (b). The behavior is similar to what was described previously. However, in contrast to $2b$=6 µm, increasing b systematically lowers σ_c, consequently higher values of δ, consistent with elastic plate theory [26]. As a consequence, the FEM results curves lie closer to the FvK predictions than those for $2b$=6 µm. The influence of the gradient weakens for wider stripes, becoming noticeable only for the steepest slope α = 0.17° (see (d)), where thick regions of film with buckle even if $\sigma_c > \sigma_{xx}^0$. For α = 0.17°, it is shown that the shift of σ_c^{TG} decreases with increasing $2b$ for the same local h, for instance, at $h(y)/h_{min}$ = 7.75 (orange curves), σ_c^{TG} drops by 33% for $2b$=12 µm, compared to 35% for $2b$=9.6 µm with respect to σ_c. This behavior holds for whatever α.

In conclusion, the effect of thickness gradient is consequently shown to be similar to the effect of the elasticity of the substrate [37], characterized by a decrease of the critical stress for buckling to occur. A gentle (*i.e.*, small slope) thickness gradient behaves like a homogenous film while a steep thickness gradient significantly modifies the local related buckled equilibrium profiles, especially close to the buckling threshold.

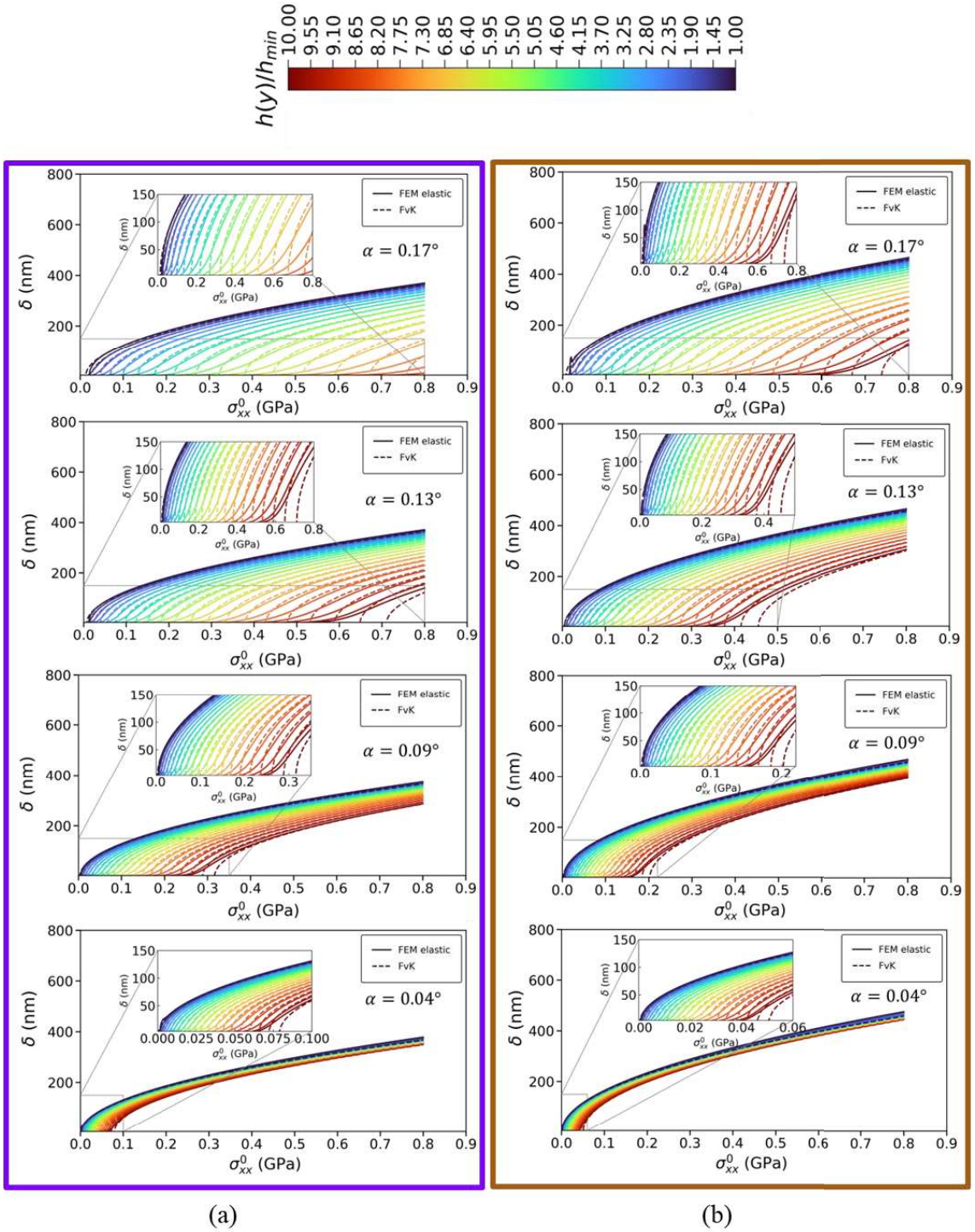

Fig. 3-20: Same as in Fig. 3-19 for various stripe widths (a) $2b$ = 9.6 µm, (b) $2b$ = 12 µm. Finite element simulations were performed for a nickel film with Young's modulus E_f = 200 GPa, Poisson's ratio ν_f =0.31 and uniaxial compressive stress $\sigma_{xx}{}^0$= 0.8 GPa and $\sigma_{yy}{}^0$ =0 GPa.

Fig. 3-21 shows the evolution of δ as a function of σ_{xx}^0 for different combinations of h, $2b$ and α. Panels (a)-(d) correspond to α = 0.04°, 0.09°, 0.13° and 0.17°, with local thicknesses of h = 37, 74, 111 and 148 nm, respectively. Each panel includes results for $2b$ = 6, 9.6 and 12 µm. Solid lines represent the FEM-computed δ extracted from previous simulation in Figs. 3-19 and 3-20 for the same local h for each α.

For α = 0.04° (see (a)), the transition from a plane state to a SSB occurs at lower σ_{xx}^0 as $2b$ increases. The same trend holds for all gradient slopes α. It is shown that the shift of σ_c^{TG} for a fixed h increases with decreasing $2b$, consistent with previous discussion. This earlier buckling becomes more pronounced as α increases, with the effect being most visible for the smaller $2b$ values across Figs. 3-21(a)-(d). In addition, δ is found to increase with $2b$ for all values of α.

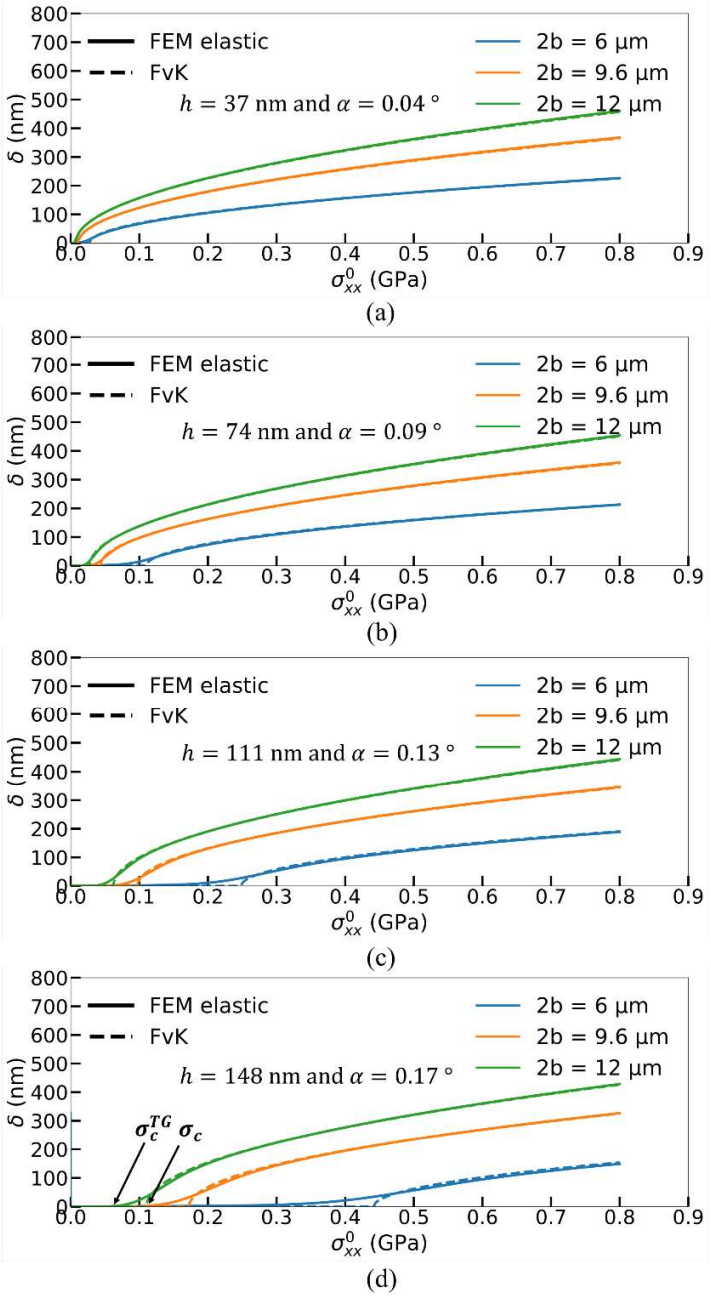

Fig. 3-21: FEM numerical results of a straight-sided buckle lying parallel to the thickness gradient $h(y)$ along the (Oy) direction. Maximum height δ of a straight-sided buckle *vs*. the applied stress σ_{xx}^{0} for various stripe widths and with the same gradient slope for α, and local thickness h: (a) h = 37 nm, (b) h = 74 nm, (c) h = 111 nm, (d) h = 148 nm. Finite element simulations were performed for a nickel film with Young's modulus E_f = 200 GPa, Poisson's ratio ν_f =0.31, and uniaxial compressive stress σ_{xx}^{0}= 0.8 GPa and σ_{yy}^{0} =0 GPa.

Having established that σ_c^{TG} depends on both $2b$ and α, the next step is to quantify this dependence explicitly. Fig. 3-22 shows σ_c^{TG} as a function of the local h for two different widths: (a) $2b$ = 6 µm and (b) 12 µm, and various α. FEM results are presented as color filled circles (each color corresponding to a different α), and the analytical Fvk prediction for a homogeneous, constant-thickness film shown as a dashed black curve. Insets provide a zoomed-in view at small h, where deviations are not clearly visible.

For $2b$ = 6 µm (see (a)), σ_c^{TG} follows a parabolic-like function with h, consistent with the FvK scaling. Remarkably, this parabolic trend is preserved for all α, showing that the gradient does not modify the fundamental h^2 dependence predicted by the plate theory. However, the results show that σ_c^{TG} is systematically shifted below the Fvk analytical, and this shift increases with α. The case of α = 0.17° exhibits the strongest deviation, indicating earlier onset of buckling for steeper gradients. The results for $2b$ = 12 µm (see (b)) show the same overall behavior but with smaller shifts in contrast to $2b$ = 6 µm.

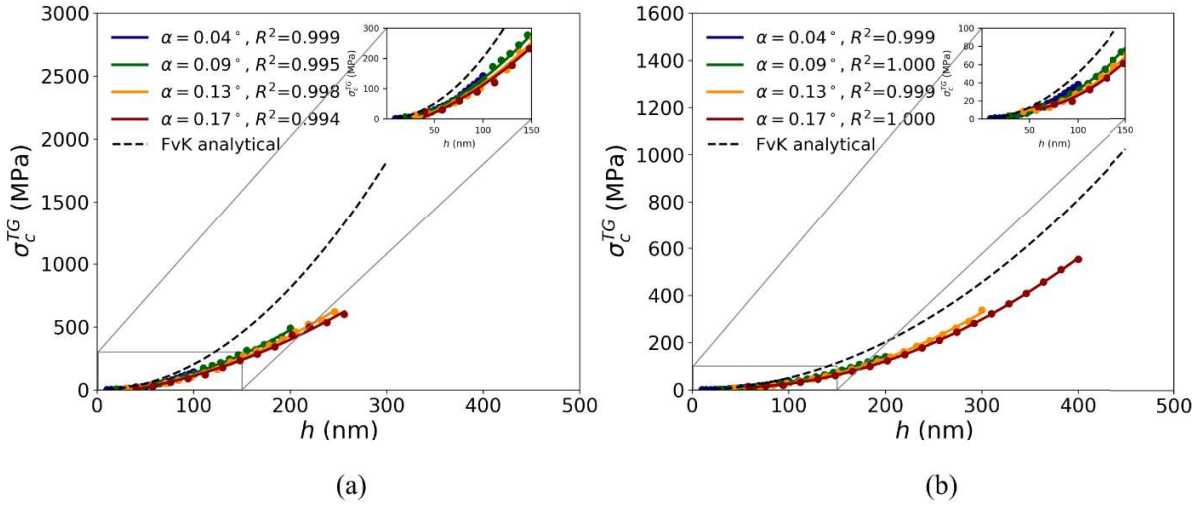

Fig. 3-22: The dependence of onset of buckling σ_c^{TG} *versus* the local film thickness h for various gradient slopes α, and two stripe widths (a) $2b$=6 µm and (b) 12 µm (b). Color points represent FEM data for various α. Dashed black line corresponds to the analytical FvK for a homogenous plate, with Eq. (3-4). The inset zoom highlighting the deviations between FEM results and the analytical FvK. Finite element simulations were performed for a nickel film with Young's modulus E_f = 200 GPa, Poisson's ratio ν_f=0.31, and uniaxial compressive stress σ_{xx}^0= 0.8 GPa and σ_{yy}^0 =0 GPa.

Fig. 3-23 presents FEM results of σ_c^{TG} as a function of $(h/b)^2$. Filled circles and squares correspond to stripe widths of $2b$ = 6 and 12 µm, respectively, and the color of the symbols denotes the gradient slope α. The analytical FvK prediction, $\sigma_c=\pi^2 E_f/(1-\nu_f^2).(h/b)^2$, is shown as a dashed line. The numerical results collapse onto straight lines, confirming that σ_c^{TG} varies linearly with $(h/b)^2$

regardless of α and $2b$. However, the offset with respect to the analytical curve depends on both α and $2b$. For a given α (*resp*. a fixed $2b$), the narrower width (*resp*. the highest α) exhibits a larger shift, consistent with what was previously discussed.

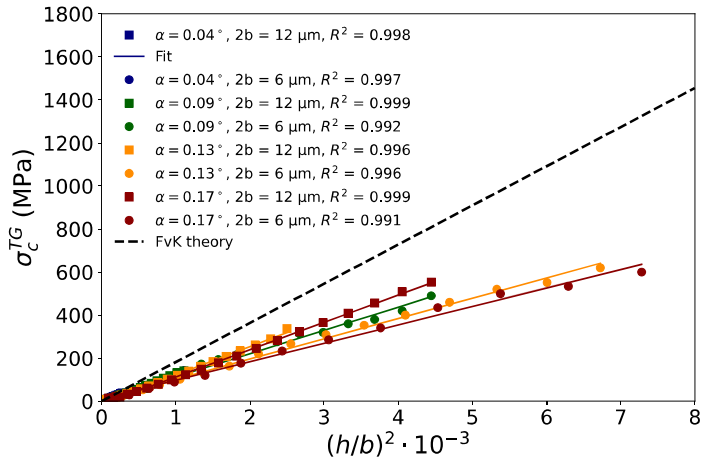

Fig. 3-23: The dependence of onset of buckling σ_c^{TG} *versus* $(h/b)^2$ for various gradient slopes α for two stripe widths $2b$ = 6 µm, and 12 µm. Color points represent FEM data for various α, while cercle symbol (data for $2b$ = 6 µm) and square (data for $2b$ = 12 µm). Dashed black line corresponds to the analytical FvK for a homogenous plate, with $\sigma_c=\pi^2 E_f/(1-\nu_f^2).(h/b)^2$. Finite element simulations were performed for a nickel film with Young's modulus E_f = 200 GPa, Poisson's ratio ν_f =0.31, and uniaxial compressive stress σ_{xx}^0= 0.8 GPa and σ_{yy}^0 =0 GPa.

3.3.4. Influence of thickness gradient on the out-of-plane displacement profile

We now assess whether the gradient also alters the post-equilibrium morphology of SSBs at the final loading. Fig. 3-24 shows the normalized out-of-plane displacement profiles, w/h, plotted as a function of the normalized (x) position to the half-width, x/b, for a nickel film of width $2b$ = 12 µm. Two gradient slopes are considered: (a) $\alpha = 0.13°$ and (b) $\alpha = 0.17°$, both evaluated at the final loading condition (when reached σ_{xx}^0 = 0.8 GPa). The color bar indicates the normalized local thickness $h(y)/h_{min}$, with h_{min} = 30 nm for (a) and 40 nm for (b). Solid curves represent to FEM profiles extracted at different $h(y)$, while the dashed curves correspond to the sinusoidal FvK solution (Eq. (3-2)) [26].

For both slopes, the FEM profiles obtained far from the critical threshold match the sinusoidal Fvk shape across the local thicknesses. This behavior was consistently observed for various $2b$ and α. In conclusion, although α was shown earlier to influence the onset of buckling, it does not modify the post-equilibrium shape far away from the critical threshold, except in regions where σ_{xx}^0 remains equal or very close to the onset buckling.

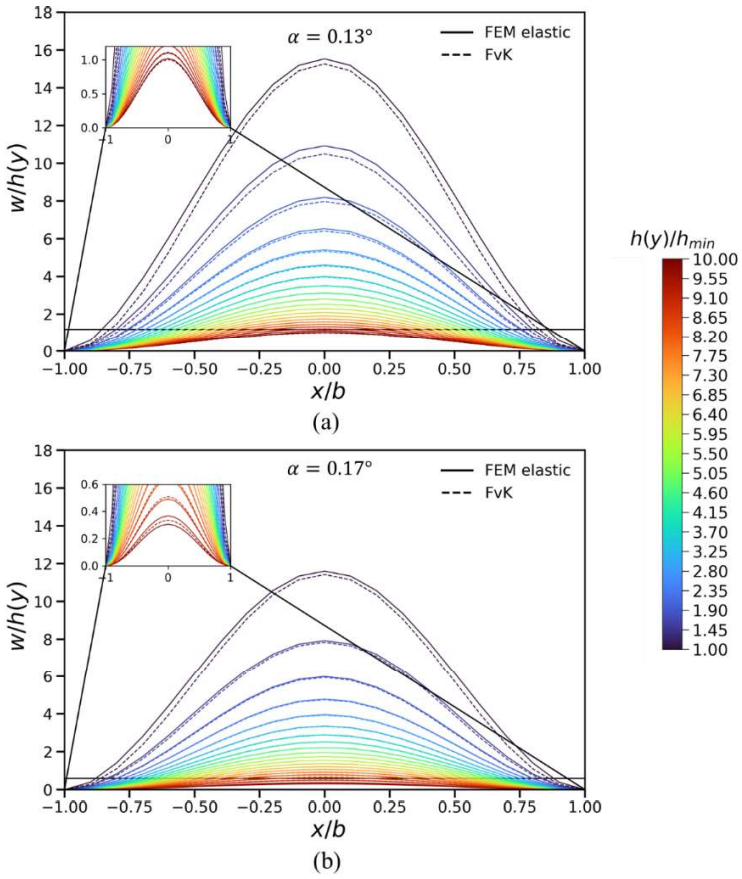

Fig. 3-24: The locally normalized out-of-plane displacement w/h of a straight-sided buckle lying parallel to the thickness gradient $h(y)$ along the (Oy) direction with respect to the normalized x position to the half-width x/b for various normalized local thickness $h(y)/h_{min}$ and gradient slope α for : (a) α=0.13° and h_{min} = 30 nm, (b) α = 0.17° and h_{min} = 40 nm. Finite element simulations were performed for a nickel film with Young's modulus E_f = 200 GPa, Poisson's ratio ν_f=0.31, stripe width $2b$ = 12 µm, and uniaxial compressive stress σ_{xx}^0= 0.8 GPa and σ_{yy}^0 =0 GPa.

3.4. FEM results of SS buckles perpendicular to the thickness gradient

We now consider nickel films with various thickness gradients along the (Ox) direction. FEM simulations were performed under uniaxial compressive stress set to σ_{xx}^0 = 0.8 GPa and σ_{yy}^0 = 0 GPa. A schematic representation of the gradient is shown on the bottom of the first FEM snapshot in Fig. 3-25. The thickness gradient is characterized by the normalized ratio h_{max}/h_{min}, with h_{max}

fixed arbitrary here to 150 nm, and h_{min} was varied from 5 nm to 150 nm. Fig. 3-25a presents snapshots of numerical results for several gradients, with h_{max}/h_{min} ranging from approximately 1.07 (gentle gradient) to 30 (steep gradient). The color contrast in Fig. 3-25a highlights the out-of-plane displacement w, with red indicating the maximum and blue the minimum value. For the case of a homogenous, constant-thickness film ($h_{max}/h_{min} = 1$), the red contrast is located at the middle indicating a symmetric buckle profile along its centerline (the dashed white line) with equal edge-to-peak distances on each side ($b_+ = b_-$), as expected from the FvK plate theory [26]. The two distances b_+ and b_- were previously defined in sub-section 3.1.2. As h_{max}/h_{min} increases the centerline is shown to be shifted towards the thinner side leading to unequal distances with ($b_+ \neq b_-$). This asymmetry becomes more pronounced for the steepest gradient h_{max}/h_{min}=30, the centerline becomes even close to the SSB edge on the right side close to h_{min} (see the FEM snapshot of h_{max}/h_{min}=30 in Fig. 3-25a).

The associated numerical profiles of the out-of-plane displacement $w(x,y)$ taking into account the variation of film thickness $h(x)$ along the (Ox) direction expressed as $[w(x,y)+h(x)]$ are extracted and presented in Fig. 3-25b, for various h_{max}/h_{min} defined by the color bar on the right side. For clarity, a vertical black dashed line at the centerline of the SS buckle in a homogenous, constant-thickness film ($h_{max}/h_{min} = 1$) was added at $x = 0$, where $b_+ = b_-$. It is observed that as h_{max}/h_{min} increases, the location of maximum height δ (the centerline) shifts toward the thinner part of the film, consequently leading to $b_+ > b_-$. Additionally, δ is also found to decrease with increasing the gradient. For instance, δ decreases by 43.4% for $h_{max}/h_{min} = 30$ compared to $h_{max}/h_{min} = 1$. Note that a smaller thickness leads to a lower localized stored elastic energy and bending stiffness in the plate [26]. This may explain our numerical and experimental observations.

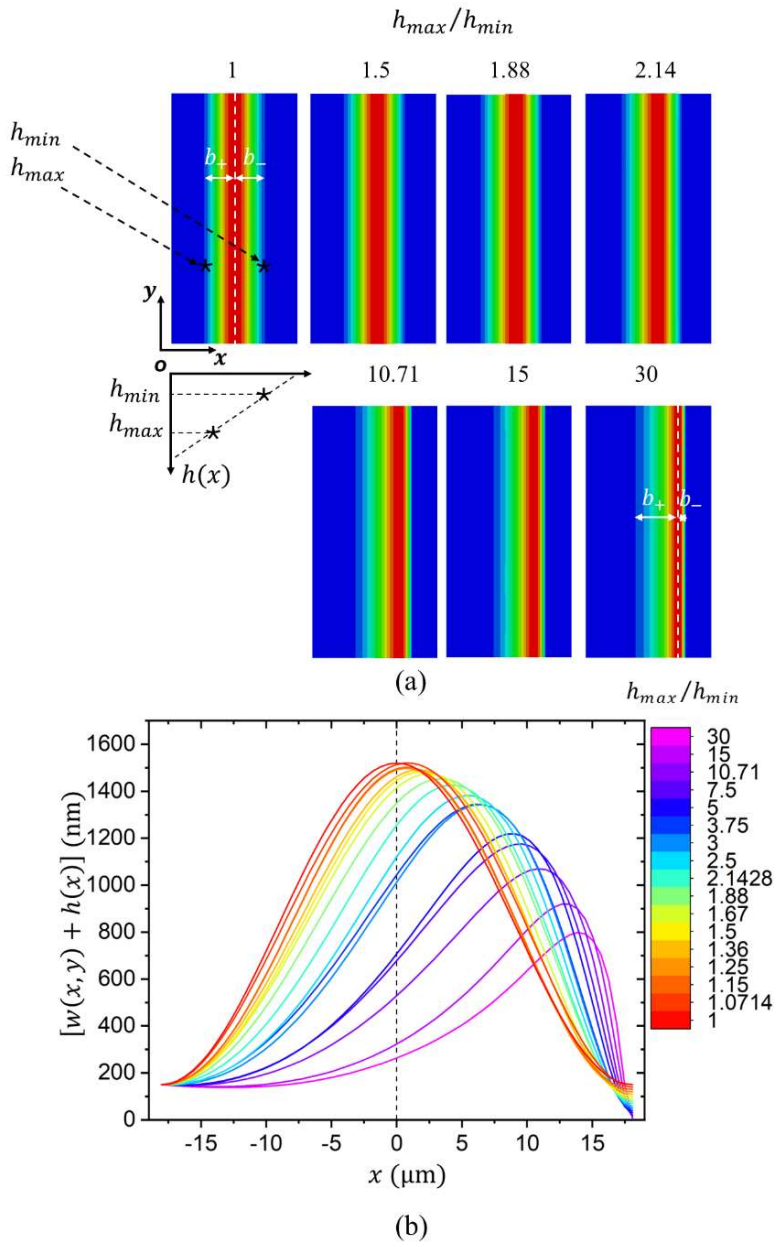

Fig. 3-25: Influence of a thickness gradient $h(x)$ perpendicular to a straight-sided buckle lying along the (Ox) direction. (a) Out-of-plane displacements with respect to the different thickness gradients (h_{max}/h_{min}) with their associated asymmetry b_+/b. (b) Mapping of equilibrium profiles of the SS buckle with respect to h_{max}/h_{min}. Finite element simulations were performed for a nickel film with Young's modulus E_f = 200 GPa, Poisson's ratio ν_f =0.31, maximum thickness h_{max} = 150 nm, stripe width $2b$ = 36 µm, and uniaxial compressive stress σ_{xx}^0= 0.8 GPa and σ_{yy}^0 =0 GPa. The number of sections N_x along the width is considered to be 60.

Finally, the asymmetry of the profiles has been characterized in Fig. 3-26, on which is plotted the edge-to-peak distance ratio b_+/b_- as a function of h_{max}/h_{min}. FEM simulations were performed for two widths $2b$ = 36 µm (blue squares) and 12 µm (red squares). For comparison, we superposed the experimental results obtained previously (see table 3-1), as blue stars. It is shown in (a) regardless of the value of $2b$ that b_+/b_- increase continuously with h_{max}/h_{min}, in accordance with experiments. This asymmetry may serve as signature for extracting the thickness gradient or b_+/b_- ratio from the SSBs morphologies. It was also possible to track this asymmetry as a function of σ_{xx}^0, even though results are not shown here, it was observed that b_+/b_- depends only on h_{max}/h_{min}. Global linear fit represented as solid violet line for our data, nevertheless at small value of h_{max}/h_{min} this fit does not agree with our results, therefore the best fit for $h_{max}/h_{min} \leq 2$ is represented as solid black line. Fig. 3-26b presents a zoom in view for small values of h_{max}/h_{min}, it can be clearly seen that it will be difficult to have a unique fit for whatever the gradient slope. Moreover, the ratio b_+/b_- increases more slowly with respect to h_{max}/h_{min}. Additionally, it implies that the mode mixity angle ψ may differ on either side of the buckle, which is expected to influence how the buckle can further grow or evolve. Investigating this effect requires incorporating a cohesive zone model (CZM) into our FEM simulations [26]. However, such analysis demands a deeper investigation of buckling-driven delamination, which will be further discussed in section 4.5 in Chapter 4.

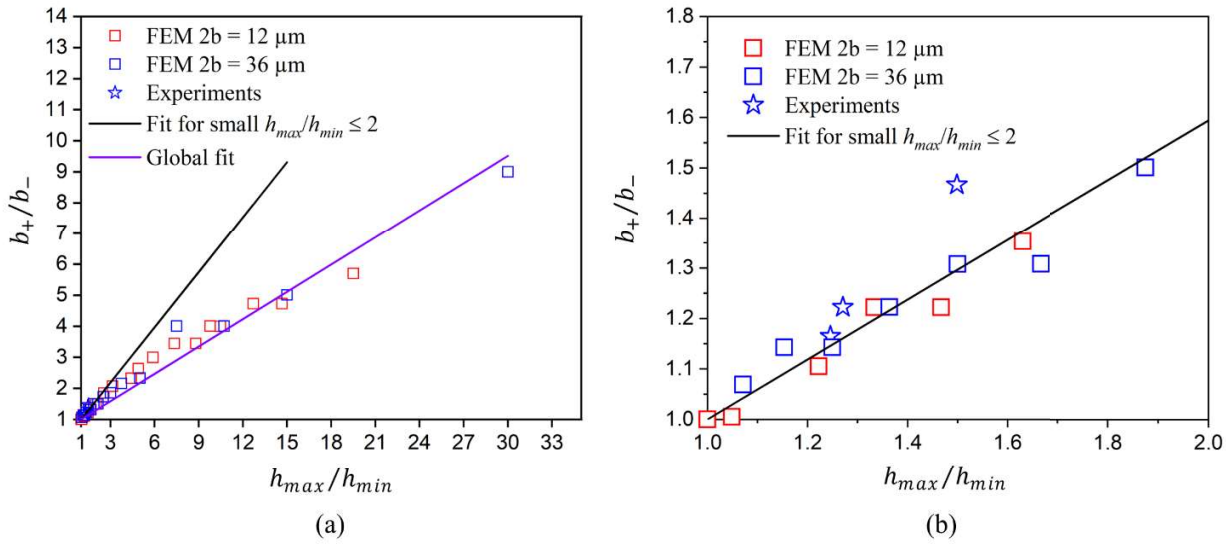

Fig. 3-26: (a) Normalized asymmetry ratio b_+/b_- *versus* h_{max}/h_{min} for various width $2b$. (b) Zoom on the region of small value h_{max}/h_{min}. Finite element simulations were performed for a nickel film with Young's modulus E_f = 200 GPa, Poisson's ratio ν_f=0.31, stripe width $2b$ = 36 µm (blue squares), 2b = 12 µm (red squares), and uniaxial compressive stress σ_{xx}^0= 0.8 GPa and σ_{yy}^0 =0 GPa. The number of sections N_x along the width is considered to be 60 and 40 for $2b$ = 36 µm and 12 µm, respectively.

Study of SS and TC buckles in nickel film exhibiting a well-controlled thickness gradient within a static approach

Building on the results presented in Fig. 3-25, we analyze the onset buckling of a SSB lying perpendicular to the thickness gradient. Two arbitrary gradients were considered, with ratio h_{max}/h_{min} = 3 and 5. For each h_{max}/h_{min}, the local thicknesses corresponding to the position of δ in the equilibrium profile are h=81 nm for h_{max}/h_{min} = 3, and h = 62 nm for h_{max}/h_{min} = 5. Fig. 3-27 presents the evolution of δ as a function of σ_{xx}^0 at these two h locations. The solid lines represent the FEM results, whereas the dashed lines depict the expected Fvk solution for these two equivalent local h. According to the Eq. (3-4), the critical buckling stresses are σ_c = 3.69 MPa, 2.16 MPa for h=81 nm and h=62 nm, respectively. In contrast, FEM calculations reveal higher onset stresses: σ_c^{TG} = 5.04 MPa and σ_c^{TG} = 2.29 MPa for h_{max}/h_{min} = 3 and 5, respectively, as shown in inset Fig. 3-27. Furthermore, it is shown that maximum height δ follow the square root function of σ_{xx}^0, in accordance with the FvK plate theory. Additionally, far from the critical threshold (onset buckling), it is shown that δ remains systematically lower than the FvK, and it becomes even lower as h_{max}/h_{min} increases. To summarize, the thickness variation along the buckle width does not only lead to an asymmetric equilibrium profile, and shift of δ, but also to increase σ_c, and lower δ with respect to a homogenous, constant-thickness film (FvK).

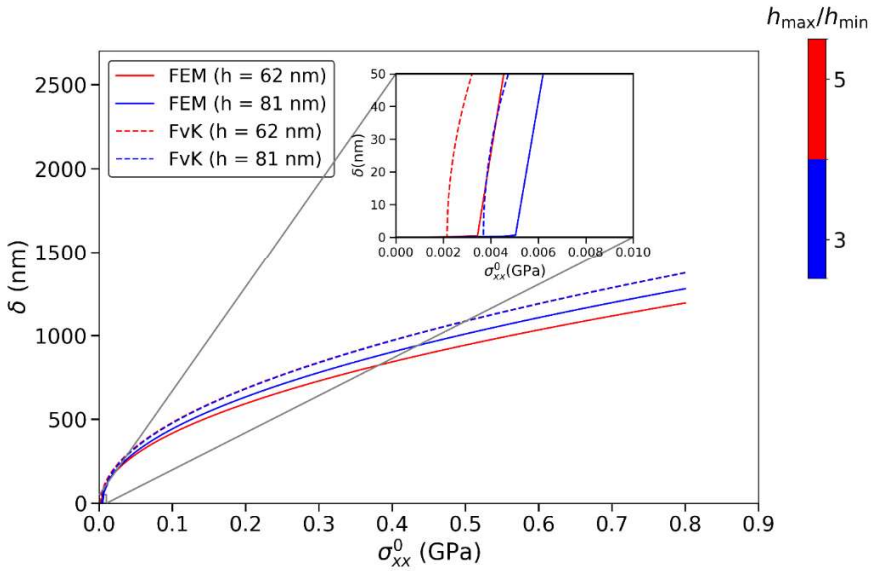

Fig. 3-27: Influence of a thickness gradient $h(x)$ perpendicular to a straight-sided buckle on the onset of buckling. Maximum height δ of a straight-sided buckle *vs*. internal stress σ_{xx}^0, for two thickness gradients h_{max}/h_{min}. Finite element simulations were performed for a nickel film with Young's modulus E_f = 200 GPa, Poisson's ratio ν_f =0.31, h_{max} = 150 nm, stripe width $2b$ = 36 µm, and uniaxial compressive stress σ_{xx}^0= 0.8 GPa and σ_{yy}^0 =0 GPa. The number of sections N_x along the width is considered to be 60.

3.5. FEM results of TC buckles parallel to the thickness gradient

3.5.1. In constant width

The equilibrium buckling structures in films exhibiting thickness gradients resulting from an isotropic stress state given by $\sigma_0 = \sigma_{xx}^0 = \sigma_{yy}^0 = 0.8$ GPa are presented in Fig. 3-28. These equi-biaxial stress components were chosen to ensure that buckling mainly occurs in the form of telephone cords. As for Fig. 3-18, the out-of-plane displacements are presented for various width $2b$ (the rows) and thickness gradient slope α (the columns), except that three different shapes may now be observed, the plane state, the SSB and the TCB (see Fig. 3-28e).

For large width ($2b$= 12 µm) and smooth gradient (α = 0.04°), a TCB developed all along the (Oy) direction (see frame (d)). As the gradient steepens, a transition from TCB to SSB is observed at thickest region (see frame (c)). This transition occurs at lower h values when α is increased. For higher α, a transition from SBB to plane state is also observed. The same behavior is shown at lower width $2b$ = 9.6 µm, except that decreasing the width leads to a transition from TCB (*resp.* SSB) to SSB (*resp.* plane state) at lower h. For α = 0.04°, the smallest width ($2b$= 6 µm) shows as a result an early TCB to a SSB transition, which was absent in wider widths. In conclusion, as the gradient increases, the two transitions are shifted to lower h.

A mapping of buckled morphologies was developed by Parry *et al*. [28], for an homogeneous plate, depending on two dimensionless parameters β_{xx} an β_{yy} , previously defined in sub-section 1.4.1 (Eq. (1-97)), given by :

$$\beta_{xx} = \frac{1-\nu_f^2}{E_f}\left(\frac{2b}{h}\right)^2 . \sigma_{xx}^0 \quad \text{and} \quad \beta_{yy} = \frac{1-\nu_f^2}{E_f}\left(\frac{2b}{h}\right)^2 . \sigma_{yy}^0 \tag{3-16}$$

It is well known that the TCBs are energetically favorable for high normalized isotropic stresses $\beta_{xx} = \beta_{yy}$ while the SSBs are expected for anisotropic normalized stresses $\beta_{xx} > \beta_{yy}$, and at lower isotopic stresses ($\beta_{xx} = \beta_{yy} < 21$). In our FEM simulations, it is shown that for a given b, the buckles evolve from TC to SS and then to the plane state as the local thickness $h(y)$ (*resp*. β_{xx}) increases (*resp*. decreases) in the thickness gradient. This mechanical behavior is consequently similar (see Eq. (3-16)) to what was observed both experimentally and numerically in the case of an homogeneous constant-thickness film [16,28,33].

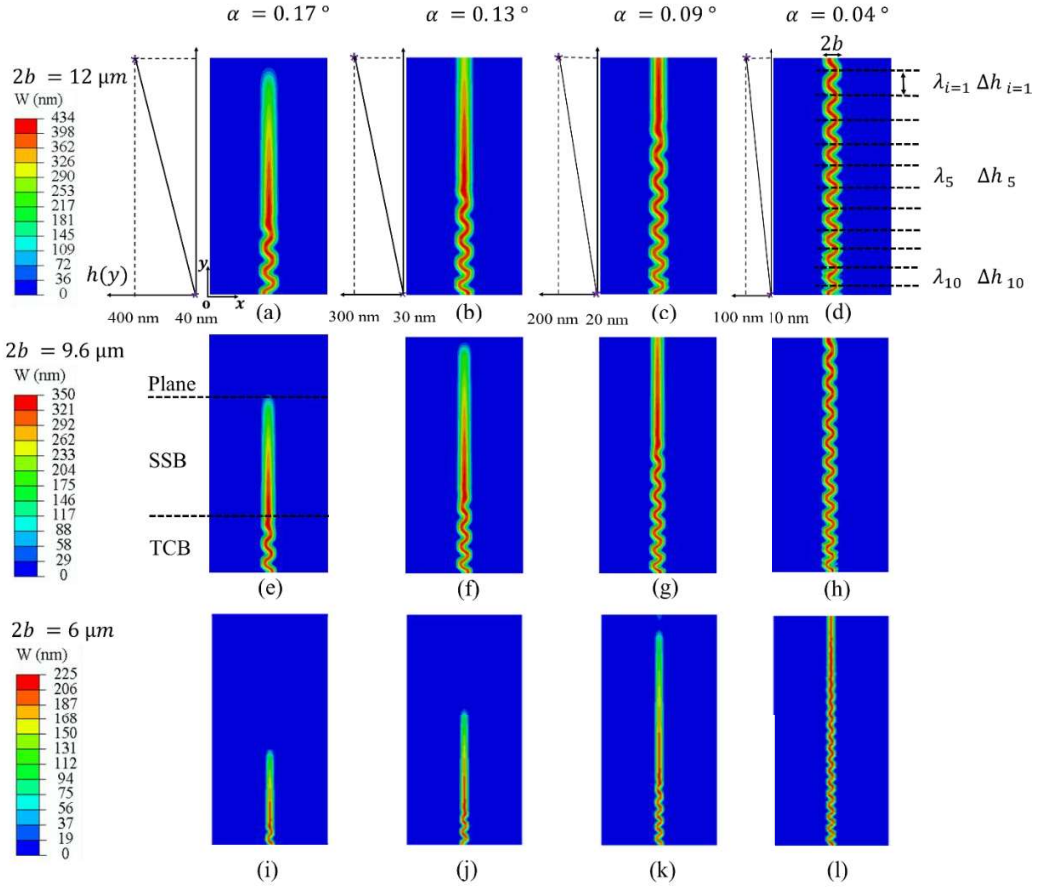

Fig. 3-28: Out-of-plane displacements of buckles lying parallel to the thickness gradient $h(y)$, for various thickness gradient slopes α and widths $2b$. (a), (e) and (i) correspond to α = 0.17°; (b), (f) and (j) to α = 0.13°; (c), (g) and (k) to α = 0.09°; (d), (h) and (l) to α = 0.04°. The stripe width of the initially-debonded zone is $2b$ = 12 µm for (a) to (d), $2b$ = 9.6 µm for (e) to (h) and $2b$ = 6 µm for (i) to (l). In (e), three equilibrium states are separated by dashed lines, the no buckling state (plane) and the buckled states characterized by straight-sided (SSB) and telephone-cord (TCB) buckles. Finite element simulations were performed for a nickel film with Young's modulus E_f = 200 GPa, Poisson's ratio ν_f=0.31, and isotropic compressive stress $\sigma_{xx}^0 = \sigma_{yy}^0$ = 0.8 GPa.

The transition from SS to TC buckles in homogenous stressed films has been extensively documented in the literature [16,32,33,45]. Moon *et al.* [45] investigated SSBs confined within stripes of increasing widths and reported that SSBs tend to evolve into TCBs as the stripe width becomes larger. Similarly, Yu *et al.* [16,33] observed this transition experimentally during the propagation of buckles in $SiAlN_x$ films. Jia *et al.* [32] further investigated this phenomenon in strained aluminum (Al) films [32] and demonstrated numerically that the critical stress for this secondary buckling, denoted here as $\sigma_{SS\text{-}TC}$, decreases as the stripe width $2b$ increases. In our FEM

simulations, $\sigma_{SS\text{-}TC}$ was found to increase with the increasing thickness h, as shown in Fig. 3-29a, and decreases with increasing b (Fig. 3-29b). The observed increases of $\sigma_{SS\text{-}TC}$ with h and its decreases with $2b$ strongly suggest a dependence on the ratio h/b, similar to that described in Eq. (3-4) for the plane state to SSB transition σ_c.

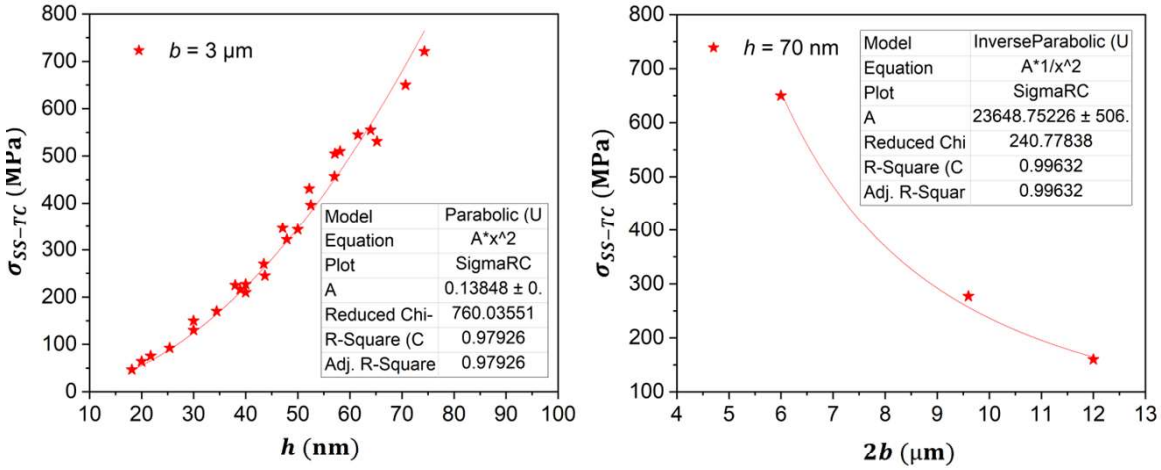

(a) (b)

Fig. 3-29: Critical stress for the straight-sided to the telephone cord transition in a thickness gradient $\sigma_{SS\text{-}TC}$ *vs*. (a) thickness h and (b) width $2b$. Finite element simulations were performed for a nickel film with Young's modulus E_f = 200 GPa, Poisson's ratio ν_f =0.31 and isotropic compressive stress $\sigma_{xx}^0 = \sigma_{yy}^0 = 0.8$ GPa.

In order to quantify this secondary buckling in films exhibiting thickness gradients, $\sigma_{SS\text{-}TC}$ has been determined from several FEM simulations by determining the stress where δ does not follow anymore a square-root function of the stress given by the Fvk plate theory. The results are reported in Fig. 3-30. A clear linear relationship is observed, resulting in a stress ratio of $\sigma_{SS\text{-}TC}/\sigma_c \approx 6.6$. This value is comparable to that reported for homogeneous, constant-thickness films, first given by Moon *et al*. [45] and later by Parry *et al*. [28].

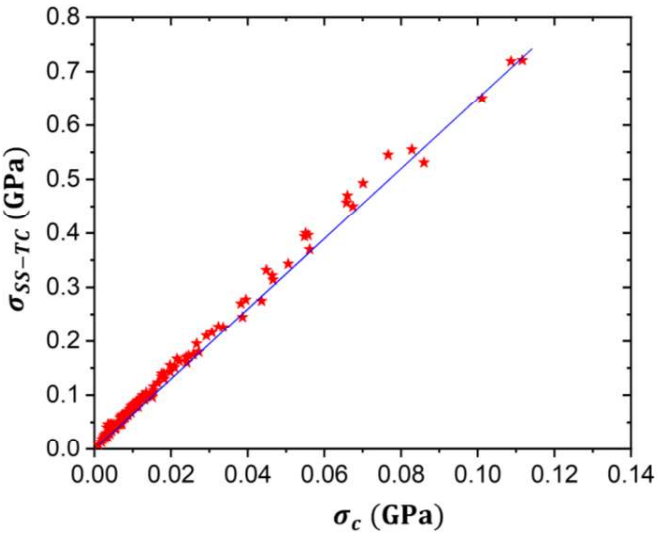

Fig. 3-30 : Critical stress for the straight-sided to the telephone cord transition in a thickness gradient, $\sigma_{SS\text{-}TC}$ *vs.* σ_c. Finite element simulations were performed for a nickel film with Young's modulus E_f = 200 GPa, Poisson's ratio ν_f =0.31 and isotropic compressive stress $\sigma_{xx}^0 = \sigma_{yy}^0$ = 0.8 GPa.

Fig. 3-31 presents the wavelength λ of a TCB as a function of its position $h(y)$ in the thickness gradient, for various half-widths b and thickness gradient a. First, it is worth noting that the $\lambda/2b$ ratio for homogeneous films typically ranges experimentally between 0.8-1.6 [22,33,45]. It is thus shown here that the thickness gradient does not modify this experimental fact. Secondly, it is observed that λ always increases with $h(y)$, both whatever the width $2b$ and the gradient intensity α, in good agreement with the experimental results. As reported by Moon *et al.* [141], an increase in film thickness leads to a higher strain energy in the film, which in turn results in larger wavelengths of the TC buckles. This trend obtained in the case of homogeneous thickness films thus aligns well with our observations in the case of a thickness gradient. It is also observed in Fig. 3-31 that λ increases with increasing b, for a given $h(y)$ (see for instance the red data for α = 0.004°). This is in accordance with both the works of Moon *et al.* [45] and Jia *et al.* mentioned previously. The evolution of λ with b for a thickness gradient is consequently similar to what is expected for a homogeneous plate [49,143]. Finally, λ does not seem to depend on the gradient intensity a (see the circle label for b= 6 µm).

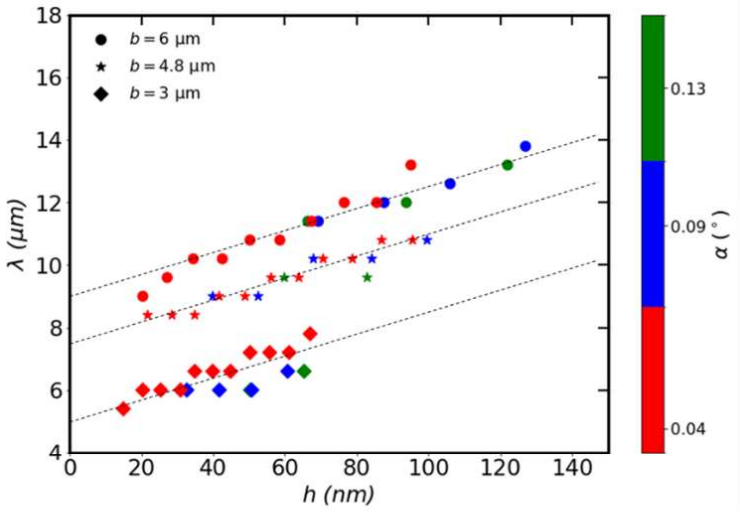

Fig. 3-31: Wavelength of a telephone-cord buckle λ vs. local thickness $h(y)$ for various half-width b and gradient intensity α. Finite element simulations were performed for a nickel film with Young's modulus E_f = 200 GPa, Poisson's ratio ν_f =0.31 and isotropic compressive stress $\sigma_{xx}^0 = \sigma_{yy}^0$ =0.8 GPa.

3.5.2. In gradient width

To further explore the combined influence of both thickness and width gradients on the morphological parameters of the TC buckle experimentally observed earlier in a nickel film, FEM simulations were performed using the mechanical model illustrated in Fig. 3-32. The boundary conditions are already described in sub-section 3.3.1 (see Fig. 3-13b). The simulation box consists of a film/substrate system of dimensions L_x = 300 µm and L_y = 600 µm. The width of the tapered delaminated stripe $2b(y)$ varies linearly from 44 µm at y=0 up to 25 µm at y=L_y, to mimic our experimental case shown in Fig. 3-11. This tapered width results in an in-plane angle $\gamma \sim 89.1°$ between the length axis of the delaminated zone and (Ox) axis. The local film thickness h along the (Oy) direction decreases from h_{max} =450 nm to h_{min} =300 nm according to Eq. (3-5). The isotropic internal compressive stress was mimicked in ABAQUS through a thermal expansion assigned to the film, as previously done.

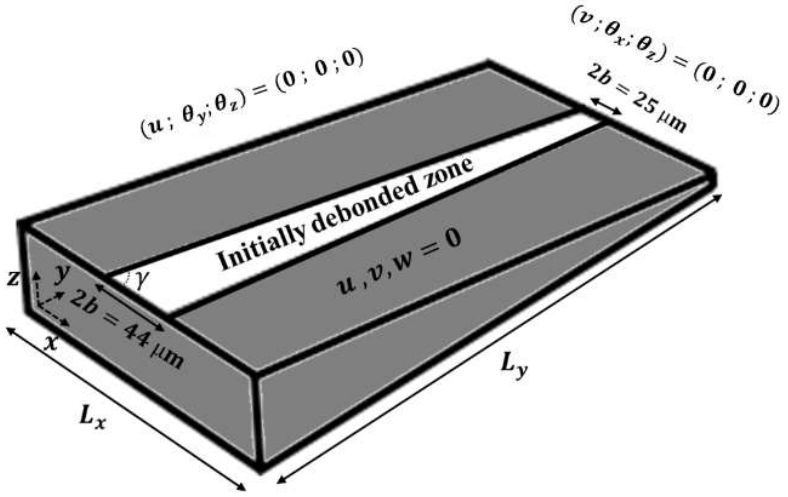

Fig. 3-32: FEM mechanical modelling and boundary conditions of the simulation box. A delaminated area is located at the middle part with a tapered strip width $2b(y)$ (see white areas). The film's thickness decreases from 450 nm at $y = 0$ to 300 nm at $y = L_y$, with the distance L_y divided into N discrete, equidistant sections width L_y/N.

The out-of-plane displacements of the tapered delaminated stripe obtained by FEM simulations are shown in Fig. 3-33 for various σ_0 ranging from (a) 0.6 to (e) 1.0 GPa. The thickness gradient (300-450nm) is highlighted on the left side, while the width gradient (25-44 µm) is shown on the right. The color bar represents the out-of-plane displacement w. It is shown in Fig. 3-33a that w decreases with decreasing film thickness h and stripe width $2b$. This trend can be explained by the fact that both h and $2b$ increase along the (Oy) direction, but $2b$ increases more rapidly than h, leading to a gradual reduction of the h/b. Consequently, σ_c decreases, which results in larger displacements w. This trend is consistent for whatever σ_0, thereby explaining the experimental observation that w locally increases with h and $2b$ (see the yellow contrast in Fig. 3-11c).

Additionally, it is shown that, whatever σ_0, the buckled structure is shaped like a telephone cord, except for σ_0 = 0.6 GPa for which a secondary buckling transition from SS to TCB is observed below a critical thickness (and a critical width) equals to h^* = 364 nm (and $2b^*$ = 32.7 µm). For isotropic stress (or close to), secondary buckling transition from SSB to TCB occurs when $\beta_t = \beta_l \approx 21$ based on The mapping of secondary buckling morphologies proposed by Parry *et al.* [28] . Later, Abbes *et al.* [46] refined this analysis by including the elastic contrast between film and substrate, characterized by the Dundurs' coefficient α_D. For E_s = 2.5 GPa and v_s = 0.37 [12,37], α_D

= 0.97. For such an elastic contrast, secondary TCB is expected under isotropic stress when $\beta_t = \beta_l \approx 23$. Experimentally, we obtain $\beta_t = \beta_l = 24.9$, consistent with Abbes *et al.* diagram [46].

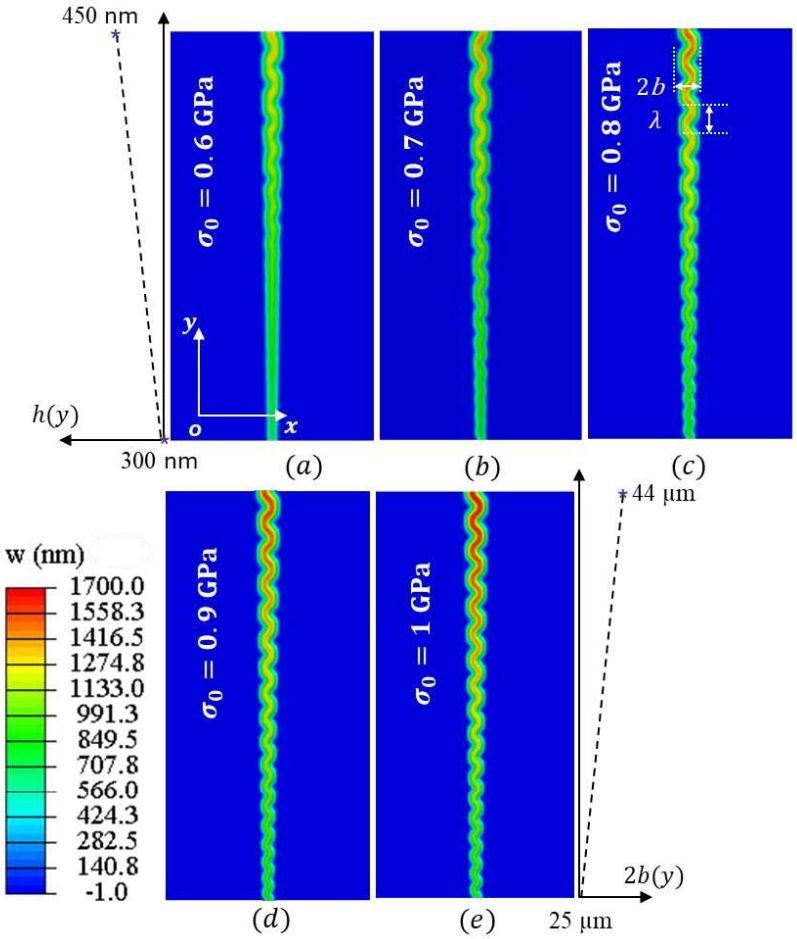

Fig. 3-33: Simulated telephone cordon buckles presented in Fig. 3-12 (Out-of-plane displacement) aligned parallel to the thickness (*resp.* width) gradient $h(y)$ (*resp.* $2b(y)$), under various internal stresses σ_0. (a), (b), (c), and (d) correspond to 0.6, 0.7, 0.8, 0.9 and 1 GPa, respectively. Finite element simulations were performed for a nickel film with Young's modulus E_f = 200 GPa, Poisson's ratio ν_f =0.31.

The maximum heights δ of the TCBs were computed from FEM at σ_0 = 0.8 GPa and were reported in Fig. 3-34a as red circles. The numerical trend agrees qualitatively with the experimental data (red stars), both showing a nearly linear decrease of δ with decreasing thickness $h(y)$. Although the experimental values are systematically higher, this can be attributed to the elastic contrast between the film and substrate. As reported by Parry *et al.* [37], such contrast enhances δ

while reducing the critical stress σ_c. Additional factors, including possible plastic deformation in the Ni film [138] or the influence of the thickness gradient itself [132], may also contribute.

To further investigate this effect, FEM simulations were repeated using the same model as in Fig. 3-32, but with a 3D elastic substrate (C3D8R elements) representing polycarbonate (E_s = 2.5 GPa, ν_s = 0.37 [12,37]). These results, reported as red squares in Fig. 3-34a, show that substrate compliance significantly increases the local height δ. The ratio between heights computed on the elastic and rigid substrates, $\delta_{FEMelastic}/\delta_{FEMrigid}$, remains nearly constant at 1.87 ± 0.03, indicating an 87% increase in δ due to substrate compliance (see Fig. 3-34c). This enhancement is consistent with previous findings for SSBs in homogeneous films [37]. The numerical normalized height $\delta/2b$ is also shown in Fig. 3-34b, including the substrate elasticity effect. Although discrepancies remain - especially for h > 380 nm - the FEM results accounting for substrate compliance exhibit much better quantitative agreement with experiments for thinner films (h < 380 nm). The average values of $\delta/2b$ are approximately 0.063 for the elastic substrate and 0.033 for the rigid substrate, confirming the amplifying effect of compliance.

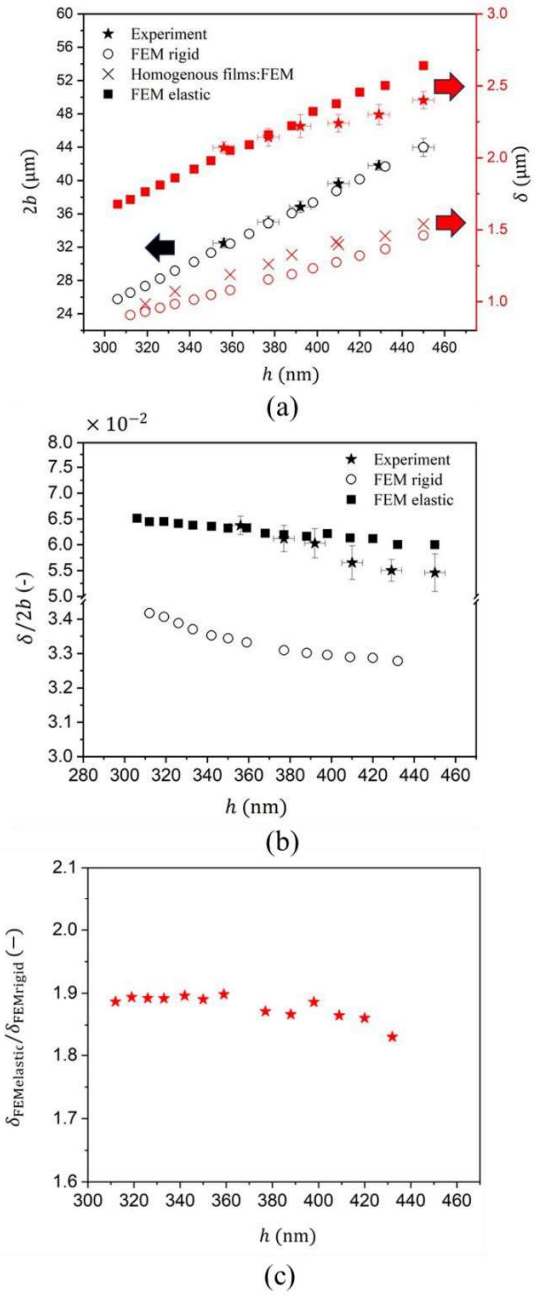

Fig. 3-34: Experimental and FEM morphological parameters of TCB in a film with both thickness and width gradients. (a) Buckle width $2b$ (black; left side) and maximum height δ (red; right side) as a function of the local film thickness h. (b) Normalized maximum height $\delta/2b$ *vs.* h. (c) Computed ratio of local heights $\delta_{\mathrm{FEMelastic}}/\delta_{\mathrm{FEMrigid}}$ *vs.* h. FEM simulations corresponding to a nickel film (E_f = 200 GPa, ν_f = 0.31) on a polycarbonate substrate (E_s = 2.5 GPa, ν_s = 0.37).

Finally, the numerically computed local wavelength λ and normalized wavelength $\lambda/2b$ are presented in Figs. 3-35a and 3-35b, respectively, for various σ_0. In all cases, λ decreases with increasing σ_0 and good agreement with experiments is achieved for σ_0 between 1.0 and 1.3 GPa. It is recalled here that the experimental stress value estimated previously from the curvature Stoney method is associated with a huge uncertainty, explaining as a result such a mismatch. Note that the agreement with experiments can be observed for the whole span of thicknesses values. The normalized wavelength $\lambda/2b$ increases with film thickness and stabilizes above $h \approx 380$ nm, approaching asymptotic values of 1.12, 1.08, 1.05 and 1.02 for $\sigma_0 = 0.8$, 0.9, 1 and 1.3 GPa, respectively - consistent with previous reports for homogeneous films [22,45].

Overall, the FEM simulations successfully capture the key experimental trends in both the height and wavelength of telephone-cord buckles across the full range of film thicknesses and internal stresses. The strong quantitative agreement particularly for $h < 380$ nm demonstrates the robustness of the numerical approach and confirms that accounting for substrate elasticity is essential to accurately reproduce the experimental behavior. In particular, comparison between experimental and numerical values of wavelength λ (or normalized wavelength $\lambda/2b$) can be used to identify the value of the internal stress σ_0 in the film, because of the remarkable consistency over all the span of thicknesses.

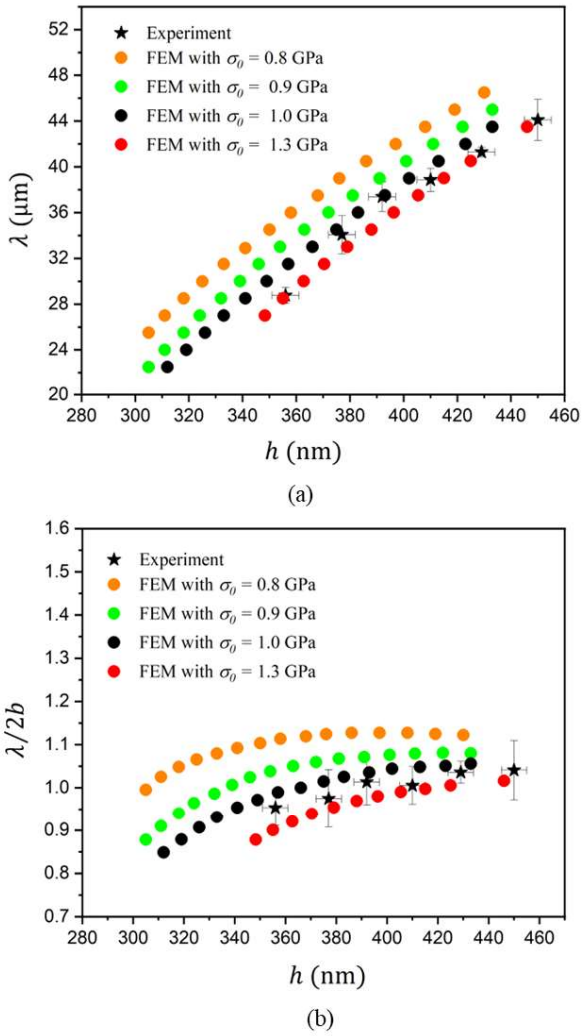

Fig. 3-35: Experimental and FEM evolution of (a) the local wavelength λ and (b) the normalized wavelength $\lambda/2b$ of TCB as a function of the local film thickness h, for various internal stresses σ_0. FEM simulations were performed for a nickel film (E_f = 200 GPa, ν_f = 0.31).

3.6. FEM results of TC buckles perpendicular to the thickness gradient

The influence of the thickness gradient on the morphology of TCBs perpendicular to the gradient direction is shown in Fig. 3-36. The simulations were performed for a nickel film subjected to various isotropic compressive stresses σ_0 (from 1 to 3 GPa). This stress range was selected to ensure that buckling occurs only in the form of TCBs [28,132]. For convenience, only

the FEM snapshots corresponding to σ_0=3 GPa are displayed in Fig. 3-36. Each snapshot corresponds to a h_{max}/h_{min} value, ranging from 1 to 3.3, with h_{max} arbitrary fixed to 150 nm (whereas h_{min} was varied from 150 to 40 nm). Across the full stress range (1 to 3 GPa), TCBs in films with small gradients remain nearly symmetric with respect to their central axis, consistent with the perfectly symmetric morphology expected for homogenous, constant-thickness films. However, as h_{max}/h_{min} increases, a pronounced asymmetry develops, with the buckle skewing laterally toward the thinner side of the film, as shown in Fig. 3-36. This behavior resembles the lateral shift of δ observed for SSBs lying perpendicular to the thickness gradient presented previously in section 3.4. However, here the effect is more spatially localized due to the inherent undulation geometry of TCBs. In addition, increasing h_{max}/h_{min} leads to an increased in the out-of-plane displacements w, in agreement with elastic theory [26]. A lower local thickness reduces the local buckling threshold σ_c (Eq. 3-4), which again results in a larger maximum height δ.

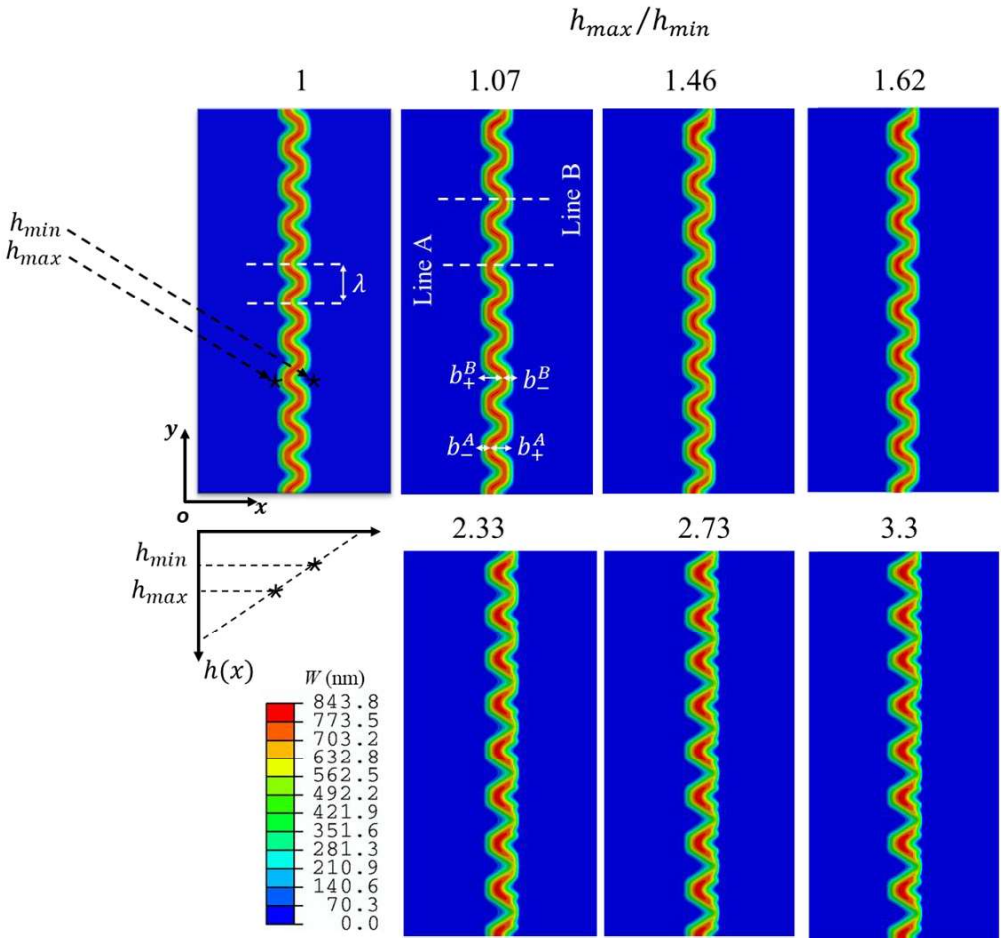

Fig. 3-36: Influence of a thickness gradient $h(x)$ lying along the (Ox) direction and perpendicular to a telephone cord buckle. Out-of-plane displacements with respect to the various thickness gradients (h_{max}/h_{min}). Finite element simulations were performed for a nickel film with Young's modulus E_f = 200 GPa, Poisson's ratio ν_f =0.31, stripe width

$2b$ = 12 µm and isotropic compressive stress σ_0 = 3.0 GPa. The number of sections N along the width is considered to be 40. h_{max} is fixed to 150 nm and h_{min} ranges 150 to 40 nm.

The morphological parameters of TCBs, defined as the edge to peak distances (b_+, b_-), and heights defined as δ_A and δ_B (see the second FEM image in Fig. 3-36) are computed along the section lines A and B, respectively. For each section, the left and right edge to peak distances were determined as b_-^A and b_+^A for line A and b_-^B and b_+^B for line B. Fig. 3-37 compares these morphological parameters for (a) a uniform film and (b) a film with a thickness gradient of h_{max}/h_{min}=2.03. In the uniform case (Fig. 3-37a), the heights in both sections are identical ($\delta_A = \delta_B$), the edge to peak distances as well ($b_-^A = b_-^B$ and $b_+^A = b_+^B$). In contrast, the gradient cases show clear asymmetry. The maximum height along section A exceeds that of section B ($\delta_A > \delta_B$). Both locations of δ_A and δ_B are systematically shifted to small local h. Therefore, the edge to peak distances along section A (b_-^A and b_+^A) becomes close to each other (more symmetrical), while they become far from each other (high asymmetrical) along B. As a result, it is shown that $b_-^A > b_-^B$ and $b_+^A < b_+^B$, this becomes more pronounced as gradient increases, as shown visually in Fig. 3-37.

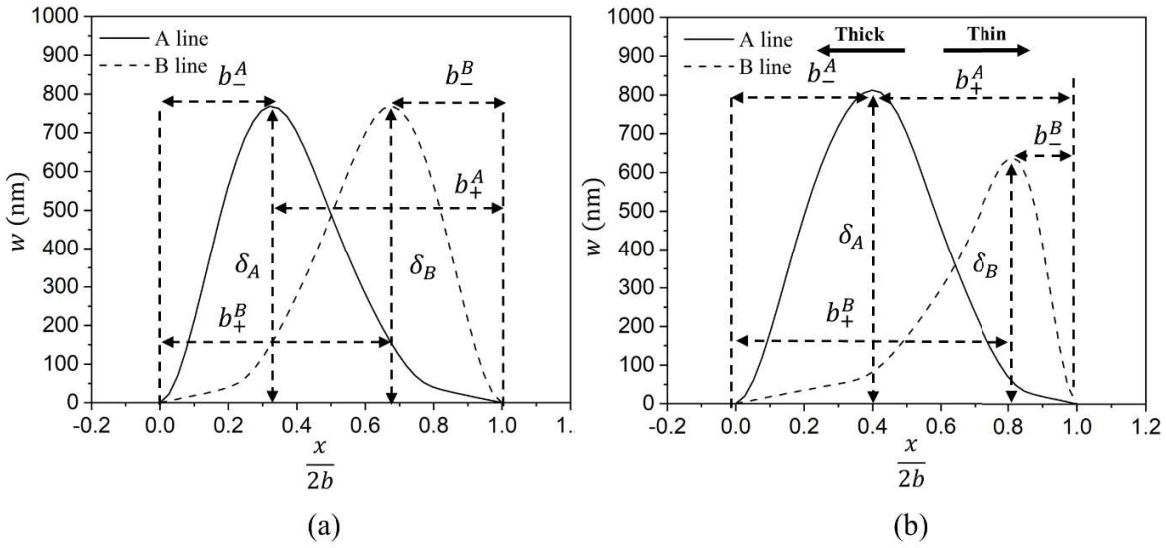

Fig. 3-37: Out-of-plane displacement profiles w *vs*. normalized x to the width $x/2b$ of the TCB in (a) a uniform film and (b) a film exhibiting a thickness gradient of h_{max}/h_{min}=2.03. Finite element simulations were performed for a nickel film with Young's modulus E_f = 200 GPa, Poisson's ratio ν_f =0.31, stripe width $2b$ = 12 µm, h_{max} = 150 nm and isotropic compressive stress σ_0 = 3.0 GPa. The number of sections N along the width is considered to be 40.

The variation of the normalized edges to peak distances ratio b_-/b_+ for section lines A and B with respect to the thickness gradient (h_{max}/h_{min}) for various σ_0 is presented in Fig. 3-38a. For the

homogenous case (h_{max}/h_{min} =1), the ratios along lines A and B are similar. It is equal to 0.66 for σ_0 = 1 GPa and decreases for increasing σ_0 (not shown here). As thickness gradient increases, b_-/b_+ for line A increases, while it decreases for line B, as shown in Fig. 3-38a. This trend is consistent with the asymmetry observed experimentally by Yang *et al.* [51] for TCBs that propagate near and parallel to the edge of the sample. In their study, FEM simulations incorporating a cohesive zone model attributed such behavior to differences in bending stiffness, elastic modulus or thickness variations. Note however that, in the present work, the TCBs are confined within a fixed stripe width, excluding the possibility of buckling-driven delamination. To quantify the relative asymmetry with respect to the gradient between lines A and B, we defined the parameter $\gamma = (b_-/b_+)_A/(b_-/b_+)_B$. Fig. 3-38b shows that γ increases monotonically with h_{max}/h_{min} for whatever σ_0, indicating that the asymmetry is only primarily influenced by the gradient. The best fit to our data yields γ=1.018$(h_{max}/h_{min})^{1.5}$. This relationship highlights the strong influence of the gradient on the in-plane TCB asymmetry. The monotonic increase of γ with respect to the thickness gradient offers a way to experimentally determine this gradient from buckles profile characteristics.

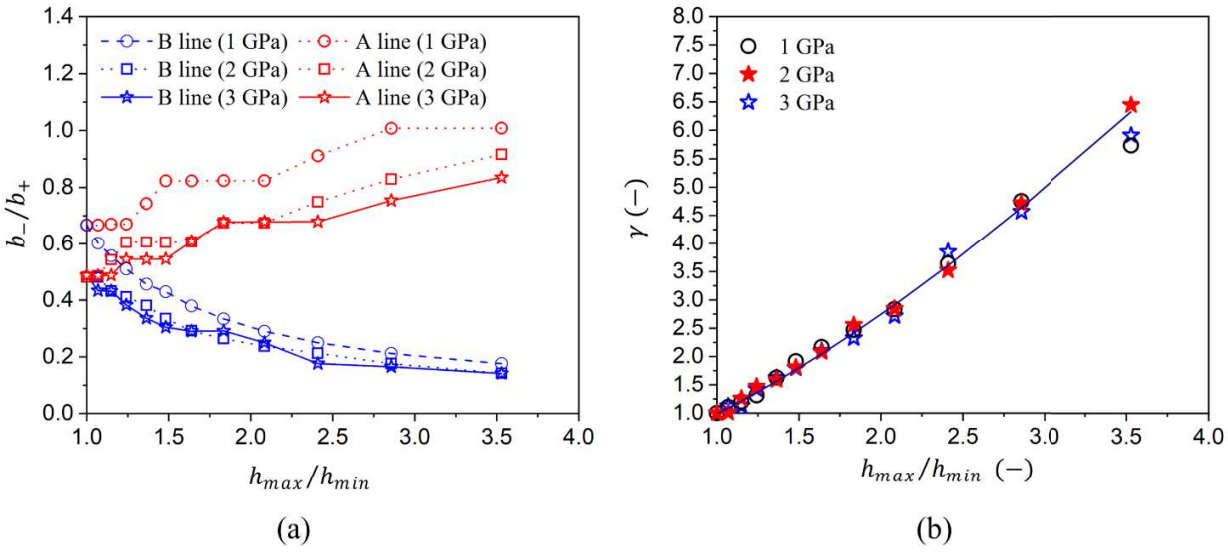

Fig. 3-38: Influence of a thickness gradient $h(x)$ perpendicular to a TCB lying along the (Oy) direction for various h_{max}/h_{min} and σ_0. (a) Dependence of the normalized edge-to-peak distance ratio b_-/b_+ along line A and B, with respect to the thickness gradient h_{max}/h_{min}. (b) Degree of asymmetry γ of the TCB along sections A and B, defined as $\gamma = (b_+/b_-)_A/(b_+/b_-)_B$, with respect to the thickness gradient. Finite element simulations were performed for a nickel film with Young's modulus E_f = 200 GPa, Poisson's ratio ν_f =0.31, stripe width $2b$ = 12 µm, h_{max} = 150 nm. The number of sections N along the width is considered to be 40.

In addition to the lateral asymmetry γ of the TCB, we examined the vertical asymmetry of the out-of-plane-displacement along lines A and B. A parameter Δ was introduced to quantify their relative difference in height ($2b$):

$$\Delta = \frac{\delta_A - \delta_B}{\delta_{ave}}, \tag{3-17}$$

with $\delta_{ave} = (\delta_A + \delta_B)/2$ the average height. Fig. 3-39 shows Δ as a function of h_{max}/h_{min}, for various σ_0. Δ increases monotonically with gradient, for whatever σ_0. At larger gradients, a slight divergence however appears, with higher σ_0 producing marginally larger values (difference of only 4% between 1 and 3 GPa). This suggests that the dependence on stress is weak compared to the dominant influence of the gradient, although elevated stress can modestly amplify vertical asymmetry at steep gradients. Like in the previous case, it seems possible to associate a level of Δ to a given thickness gradient on a one-to-one basis.

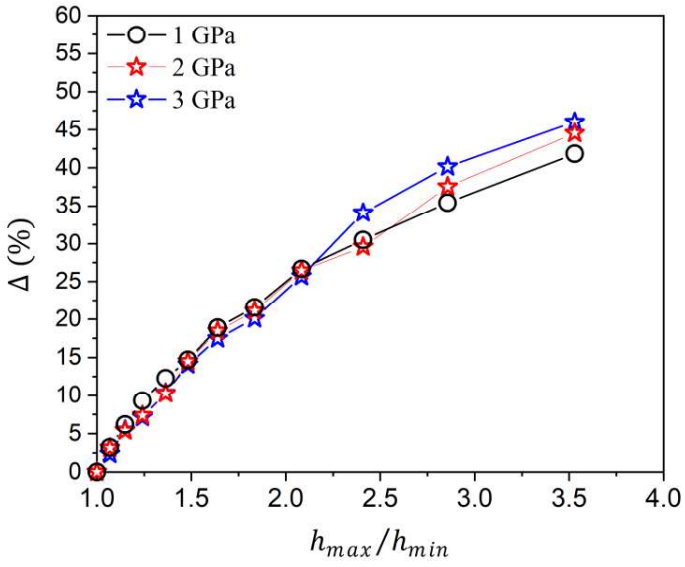

Fig. 3-39: Influence of a thickness gradient $h(x)$ perpendicular to a telephone cord buckle lying along the (Oy) direction. Relative height difference Δ with respect to the thickness gradient h_{max}/h_{min} for various σ_0. Finite element simulations were performed for a nickel film with Young's modulus E_f = 200 GPa, Poisson's ratio ν_f =0.31, stripe width $2b$ = 12 µm, h_{max} = 150 nm. The number of sections N along the width is considered to be 40.

Fig. 3-40 presents γ in (a) and Δ in (b) as a function of gradient for various values of width ($2b$). Both γ and Δ seem to be not dependent on $2b$. Overall, these results confirm that the thickness

gradient along the buckle width is the primary parameter that controls both the lateral and the vertical asymmetry in TCBs. The buckle profile consistently skews toward the thinner region, reinforcing the prior results drawn for SSBs and highlighting the important role of the thickness variations in post-buckling morphologies of delaminated thin films. It is worth noting that the asymmetry of TCBs can somehow depend on the internal stress σ_0 in non-confined stripe widths. Yang *et al*. [51] demonstrated that increasing σ_0 enhances both γ and Δ. This can be attributed to the tendency of TCBs to expand laterally, particularly in thicker regions of the film, where the higher stored strain energy promotes buckling-driven delamination. In conclusion, the monotonic relationship between the parameters Δ and γ and the thickness gradient offers a potential diagnostic tool: local gradient values can be inferred directly from measured buckle profiles. Such an approach could prove valuable for non-destructive characterization of thin films in microelectronics, flexible devices, or coatings, where local stress and thickness variations critically affect performance and reliability.

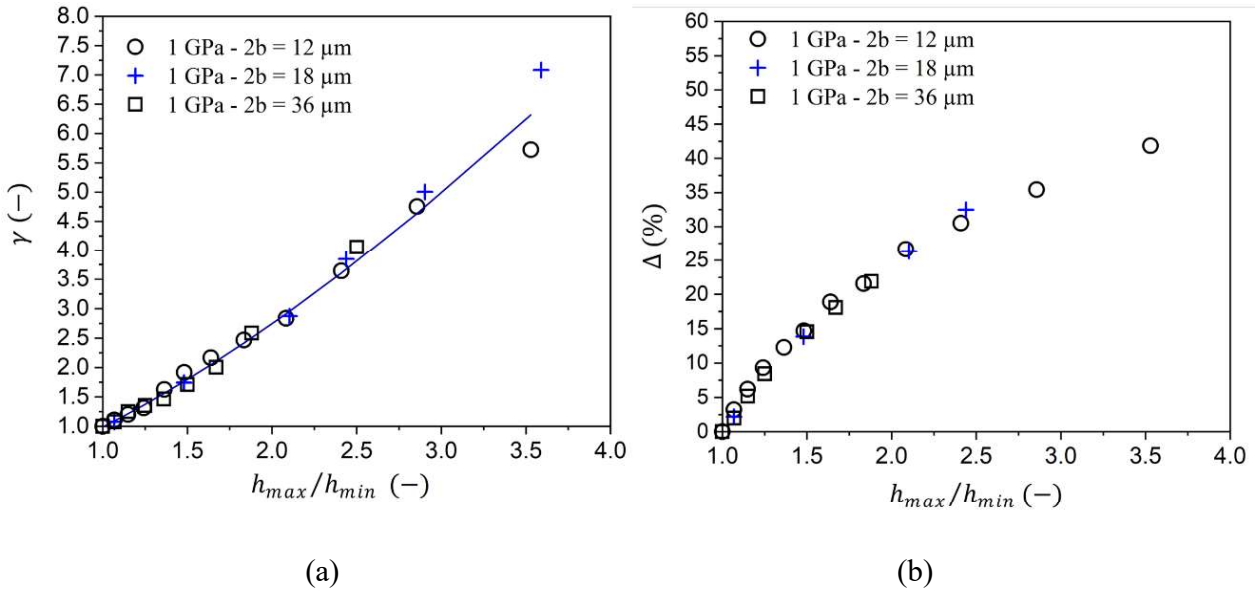

(a) (b)

Fig. 3-40: (a) Relative height difference Δ and (b) degree of asymmetry γ of the TC buckle, with respect to the thickness gradient h_{max}/h_{min}.. Finite element simulations were performed for a nickel film with Young's modulus E_f = 200 GPa, Poisson's ratio ν_f =0.31, h_{max} = 150 nm and isotropic compressive stress σ_0 = 1 GPa. The number of sections N along the width are considered to be 40, 60 and 120 for $2b$ = 12, 18 and 36 µm, respectively.

3.7. Conclusion

In this chapter, we investigated the effect of well-controlled-thickness gradients on the buckling morphologies of thin films through a combined experimental and finite element method (FEM) approach within the framework of elastic plate theory. Nickel films with well-defined thickness gradients were deposited by ion beam sputtering and subjected to uniaxial compression using a Deben microtest stage, inducing mainly straight-sided buckles (SSBs). Upon the release of the external stress, the SSBs evolved into telephone-cord buckles (TCBs). The resulting buckles were characterized using optical microscopy, white-light interferometry and atomic force microscopy (AFM). Simulations using the finite elements method were conducted to systematically investigate the influence of different thickness gradients on buckling morphologies. The numerical results are presented, compared to the experimental results and discussed.

Our experiments showed that the maximum height δ of SSBs aligned parallel to the thickness gradient decreases with increasing the local thickness h for a given width $2b$, and the equilibrium profiles of the buckles can be fitted as a sinusoidal shape, consistent with Foppl-Von Karman (Fvk) elastic plate theory. However, the measured δ values were systematically higher than those predicted by classical elastic plate theory, which we attributed to the elastic compliance of the polycarbonate substrate. SSBs were observed to preferentially propagate toward thicker regions as the external compressive stress increased, which confirmed that this observation is within a static approach since propagating toward thicker regions in the gradient requires increasing the compressive stress to overcome the critical stress. When SSB profiles were extracted along directions misaligned with respect to the gradient direction, the thickness variations across the buckle width resulted in asymmetric profiles, characterized by a shift of the maximum height toward the thinner side and unequal edge to peak distances (b_+, b_-). Telephone cord buckles (TCBs) lying along the thickness gradient were also analyzed. For constant width, the TCB wavelength λ increases with local thickness, consistent with the higher elastic energy stored in thicker regions. In TCB exhibiting a width gradient, both λ and the delaminated width $2b$ decrease with decreasing local thickness.

FEM simulations were performed to study SSBs and TCBs oriented both parallel and perpendicular to the thickness gradient. For SSBs aligned with the gradient, FEM confirmed the decrease of δ with increasing h, consistent with both experiments and theory. However, FEM results underestimated the measured heights. Refinning the FEM results by accounting for the elastic contrast significantly improved the agreement. The onset buckling stress σ_c^{TG} in films exhibiting thickness gradient was found to depend on both the gradient slope α and the delaminated width $2b$. For a given $2b$, increasing α led to larger deviations of σ_c^{TG} from the analytical critical stress σ_c for homogenous films. Similarly, for a fixed α, decreasing the width $2b$ amplified this deviation. Nevertheless, far from the onset buckling, the Föppl–von Kármán (FvK) plate theory still accurately described the post-buckling equilibrium profiles. In particular, the thinnest regions of the film followed the FvK solution from the onset of buckling as far as the internal stress is

sufficiently larger compared to σ_c. For SSBs oriented perpendicular to the gradient, FEM captured the observed asymmetry, showing that the ratio b_+/b_- increases monotonically with the thickness ratio h_{max}/h_{min}, and is largely independent of internal stress and buckle width. These results demonstrate that the buckle asymmetry can serve as a non-destructive diagnostic tool for determining local thickness gradients in thin films. Similarly, FEM simulations of TCBs lying parallel to the gradient in films with constant width reproduced experimental observations, in particular: λ increases with both local thickness and delaminated width $2b$. In films with a thickness gradient, depending on the gradient slope and width, three morphologies were observed simultaneously: TCBs at low thickness, SSBs at intermediate thickness, and flat regions at higher thickness. Hence, the SS to TC buckles transition depends strongly on local thickness, while the thickness gradient does not alter the known criterion for secondary buckling. For TCBs lying parallel to the gradient with variable delaminated width, λ was found to increase with both h and $2b$, confirming that the SS to TC buckles transition depends primarily on the ratio h/b rather than h alone. Finally, FEM analyses of TCBs oriented perpendicular to the gradient revealed pronounced lateral and vertical asymmetries resulting from the thickness variation across the buckle width. In particular, the geometric descriptors Δ and γ increase monotonically with the gradient while remaining independent of stress and width, confirming their potential as non-destructive tools to infer local gradient values from measured buckle profiles in microelectronics, flexible devices, or coatings.

Overall, this chapter establishes a clear relationship between local thickness variations and buckle morphology, demonstrating that controlled gradients systematically influence SSB and TCB characteristics. The dual combined experimental and numerical approach not only validates elastic plate theory in gradient films but also provides novel tools for non-destructive characterization of local film properties. These insights lay the foundation for the subsequent chapter, where cohesive zone modeling will be used to explore the role of interfacial toughness and mode mixity on buckling-driven delamination.

3.8. Résumé en Français

Ce chapitre explore l'influence des gradients d'épaisseur bien contrôlés sur les morphologies de flambage dans des films de nickel déposés sur des substrats en polycarbonate (PC), en se concentrant à la fois sur les rides droites (SSBs) et les cloques en forme de « corde de téléphone » (TC). Les films de nickel ont été soumis à une compression uniaxiale à l'aide d'une cellule de microtest Deben, ce qui a induit une variété de morphologies de flambage, principalement des cloques SS et TC. Après le relâchement de la contrainte externe appliquée au substrat, les morphologies résultantes ont été caractérisées par microscopie optique, interférométrie à lumière blanche et microscopie à force atomique. Afin d'explorer systématiquement l'influence de différents gradients d'épaisseur sur les structures de flambage, des simulations par la méthode des éléments finis (FEM) ont été réalisées. Les résultats numériques sont présentés, comparés aux observations expérimentales et discutés en détail.

I. Ride droite (SSB) dans un film avec gradient d'épaisseur

- ***Ride parallèle au gradient***

Fig. 3-41 présente une ride droite (*straight sided buckle*) dans un film de nickel présentant un gradient d'épaisseur montré sur le côté gauche dans (a), sur la droite sont indiqués les localisations où les mesures AFM ont été effectuées. Les résultats expérimentaux montrent que la hauteur de la ride diminue avec l'épaisseur, ce qui est également confirmé par simulation des éléments finis (FEM), comme le montre la Fig. 3-41b. Le calcul FEM prenant en compte l'élasticité du substrat améliore l'accord avec les expériences (voir les symboles triangles et étoiles).

Le gradient d'épaisseur (α) a un impact significatif sur le flambage: près du seuil critique, la hauteur maximale (δ) mesurée s'écarte de la théorie classique de FvK, surtout pour les fortes épaisseurs. L'augmentation de l'épaisseur décale fortement le seuil critique (σ_c^{TG}), permettant même un flambage non prédit par la théorie pour les plus grands gradients d'épaisseur, comme montre la Fig. 3-42. Ces résultats démontrent que l'effet du gradient affecte à la fois la contrainte critique (σ_c) et la hauteur (δ), d'autant plus que le gradient est abrupt.

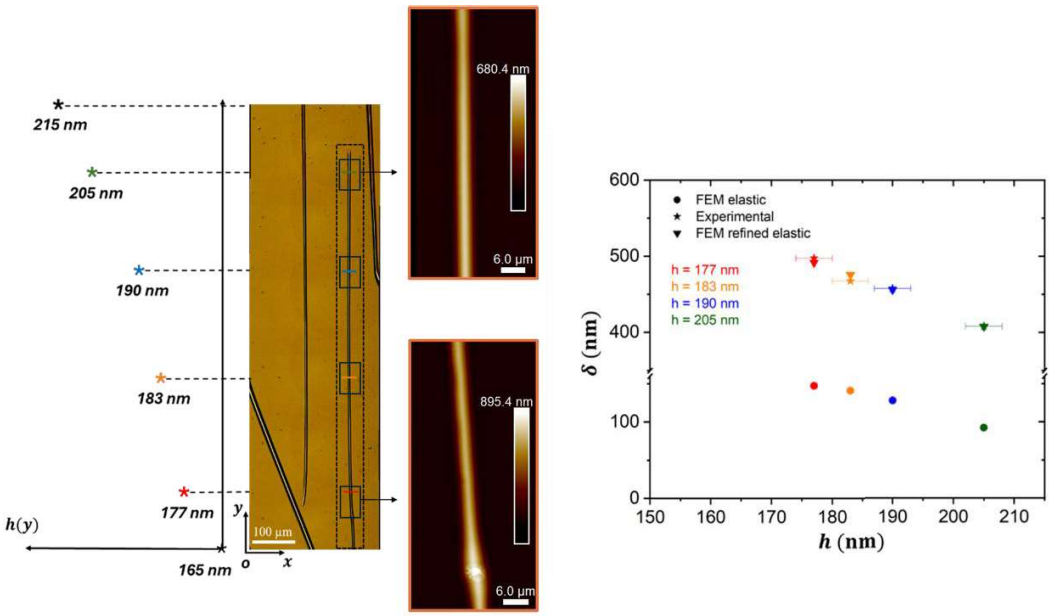

Fig. 3-41: (a) Caractérisation optique et AFM du film de nickel SSB2 présentant un gradient d'épaisseur. (b) Hauteur maximale de la ride (δ) en fonction de l'épaisseur locale (h). Les résultats expérimentaux et les simulations FEM confirment que δ diminue lorsque h augmente. La prise en compte de l'élasticité du substrat améliore l'accord avec l'expérience.

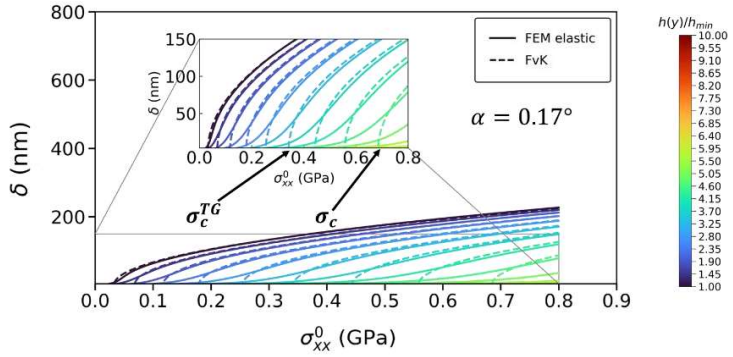

Fig. 3-42: L'évolution de la hauteur maximale δ d'une ride droite en fonction de la contrainte interne σ_{xx}^0, pour différentes épaisseurs locales normalisées $h(y)/h_{min}$.

- ***Ride perpendiculaire au gradient***

La ride droite observée expérimentalement (voir Fig. 3-43a, b) présente une asymétrie inhabituelle au niveau de sa ligne médiane ($b_+ \neq b_-$). Cette asymétrie est ensuite étudiée plus en

détail dans des simulations par éléments finis (FEM) (voir Fig. 3-43c, d), lesquelles révèlent que la variation d'épaisseur du film le long du profil de la ride droite (SS) est la cause principale de cette asymétrie.

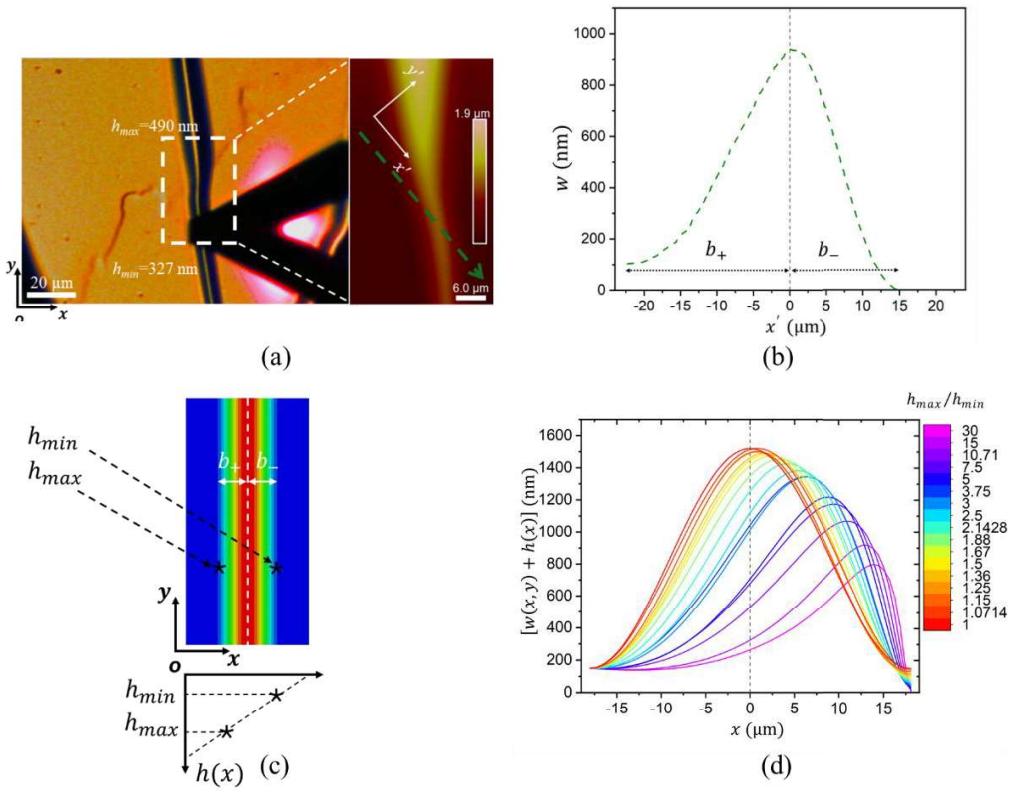

Fig. 3-43: (a) Caractérisation optique et AFM d'une ride droite présentant un gradient d'épaisseur. (b) Profil de déplacement hors plan w le long de l'axe x', mesuré à un angle de 40° par rapport à la direction du gradient (Ox). (c) Déplacement hors plan schématisé en fonction du gradient d'épaisseur. Ce diagramme représente la variation du déplacement hors plan en fonction du profil d'épaisseur. (d) Profils d'équilibre de la ride (SS buckle), montrant la variation du déplacement ($w(x, y) + h(x)$) en fonction du rapport de gradient h_{max}/h_{min}.

II. Cordon téléphonique dans un gradient d'épaisseur

- ***Cordon téléphonique parallèle au gradient***

Expérimentalement, nous avons observé des cloques en cordon téléphonique (TCB) se propageant parallèlement au gradient d'épaisseur. Contrairement aux films homogènes, la longueur

d'onde λ de la TCB diminue avec la diminution de l'épaisseur dans le gradient (Fig. 3-44a), un comportement confirmé par les simulations FEM (Fig. 3-43b). Nous avons également montré que λ augmente avec l'épaisseur (h) et la largeur ($2b$). Dans les films à gradient, nous observons à la fois la TCB et la SSB (ride droite), en raison de la variation d'épaisseur. L'analyse révèle que la transition de la SSB à la TCB se produit lorsque $\sigma_{SS\text{-}TC}/\sigma_c \approx 6.6$.

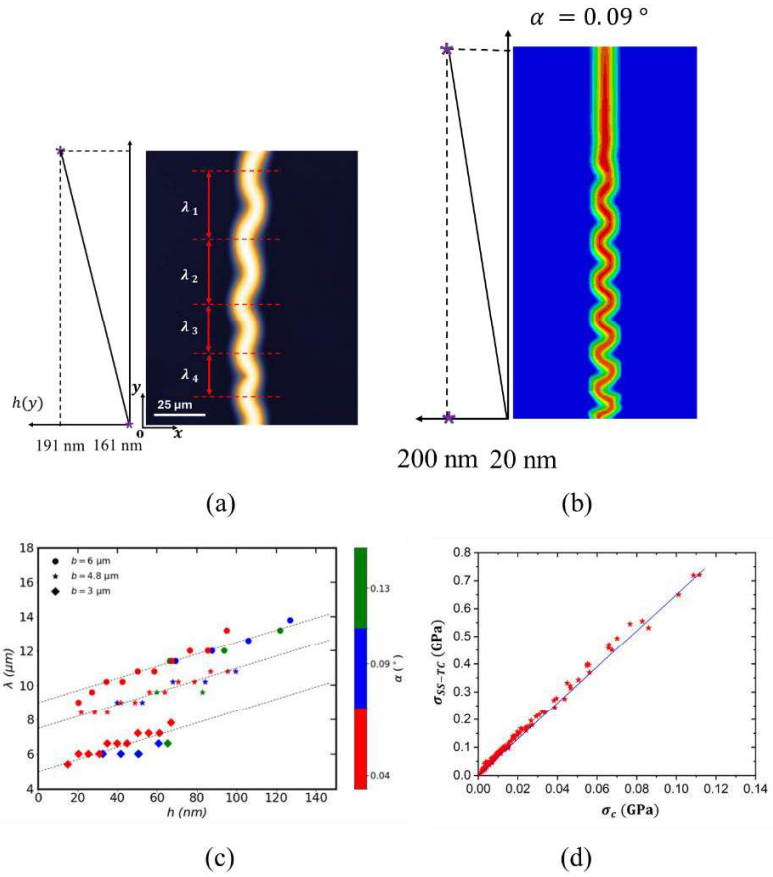

Fig. 3-44: (a) Structure de flambage en cordon téléphonique (*Telephone cord buckling*) de largeur constante $2b$ = 19.38 µm orientée parallèlement au gradient d'épaisseur le long de la direction (Oy). (b) Déplacement hors plan schématisé en fonction du gradient d'épaisseur. (c) Longueur d'onde (λ) d'une cloque en cordon téléphonique en fonction de l'épaisseur locale $h(y)$ pour différentes demi-largeurs b et différentes pentes de gradient α. (d) Contrainte critique pour la transition de la cloque à rides droits au cordon téléphonique dans un gradient d'épaisseur, $\sigma_{SS\text{-}TC}$ en fonction de σ_c.

- ***Cordon téléphonique perpendiculaire au gradient***

Les analyses par éléments finis (FEM) des TCB orientées perpendiculairement au gradient ont révélé des asymétries latérales et verticales prononcées, caractérisées respectivement par $\gamma = (b_+/b_-)_A/(b_+/b_-)_B$ et $\Delta = 2.(\delta_A - \delta_B)/(\delta_A + \delta_B)$, et résultant de la variation d'épaisseur à travers la largeur de la cloque. En particulier, il est démontré que les deux paramètres Δ et γ augmentent de manière monotone avec le gradient, indépendamment de la contrainte interne et de la largeur, comme le montre la Fig. 3-45. Par conséquent, les simulations FEM démontrent que les deux paramètres (Δ, γ) offrent également des outils non destructifs pour évaluer les valeurs de gradient locales à partir des profils des cloques mesurés dans les revêtements.

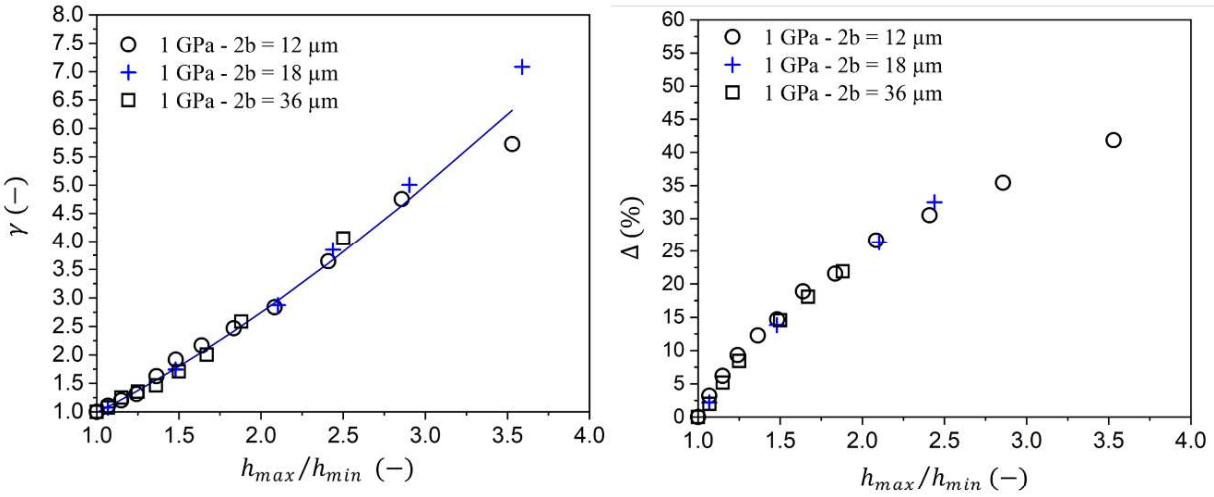

Fig. 3-45: (a) Différence de hauteur relative (Δ) et (b) degré d'asymétrie (γ) de la cloque en cordon téléphonique (TCB), en fonction du gradient d'épaisseur h_{max}/h_{min}.

Ce chapitre établit une relation claire entre les variations d'épaisseur locales et la morphologie du flambage, démontrant que les gradients contrôlés influencent systématiquement les caractéristiques des ride droites (SSB) et des flambages en cordon téléphonique (TCB). L'approche combinée, expérimentale et numérique, valide non seulement la théorie des plaques élastiques dans les films à gradient, mais fournit également de nouveaux outils pour la caractérisation non destructive des propriétés locales du film. Ces découvertes constituent la base du chapitre suivant, dans lequel la modélisation en zone cohésive sera utilisée pour explorer le rôle de la ténacité interfaciale et du mixite modale sur le délaminage induit par le flambage.

Chapter 4

4. Buckling driven delamination in nickel film within a dynamic approach

This chapter investigates buckling-driven delamination in nickel thin films with well-controlled thickness gradients, analyzed within the framework of elastic plate theory. Building on Chapter 3, in which the morphology of buckling structures in gradient films has been characterized within a static approach, we now focus on the mechanics of buckle propagation. We begin by briefly discussing the spontaneous buckles that appear immediately after deposition and their time evolution, highlighting the complexity of uncontrolled delamination. The main focus will be given to straights-sided blisters (SSBs). SSBs are mainly triggered by straining the substrate under controlled incremental loading. This controlled approach enables a systematic study of the SSBs growth and provides the experimental basis for quantitative mechanical analysis. Next, we formulate the mechanical problem of buckling-driven delamination and solve it numerically using finite element method (FEM) simulations with a cohesive zone model (CZM). The model is validated on constant-thickness films against analytical predictions and then applied to reproduce the experimentally observed propagation of SSBs in gradient films. The primary objective is to determine the interfacial toughness and its dependence on mode mixity. Unlike most previous studies which assume a fixed value of the parameter η used to define the sensitivity of the toughness to mode II (commonly set to 0.7), we propose a quantitative strategy to extract this parameter directly by fitting FEM–CZM simulations to controlled SSBs propagation. Additionally, mode mixity of SSB lying perpendicular to the thickness gradient will be explored. The results of this chapter were the origin of one paper submitted to "Materialia journal" [148].

4.1. Spontaneous buckling in homogenous films

To motivate the investigation of controlled buckle propagation in thin films with well-defined thickness gradients, we first illustrate the phenomenon of uncontrolled, spontaneous buckling in homogenous metallic films deposited on PC and Si substrates. Fig. 4-1 shows optical images of 940 nm nickel thick film on a PC substrate, observed after (a) three days and (b) six-months of deposition. Various buckling morphologies can be observed, including SSBs, TCBs and secondary buckling branches. Over time, these buckles grow, expand in size and evolve, as shown in Fig. 4-1 indicating continuous stress-driven delamination.

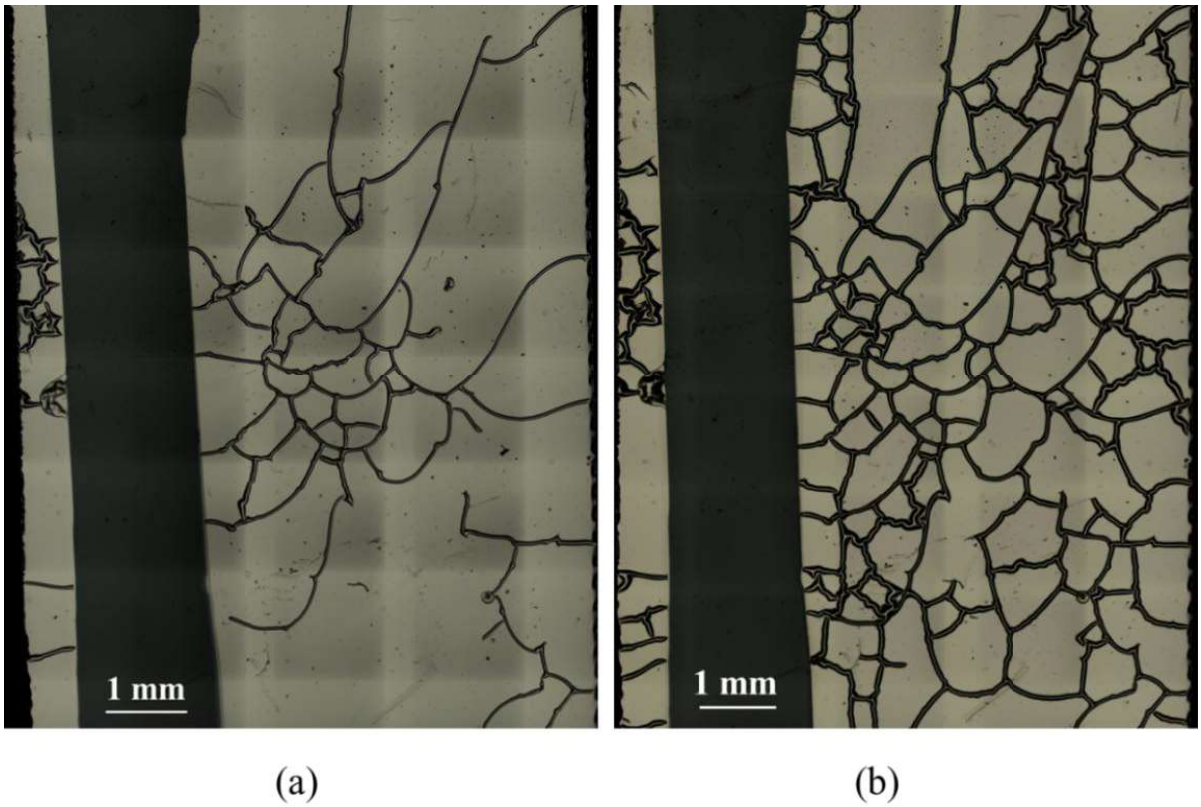

Fig. 4-1: Optical image of spontaneous buckles in Ni (940 nm)/PC. (a) Three days and (b) six months after deposition.

Spontaneous buckling was also observed after a few days of deposition in molybdenum (Mo) thin films, as shown Fig. 4-2. This figure presents an optical image of 300 nm Mo film deposited on a 100 μm silicon (Si) wafer. Spontaneous TCBs appear almost immediately after deposition, often expanding over large distances and crossing the entire film. This behavior has been also reported in SiAlNx films by Yu *et al.* [149]. Such uncontrolled buckles may severely compromise the functionality and performance of the film [8,9].

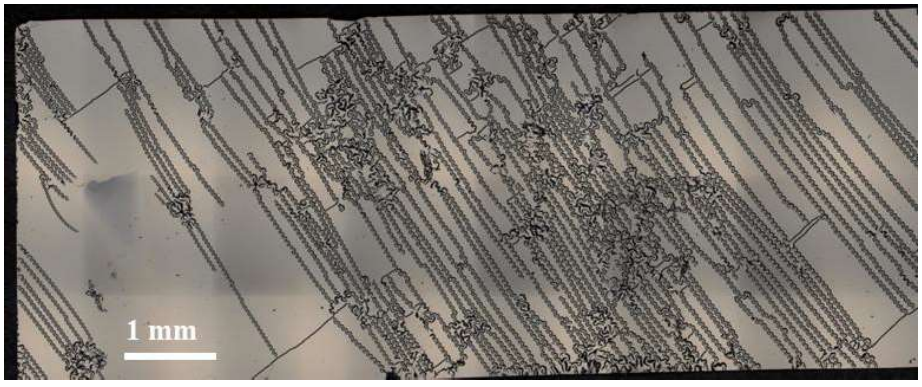

Fig. 4-2: Optical image of spontaneous buckles, mainly TCBs in Mo (300nm)/Si(100µm), taken shortly after few days of deposition.

From an industrial perspective, limiting such spontaneous, buckling driven delamination is critical to ensure film performance and reliability. Although the formations of spontaneous buckles is uncontrolled, valuable mechanical properties such as Young's modulus, internal stress and interfacial adhesion can be assessed from their morphology [22,26,36,42]. To address this, we introduce a thickness gradient strategy that allows precise control of the elastic energy stored in the film and enables a systematic study of buckle propagation under well-defined conditions. This approach also enables the identification of interfacial toughness properties in film/substrate systems.

4.2. Experimental results of SS buckles in films lying parallel to the thickness gradient

To explore how interfacial toughness controls buckle propagation in nickel films exhibiting thickness gradients, we performed stepwise uniaxial compression experiments on Ni/PC films with well-controlled thickness gradients. Sample C (Fig. 4-3a) was selected for this study. The thickness gradient was characterized by white interferometric optical microscopy and is schematically represented on the left side of Fig. 4-3a, ranging from 580 nm (thick end) to 10 nm (thin end) along the (*Oy*) direction. Some spontaneous buckles were observed in the as-deposited sample due to residual stress (see the circle dashed lines in Fig. 4-3a). However, they were randomly oriented and not suitable for quantitative analysis.

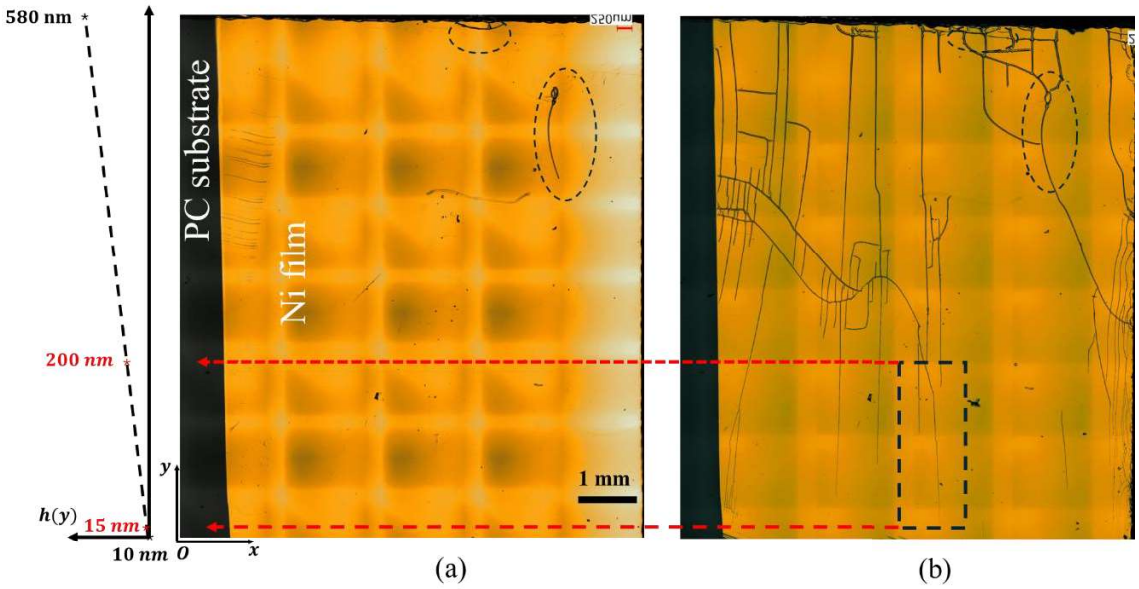

Fig. 4-3: Optical images of sample C. (a) as deposited and (b) after final loading. The thickness gradient is shown on the left side, with h varying from 10 to 580nm along the (Oy) direction.

To initiate and control buckle propagation along the thickness gradient direction (Oy direction), the PC substrate was incrementally strained along (Ox) using a Deben microtest stage. Assuming a full strain transfer at the film/substrate interface, the in-plane stresses in the film are given by [135]:

$$\sigma_{xx}^{f} = \Delta\sigma_{xx}^{f} + \sigma_0, \text{ with } \Delta\sigma_{xx}^{f} = \frac{E_f}{E_s}\frac{1-\nu_f\nu_s}{1-\nu_f^2}\sigma_a^s, \tag{4-1}$$

and

$$\sigma_{yy}^{f} = \Delta\sigma_{yy}^{f} + \sigma_0, \text{ with } \Delta\sigma_{yy}^{f} = \frac{E_f}{E_s}\frac{\nu_f-\nu_s}{1-\nu_f^2}\sigma_a^s, \tag{4-2}$$

where σ_a^s is the applied stress. Note that σ_{jj}^f (j=x, y) is the total stress in the film accounting for the internal stress σ_0 and the transferred stress $\Delta\sigma_{jj}^f$, while the j represents the direction of the stress. The elastic properties of the Ni film and PC substrate were given by E_f = 200 GPa, ν_f = 0.31 and E_s = 2.5 GPa, ν_s = 0.37, respectively [12,37]. Buckles were mainly characterized by AFM (Dimension Icon, Bruker), performed *in situ* at each loading step, labeled as S_i with i=1 to 6 corresponding to the step number. Fig. 4-4 shows the stress-strain curve, where the red and black

curves represent the in-plane stress components σ_{xx}^f and σ_{yy}^f, respectively. The vertical dashed lines represent the applied stress in the film, σ_{xx}^f and σ_{yy}^f, for each S_i. The stress-strain curve reveals elastic hysteresis typical of viscoelastic (PC) materials [131] and confirms recoverable elastic deformation up to 3.5 % strain. The values of the in-plane stress components of each loading step S_i are reported in table 4-1. Note that the induced compressive stress in the film along the (Ox) direction $\Delta\sigma_{xx}^f$, was multiplied by 1.77 after straining, while the one along the (Oy) is only reduced by 12% by the Poisson effect with respect to the internal stress σ_0.

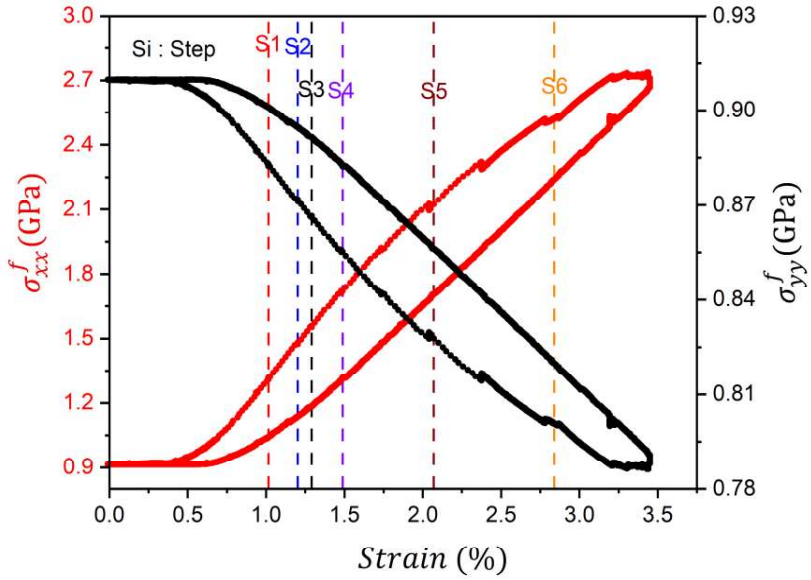

Fig. 4-4: Stress-strain curve of the PC substrate. S_i represents the loading step i (i varies from 1 to 6), reporting in table 4-1.

Loading steps	Critical thickness h^* of buckle arrest (nm)	Transversal stress in the film σ_{xx}^f (GPa)	Longitudinal stress in the film σ_{yy}^f (GPa)	Maximum height δ_{front} (nm)	Buckle width $2b_{front}$ (µm)
S_1	153	1.31	0.88	669	6.6
S_2	108	1.47	0.87	372	5.3
S_3	88	1.56	0.86	359	4.3
S_4	60	1.71	0.85	300	3.62
S_5	38	2.11	0.83	263	3.3
S_6	25	2.52	0.80	160	2.9

Table 4-1: Experimental morphological and mechanical characteristics of the straight-sided buckle propagating in the thickness gradient direction shown in Fig. 4-5. The internal stress in the film σ_0=0.91 GPa.

Fig. 4-3b shows the sample after the final loading step. As expected from a mechanical point of view [28,32,132,135–137], several induced SSBs are lying perpendicular to the compression axis (*Ox*), *i.e.* downward through the thickness gradient along the direction (*Oy*). Additionally, as shown in Fig. 4-3b, SSBs tend to nucleate in thicker regions of the film, where their buckle width is larger compared to the very thin regions. The SSB located within the dashed rectangle was the one of interest and was tracked throughout each loading step S_i. This SSB is shown in Fig. 4-5 at the final loading stage. The thickness gradient is shown on the left side of the optical image, ranging from the thicker upper part (170 nm) down to 10 nm on the lower part and lying along the (O*y*) direction. Initially, during the first loading S_1 (σ_{xx}^f = 1.31 GPa, σ_{yy}^f = 0.88 GPa), the buckle propagated from its initial position at h = 200 nm to a critical thickness, labelled h^*=153 nm, at which the buckle arrests. We define the buckle arrest as the point at which the buckle front no longer advances, even when maintaining constant loading. This process was repeated for steps S_2 to S_6, resulting in successive arrest positions at h^*=108, 88, 60, 38 and 25 nm, respectively. These buckle front arrest locations characterized by h^* and shown as horizontal-colored lines provide a direct experimental basis for assessing the interfacial fracture toughness. For convenience, only the AFM images of the buckle front at S_1 and S_4 are presented on the right side, illustrating the characteristic half-spherical morphology of the SSB front [26]. It is worth noting that, even at loadings beyond S_6 (σ_{xx}^f = 2.7 GPa), no further propagation occurs, confirming that the stored elastic energy is no more sufficient to overcome the interface toughness at such a very low film thickness. This behavior results from the competition between the elastic energy release rate and

the interfacial toughness [26]. As the SSB propagates down, toward the thinner regions, the stored elastic energy is reduced, the energy release rate as well. The buckle propagation becomes consequently impossible.

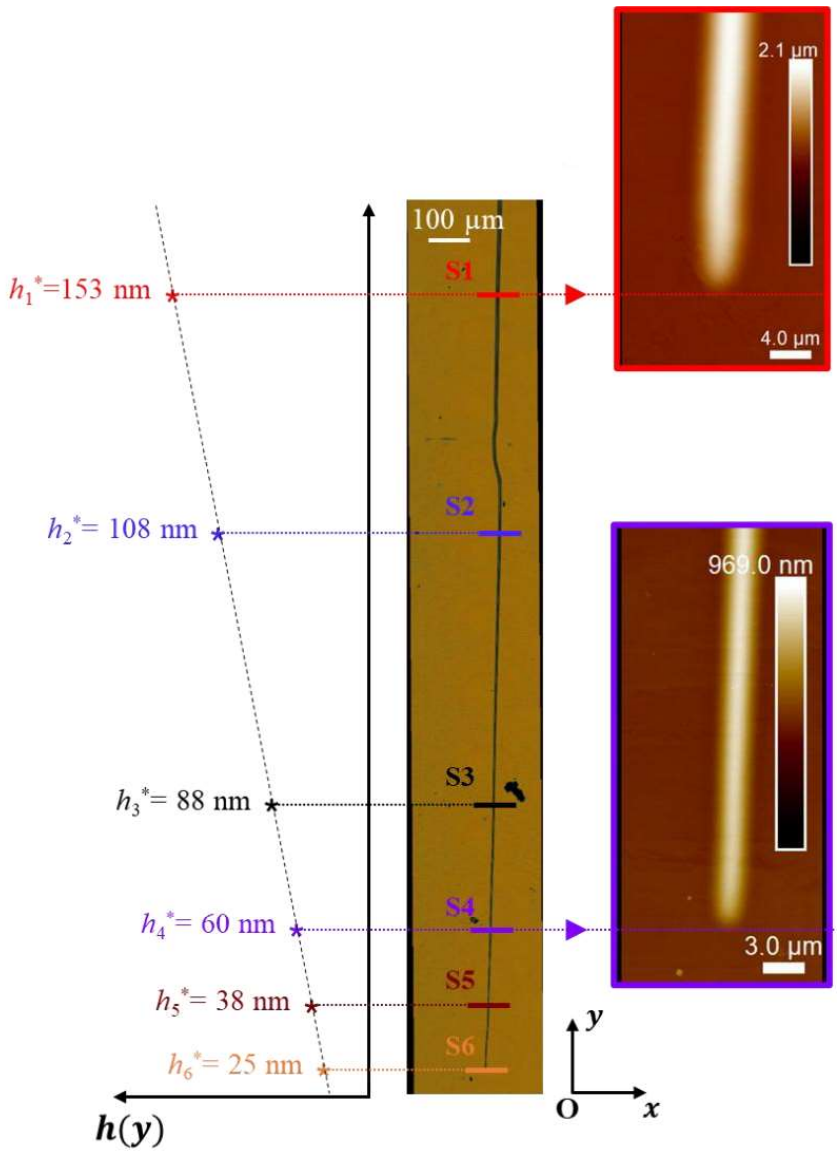

Fig. 4-5: Straight-sided buckle in a nickel film deposited on a polycarbonate substrate propagating along a thickness gradient lying along the (*Oy*) direction. The optical image in the middle was obtained at the final loading stage. The thickness gradient is shown on the left side, ranging from the thicker upper part down to the thinner lower. Six loading increments were performed by uniaxial compression of the substrate along the (*Ox*) axis. The critical thickness of arrest of the buckle is reported for each loading step S_i as horizontal color lines. For convenience, only the atomic force microscopy investigations of the loading steps S_1 and S_4 are presented on the right side.

To quantitatively compare the buckle morphology at each loading steps S_i, we extracted the buckle width ($2b$) and height (δ) of the SSB from AFM measurements. The experimental values of $2b$ and δ are summarized in Table 4-1. It can be clearly seen that both the maximum height δ and width $2b$ decrease as the film becomes thinner consistently with reduced elastic energy available to drive the interfacial delamination. δ and $2b$ were plotted as a function of G_0, where G_0 is the elastic strain energy per unit area stored in the unbuckled given by Eq. (1-89) as [26]:

$$G_0 = \frac{h_f}{2E_f}\left[\sigma_{xx}^2 + \sigma_{yy}^2 - 2\nu_f\sigma_{xx}\sigma_{yy} + 2(1+\nu_f)\sigma_{xy}^2\right], \tag{4-3}$$

As shown in Fig. 4-6, both δ and $2b$ decrease monotonically with G_0, reflecting the reduction in elastic energy available to drive delamination [26]. However, this is only a qualitive explanation since we cannot estimate neither the interfacial toughness nor the energy stored in the elastic film on compliant substrate, such as PC.

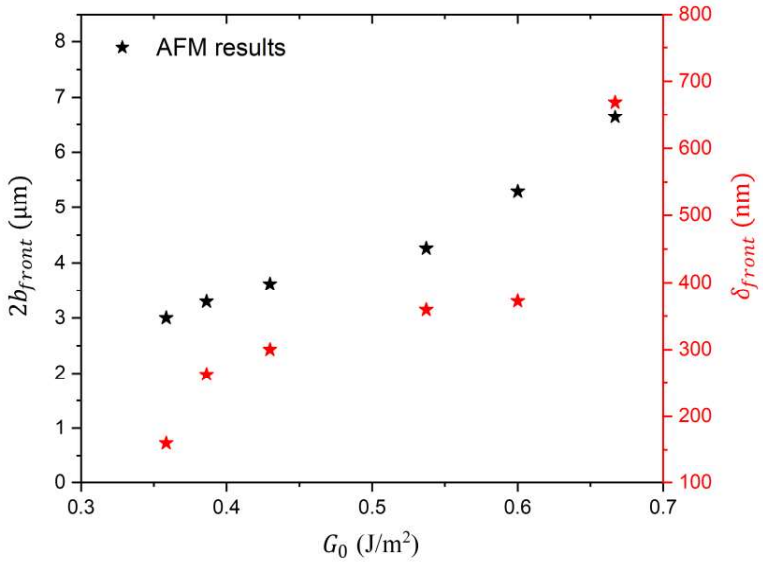

Fig. 4-6: Morphological parameters of the straight-sided buckle extracted from AFM investigation (table 4-1). The front width $2b_{front}$ is plotted on the left and the front height δ_{front} on the right, as a function of the elastic strain energy stored in the unbuckled plate per unit area G_0.

A similar analysis was conducted on sample D, following six incremental loading steps. Fig. 4-7 shows one SSB at the final state of loading. The thickness gradient is shown on the left side of

the optical image ranging from 200 nm down to approximately 30 nm on the lower part and lying along the (O*y*) direction. For convenience, only the AFM images of the buckle front at S_1 and S_5 are presented on the right side. Table 4-2 lists the experimental values of σ_{xx}^f, σ_{yy}^f, h^*, δ, and $2b$ for each step. Here, $\Delta\sigma_{xx}^f$ increases by a factor of 2.2, while $\Delta\sigma_{yy}^f$ decreases by ≈ 15% with respect to σ_0. Both δ and $2b$ decrease with decreasing thickness, confirming the reproducibility of the observed propagation-arrest behavior.

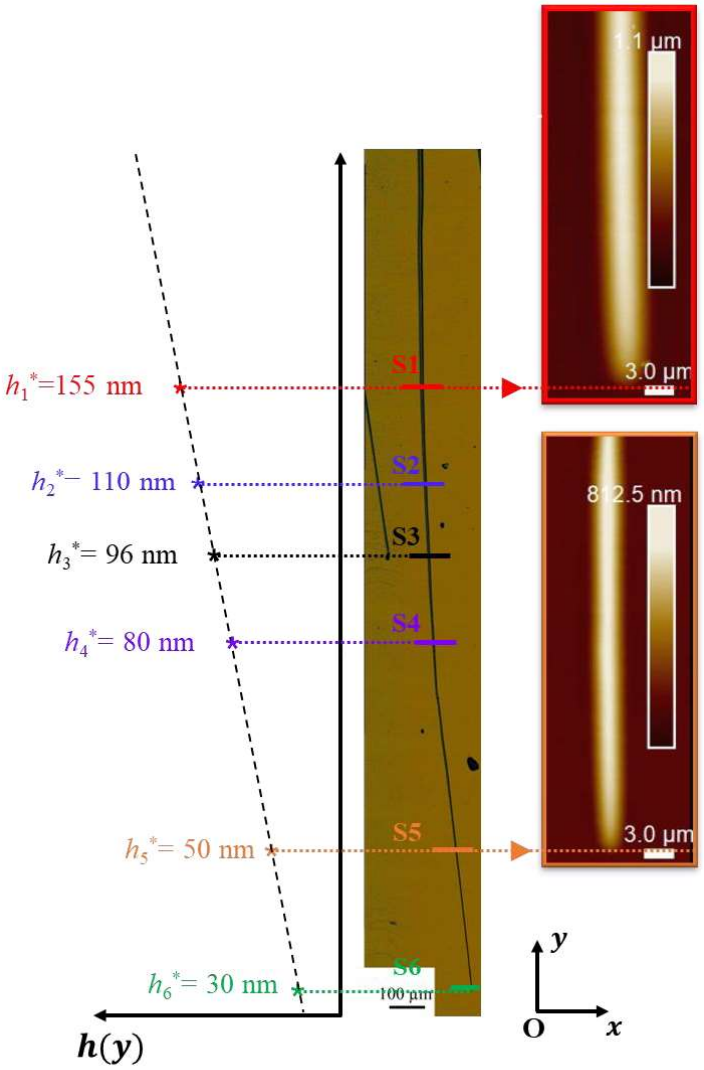

Fig. 4-7: Straight-sided buckle in a nickel film deposited on a polycarbonate substrate propagating along a thickness gradient lying along the (*Oy*) direction. The optical image in the middle was obtained at the final loading stage. The thickness gradient is shown on the left side, ranging from the thicker upper part down to the thinner lower. Seven loading increments were performed by uniaxial compression of the substrate along the (*Ox*) axis. The critical thickness of arrest of the buckle is reported for each loading step S_i as horizontal color lines. For convenience, only the atomic force microscopy investigations of the loading steps S_1 and S_5 are presented on the right side.

Loading steps	Critical thickness h^* of buckle arrest (nm)	Transversal stress in the film σ_{xx}^f (GPa)	Longitudinal stress in the film σ_{yy}^f (GPa)	Maximum height δ_{front} (nm)	Buckle width $2b_{front}$ (μm)
S_1	155	1.21	0.78	506	7.3
S_2	110	1.33	0.775	437	6.3
S_3	96	1.41	0.77	400	6
S_4	80	1.56	0.76	380	5.3
S_5	50	2.0	0.73	340	4.7
S_6	30	2.6	0.69	240	2.8

Table 4-2: Experimental morphological and mechanical characteristics of the straight-sided buckle propagating in the thickness gradient shown in Fig. 4-7. The internal stress in the film σ_0=0.81±0.1 GPa.

In conclusion, stepwise uniaxial compression experiments were performed on a nickel film deposited on a polycarbonate substrate exhibiting a well-defined thickness gradient along the (*Oy*) direction, from 580 nm to 10 nm. The propagation of SSBs was controlled and tracked at each loading step using a Deben microtest stage and characterized *in situ* with AFM. It is shown that as the applied stress increased from 1.31 GPa to 2.52 GPa, SSB propagated from a local thickness of h=200 nm toward thinner regions until arrest, with h^* decreasing from 153 nm to 25 nm. Both buckle width ($2b$) and maximum height (δ) decreased consistently with the reduced elastic energy available to drive delamination. Similar behavior was observed on another sample, confirming the reproducibility of the propagation arrest process. Arrest occurs when the local energy release rate at the front becomes lower than the interfacial fracture energy, providing a qualitative understanding of how to measure interfacial fracture in gradient-thickness films.

4.3. Mechanical numerical modeling

The mechanical model used for buckling-driven delamination of thin films exhibiting thickness gradient will be described in this section starting from description of the model, such the boundary

conditions, loading methods and dimensions, to the implementation of the cohesive zone model in our simulations.

4.3.1. Implementation of the numerical model

The three-dimensional (x, y, z) geometrical model is illustrated in Fig. 4-8. It consists of a parallelepiped with dimensions $L_x = 60$ µm and $L_y = 120$ µm, representing the nickel film deposited on a polycarbonate (PC) substrate. The film has a thickness gradient along the (Oy) direction resulting in a thickness $h(y)$. The model is composed of two parts: a film and its associated substrate. The Nickel film is modeled as a 2D elastic plate with a Young's modulus of $E_f = 200$ GPa and a Poisson's ratio $\nu_f = 0.31$ [12,37,146]. The substrate is treated as a 3D elastic body representing polycarbonate, with a Young's modulus $E_s = 2.5$ GPa and a Poisson's ratio $\nu_s = 0.37$ [12,37]. The film is meshed using four-node plane strain elements with reduced integration (S4R), while the substrate is constituted of eight-node linear brick elements (C3D8R). The substrate thickness is chosen sufficiently large ($h_s = 12$ µm).

At a given point $M(x, y, z)$, the displacement and rotation vectors are respectively denoted: $\vec{u} = u\vec{e}_x + v\vec{e}_y + w\vec{e}_z$ and $\vec{\theta} = \theta_x\vec{e}_x + \theta_y\vec{e}_y + \theta_z\vec{e}_z$. Boundary conditions for the film are applied only along its edges: the nodes at $x = 0$ and $x = L_x$ are constrained with $u = 0$, $\theta_y = 0$ and $\theta_z = 0$. Similarly, the nodes along the lines at $y = 0$ and $y = L_y$ are constrained with $v = 0$, $\theta_x = 0$ and $\theta_z = 0$. The substrate is subjected to symmetric boundary conditions along the (Ox) and (Oy) faces; its bottom substrate is fixed in the out-of-plane direction (w=0). To model the thickness gradient observed experimentally along the (Oy) direction, $h(y)$ was defined using the same equation used previously in Eq. (3-6) in sub-section 3.4.1.

In order to simulate the buckling-driven delamination, adhesion between the film and the substrate is taken into account by introducing a surface based-cohesive model. The chosen law is a linear-softening model, which assumes a linear relationship between the traction $\vec{T} = T_n\vec{e}_n + T_t\vec{e}_t$ and the opening displacement $\vec{\delta} = \delta_n\vec{e}_n + \delta_t\vec{e}_t$, where $\vec{e}_n$ and $\vec{e}_t$ denote the unit vector of the normal and tangential direction to the surface, respectively. The T versus δ relationship is represented in Fig. 4-8b, as described in Eq. (1-81). Before reaching the peak traction, the traction-separation law is linear and reversible, with $T_n = K_n\,\delta_n$ and $T_t = K_t\,\delta_t$.. K_n and K_t represent the normal and shear interface stiffness, respectively.

A quadratic damage initiation criterion is selected:

$$\left(\frac{T_n}{T_n^0}\right)^2 + \left(\frac{T_t}{T_t^0}\right)^2 = 1, \tag{4-4}$$

where T_n^0 and T_t^0 are the pure mode I (resp. pure mode II) peak traction parameters. The values of T_n and T_t obtained when the criterion is fulfilled (*i.e.* at damage initiation) are respectively denoted T_n^i and T_t^i. The mode-mixity-dependent fracture energy $G_C(\psi)$, which represents the total energy

required for interface fracture (see Fig. 4-8c), is assumed to depend on the mode mixity angle ψ according to the Hutchinson and Suo formula [26]:

$$G_C(\psi) = G_{IC}\left(1 + tan^2(\eta\psi)\right), \text{ with } tan(\psi) = \frac{T_t^i}{T_n^i}, \tag{4-5}$$

where $G_C(\psi=0°)=G_{IC}$ and $G_C(\psi=90°)=G_{IIC}$ are the mode I and II interfacial toughness, respectively. The non-dimensional parameter $\eta \in [0\text{-}1]$ controls sensitivity to mode mixity: values near zero imply weak dependence, while values near unity indicate a strong dependence.

Once the peak traction is reached, a linear softening takes place, resulting in decreasing the traction, as illustrated in Fig. Fig. 4-8b. The softening is managed by a stiffness reduction by the factor (*1-d*) where *d* can be interpreted as a damage variable, starting at 0 and reaching 1 at complete separation.

All nodes of the film are bonded to the substrate through this cohesive law, except for those located in a predefined delaminated area of size $l_x = l_y = 12$ µm, which are left free to buckle. This area is necessary for initiation of buckling driven delamination. To prevent interpenetration of the film into the substrate, a unilateral hard contact condition $w(x, y) \geq 0$ is applied. This constraint improves convergence and numerical stability. To mimic the experimental stress components (see Table 4-1), we use the expressions of the thermoelastic and the thermal loading (see Eqs. 3-10, 3-11, 3-12).

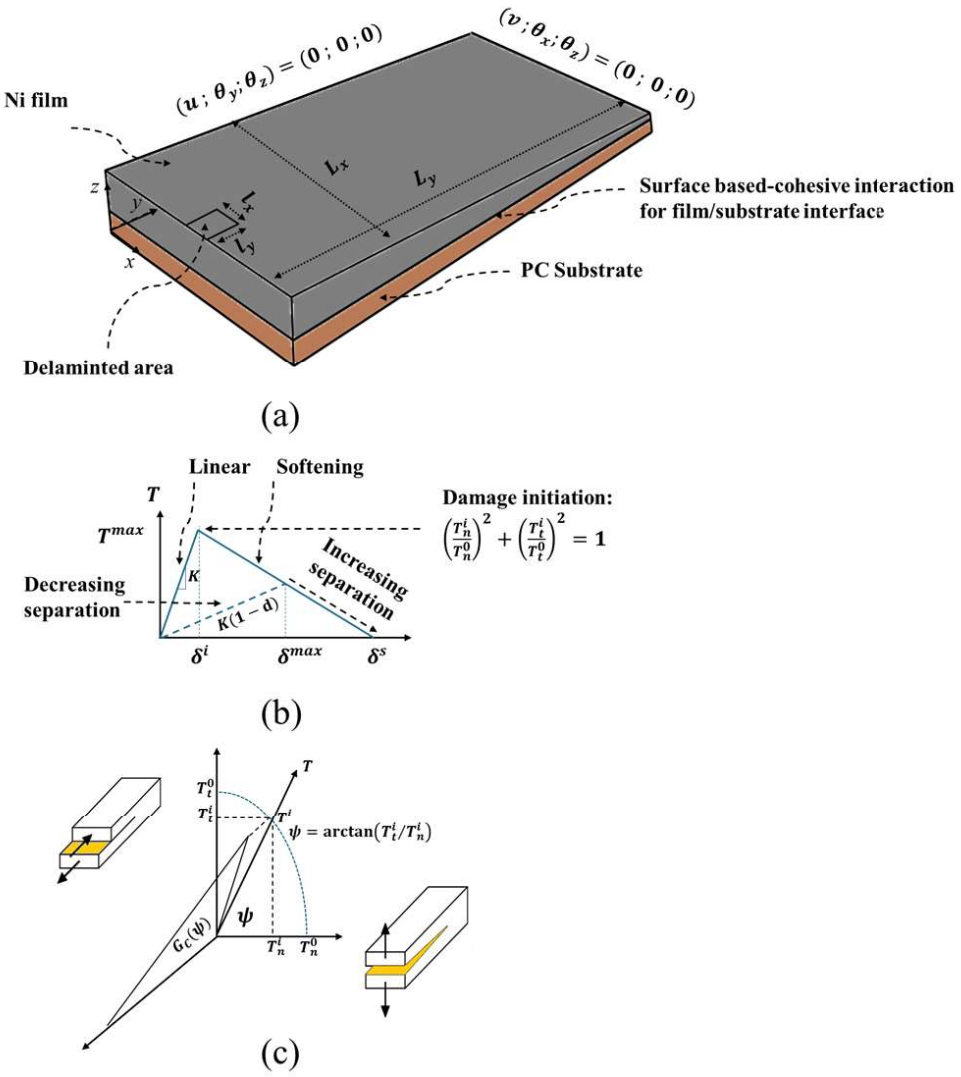

Fig. 4-8: (a) Schematic illustration of the 3D geometrical model illustrating the variation of thickness of the Ni film along the *Oy* direction. (b) Bilinear traction-separation law used for modeling interfacial damage between the film and substrate. (c) Mode-mixity dependent interfacial toughness $G_c(\psi)$, representing the total energy required for interface fracture.

Buckling initiation is triggered by applying a small initial out-of-plane shift of the nodes (geometrical imperfection (Eq. 3-13)) in the delaminated area. Buckling-driven delamination is an inherently dynamic process involving nonlinear geometry and cohesive failure; therefore, a dynamic explicit scheme is employed. Although dynamic solvers are commonly used, special care must be taken to ensure that the simulation is carried out in a quasi-static framework and that the kinetic energy remains negligible compared to the strain energy throughout the analysis to prevent non-physical effects. To perform the simulations in a quasi-static framework, the loading is set to increase progressively (smooth amplitude) from the initial state at 0 to a predefined value σ_0,

reached at time t_i, while σ_o remains constant above t_i. Additionally, a small viscous pressure is applied to the top surface of the film to damp high frequencies dynamic oscillations without introducing artificial energy. Throughout the simulations, the total energy components are monitored to ensure physical accuracy and reproducibility of real experimental conditions. In all simulations reported here, the time conditions are arbitrarily set to $t_i = 2$ ms and $t_f = 80$ ms.

The cohesive law parameters are chosen as follows:

- For the damage initiation, the maximum traction components are set to T_n^0=18MPa, T_t^0=39MPa, unless otherwise specified.
- The normal and shear stiffness are chosen as K_n=K_t=1.0×10^8 MPa/mm. Hence, they are sufficiently high to ensure computational stability and to maintain perfect bonding until damage initiation.

Note that the value of T_n^0 is consistent with an interfacial separation of the order of the maximum film thickness where the SSB was initiated (see discussion in Fig. 4-5), $\delta^s \sim h_{max}$= 200 nm. T_n^0 can be estimated using the relationship $T_n^0=2G_{IC}/\delta^s$ [150], where G_{IC} values for metal-polymer interfaces are of several J/m^2 [151].

4.3.2. FEM validation against analytical model

To validate the FEM mechanical model, we first consider a homogenous nickel film of thickness $h_f = 200$ nm deposited on a rigid substrate, under uniaxial compression stress $\sigma_{xx}^f = 1.213$ GPa ($\sigma_{yy}^f = 0$ GPa). The cohesive interface at film/substrate interface is modeled using a bilinear traction-separation law with the damage initiation parameters described previously and a mixed-mode toughness $G_C(\psi)$ following the Hutchinson–Suo law (Eq. 4-5), with mode-mixity parameter $\eta = 0.9$. According to elastic plate theory (Eq. 1-54), this results in a critical buckling stress $\sigma_c = \sigma_{xx}^f/6$.

Fig. 4-9 illustrates the time evolution of key field variables: the out-of-plane displacement w, the scalar damage variable d, the stored elastic energy per unit surface G^* and the mode mixity angle ψ for two mode I interfacial toughness: (a) $G_{IC} = 0.8$ J/m^2 and (b) $G_{IC} = 0.3$ J/m^2, at two time steps: t_i (residual stress σ_0 is reached) and t_f (damage or propagation under constant load). The defect region is highlighted with dashed white squares.

For $G_{IC} = 0.8$ J/m^2, a SSB forms at the defect zone once σ_c is reached, in agreement with FvK [26]. At t_i the interface begins to degrade (d>0), indicating that the initiation criteria is met. However, the buckle does not propagate between t_i and t_f. To explain this, the elastic strain energy stored in the unbuckled plate per unit area is calculated from Eq. (4-3), giving an analytical value of $G_0 = 0.735$ J/m^2, which is below $G_{IC} = 0.8$ J/m^2, explaining the arrest, consistent with analytical predictions [26]. Additionally, we computed G^* at different times (t_i, t_f), as shown in Fig. 4-10. The local elastic energy stored G^* in the bonded film matches perfectly the calculated analytical

value G_0. In addition, the local energy at the buckle front is significantly higher than in the unbuckled film, confirming high stress at the crack tip, in agreement with prior studies [12,26].

At the lateral edges of the buckle, ψ reaches 90°, corresponding to a pure mode II. Under such conditions, the interfacial toughness G_C ($\psi = 90°$) becomes significantly higher, reinforcing lateral stabilization and preventing sideways propagation. In contrast, ψ at the buckle front is around 24°, indicating strong mode I contribution. Since $G_0 < G_C(\psi)$ at the front, propagation is energetically unfavorable [26,69].

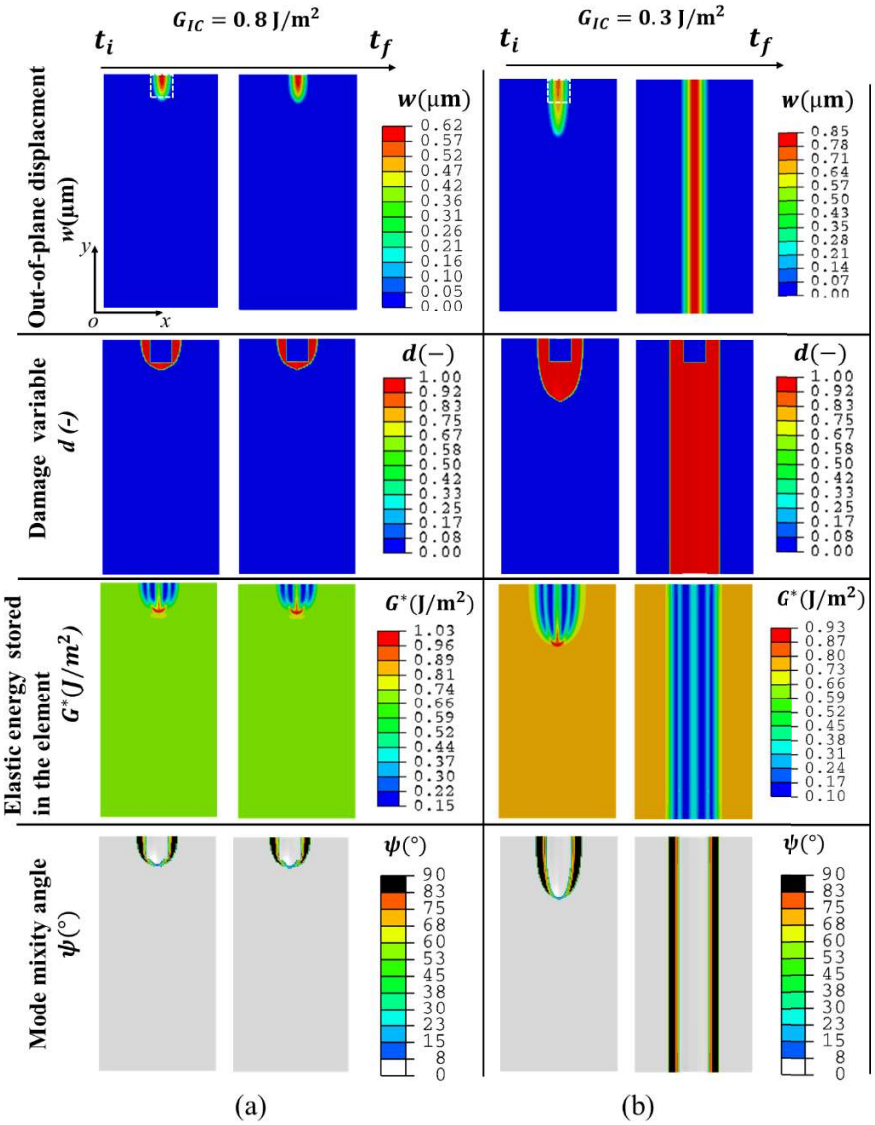

Fig. 4-9: Comparison of the SS buckle evolution for interfacial toughness G_{IC} (a) = 0.8 J/m² and G_{IC} (b) = 0.3 J/m². An initial defect of square geometry of length l_x = 12 µm is highlighted by a square white dashed line. Out-of-plane displacement w, scalar damage variable d, elastic energy stored in the element G^*(J/m²) and mode mixity angle ψ(°) obtained for a Ni film on a rigid substrate (h_f = 200 nm, E_f = 200 GPa, ν_f = 0.31, σ_{xx}^f = 1.213

GPa, σ_{yy}^{f} = 0 GPa, T_n^0 = 18 MPa, T_t^0 = 39 MPa, η = 0.9, t_i = 0.002 s, t_f = 0.008 s). The time evolution is shown in each row, from the initial time t_i, where σ_o is initially reached up to t_f, the end of the simulation.

For the lower toughness G_{IC} = 0.3 J/m^2, the simulation shows clear buckle propagation beyond the defect at t_i, confirmed by the damage variable d. The buckle propagates in steady state along the length of the film in uniform shape. G_0 remains the same since it only depends on film thickness, material properties and residual stress. Therefore, in this case $G_0 > G_{IC}$, allowing the delamination and buckle propagation to occur. At the buckle front, high energy concentration is observed, confirming the stress near the front is higher than far from the buckle. Regardless, the interfacial toughness G_{IC} in our FEM simulations, the sides of the SS buckle remain stable due to ψ = 90°, which increases the local interfacial toughness $G_C(\psi)$, despite the lower base G_{IC} value.

4.3.3. Impact of substrate compliance

To assess the effect of substrate compliance, simulations were repeated for a nickel film on a PC substrate. The elastic mismatch is characterized by the Dundurs' parameter α_D (Eq.1-64) that takes a value of α_D = 0.975 for Ni/PC system. Fig. 4-10 presents FEM results of field variables (w, d, G, ψ) for both toughness (a) G_{IC} = 0.8 J/m^2 and (b) 0.3 J/m^2. In contrast to the rigid substrate. The out-of-plane displacement w increases significantly, particularly at t_f. Additionally, even at G_{IC} = 0.8 J/m^2, propagation occurs, showing that compliance increase the energy release rate for delamination, as reported in the literatures [34–36]. At t_i, the stored energy G^* in the bonded region far from the buckle matches the analytical value G_0 = 0.735 J/m^2. However, as propagation proceeds at t_f, G^* in the bonded film drops significantly and no longer matches the G_0 value. This energy reduction may be attributed to the substrate deformation and the absorption of some of the stored energy. ψ shows a strong mode I contribution at the front, while a strong mode II contribution is observed along the sides. The contrast between the rigid and compliant substates clearly shows that compliance leads to lower values of ψ along the edges and enhances buckling-driven delamination.

These findings validate the FEM mechanical model for both rigid and compliant substrates, highlighting that accounting for the PC substrate is necessary for realistic simulations of thickness gradient films. Simulations on rigid substrates can lead to inaccurate interpretation, as supported by studies of Zak *et al.* [14,15], Boijoux *et al.* [92], Cotterell *et al.* [35], Hutchinson *et al.* [26,36]. The question that arises now is whether this uniform propagation in width and height behavior will still hold in the case of films with a thickness gradient, or whether new instability patterns will emerge. This will be addressed in the next section.

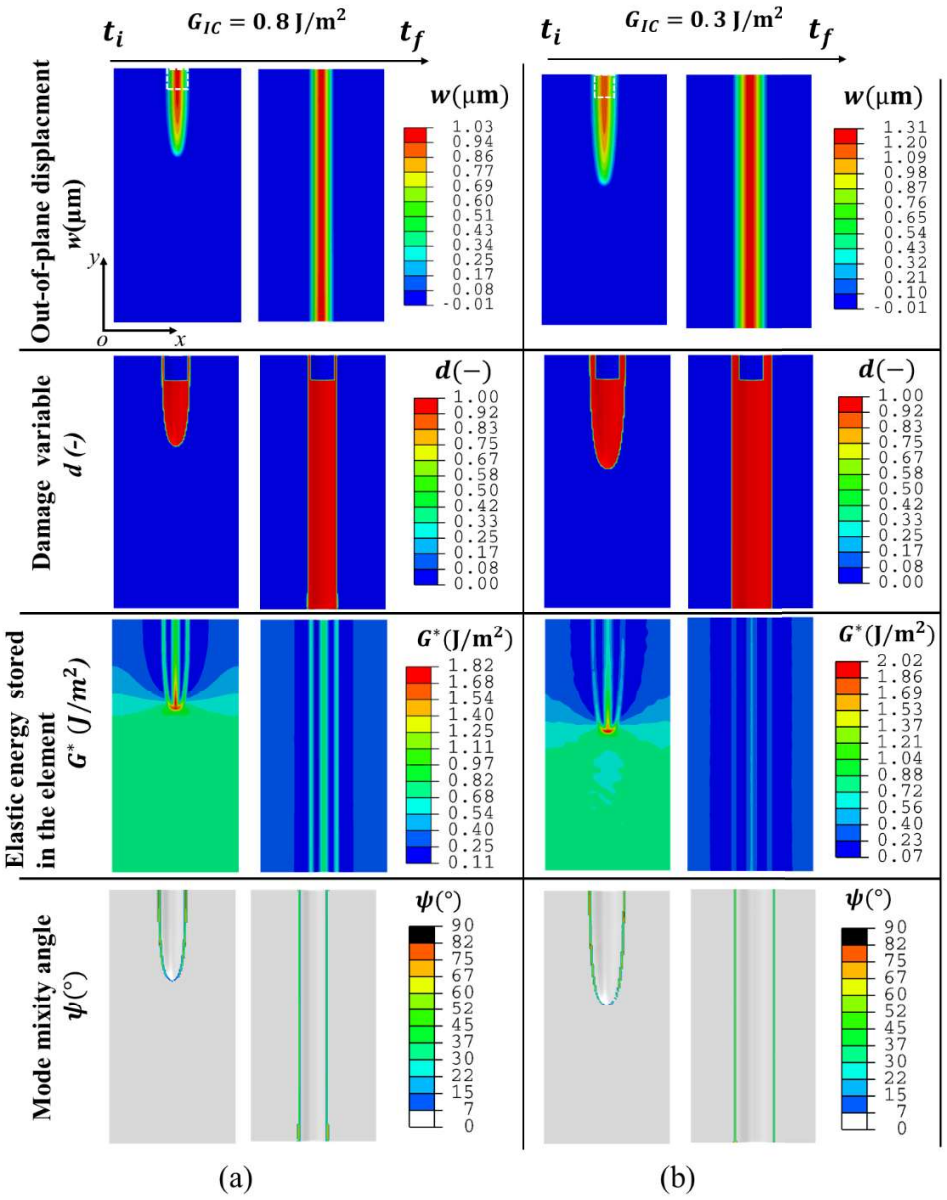

Fig. 4-10: Comparison of the SS buckle evolution for interfacial toughness G_{IC} (a) = 0.8 J/m² and G_{IC} (b) = 0.3 J/m². An initial defect of square geometry of length l_x = 12 μm is highlighted by a square white dashed line. Out-of-plane displacement w, scalar damage variable d, elastic energy stored in the element G^*(J/m²), and mode mixity angle $\psi(°)$ obtained for a Ni film on PC substrate (h_f = 200 nm, h_s = 12 μm E_f = 200 GPa, ν_f = 0.31, E_s = 2.5 GPa, ν_s = 0.37, σ_{xx}^f = 1.213 GPa, σ_{yy}^f = 0 GPa, T_n^0 = 18 MPa, T_t^0 = 39 MPa, η = 0.9, t_i = 0.002 s, t_f = 0.08 s). The time evolution is shown on each row, from the initial time t_i, where σ_o is initially reached up to t_f, the end of the simulation.

4.4. Buckling-driven delamination of SS buckle lying parallel to the thickness gradient

4.4.1. Validity of the mechanical model in case of rigid substrate

Before addressing the FEM simulations on a compliant PC substrate, we first validate our CZM implementation on a rigid substrate, where the solution can be directly compared with analytical predictions. We consider a nickel film on a rigid substrate with compressive stresses set to match the first experiment loading step S_1 (Table 4-1): σ_{xx}^0 = 1.31 GPa and σ_{yy}^0 = 0.88 GPa. The film exhibits a linear thickness gradient $h(y)$ ranging from 200 nm to 10 nm, similarly to what was experimentally observed. For the CZM implementation, the damage initiation parameters described previously are used. The mode interfacial toughness G_{IC} is varied until the arrest thickness h^* matches the experimentally observed value, h^* = 153 nm, while keeping the mode-mixity parameter fixed at η = 0.9 [26]. This yields an optimum value of G_{IC} = 0.52 J/m^2.

Fig. 4-11a shows the out-of-plane displacement w of a SSB propagating in the thickness gradient $h(y)$ along the (Oy) direction, with the thickness gradient shown on the left side. On the right side, the computed mode mixity angle ψ is presented. The results show that both the w and the buckle width 2b decrease with decreasing the film thickness h. Additionally, the computed ψ shows a value of 90° at the buckle sides, leading to $G_C(\psi)= G_{IIC}$, which prevents the lateral expansion of the SSB. At the buckle front, $\psi \approx (24.6\pm9)°$, highlighting strong mode I contributions to $G_C(\psi)$. To explain the arrest at h^* = 153nm, we computed the local stored energy G_0 along the plate length ((Oy) direction) far from the delaminated zone and compared it with the analytical prediction from Eq. (4-3). Fig. 4-11b shows the computed stored energy labeled as FEM and analytical *versus* the local thickness. FEM results demonstrate a very good agreement with analytical prediction and confirm the expected linear dependence of G_0 on h. At the arrest location (see the blue cross), G_0 = 0.68 J/m^2, additionally at buckle front, the interfacial toughness is calculated using Eq. (4-5) from the computed ψ, gives a value of $G(\psi)$=0.61±0.0702 J/m^2, and in the order of G_0 , thereby explaining the observed arrest of buckle propagation.

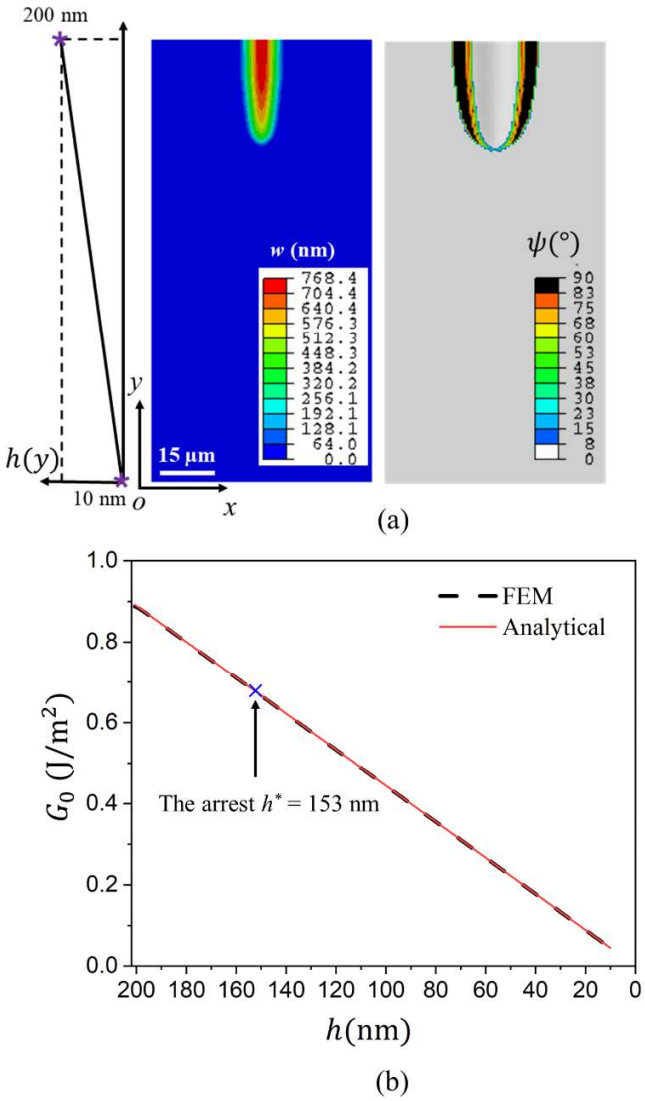

Fig. 4-11: FEM simulations of a straight-sided buckle propagating in a thickness gradient $h(y)$ lying along the (Oy) direction. (a) Out-of-plane displacements w on the right side and mode mixity angle ψ on the left side. FEM/CZM simulations for a nickel film deposited on a rigid substrate (E_f = 200GPa, ν_f = 0.31, h_{max} = 200 nm, h_{min} = 10 nm, σ_{xx}^f = 1.31 GPa, σ_{yy}^f = 0.88 GPa, T_n^0 = 18 MPa, T_t^0 =39 MPa, η = 0.9, G_{IC} = 0.52 J/m²).

4.4.2. Identification of interfacial toughness properties

We proceed to compare the FEM results with the experimental observations shown in Fig. 4-5. Fig. 4-12 presents a FEM analysis of a SSB propagating in a thickness gradient $h(y)$ ranging from 200 to 10 nm, similarly to what was experimentally observed, taking now into account the

elasticity of the substrate. The FEM investigations were conducted at each loading step S_i taking into account the values of the stress state of the film given in Table 4-1. For convenience, only the loading steps S_1, S_3 and S_6 have been reported in Fig. 4-12. The interfacial toughness $Gc(\psi)$ used here was arbitrary set using G_{IC}=1.6 J/m^2 and η=0.9. Fig. 4-12a presents the out-of-plane displacement of the film (see the color bar on the right side). The buckle is initiated from a small free-cohesive zone (upper part) and then propagates downward through the thickness gradient until its arrest at a critical value labelled in the following h_i^*, for i varying from 1 to 6. The buckle becomes narrower and exhibits lower height as it propagates through the thickness gradient, leading to a kind of tapered buckle close to the arrest point. Note however that the buckle front can be well defined as a spherical shape whatever the loading conditions S_i. It is shown that h_i^* is decreased as the loading stress is increased from S_1 to S_6. The SSB goes consequently further ahead in the thickness gradient in agreement with the increasing elastic energy stored in the film. At a given loading step S_i, the maximum height and the buckle width decreases as h decreases. Additionally, at a given h, the maximum height of the buckle is increased as a result from S_1 to S_6, the width as well (see the color bar on the right side in Fig. 4-12a). The numerical ψ distribution around the propagating SSB is shown in Fig. 4-12b. Notably, ψ remains low at the buckle front whatever the loading steps S_i, around ψ=24°, indicating a dominant mode I opening at the crack tip [26,35,152–154]. Conversely, ψ is significantly higher along the buckle sides, starting at approximately 70° in S_1 and increasing with the loading steps to reach finally 90° at S_6. This explains why the SSB preferentially grows at the front rather than the sides where the predominancy of mode II fracture prohibits further delamination.

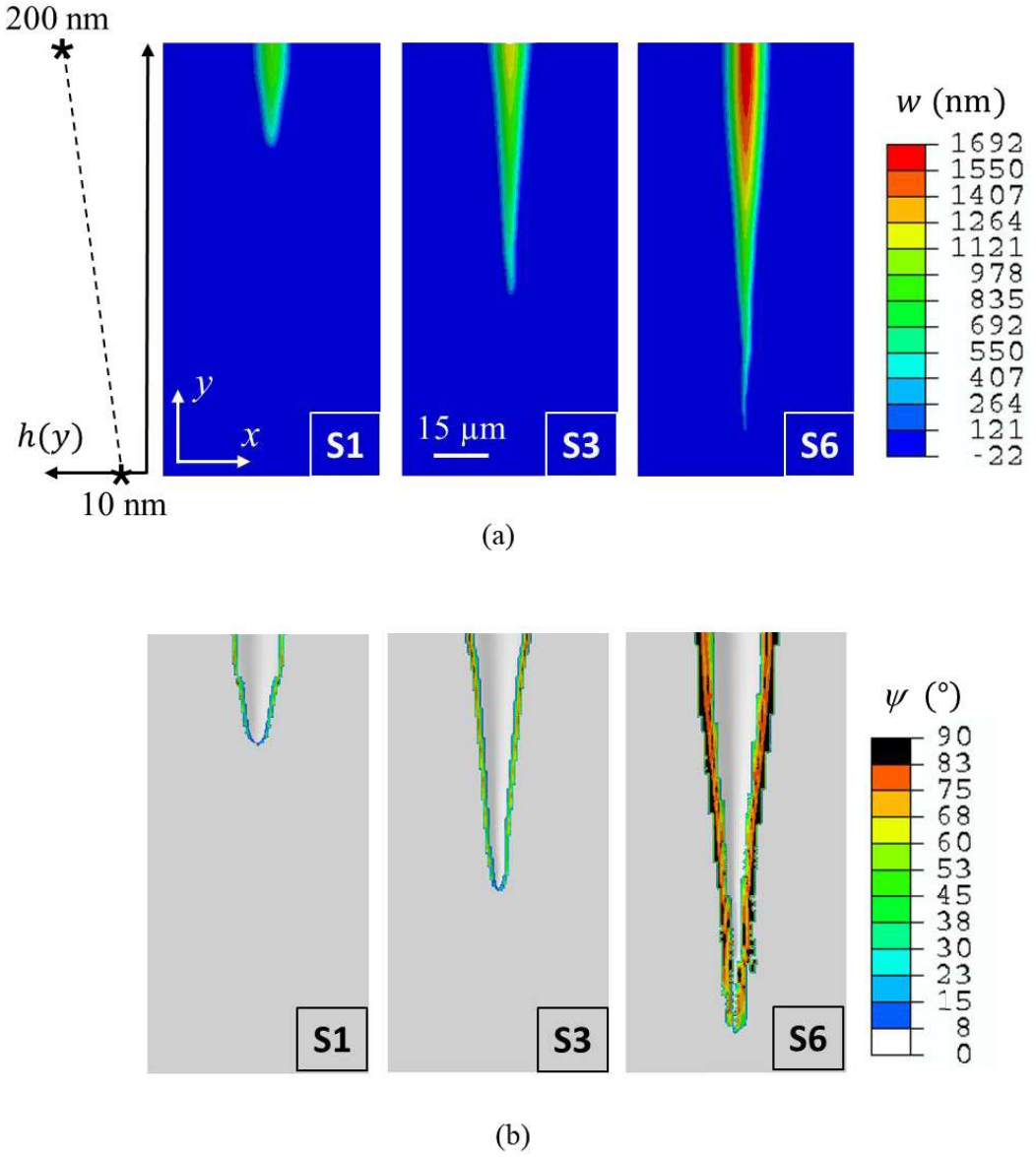

Fig. 4-12: Numerical simulations of a straight-sided buckle propagating in a thickness at three different loading steps S_1, S_3 and S_6. (a) Out-of-plane displacements. The thickness gradient $h(y)$ is lying along the (Oy) direction, as shown on the left side. (b) Mode mixity angle ψ. FEM/CZM simulations for a nickel film deposited on polycarbonate substrate (E_f=200 GPa, ν_f= 0.31, E_s=2.5 GPa, ν_s= 0.37, h_{max}=200 nm, h_{min}=10 nm, T_n^0 = 18 MPa, T_t^0 =39 MPa, η = 0.9, G_{IC} = 1.6 J/m²).

The evolution of the critical thickness for SSB arrest, h^*, is presented in Fig. 4-13a as a function of G_{IC}, for various loading steps S_i (the experimental ones) and for an arbitrary value of η fixed

here to 0.9. Each loading step is represented by a distinct color. It is shown first that h^* decreases while G_{IC} is decreased. The smaller the interfacial toughness is, the further the SSB propagates in the thinner region of the plate. Secondly, for a given G_{IC}, increasing the loading stress leads to significantly decreasing h^*. On the right side of Fig. 4-13a are reported the different critical thickness values extracted from the loading experiments. It is shown that our FEM simulations for G_{IC}=1.6 J/m² and η=0.9 agree the experiment. However, it will be necessary to explore various values of G_{IC} and η in order to find other couples that may match our experimental data. Therefore, a parametric study was conducted to identify the combinations of toughness parameters (G_{IC} ; η) that best matches the experimental arresting positions h_i^* at each loading step S_i, for i ∈ [1-4]. The numerical FEM results are presented in Fig. 4-13b. As expected from Eq. (1-80), reducing the η parameter results in having to increase G_{IC}, whatever S_i. Additionally, it demonstrates that a unique combination is found for fitting all the loading steps, given by G_{IC}=1.6 J/m² and η=0.9.

In conclusion, we succeeded to experimentally control the propagation of buckles through a well-defined thickness gradient, following successive loading steps. The buckles are characterized by straight-sides parallel to the thickness gradient and a curved propagating front. Increasing stress allows for the buckles to go ahead further in the thinner part of plate. Finite elements method simulations including cohesive zone model confirmed that the propagation of the buckles is controlled by the mode mixity at the curved crack front. It is shown that the critical thickness where the buckle stops is a relevant criterium to fully quantify the film/substrate interfacial toughness. In particular, we succeeded to numerically determine, for the first time to our knowledge, the value of the non-dimensional parameter η included in the now well-established phenomenological law proposed by Hutchinson *et al*., that is usually arbitrary fixed in most studies.

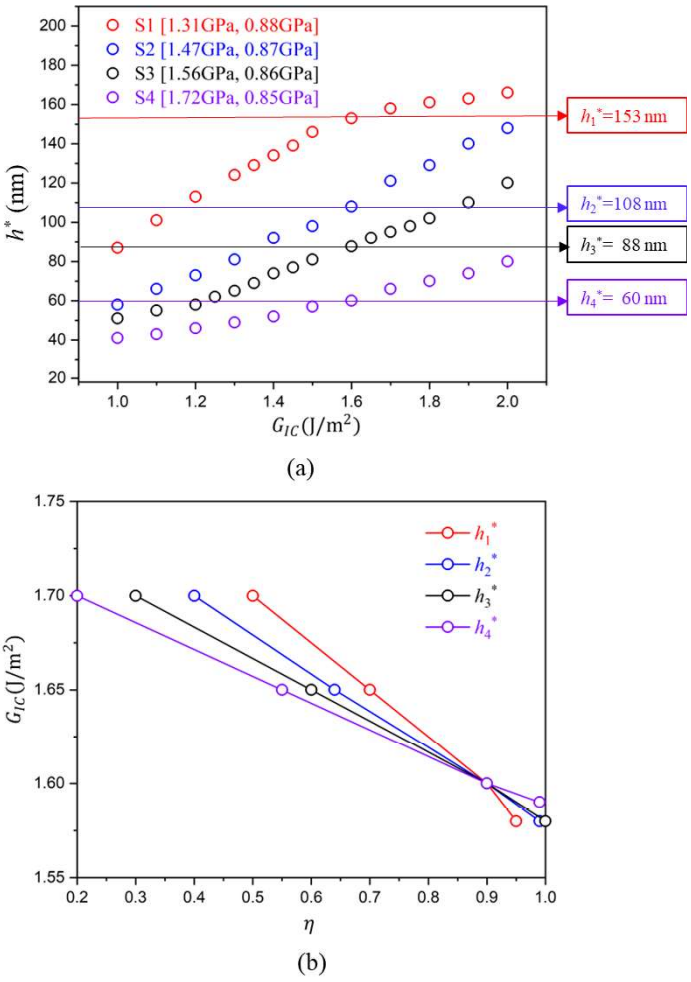

Fig. 4-13: FEM interfacial toughness characteristics. (a) Critical thickness of arrest of the buckle h^* *versus* G_{IC} for four loading steps from S_1 to S_4, for η =0.9. The loading state (σ_{xx}^f,σ_{yy}^f) given in Table 1 for each S_i is recalled in the legend, the experimental values of h^* as horizontal color lines as well. (b) Numerical interfacial toughness (G_{IC}, η) combination for the four loading step S_i allowing to mimic the experimental arresting buckle thicknesses h^*_i. FEM/CZM simulations for a nickel film deposited on polycarbonate substrate (E_f=200 GPa, ν_f= 0.31, E_s=2.5 GPa, ν_s= 0.37, h_{max}=200 nm, h_{min}=10 nm, T_n^0 = 18 MPa, T_t^0 =39 MPa).

4.5. Effect of SS buckles perpendicular to the thickness gradient on the mode mixity angle

In section 3.6 we have demonstrated a SSB lying perpendicular to the thickness gradient leading to an asymmetrical profile, with shifted maximum height towards the thinner region of the film.

This asymmetry implies that the mode mixity angle ψ may differ on either side of the buckle, which is expected to influence how the buckle can further grow or evolve. Therefore, we first performed a rough assessment of ψ using the framework developed by Hutchinson and Suo. It is known, for a straight-sided buckle on rigid substrate, that ψ increases (in absolute value) with the increase of the stress ratio σ_0/σ_c. As σ_c is proportional to $(h/b)^2$, the evolution of ψ depends on how the ratio h/b evolves. Due to the thickness gradient, the h value is not the same on the left and right sides. Additionally, due to the asymmetrical character of the buckle, the half width b is shown to be higher on the thicker part, smaller on the thinner part. We showed that the increase of h is comparably higher than the increase of b, according to Fig. 3-27, $(h_{max}/b_+) > (h_{min}/b_-)$. The σ_0/σ_c is consequently smaller on the thick part, higher on the thin part. The ψ angle and the resulting toughness would thus be expected to be smaller on the thick part, which should influence how the buckle can further grow/evolve, in particular preferentially towards the thick part.

To move beyond this rough assessment, we implemented a cohesive zone model in our FEM simulations. The FEM model is shown in Fig. 4-14, similar to the one described in Fig. 3-17a, with the addition that the film/substrate interface is modeled using cohesive surface based interaction. The same parameters for the CZM used in previous section are used here. The thickness gradient is applied along the (Ox) direction.

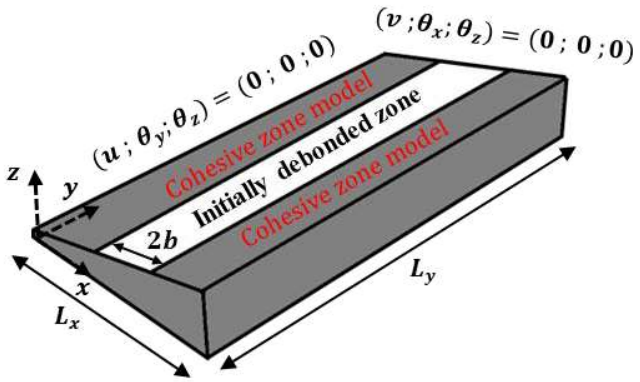

Fig. 4-14: FEM configuration with cohesive zone model. Film is considered to be elastic film with E_f = 200 GPa and ν_f = 0.31 and the substrate rigid. Internal stress: σ_0 = 0.8 GPa. Width $2b$ = 12 µm. Thickness gradient: h_{max} = 170 nm, h_{min} = 60 nm. Cohesive zone parameters: normal loading T_n^0 = 18 MPa, shear loading T_s^0 = 39 MPa. Interfacial toughness of the film/substrate: G_{IC} = 0.36 J/m^2 and η = 0.9.

FEM simulations were performed using a dynamic explicit solver. A smooth step is used to apply internal stress, to avoid any dynamic effects. To damp out the inherent dynamic effects, viscous pressure is used. The FEM results were extracted at equilibrium (the final loading state). Fig. 4-15a presents the out-of-plane displacement w of a SS buckle lying perpendicular to the thickness gradient $h(x)$, the red contrast highlights the highest values of the out-of-plane displacement. The thickness gradient is highlighted below Fig. 4-15a, the film being thicker on the

left side and thinner on the right. The damage variable d(-) is presented in Fig. 4-15b. The associated mode mixity angle ψ on both sides of the SS buckle is shown in Fig. 4-15c.

The profile of the SS buckle is shown to be shifted toward thinner part of the film, as shown in Fig. 4-15a. Additionally, the damage variable in Fig. 4-15b shows a significant damaged interface on the thicker part of the film compared to the thinner region. This can be explained by the fact that higher thickness corresponds to higher stored elastic energy. The mode mixity angle ψ presented in Fig. 4-15c demonstrated that ψ is lower at the thinner side of the film, while it is higher at the thicker side of the film, which surprisingly contradicts the expectations based on the analytical formulas discussed above. Therefore, we conclude that the thickness gradient not only results in an asymmetrical SS buckle and a shifted maximum height towards the thinner part of the film as shown in section 3.6, but should result in different ψ mode mixity angles on each side [26], with ψ being higher on the thicker side, the reverse on the thinner.

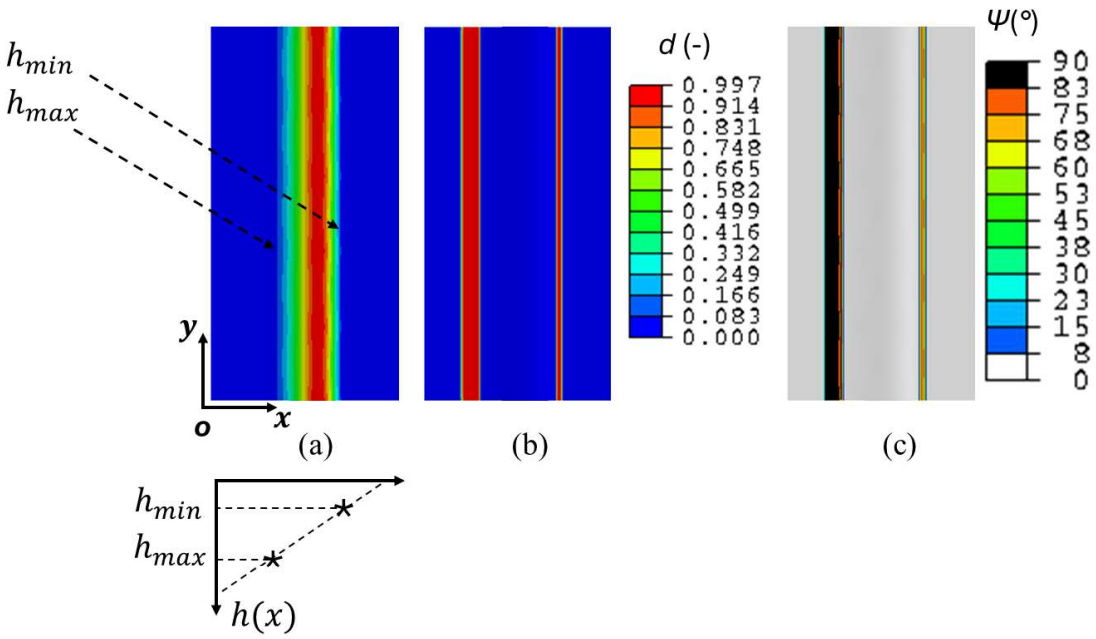

Fig. 4-15: (a) Out-of-plane displacement w. (b) The damage variable d. (c) ψ angle (see the color bar on the right) along the two sides of an asymmetrical straight-sided buckle. FEM simulations with parameters given in Figure 3-15. FEM/CZM simulations for a nickel film deposited on a rigid substrate (E_f = 200GPa, ν_f = 0.31, h_{max} = 170 nm, h_{max} = 60 nm, $2b$ = 12 µm, T_n^0 = 18 MPa, T_t^0 =39 MPa, η = 0.9, G_{IC} = 0.36 J/m², σ_0 = 0.78 GPa).

4.6. Conclusion

In this chapter, the buckling-driven delamination of thin films with controlled thickness gradients was investigated using a combined experimental and numerical approach. We first examined spontaneous buckling in homogeneous, constant-thickness films, demonstrating its implications for film reliability and mechanical performance. We then conducted stepwise uniaxial compression experiments on nickel films deposited on polycarbonate substrates with well-defined thickness gradients. In situ atomic force microscopy (AFM) enabled direct observation of the propagation and arrest of straight-sided buckles (SSBs) aligned with the gradient, revealing the strong coupling between local thickness, applied compressive stress, and buckle morphology.

Experimentally, SSBs were observed to arrest in thinner regions, where the energy release rate becomes insufficient to sustain delamination. Both the out-of-plane displacement and buckle width decreased with decreasing thickness, confirming that local thinning reduces the driving energy available for delamination.

To quantify these mechanisms, a finite element model (FEM) based on elastic plate theory was developed and combined with a cohesive zone model (CZM) incorporating the mixed-mode interfacial toughness formulation of Hutchinson and Suo. The model contained two unknown interfacial parameters—the mode I toughness G_{IC} and the mode-mixity sensitivity parameter η which were calibrated by reproducing the experimentally observed propagation and arrest of buckles in graded films. The model was first validated against analytical solutions for homogeneous films on both rigid and compliant substrates and then extended to graded geometries. By systematically varying G_{IC} and η to match experimental arrest positions, a unique parameter set was identified: G_{IC} = 1.6 J/m2 and η = 0.9. To our knowledge, this represents the first joint identification of these two interfacial parameters from buckle-driven delamination experiments, and the value of η may be transferable to a broader class of metallic films.

Parametric simulations further showed that decreasing G_{IC} promotes longer buckle propagation into thinner regions of the gradient, whereas increasing the applied stress reduces the arrest distance. The maximum height and width of the SSBs were also predicted to decrease with decreasing thickness, in agreement with experiments. Analysis of mode mixity demonstrated a predominance of mode I at the buckle front and a transition to mode II along the sides, approaching pure mode II at higher stresses. For SSBs oriented perpendicular to the thickness gradient, thickness variations across the buckle width were shown to strongly influence mode mixity, with higher values on the thicker side and lower values on the thinner side, in contrast to what might be anticipated from a preliminary application of basic SSB mechanical formulas.

Overall, the combined experimental and numerical analyses provide a detailed understanding of delamination morphology in films with thickness gradients. The interplay between local thickness, stored elastic energy, and interfacial toughness has been quantified, leading to a predictive framework for extracting interfacial properties and mode-mixity parameters. These results offer

valuable guidelines for the design of graded thin-film systems with controlled delamination behavior and improved mechanical reliability.

4.7. Résumé en français

Ce chapitre explore le délaminage induit par flambage dans des films minces de nickel présentant des gradients d'épaisseur bien contrôlés, analysé dans le cadre de la théorie des plaques élastiques. Faisant suite à la caractérisation morphologique statique du Chapitre 3, l'accent est mis ici sur la mécanique de la propagation des cloques et la quantification des propriétés interfaciales. L'approche méthodologique combine des expériences de compression uniaxiale par paliers sur substrat souple (PC) et des simulations numériques par la méthode des éléments finis (FEM) intégrant un Modèle de Zone Cohésive (CZM). L'objectif principal est d'identifier de manière unique la ténacité interfaciale (G_{IC}) et son paramètre de sensibilité au mode mixte η.

I. Cloquages spontanés

L'étude commence par la démonstration du flambage spontané et incontrôlé observé dans les films métalliques homogènes après dépôt. Des images optiques de films de nickel sur substrat PC (Fig. 4-16a et b) montrent l'évolution et l'expansion de diverses morphologies de cloques (SSBs, TCBs) sur plusieurs mois. La Figure 4-16c montre des flambages spontanés en cordons de téléphone (TCBs) dans un film de Molybdène (Mo, 300 nm) déposé sur un substrat de silicium (Si, 100 µm). Ces TCBs apparaissent presque immédiatement et s'étendent sur de longues distances. Ce phénomène, qui compromet la fiabilité industrielle des films, motive le recours à une stratégie de contrôle.

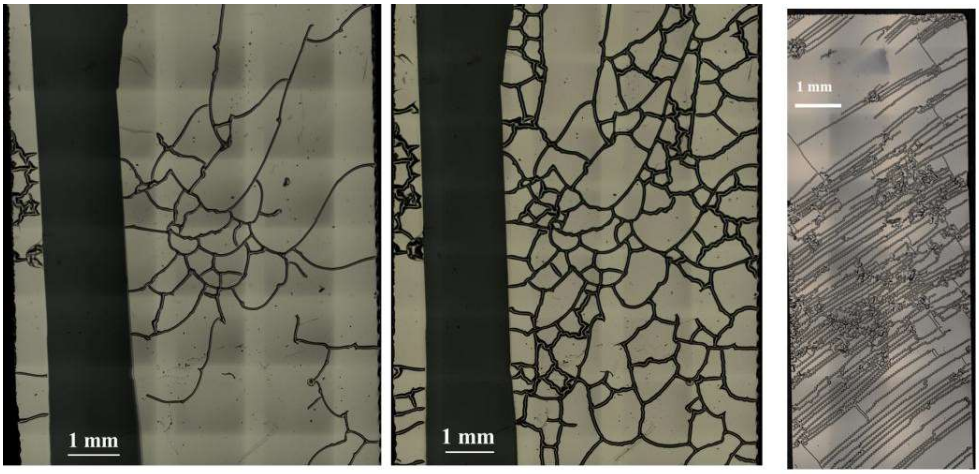

Fig. 4-16: Image optique de flambages spontanés dans (a) Ni (940 nm) / PC, observés (a) trois jours et (b) six mois après le dépôt. (c) Flambages en cordons de téléphone (TCBs) spontanés dans un film de Mo (300 nm) sur Si (100 µm) observés peu après le dépôt.

II. Contrôle de la propagation des rides droites dans un gradient d'épaisseur

Afin de permettre une analyse quantitative, la propagation des cloques est contrôlée grâce à des films possédant un gradient d'épaisseur et l'application d'une contrainte externe incrémentale. L'échantillon C (Ni/PC) est sélectionné, avec une épaisseur variant de 580 nm à 10 nm le long de la direction (*Oy*). Le substrat PC est contraint par paliers le long de l'axe (*Ox*) à l'aide d'un dispositif Deben microtest. Les contraintes sont suivies (Fig. 4-17a) et les déformations sont caractérisées *in situ* à chaque chargement (S_i) par AFM. Les expériences de compression induisent la nucléation de SSBs. Initialement, à chaque étape de chargement S_i, les rides propagent vers les régions minces jusqu'à atteindre une épaisseur critique d'arrêt h_i^*. Pour l'échantillon C, en augmentant la contrainte appliquée (de σ_{xx}^f =1.31 GPa à σ_{xx}^f =2.52 GPa), l'épaisseur critique d'arrêt h^* diminue de 153 nm à 25 nm (Comme montre la Fig. 4-17b). L'arrêt se produit lorsque le taux local de libération d'énergie élastique à l'avant du cloque devient insuffisant pour vaincre la ténacité interfaciale, ce qui résulte d'une compétition entre l'énergie motrice et la résistance de l'interface.

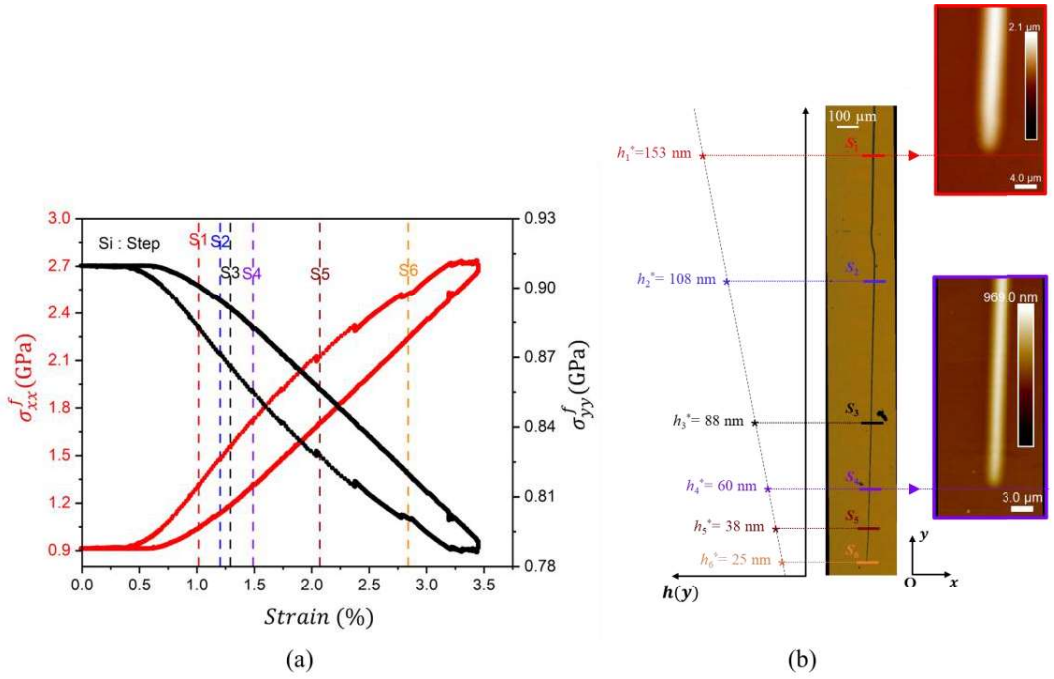

Fig. 4-17: (a) Courbe contrainte-déformation du substrat PC et étape de chargement. (b) Image optique et AFM illustrant la propagation et l'arrêt des SSBs dans le gradient.

- ***Modélisation numérique par éléments finis et zone cohésive***

L'approche consiste à identifier les paramètres inconnus (G_{IC}, η) en reproduisant les positions d'arrêt expérimentales h_i^*. Le protocole d'identification implique l'ajustement des simulations

FEM-CZM, afin que l'épaisseur d'arrêt h_i^* prédite corresponde aux valeurs expérimentales de h_i^* pour chaque étape de chargement S_i. Les résultats numériques en Fig. 4-18a montrent que la hauteur maximale (δ) et la largeur ($2b$) des rides droites diminuent avec la réduction de l'épaisseur du film, ce qui est en accord avec les observations expérimentales. Une étude paramétrique a permis d'identifier une combinaison unique des paramètres qui reproduit fidèlement toutes les positions d'arrêt expérimentales (S_1 à S_4), cette combination a été identifiée: G_{IC} =1.6 J/m^2 et η = 0.9. Cette identification conjointe des deux paramètres du ténacité sont très importants, en particulier η, souvent fixé arbitrairement dans la plupart des études.

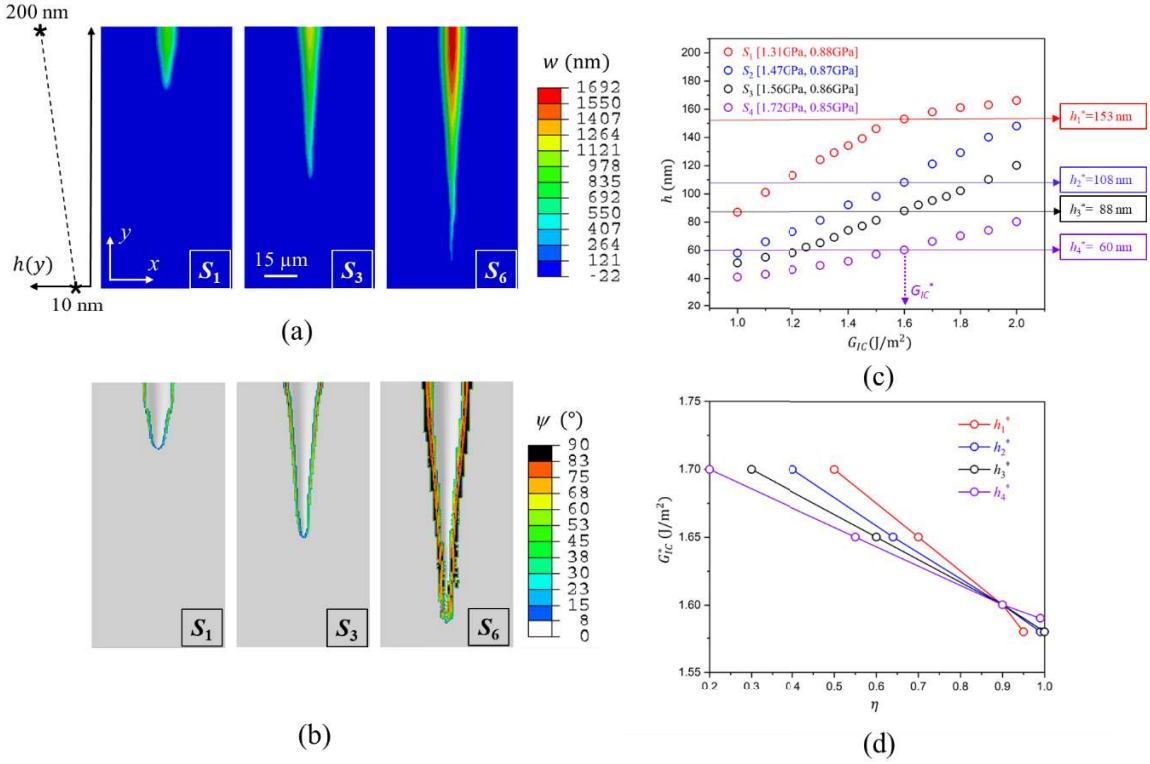

Fig. 4-18: Caractéristiques de la ténacité interfaciale FEM. (a) Déplacements hors-plan w et 5 (b) angle de mode mixité (ψ) simulés pour les étapes S_1, S_3 et S_6. (b) Épaisseur critique d'arrêt h_i^* simulée en fonction de G_{IC} pour quatre paliers de chargement. (c) Combinaisons numériques de ténacité interfaciale (G_{IC}, η) permettant de reproduire les épaisseurs d'arrêt expérimentales h_i^*.

III. Cloques perpendiculaires au gradient et effet sur le mode mixte

Les simulations présentes en Fig. 4-19 de SSBs orientés perpendiculairement au gradient ont montré que l'angle ψ est plus élevé sur le côté le plus épais du film et plus faible sur le côté mince, ce qui contredit les prévisions simplifiées.

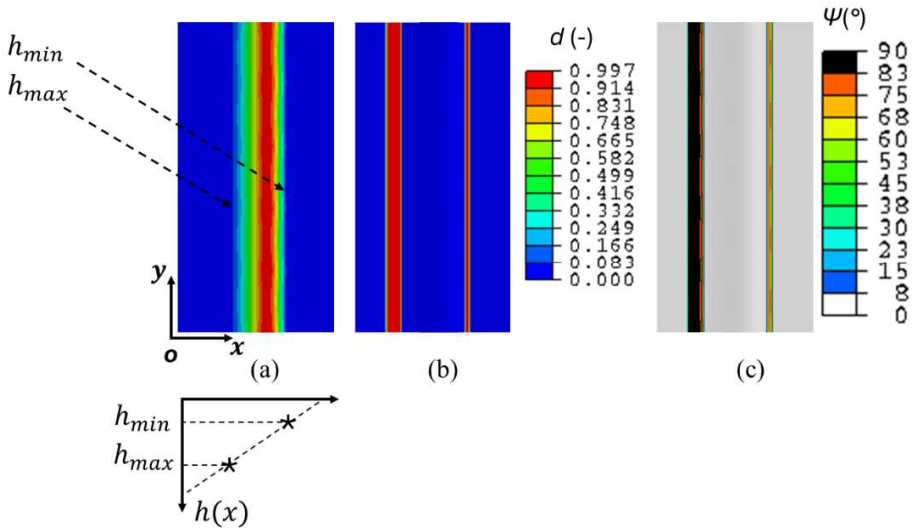

Fig. 4-19: (a) Déplacement hors plan *w*. (b) Variable d'endommagement *d*. (c) Angle ψ (voir l'échelle de couleurs à droite) le long des deux flancs d'une cloque à flancs droits asymétrique.

I. Synthesis

General conclusion

This thesis reports a combined theoretical, experimental and numerical study of the buckling and buckling-driven delamination in thin films exhibiting well-controlled thickness gradients. The work establishes a comprehensive framework that links local film thickness, residual and in-plane stresses, and interfacial properties within both static and dynamic aspects. It progresses from theoretical foundations to experimental setups and finally to numerical modeling capable of predicting the mechanical properties of film/substrate systems from buckling structures and delamination.

The first chapter covers the theoretical basis required to understand buckling morphologies and delamination phenomena in thin film/substrate systems. Starting from the elastic plate theory, using the Föppl–Von Kármán (Fvk) equations, the mathematical foundation of the straight-sided buckle (SSB) is fully described. The analysis of the SSB was detailed revealing the relationship between buckle height, width and residual stress. Subsequently, a detailed overview of the fracture mechanics, including energy release rate and mixed-mode angle was given to describe the crack growth along an interface. The chapter also introduces the cohesive zone model (CZM), which enables a gradual and more realistic description of interfacial separation between bonded materials through traction-separation laws. By incorporating the Hutchinson-Suo model and Dundurs' parameters, we highlighted the influence of elastic mismatch on the interfacial toughness through the mode mixity angle ψ in the SSB. Finally, the origin of telephone cord buckles (TCBs) was described either from secondary buckling or from the instability of the crack front during delamination, emphasizing how the buckle front propagates with alternate pining points on the left and on the right of the front due to $\psi=atan(T_t^i/T_n^i)$. Altogether, Chapter 1 provides the theoretical foundation for the experimental and numerical analyses developed in this thesis.

The second chapter focuses on the experimental protocols that were developed to produce and characterize thin films exhibiting well-controlled thickness gradients. Nickel was selected for its mechanical strength, while polycarbonate served as a compliant substrate suitable for mechanical loading. A key achievement of this thesis was the design and implementation of a custom-built mobile shutter integrated into the NORDIKO machine (ion beam sputtering (IBS) deposition system). This setup allows us to finely control the shutter speeds, leading to continuous thickness gradients across the film length, which was crucial for the thesis project. After deposition, the internal residual stress was estimated using Stoney's curvature method, while the thickness gradient was characterized via white-light interferometry. Surface morphology and mechanical responses under compression were investigated using atomic force microscopy (AFM), both before and during *in-situ* uniaxial loading with a Deben micro-compression stage. The developed experimental protocols allow us to control the buckle initiation, propagation and morphology evolution.

The third chapter investigates the influence of controlled-thickness gradients on the buckling morphologies of thin films through a combined experimental and numerical study using finite element method (FEM) simulations within the framework of elastic plate theory. The deposited graded nickel films were subjected to uniaxial compression, leading initially to SSBs that evolved into TCBs upon releasing external stress.

The experimental observations highlight several key findings. First, the maximum height δ of SSBs aligned parallel to the thickness gradient decreases with increasing the local thickness h for a given width $2b$, and the equilibrium profiles of the buckles can be fitted as a sinusoidal shape, consistent with the Fvk elastic plate theory. However, the measured heights were systematically higher than the analytical predictions, which was attributed to the elastic compliance of the polycarbonate substrate. Second, SSBs preferentially propagated toward thicker regions, confirming that larger external compressive stresses are required to maintain buckling propagation in the gradient direction, an observation consistent with a static approach. FEM simulations were performed to study SSBs oriented parallel to the thickness gradient. For SSBs aligned with the gradient, FEM confirmed the decrease of δ with increasing h, consistent with both experiments and theory. However, FEM results underestimated the measured heights. Refinning the FEM results by accounting for the elastic contrast significantly improved the agreement. The onset buckling stress σ_c^{TG} in films exhibiting thickness gradient was found to depend on both the gradient slope α and the delaminated width $2b$. For a given $2b$, increasing α led to larger deviations of σ_c^{TG} from the analytical critical stress σ_c for homogenous films. Similarly, for a fixed α, decreasing the width $2b$ amplified this deviation. Additionally, far from the onset buckling, the FvK plate theory still accurately described the post-buckling equilibrium profiles. In particular, the thinnest regions of the film followed the FvK solution from the onset of buckling as far as the internal stress is sufficiently larger compared to σ_c. When the buckle profiles were extracted along directions misaligned with respect to the gradient direction, asymmetric profiles were observed, characterized by a shift of the maximum height toward the thinner side, resulting in unequal edge to peak distances (b_+, b_-). FEM simulations demonstrate that thickness variations along the buckle profile are the primary cause of the SSB asymmetry, they also show that the ratio b_+/b_- increases monotonically with the thickness gradient characterized by the ratio $h_{\max}/h_{min}$, independent of stress and the buckle width. These results demonstrate that the buckle asymmetry can serve as a non-destructive diagnostic tool for determining local thickness gradients in thin films.

TCBs lying parallel to the thickness gradient were also analyzed. For constant width, the wavelength λ of the TCB increases with local thickness, consistent with the higher elastic energy stored in thicker regions. In TCB exhibiting a width gradient, both λ and $2b$ decrease with local thickness. Similarly, FEM simulations of TCBs lying parallel to the gradient in films with constant width reproduced experimental observations. In particular, λ increases with both local thickness and delaminated width $2b$. In films with a thickness gradient, depending on the gradient slope and width, three morphologies were observed simultaneously: TCBs at low thickness, SSBs at intermediate thickness, and flat regions at higher thickness. It is shown that the SS to TC buckles transition strongly depends on local thickness and on $2b$, and that the thickness gradient does not

change the known criterion for secondary buckling (σ_0/σ_c >6.6). For TCBs lying parallel to the gradient with variable delaminated width $2b$, λ was found to increase with both h and $2b$, confirming that the transition from SS to TC buckles depends primarily on the ratio h/b rather than h alone. Finally, FEM analyses of TCBs oriented perpendicular to the gradient revealed pronounced lateral and vertical asymmetries characterized by $\gamma = (b_+/b_-)_A/(b_+/b_-)_B$ and $\Delta = 2.(\delta_A - \delta_B)/\delta_A + \delta_B)$, respectively, resulting from the thickness variation across the buckle width. In particular, the two parameters Δ and γ are shown to increase monotonically with the gradient independent of the internal stress, and width. Therefore, FEM simulations demonstrate that the two parameters (Δ, γ) also offer non-destructive tools to assess local gradient values from measured buckle profiles in coatings. Overall, this chapter establishes a clear relationship between local thickness variations and buckle morphology, demonstrating that controlled gradients systematically influence SSB and TCB characteristics.

In the fourth chapter, the buckling-driven delamination in thin films exhibiting well-controlled thickness gradients was investigated using a combined experimental and numerical study. We first examined spontaneous buckling in homogeneous, constant-thickness films, demonstrating its implications for film reliability and mechanical performance. We then conducted stepwise uniaxial compression *in situ* with AFM on nickel films deposited on polycarbonate substrates with well-defined thickness gradients. This enables direct observation of the propagation and arrest of SSBs along the gradient, revealing the strong coupling between local thickness, applied compressive stress, and buckle morphology. Experimentally, SSBs were observed to nucleate in thicker regions, and arrest in thinner regions, where the energy release rate becomes insufficient to sustain delamination. Both the out-of-plane displacement and buckle width decrease with decreasing thickness, confirming that the reduction of thickness reduces the driving energy available for delamination. To quantify these mechanisms, a finite element (FE) model based on elastic plate theory was developed and combined with a CZM incorporating the mixed-mode interfacial toughness formulation of Hutchinson and Suo. The model was first validated against analytical solutions for homogeneous films on both rigid and compliant substrates and then extended to graded films. The Hutchinson and Suo empirical toughness includes the mode I toughness G_{IC} and an unknown parameter called the mode-mixity sensitivity parameter η (usually arbitrary fixed to 0.7). By systematically varying G_{IC} and η to match experimental arrest positions, a unique parameter set was identified: G_{IC} = 1.6 J/m^2 and η = 0.9. To the best of our knowledge, this represents the first identification of these two interfacial parameters from buckle-driven delamination experiments, and the value of η may be transferable to a broader class of metallic films. Parametric simulations further showed that decreasing G_{IC} promotes longer buckle propagation into thinner regions of the gradient, whereas increasing the applied stress reduces the arrest distance. The maximum height and width of the SSBs were also predicted to decrease with decreasing thickness, in agreement with experiments. Analysis of mode mixity demonstrated a predominance of mode I at the buckle front and a transition to mode II along the sides, approaching pure mode II at higher stresses.

For SSBs oriented perpendicular to the thickness gradient, thickness variations across the buckle width were shown to strongly influence mode mixity, with higher values on the thicker side and lower values on the thinner side, in contrast to what might be anticipated from a preliminary application of basic SSB mechanical formulas.

Overall, the combined experimental and numerical study provides a detailed understanding of the buckling-driven delamination in graded film systems. The interplay between local thickness, stored elastic energy, and interfacial toughness has been quantified, leading to a predictive framework for extracting interfacial properties and mode-mixity parameters. These results offer valuable guidelines for the design of graded thin-film systems with controlled delamination behavior and improved mechanical reliability.

Perspectives

Future work should aim at investigating the propagation of TCBs along the thickness gradient. Achieving this experimentally requires implementing biaxial loading in the Deben microtest stage to induce and control TCB formation. Such an approach would deepen our understanding of buckle evolution. A relevant study by F. Paumier *at al*. [50] reported in Fig. I-1a confined TCBs in Y_2O_3 film deposited on GaAs substrate exhibiting thickness gradient from approximately 50 to 30 nm. They attributed the arrest to a reduction of the stored elastic energy release rate with decreasing film thickness h. In their experiments, Y_2O_3 oxide films were deposited by ion beam sputtering using a RF ion argon source at 400°C on GaAs substrates with high residual stress estimated to be around 8.5 GPa in compression. Within this context, FEM/CZM simulations could provide valuable insight into the interfacial properties of film/substrate systems by fitting numerical arrest data to experimental data, as was successfully done for straight-sided buckles (SSBs) in Chapter 4. To explore this idea, FEM simulations were preliminary performed using the same material properties used throughout this work and the mechanical model used in section 4.3.1. For the implementation of CZM, the maximum traction components are set arbitrarily to (T_n^0, T_t^0) = (18 MPa, 117 MPa), the mode I interfacial toughness G_{IC} = 0.9 J/m^2 and the mode-mixity parameter is fixed at η = 0.9 [26]. A partially equibiaxial compression ($\sigma_{xx}^0/\sigma_{xx}^0$=1.136) with σ_{xx}^f = 2.0 GPa and σ_{yy}^f = 1.76 GPa is applied to ensure controlled propagation along the gradient.

The simulated out-of-plane displacement w (Fig. I-1b) shows that for h_{max}/h_{min} = 1, the TCB propagates uniformly along the (Oy) direction with constant height δ, width $2b$ and wavelength λ, as expected for an homogenous film [24]. Introducing a small gradient (h_{max}/h_{min} = 1.053) already leads to noticeable changes: δ, $2b$ and λ decrease with decreasing $h(y)$. This effect becomes more pronounced for steeper gradients, for which a buckle arrest is numerically observed at a critical thickness h^*=170 nm. Regardless of the gradient, the computed mode mixity angle ψ (Fig. I-1c) shows ψ = 90° on the buckle sides and sagged regions, meaning that delamination cannot proceed in mode II, since $G_C(\psi) = G_{IIC}$. For h_{max}/h_{min} between 1.25 and 1.333, the curved buckle front exhibits a reduced mode mixity (ψ = 62°). Anyway, buckle arrest still occurs at the same critical thickness h^*, indicating that arrest is primarily governed by the decrease in energy release rate, associated with decreasing h, rather than by ψ. These findings suggest that telephone cord buckle arrest under a gradient could also provide direct access to the mode I interfacial toughness G_{IC}. Finally, no SSBs were observed at the TCBs tips in the experiments (Fig. 4-17), consistent with FEM results. This strongly support that the TCBs originate from the instability of the crack front during delamination [30,31], rather than from secondary buckling of pre-existing SSBs, as reported in several studies [24,26,28].

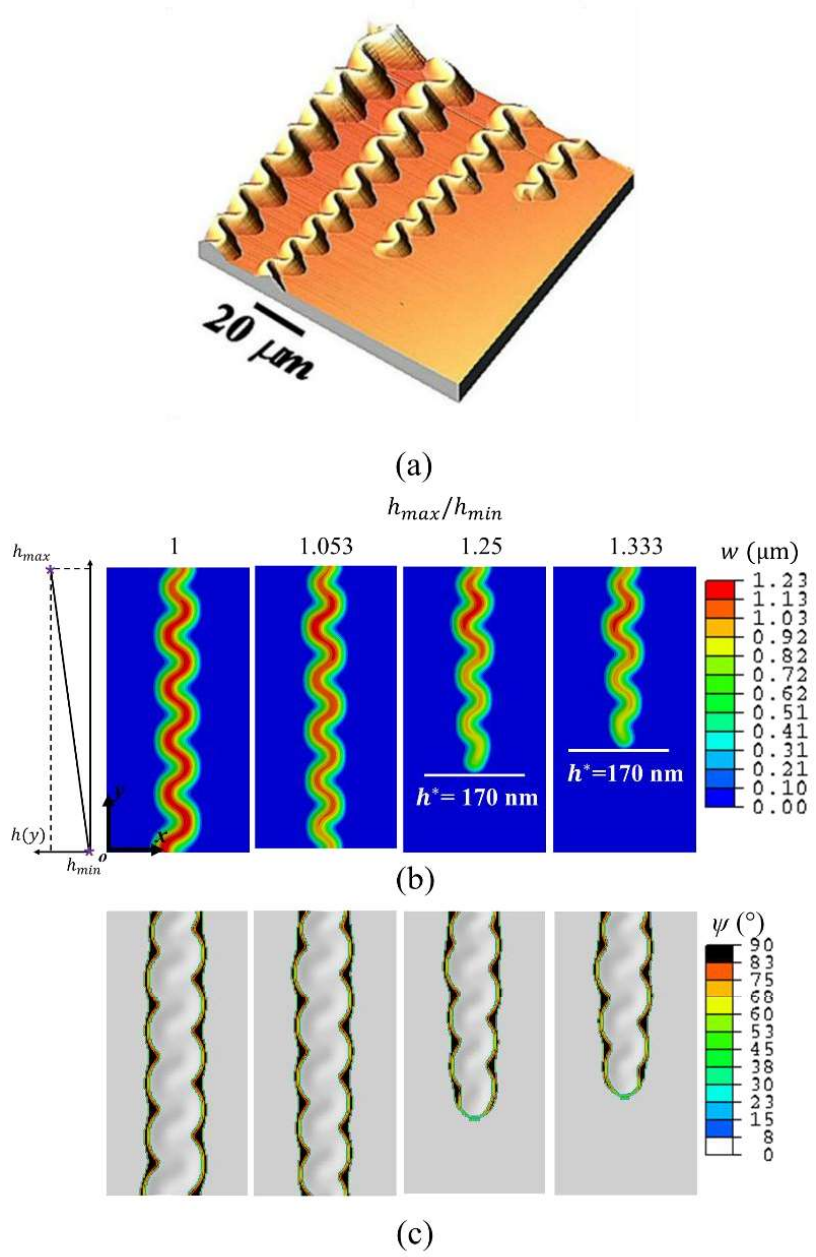

Fig. I-1: (a) AFM observations of confined TCBs propagating in Y_2O_3 film on GaAs substrate exhibiting thickness gradient of 50 to 30nm, adopted from [50]. Numerical simulations of a TCB propagating in various thickness gradient (h_{max}/h_{min}) along the (Oy) direction, shown on the left side. Each column presents various thickness gradient, represented as h_{max}/h_{min}. (b) Out-of-plane displacement w. (c) Mode mixity angle ψ. FEM/CZM simulations for a film deposited on a rigid substrate (E_f = 200GPa, ν_f = 0.31, h_{max} = 200 nm, l = 12 µm, T_n^0 = 18 MPa, T_t^0 =117 MPa, η = 0.9, G_{IC} = 0.9 J/m², σ_{xx}^f = 2.0 GPa, σ_{yy}^f = 1.76 GPa.

Bibliography

[1] M. Ardahe, M.R. Hantehzadeh, M. Ghoranneviss, Effect of Growth Temperature on Physical Properties of MoS2 Thin Films Synthesized by CVD, J. Electron. Mater. 49 (2020) 1002–1008. https://doi.org/10.1007/s11664-019-07796-1.

[2] S.R. Choi, J.W. Hutchinson, A.G. Evans, Delamination of multilayer thermal barrier coatings, Mechanics of Materials 31 (1999) 431–447. https://doi.org/10.1016/S0167-6636(99)00016-2.

[3] M. Vančo, J. Krmela, F. Pešlová, The Use of PVD Coating on Natural Textile Fibers, Procedia Engineering 136 (2016) 341–345. https://doi.org/10.1016/j.proeng.2016.01.220.

[4] H. Usui, Formation of polymer thin films and interface control by physical vapor deposition, in: Nanostructured Thin Films II, SPIE, 2009: pp. 63–74. https://doi.org/10.1117/12.828673.

[5] A.F. Abdulrahman, R.Y. Mohammed, S.M. Ahmed, S.M. Hamad, Synthesis of lead oxide thin films by using physical vapor deposition technique, Materials Today: Proceedings 42 (2021) 2752–2755. https://doi.org/10.1016/j.matpr.2020.12.716.

[6] G. Abadias, E. Chason, J. Keckes, M. Sebastiani, G. Thompson, E. Barthel, G. Doll, C. Murray, C. Stoessel, L. Martinu, Review Article: Stress in thin films and coatings: Current status, challenges, and prospects, Journal of Vacuum Science & Technology A: Vacuum, Surfaces, and Films 36 (2018) 020801. https://doi.org/10.1116/1.5011790.

[7] A.M. Engwall, Z. Rao, E. Chason, Origins of residual stress in thin films: Interaction between microstructure and growth kinetics, Materials & Design 110 (2016) 616–623. https://doi.org/10.1016/j.matdes.2016.07.089.

[8] M. Abdoos, B. Bose, S. Rawal, A.F.M. Arif, S.C. Veldhuis, The influence of residual stress on the properties and performance of thick TiAlN multilayer coating during dry turning of compacted graphite iron, Wear 454–455 (2020) 203342. https://doi.org/10.1016/j.wear.2020.203342.

[9] V. Teixeira, Residual stress and cracking in thin PVD coatings, Vacuum 64 (2002) 393–399. https://doi.org/10.1016/S0042-207X(01)00327-X.

[10] G.H. Wells, T. Hopf, K.V. Vassilevski, E. Escobedo-Cousin, N.G. Wright, A.B. Horsfall, J.P. Goss, A.G. O'Neill, M.R.C. Hunt, Determination of the adhesion energy of graphene on SiC(0001) via measurement of pleat defects, Applied Physics Letters 105 (2014) 193109. https://doi.org/10.1063/1.4901941.

[11] E.A. Fodeke, Mechanical behaviour of 2D materials on strained substrates: experimental investigation on MoS_2, (n.d.).

[12] C. Coupeau, R. Boijoux, Y. Ni, G. Parry, Interacting straight-sided buckles: An enhanced attraction by substrate elasticity, Journal of the Mechanics and Physics of Solids 124 (2019) 526–535. https://doi.org/10.1016/j.jmps.2018.11.010.

[13] G. Parry, C. Coupeau, J. Colin, A. Cimetière, J. Grilhé, Buckling and post-buckling of stressed straight-sided wrinkles: experimental AFM observations of bubbles formation and finite element simulations, Acta Materialia 52 (2004) 3959–3966. https://doi.org/10.1016/j.actamat.2004.05.011.

[14] H.M. Jensen, I. Sheinman, Straight-sided, buckling-driven delamination of thin films at high stress levels, International Journal of Fracture 110 (2001) 371–385. https://doi.org/10.1023/A:1010821918325.

[15] C. Coupeau, J.F. Naud, F. Cleymand, P. Goudeau, J. Grilhé, Atomic force microscopy of in situ deformed nickel thin films, Thin Solid Films 353 (1999) 194–200. https://doi.org/10.1016/S0040-6090(99)00369-7.

[16] S.-J. Yu, M.-G. Chen, P.-Z. Si, H. Zhou, J. Chen, X.-F. Zhang, Y.-J. Zhang, Transitions from straight-sided to telephone cord buckles in SiAlNx films, Thin Solid Films 550 (2014) 480–485. https://doi.org/10.1016/j.tsf.2013.10.145.

[17] D. Lloyd, X. Liu, N. Boddeti, L. Cantley, R. Long, M.L. Dunn, J.S. Bunch, Adhesion, Stiffness, and Instability in Atomically Thin MoS2 Bubbles, Nano Lett. 17 (2017) 5329–5334. https://doi.org/10.1021/acs.nanolett.7b01735.

[18] A. Ruffini, A. Finel, J. Colin, J. Durinck, Effect of interface plasticity on circular blisters, Scripta Materialia 113 (2016) 222–225. https://doi.org/10.1016/j.scriptamat.2015.10.038.

[19] J. Colin, C. Coupeau, J. Grilhé, Plastic Folding of Buckling Structures, Phys. Rev. Lett. 99 (2007) 046101. https://doi.org/10.1103/PhysRevLett.99.046101.

[20] K. Meng, G. Parry, M.A. Hurier, C. Tromas, C. Coupeau, Influence of elasto-plastic behavior of thin films on circular buckling structures, International Journal of Solids and Structures 304 (2024) 113032. https://doi.org/10.1016/j.ijsolstr.2024.113032.

[21] B. Eren, L. Marot, G. Günzburger, P.-O. Renault, T. Glatzel, R. Steiner, E. Meyer, Hydrogen-induced buckling of gold films, J. Phys. D: Appl. Phys. 47 (2013) 025302. https://doi.org/10.1088/0022-3727/47/2/025302.

[22] J.-Y. Faou, G. Parry, S. Grachev, E. Barthel, Telephone cord buckles—A relation between wavelength and adhesion, Journal of the Mechanics and Physics of Solids 75 (2015) 93–103. https://doi.org/10.1016/j.jmps.2014.11.008.

[23] M.J. Cordill, D.F. Bahr, N.R. Moody, W.W. Gerberich, Adhesion measurements using telephone cord buckles, Materials Science and Engineering: A 443 (2007) 150–155. https://doi.org/10.1016/j.msea.2006.08.027.

[24] Yong Ni, Senjiang Yu, Hongyuan Jiang, L. He1, The shape of telephone cord blisters, Nature Communications 8 (2017). https://doi.org/10.1116/1.5011790.

[25] J.-Y. Faou, S. Grachev, E. Barthel, G. Parry, From telephone cords to branched buckles: A phase diagram, Acta Materialia 125 (2017) 524–531. https://doi.org/10.1016/j.actamat.2016.12.025.

[26] J.W. Hutchinson, Z. Suo, Mixed Mode Cracking in Layered Materials, in: J.W. Hutchinson, T.Y. Wu (Eds.), Advances in Applied Mechanics, Elsevier, 1991: pp. 63–191. https://doi.org/10.1016/S0065-2156(08)70164-9.

[27] M.J. Cordill, D.F. Bahr, N.R. Moody, W.W. Gerberich, Recent developments in thin film adhesion measurement, IEEE Transactions on Device and Materials Reliability 4 (2004) 163–168. https://doi.org/10.1109/TDMR.2004.829071.

[28] G. Parry, A. Cimetière, C. Coupeau, J. Colin, J. Grilhé, Stability diagram of unilateral buckling patterns of strip-delaminated films, Phys. Rev. E 74 (2007) 066601. https://doi.org/10.1103/PhysRevE.74.066601.

[29] F. Cleymand, J. Colin, C. Coupeau, J. Grilhé, Stability of wrinkling patterns: from straight-sided to worm-like structures, The European Physical Journal Applied Physics 17 (2002) 173–178. https://doi.org/10.1051/epjap:2002009.

[30] J.-Y. Faou, G. Parry, S. Grachev, E. Barthel, How Does Adhesion Induce the Formation of Telephone Cord Buckles?, Phys. Rev. Lett. 108 (2012) 116102. https://doi.org/10.1103/PhysRevLett.108.116102.

[31] J.W. Hutchinson, M.D. Thouless, E.G. Liniger, Growth and configurational stability of circular, buckling-driven film delaminations, Acta Metallurgica et Materialia 40 (1992) 295–308. https://doi.org/10.1016/0956-7151(92)90304-W.

[32] H. Jia, S. Wang, P. Goudeau, L. Li, X. Xue, Investigation of buckling transition from straight-sided to telephone-cord wrinkles in Al films, J. Micromech. Microeng. 23 (2013) 045014. https://doi.org/10.1088/0960-1317/23/4/045014.

[33] S.-J. Yu, X.-F. Xiao, M.-G. Chen, H. Zhou, J. Chen, P.-Z. Si, Z.-W. Jiao, Morphological selections and dynamical evolutions of buckling patterns in SiAlN*x* films: From straight-sided to telephone cord or bubble structures, Acta Materialia 64 (2014) 41–53. https://doi.org/10.1016/j.actamat.2013.11.038.

[34] M. Zhao, J. Zhou, F. Yang, T. Liu, T.-Y. Zhang, Effects of substrate compliance on circular buckle delamination of thin films, Engineering Fracture Mechanics 74 (2007) 2334–2351. https://doi.org/10.1016/j.engfracmech.2006.11.007.

[35] B. Cotterell, Z. Chen, Buckling and cracking of thin films on compliant substrates under compression, International Journal of Fracture 104 (2000) 169–179. https://doi.org/10.1023/A:1007628800620.

[36] H.-H. Yu, J.W. Hutchinson, Influence of substrate compliance on buckling delamination of thin films, (n.d.).

[37] G. Parry, J. Colin, C. Coupeau, F. Foucher, A. Cimetière, J. Grilhé, Effect of substrate compliance on the global unilateral post-buckling of coatings: AFM observations and finite element calculations, Acta Materialia 53 (2005) 441–447. https://doi.org/10.1016/j.actamat.2004.09.039.

[38] P.C.P. Bouten, M.A.J. van Gils, Buckling failure of compressive loaded hard layers in flexible devices, MRS Online Proceedings Library (OPL) 843 (2004) T4.9. https://doi.org/10.1557/PROC-843-T4.9.

[39] O. van der Sluis, A.A. Abdallah, P.C.P. Bouten, P.H.M. Timmermans, J.M.J. den Toonder, G. de With, Effect of a hard coat layer on buckle delamination of thin ITO layers on a compliant elasto-plastic substrate: An experimental–numerical approach, Engineering Fracture Mechanics 78 (2011) 877–889. https://doi.org/10.1016/j.engfracmech.2011.01.013.

[40] Y. Zhang, Y. Liu, The Mexican hat effect on the delamination buckling of a compressed thin film, Acta Mech Sin 30 (2014) 927–932. https://doi.org/10.1007/s10409-014-0088-8.

[41] R. Boijoux, G. Parry, C. Coupeau, Buckle depression as a signature of Young's modulus mismatch between a film and its substrate, Thin Solid Films 645 (2018) 379–382. https://doi.org/10.1016/j.tsf.2017.11.011.

[42] C. Coupeau, From thin film and coating buckling structures to mechanical properties, Materials Science and Engineering: A 483–484 (2008) 617–619. https://doi.org/10.1016/j.msea.2006.09.181.

[43] Buckling Structures, A Relevant Signature of the Mechanical Properties of Film/Substrate Systems, MPS (2024). https://doi.org/10.47485/2832-9384.1046.

[44] M.W. Moon, H.M. Jensen, J.W. Hutchinson, K.H. Oh, A.G. Evans, The characterization of telephone cord buckling of compressed thin films on substrates, Journal of the Mechanics and Physics of Solids 50 (2002) 2355–2377. https://doi.org/10.1016/S0022-5096(02)00034-0.

[45] M.-W. Moon, K.-R. Lee, K.H. Oh, J.W. Hutchinson, Buckle delamination on patterned substrates, Acta Materialia 52 (2004) 3151–3159. https://doi.org/10.1016/j.actamat.2004.03.014.

[46] F.-Z. Abbes, C. Coupeau, J. Durinck, M. Talea, Y. Ni, G. Parry, Effect of substrate elasticity on thin film buckle morphologies: A phase diagram, Surface and Coatings Technology 408 (2021) 126817. https://doi.org/10.1016/j.surfcoat.2020.126817.

[47] E.A. Jagla, Modeling the buckling and delamination of thin films, Phys. Rev. B 75 (2007) 085405. https://doi.org/10.1103/PhysRevB.75.085405.

[48] Y.-J. Zhang, S.-J. Yu, H. Zhou, M.-G. Chen, Z.-W. Jiao, THICKNESS DEPENDENCE OF BUCKLING PATTERNS OF Ta FILMS SPUTTERED ON GLASS SUBSTRATES, Surf. Rev. Lett. 19 (2012) 1250022. https://doi.org/10.1142/S0218625X12500229.

[49] S.-J. Yu, Y.-J. Zhang, M.-G. Chen, Telephone cord buckles in wedge-shaped Fe films sputtering deposited on glass substrates, Thin Solid Films 518 (2009) 222–226. https://doi.org/10.1016/j.tsf.2009.07.134.

[50] F. Paumier, R.J. Gaboriaud, C. Coupeau, Buckling phenomena in Y2O3 thin films on GaAs substrates, Appl. Phys. Lett. 82 (2003) 2056–2058. https://doi.org/10.1063/1.1558971.

[51] D. Yang, L. Ma, Y. Sun, C. Coupeau, Y. Ni, S. Yu, Symmetry breaking and high-order instability of telephone cord buckles triggered by in-plane gradients of thin films, Engineering Fracture Mechanics 306 (2024) 110209. https://doi.org/10.1016/j.engfracmech.2024.110209.

[52] L.D. Landau, L.P. Pitaevskii, A.M. Kosevich, E.M. Lifshitz, Theory of Elasticity: Volume 7, Elsevier, 2012.

[53] J.R. Barber, Elasticity, Springer Netherlands, 2002.

[54] Föppl: Vorlesungen über technische Mechanik: bd.... - Google Scholar, (n.d.). https://scholar.google.com/scholar_lookup?title=Vorlesungen+%C3%BCber+technische+Mechanik&publication_year=1921& (accessed April 19, 2023).

[55] T.V. Kármán, Festigkeitsprobleme im Maschinenbau, Teubner, 1910.

[56] Kirchhoff-Love Theory - an overview | ScienceDirect Topics, (n.d.). https://www.sciencedirect.com/topics/engineering/kirchhoff-love-theory (accessed September 22, 2024).

[57] J. Dundurs, Discussion: ``Edge-Bonded Dissimilar Orthogonal Elastic Wedges Under Normal and Shear Loading'' (Bogy, D. B., 1968, ASME J. Appl. Mech., 35, pp. 460-466), Journal of Applied Mechanics 36 (1969) 650. https://doi.org/10.1115/1.3564739.

[58] A.G. Evans, J.W. Hutchinson, Effects of non-planarity on the mixed mode fracture resistance of bimaterial interfaces, Acta Metallurgica 37 (1989) 909–916. https://doi.org/10.1016/0001-6160(89)90017-5.

[59] S. Zak, A. Lassnig, M. Hrstka, M.J. Cordill, Buckling-induced delamination: Connection between mode-mixity and Dundurs parameters, Theoretical and Applied Fracture Mechanics 122 (2022) 103647. https://doi.org/10.1016/j.tafmec.2022.103647.

[60] A. Lassnig, B. Putz, S. Hirn, D.M. Többens, C. Mitterer, M.J. Cordill, Adhesion evaluation of thin films to dielectrics in multilayer stacks: A comparison of four-point bending and stressed overlayer technique., Materials & Design 200 (2021) 109451. https://doi.org/10.1016/j.matdes.2021.109451.

[61] G.C. Gruber, A. Lassnig, S. Zak, C. Gammer, M.J. Cordill, R. Franz, Synthesis and structure of refractory high entropy alloy thin films based on the MoNbTaW system, Surface and Coatings Technology 439 (2022) 128446. https://doi.org/10.1016/j.surfcoat.2022.128446.

[62] C. He, J. Li, X. Wu, P. Chen, J. Zhao, K. Yin, M. Cheng, W. Yang, G. Xie, D. Wang, D. Liu, R. Yang, D. Shi, Z. Li, L. Sun, G. Zhang, Tunable Electroluminescence in Planar Graphene/SiO2 Memristors, Advanced Materials 25 (2013) 5593–5598. https://doi.org/10.1002/adma.201302447.

[63] Y. Travaly, L. Zhang, Y. Zhao, R. Pfeffer, K. Uhrich, F. Cosandey, E. Garfunkel, T.E. Madey, Nucleation, growth, and aggregation of gold on polyimide surfaces, Journal of Materials Research 14 (1999) 3673–3683. https://doi.org/10.1557/JMR.1999.0496.

[64] S.J. Lee, T.H. Kim, B.-H. Jeong, K.N. Kim, G.Y. Yeom, Properties of tungsten thin film deposited using inductively coupled plasma assisted sputtering for next-generation interconnect metal, Thin Solid Films 674 (2019) 64–70. https://doi.org/10.1016/j.tsf.2019.01.051.

[65] A.I. Oliva, R.D. Maldonado, O. Ceh, J.E. Corona, H.G. Riveros, Study of a bimaterial system by an improved dynamical thermal model, Surf. Rev. Lett. 12 (2005) 289–298. https://doi.org/10.1142/S0218625X05007025.

[66] K. Imai, X. Zhou, X. Liu, Application of Zr and Ti-Based Bulk Metallic Glasses for Orthopaedic and Dental Device Materials, Metals 10 (2020) 203. https://doi.org/10.3390/met10020203.

[67] F. Alves, B. Kearney, D. Grbovic, N.V. Lavrik, G. Karunasiri, Strong terahertz absorption using SiO2/Al based metamaterial structures, Applied Physics Letters 100 (2012) 111104. https://doi.org/10.1063/1.3693407.

[68] S.V. Dmitriev, N. Yoshikawa, M. Kohyama, S. Tanaka, R. Yang, Y. Kagawa, Atomistic structure of the Cu(1 1 1)/α-Al2O3(0 0 0 1) interface in terms of interatomic potentials fitted to ab initio results, Acta Materialia 52 (2004) 1959–1970. https://doi.org/10.1016/j.actamat.2003.12.037.

[69] A.A. Griffith, The Phenomena of Rupture and Flow in Solids, Philosophical Transactions of the Royal Society of London Series A 221 (1921) 163–198. https://doi.org/10.1098/rsta.1921.0006.

[70] K.M. Liechti, Y.S. Chai, Asymmetric Shielding in Interfacial Fracture Under In-Plane Shear, Journal of Applied Mechanics 59 (1992) 295–304. https://doi.org/10.1115/1.2899520.

[71] B.M. Malyshev, R.L. Salganik, The strength of adhesive joints using the theory of cracks, Int J Fract 1 (1965) 114–128. https://doi.org/10.1007/BF00186749.

[72] D.S. Dugdale, Yielding of steel sheets containing slits, Journal of the Mechanics and Physics of Solids 8 (1960) 100–104. https://doi.org/10.1016/0022-5096(60)90013-2.

[73] G.I. Barenblatt, The Mathematical Theory of Equilibrium Cracks in Brittle Fracture, 7 (1962) 55–129. https://doi.org/10.1016/S0065-2156(08)70121-2.

[74] G.T. Camacho, M. Ortiz, Computational modelling of impact damage in brittle materials, International Journal of Solids and Structures 33 (1996) 2899–2938. https://doi.org/10.1016/0020-7683(95)00255-3.

[75] F.H. Wittmann, K. Rokugo, E. Brühwiler, H. Mihashi, P. Simonin, Fracture energy and strain softening of concrete as determined by means of compact tension specimens, Materials and Structures 21 (1988) 21–32. https://doi.org/10.1007/BF02472525.

[76] P. Petersson, Crack growth and development of fracture zones in plain concrete and similar materials, Report TVBM (1981). https://www.semanticscholar.org/paper/Crack-growth-and-development-of-fracture-zones-in-Petersson/b172327b08f3790b282ddb555648d4103ad059d0 (accessed March 1, 2025).

[77] M. Ortiz, A. Pandolfi, FINITE-DEFORMATION IRREVERSIBLE COHESIVE ELEMENTS FOR THREE-DIMENSIONAL CRACK-PROPAGATION ANALYSIS, (1999).

[78] V. Tvergaard, J.W. Hutchinson, The influence of plasticity on mixed mode interface toughness, Journal of the Mechanics and Physics of Solids 41 (1993) 1119–1135. https://doi.org/10.1016/0022-5096(93)90057-M.

[79] I. Scheider, W. Brocks, Simulation of cup–cone fracture using the cohesive model, Engineering Fracture Mechanics 70 (2003) 1943–1961. https://doi.org/10.1016/S0013-7944(03)00133-4.

[80] V. Tvergaard, Effect of fibre debonding in a whisker-reinforced metal, Materials Science and Engineering: A 125 (1990) 203–213. https://doi.org/10.1016/0921-5093(90)90170-8.

[81] K. Park, G.H. Paulino, Cohesive Zone Models: A Critical Review of Traction-Separation Relationships Across Fracture Surfaces, Applied Mechanics Reviews 64 (2011) 060802. https://doi.org/10.1115/1.4023110.

[82] G. Li, C. Li, Linking bilinear traction law parameters to cohesive zone length for laminated composites and bonded joints, 1 1 (2014) 177–196. http://techno-press.org/content/?page=article&journal=aas&volume=1&num=2&ordernum=3 (accessed July 10, 2025).

[83] H. Heriana, R.M.M.C. Marbun, B.K. Hadi, D. Widagdo, M. Kusni, Numerical Simulation of Transverse Crack on Composite Structure Using Cohesive Element, Journal of Composites Science 8 (2024) 158. https://doi.org/10.3390/jcs8040158.

[84] K. Salomonsson, T. Andersson, WEIGHTED POTENTIAL METHODOLOGY FOR MIXED MODE COHESIVE LAWS, in: 2010. https://www.semanticscholar.org/paper/WEIGHTED-POTENTIAL-METHODOLOGY-FOR-MIXED-MODE-LAWS-Salomonsson-Andersson/b20494b389ef2e4a0192e8e2f628fbcd56de30af (accessed July 10, 2025).

[85] X.-P. Xu, A. Needleman, Void nucleation by inclusion debonding in a crystal matrix, Modelling Simul. Mater. Sci. Eng. 1 (1993) 111. https://doi.org/10.1088/0965-0393/1/2/001.

[86] V. Tvergaard, J.W. Hutchinson, The relation between crack growth resistance and fracture process parameters in elastic-plastic solids, Journal of the Mechanics and Physics of Solids 40 (1992) 1377–1397. https://doi.org/10.1016/0022-5096(92)90020-3.

[87] A. Needleman, A Continuum Model for Void Nucleation by Inclusion Debonding, Journal of Applied Mechanics 54 (1987) 525–531. https://doi.org/10.1115/1.3173064.

[88] A. Needleman, An analysis of tensile decohesion along an interface, Journal of the Mechanics and Physics of Solids 38 (1990) 289–324. https://doi.org/10.1016/0022-5096(90)90001-K.

[89] H.M. Jensen, Energy release rates and stability of straight-sided, thin-film delaminations, Acta Metallurgica et Materialia 41 (1993) 601–607. https://doi.org/10.1016/0956-7151(93)90090-F.

[90] S. Žák, A. Lassnig, Elastic Mismatch Influence on Modes I and II Ratio during Buckling-induced Delamination, Procedia Structural Integrity 43 (2023) 23–28. https://doi.org/10.1016/j.prostr.2022.12.229.

[91] I. Monetto, L. Barbieri, C. Berggreen, R. Massabò, Fracture Mechanics solutions and operative formulae for isotropic bi-material layers with large elastic mismatch, Theoretical and Applied Fracture Mechanics 121 (2022). https://doi.org/10.1016/j.tafmec.2022.103451.

[92] R. Boijoux, G. Parry, J.-Y. Faou, C. Coupeau, How soft substrates affect the buckling delamination of thin films through crack front sink-in, Applied Physics Letters 110 (2017) 141602. https://doi.org/10.1063/1.4979614.

[93] H.R. Kaufman, J.J. Cuomo, J.M.E. Harper, Technology and applications of broad-beam ion sources used in sputtering. Part I. Ion source technology, Journal of Vacuum Science and Technology 21 (1982) 725–736. https://doi.org/10.1116/1.571819.

[94] R. Garg, S. Gonuguntla, S. Sk, M.S. Iqbal, A.O. Dada, U. Pal, M. Ahmadipour, Sputtering thin films: Materials, applications, challenges and future directions, Advances in Colloid and Interface Science 330 (2024) 103203. https://doi.org/10.1016/j.cis.2024.103203.

[95] V. Teixeira, J. Carneiro, P. Carvalho, E. Silva, S. Azevedo, C. Batista, 11 - High barrier plastics using nanoscale inorganic films, in: J.-M. Lagarón (Ed.), Multifunctional and Nanoreinforced Polymers for Food Packaging, Woodhead Publishing, 2011: pp. 285–315. https://doi.org/10.1533/9780857092786.1.285.

[96] Société CRYO TECHNIQUES ET COUCHES MINCES : Chiffre d'affaires, statuts, extrait d'immatriculation, (n.d.). https://www.pappers.fr/entreprise/cryo-techniques-et-couches-minces-411586381 (accessed May 11, 2025).

[97] K.S. Teh, Y.T. Cheng, C. Sambucetti, Selective plating of nickel ceramic composite films for MEMS applications, Technical Digest. MEMS 2002 IEEE International Conference. Fifteenth IEEE International Conference on Micro Electro Mechanical Systems (Cat. No.02CH37266) (2002) 384–387. https://doi.org/10.1109/MEMSYS.2002.984283.

[98] S.D. Leith, D.T. Schwartz, Through-mold electrodeposition using the uniform injection cell (UIC): Workpiece and pattern scale uniformity, Electrochimica Acta 44 (1999) 4017–4027. https://doi.org/10.1016/S0013-4686(99)00162-0.

[99] J. Gobet, F. Cardot, J. Bergqvist, F. Rudolf, Electrodeposition of 3D microstructures on silicon, J. Micromech. Microeng. 3 (1993) 123–130. https://doi.org/10.1088/0960-1317/3/3/007.

[100] J.A. Thornton, D.W. Hoffman, Stress-related effects in thin films, Thin Solid Films 171 (1989) 5–31. https://doi.org/10.1016/0040-6090(89)90030-8.

[101] L. Hollang, E. Hieckmann, D. Brunner, C. Holste, W. Skrotzki, Scaling effects in the plasticity of nickel, Materials Science and Engineering: A 424 (2006) 138–153. https://doi.org/10.1016/j.msea.2006.03.002.

[102] T. Yamamoto, K. Igawa, H. Tang, C.-Y. Chen, T.-F.M. Chang, T. Nagoshi, O. Kudo, R. Maeda, M. Sone, Effects of current density on mechanical properties of electroplated nickel with high speed sulfamate bath, Microelectronic Engineering 213 (2019) 18–23. https://doi.org/10.1016/j.mee.2019.04.012.

[103] S. Kainth, P. Sharma, P.K. Diwan, O.P. Pandey, Shaping the Future: Innovations in Silicon Wafer Production and Finishing, Silicon 16 (2024) 6479–6497. https://doi.org/10.1007/s12633-024-03168-5.

[104] M. Arif, M. Rahman, W.Y. San, A state-of-the-art review of ductile cutting of silicon wafers for semiconductor and microelectronics industries, Int J Adv Manuf Technol 63 (2012) 481–504. https://doi.org/10.1007/s00170-012-3937-2.

[105] F.F. Villa, Silicon Properties and Crystal Growth, in: B. Vigna, P. Ferrari, F.F. Villa, E. Lasalandra, S. Zerbini (Eds.), Silicon Sensors and Actuators: The Feynman Roadmap, Springer International Publishing, Cham, 2022: pp. 3–33. https://doi.org/10.1007/978-3-030-80135-9_1.

[106] L. Zhang, Silicon Process and Manufacturing Technology Evolution: An overview of advancements in chip making, IEEE Consumer Electronics Magazine 3 (2014) 44–48. https://doi.org/10.1109/MCE.2014.2317896.

[107] V.-M. Airaksinen, Chapter 15 - Silicon Wafer and Thin Film Measurements, in: M. Tilli, T. Motooka, V.-M. Airaksinen, S. Franssila, M. Paulasto-Kröckel, V. Lindroos (Eds.), Handbook of Silicon Based MEMS Materials and Technologies (Second Edition), William Andrew Publishing, Boston, 2015: pp. 381–390. https://doi.org/10.1016/B978-0-323-29965-7.00015-4.

[108] M.R. Marks, Z. Hassan, K.Y. Cheong, Characterization Methods for Ultrathin Wafer and Die Quality: A Review, IEEE Transactions on Components, Packaging and Manufacturing Technology 4 (2014) 2042–2057. https://doi.org/10.1109/TCPMT.2014.2363570.

[109] D. Resnik, U. Aljančič, D. Vrtačnik, M. Možek, S. Amon, Mechanical stress in thin film microstructures on silicon substrate, Vacuum 80 (2005) 236–240. https://doi.org/10.1016/j.vacuum.2005.08.001.

[110] F. Ericson, S. Greek, J. Söderkvist, J.-Å. Schweitz, High-sensitivity surface micromachined structures for internal stress and stress gradient evaluation, J. Micromech. Microeng. 7 (1997) 30. https://doi.org/10.1088/0960-1317/7/1/006.

[111] S. Spiga, A. Castaldini, A. Cavallini, M.L. Polignano, F. Cazzaniga, Denuded zone and diffusion length investigation by electron beam induced current technique in intrinsically gettered Czochralski silicon, Journal of Applied Physics 85 (1999) 1395–1400. https://doi.org/10.1063/1.369271.

[112] Film de polycarbonate Exolon® GP, (n.d.). https://www.goodfellow.com/fr/exolon-gp-polycarbonate-film-group (accessed May 11, 2025).

[113] P.-Y. Chen, W.-C. Wang, Y.-T. Wu, Experimental investigation of thin film stress by Stoney's formula, Measurement 143 (2019) 39–50. https://doi.org/10.1016/j.measurement.2019.04.080.

[114] K. Röll, Analysis of stress and strain distribution in thin films and substrates, Journal of Applied Physics 47 (1976) 3224–3229. https://doi.org/10.1063/1.323119.

[115] R. Boijoux, Influence de l'élasticité du substrat sur la genèse, propagation et coalescence des structures de cloquage de revêtements et films minces., These de doctorat, Université Grenoble Alpes (ComUE), 2017. https://theses.fr/2017GREAI085 (accessed May 11, 2025).

[116] N. Guyot, Y. Harmand, A. Mézin, The role of the sample shape and size on the internal stress induced curvature of thin-film substrate systems, International Journal of Solids and Structures 41 (2004) 5143–5154. https://doi.org/10.1016/j.ijsolstr.2004.03.015.

[117] A. Mézin, Coating internal stress measurement through the curvature method: A geometry-based criterion delimiting the relevance of Stoney's formula, Surface and Coatings Technology 200 (2006) 5259–5267. https://doi.org/10.1016/j.surfcoat.2005.06.018.

[118] A.H. Choi, B. Ben-Nissan, A. Bendavid, B. Latella, 6 - Mechanical behavior and properties of thin films for biomedical applications, in: H.J. Griesser (Ed.), Thin Film Coatings for Biomaterials and Biomedical Applications, Woodhead Publishing, 2016: pp. 117–141. https://doi.org/10.1016/B978-1-78242-453-6.00006-7.

[119] D.G. Abdelsalam, B. Yao, D.G. Abdelsalam, B. Yao, Interferometry and its Applications in Surface Metrology, in: Optical Interferometry, IntechOpen, 2017. https://doi.org/10.5772/66275.

[120] B. Bhushan, J.C. Wyant, C.L. Koliopoulos, Measurement of surface topography of magnetic tapes by Mirau interferometry, Appl. Opt., AO 24 (1985) 1489–1497. https://doi.org/10.1364/AO.24.001489.

[121] 1 Coherence Correlation Interferometry in Surface Topography Measurements, in: 2012. https://www.semanticscholar.org/paper/1-Coherence-Correlation-Interferometry-in-Surface/38b8f0f6aa7d7c5d3586cf3b3734536bc34c36df (accessed May 11, 2025).

[122] G. Binnig, C.F. Quate, Ch. Gerber, Atomic Force Microscope, Phys. Rev. Lett. 56 (1986) 930–933. https://doi.org/10.1103/PhysRevLett.56.930.

[123] M.L. Bloo, H. Haitjema, W.O. Pril, Deformation and wear of pyramidal, silicon-nitride AFM tips scanning micrometre-size features in contact mode, Measurement 25 (1999) 203–211. https://doi.org/10.1016/S0263-2241(99)00004-4.

[124] K. Kimura, K. Kobayashi, H. Yamada, T. Horiuchi, K. Ishida, K. Matsushige, Orientation control of ferroelectric polymer molecules using contact-mode AFM, European Polymer Journal 40 (2004) 933–938. https://doi.org/10.1016/j.eurpolymj.2004.01.015.

[125] Q. ZHONG, D. INNISS, K. KJOLLER, V.B. ELINGS, Fractured polymer/silica fiber surface studied by tapping mode atomic force microscopy, Surf. Sci 290 (1993) L688–L692.

[126] S.N. Magonov, V. Elings, M.-H. Whangbo, Phase imaging and stiffness in tapping-mode atomic force microscopy, Surface Science 375 (1997) L385–L391. https://doi.org/10.1016/S0039-6028(96)01591-9.

[127] Atomic force microscope–force mapping and profiling on a sub 100-Å scale | Journal of Applied Physics | AIP Publishing, (n.d.). https://pubs.aip.org/aip/jap/article-abstract/61/10/4723/172389/Atomic-force-microscope-force-mapping-and (accessed February 24, 2025).

[128] B. Pittenger, N. Erina, C. su, Quantitative mechanical property mapping at the nanoscale with PeakForce QNM, 2010. https://doi.org/10.13140/RG.2.1.4463.8246.

[129] P. Trtik, J. Kaufmann, U. Volz, On the use of peak-force tapping atomic force microscopy for quantification of the local elastic modulus in hardened cement paste, Cement and Concrete Research 42 (2012) 215–221. https://doi.org/10.1016/j.cemconres.2011.08.009.

[130] K. Xu, W. Sun, Y. Shao, F. Wei, X. Zhang, W. Wang, P. Li, Recent development of PeakForce Tapping mode atomic force microscopy and its applications on nanoscience, Nanotechnology Reviews 7 (2018) 605–621. https://doi.org/10.1515/ntrev-2018-0086.

[131] J.D. Ferry, H.S. Myers, Viscoelastic Properties of Polymers, J. Electrochem. Soc. 108 (1961) 142C. https://doi.org/10.1149/1.2428174.

[132] M. Chargaoui, G. Parry, C. Coupeau, On the morphology of buckling structures in a controlled-thickness gradient: finite element method and experimental studies, Thin Solid Films (2025) 140693. https://doi.org/10.1016/j.tsf.2025.140693.

[133] M. Chargaoui, G. Parry, C. Coupeau, Secondary telephone cord buckle in thickness gradient and tapered delamination, (2025). https://doi.org/10.2139/ssrn.5870785.

[134] M. Chargaoui, G. Parry, Y. Ni, C. Coupeau, Morphology of telephone cord buckles in films lying perpendicular to a thickness gradient: a finite element numerical study,

Submitted to Proceedings of the Institution of Mechanical Engineers, Part C: Journal of Mechanical Engineering Science (2025).

[135] F. Cleymand, C. Coupeau, J. Grilhé, Experimental investigation of the instability of buckling patterns: from straight-sided to wormlike structures, Scripta Materialia 44 (2001) 2623–2627. https://doi.org/10.1016/S1359-6462(01)00969-1.

[136] F. Cleymand, C. Coupeau, J. Grilhé, Atomic force microscopy investigation of buckling patterns of nickel thin films on polycarbonate substrates, Philosophical Magazine Letters 82 (2002) 477–482. https://doi.org/10.1080/09500830210154688.

[137] A.A. Abdallah, P.C.P. Bouten, J.M.J. den Toonder, G. de With, Buckle initiation and delamination of patterned ITO layers on a polymer substrate, Surface and Coatings Technology 205 (2011) 3103–3111. https://doi.org/10.1016/j.surfcoat.2010.11.025.

[138] K. Meng, G. Parry, M.A. Hurier, N. Ben Dahmane, C. Coupeau, Elastic-plastic buckling of gold thin films into straight-sided blisters, Surface and Coatings Technology 482 (2024) 130642. https://doi.org/10.1016/j.surfcoat.2024.130642.

[139] S. Žák, A. Lassnig, M.J. Cordill, R. Pippan, Finite element-based analysis of buckling-induced plastic deformation, Journal of the Mechanics and Physics of Solids 157 (2021) 104631. https://doi.org/10.1016/j.jmps.2021.104631.

[140] N.B. Dahmane, Study of buckling and delamination of ductile thin films on rigid substrates, phdthesis, Université Grenoble Alpes, 2018. https://theses.hal.science/tel-02012703 (accessed March 30, 2023).

[141] M.W. Moon, H.M. Jensen, J.W. Hutchinson, K.H. Oh, A.G. Evans, The characterization of telephone cord buckling of compressed thin films on substrates, Journal of the Mechanics and Physics of Solids 50 (2002) 2355–2377. https://doi.org/10.1016/S0022-5096(02)00034-0.

[142] N. Matuda, S. Baba, A. Kinbara, Internal stress, young's modulus and adhesion energy of carbon films on glass substrates, Thin Solid Films 81 (1981) 301–305. https://doi.org/10.1016/0040-6090(81)90514-9.

[143] J. S. Sharp, N. M. Roberts, Thickness dependence of telephone cord blister formation in solvent swollen films of polydimethylsiloxane, Soft Matter 19 (2023) 7796–7803. https://doi.org/10.1039/D3SM01051A.

[144] K. Pan, Y. Ni, L. He, Effects of interface sliding on the formation of telephone cord buckles, Phys. Rev. E 88 (2013) 062405. https://doi.org/10.1103/PhysRevE.88.062405.

[145] A.M. Collection, Abaqus Analysis User's Guide, Dassault Systèmes; Simulia Corp., Providence, RI, USA, 2013.

[146] F. Foucher, C. Coupeau, J. Colin, A. Cimetière, J. Grilhé, How Does Crystalline Substrate Plasticity Modify Thin Film Buckling?, Phys. Rev. Lett. 97 (2006) 096101. https://doi.org/10.1103/PhysRevLett.97.096101.

[147] G.A. Maugin, Duhamel's Pioneering Work in Thermo-elasticity and Its Legacy, in: G.A. Maugin (Ed.), Continuum Mechanics Through the Eighteenth and Nineteenth Centuries: Historical Perspectives from John Bernoulli (1727) to Ernst Hellinger (1914), Springer International Publishing, Cham, 2014: pp. 69–75. https://doi.org/10.1007/978-3-319-05374-5_5.

[148] M. Chargaoui, G. Parry, C. Coupeau, Towards the Quantification of the Interfacial Toughness Through Buckle Propagation in Controlled Thickness Gradient, (2025). https://doi.org/10.2139/ssrn.5894282.

[149] S.-J. Yu, Y.-C. Shi, M.-G. Chen, P.-Z. Si, Y. Zhou, X.-F. Zhang, J. Chen, H. Zhou, Z.-W. Jiao, Coalescence behaviors of telephone cord buckles in SiAlNx films, Surface and Coatings Technology 232 (2013) 884–890. https://doi.org/10.1016/j.surfcoat.2013.06.117.

[150] S. Yu, J. Zhang, H. Li, L. Li, Y. Ni, Controllable Buckle Delaminations in Polymer-Supported Periodic Gradient Films by Mechanical Compression, Langmuir 38 (2022) 13469–13476. https://doi.org/10.1021/acs.langmuir.2c01939.

[151] K. Wu, J.Y. Zhang, G. Liu, P. Zhang, P.M. Cheng, J. Li, G.J. Zhang, J. Sun, Buckling behaviors and adhesion energy of nanostructured Cu/X (X=Nb, Zr) multilayer films on a compliant substrate, Acta Materialia 61 (2013) 7889–7903. https://doi.org/10.1016/j.actamat.2013.09.028.

[152] H.-H. Yu, J.W. Hutchinson, Influence of substrate compliance on buckling delamination of thin films, International Journal of Fracture 113 (2002) 39–55. https://doi.org/10.1023/A:1013790232359.

[153] W. Zhu, Y.C. Zhou, J.W. Guo, L. Yang, C. Lu, Quantitative characterization of the interfacial adhesion of Ni thin film on steel substrate: A compression-induced buckling delamination test, Journal of the Mechanics and Physics of Solids 74 (2015) 19–37. https://doi.org/10.1016/j.jmps.2014.09.012.

[154] S. Faulhaber, C. Mercer, M. Moon, J. Hutchinson, A. Evans, Buckling delamination in compressed multilayers on curved substrates with accompanying ridge cracks, Journal of the Mechanics and Physics of Solids 54 (2006) 1004–1028. https://doi.org/10.1016/j.jmps.2005.11.005.

Abstract

Thin films and coatings play a crucial role in a wide range of technological applications, such as microfluidics, microelectronics, optical devices, and thermal barrier systems. These films, commonly produced by physical vapor deposition techniques, often exhibit large intrinsic stresses, either compressive or tensile, sometimes reaching several gigapascals. Such stresses can lead to various damages, reducing the films' functionality. Despite its undesirable nature, buckling can provide valuable insights into mechanical properties, such as film/substrate Young's moduli, internal stress or interfacial toughness. This thesis investigates the influence of a controlled thickness gradient on the morphology and evolution of buckling-driven delamination in nickel thin films deposited by ion beam sputtering on polycarbonate substrates, using this gradient to assess mechanical properties. The nickel films were externally compressed to induce mainly straight-sided buckles. Experimental observations revealed that the height of straight-sided buckles aligned parallel to the thickness gradient decreases with increasing thickness, while those oriented perpendicular to the gradient display asymmetric equilibrium profiles, with their maximum heights shifted toward the thinner region, leading to unequal edge to peak distances. Upon release of external stress, secondary buckling of telephone-cord buckles aligned parallel to the gradient was observed, with wavelengths and stripe widths decreasing as local thickness decreased. Finite element modeling was used to systematically analyze the effects of internal stress, delaminated width, the gradient slope and finally tapered width. The transition from the plane state to the telephone cord, through the straight-sided buckle, has been fully characterized, consistent with our experimental findings. Additionally, the morphological parameters of telephone cord buckling structures lying perpendicular to a thickness gradient has been fully characterized. The results highlighted that both in-plane and out-of-plane asymmetries are controlled by the gradient slope rather than the internal stress or buckle width. A predictive scaling law was established to quantify these asymmetries, providing a new framework for analyzing non-uniform thin-film buckling. Finally, the propagation of straight-sided buckles along the gradient was exploited as an energetical criterium to assess the interfacial toughness. Experimentally, buckles propagate under compressive stress from thicker regions and arrest consistently as thickness decreases, where available elastic energy was insufficient for further delamination. This arrest mechanism is captured through finite element simulations incorporating a cohesive zone model. Analysis of the mode mixity angle shows reveals predominant fracture mode I at the buckle front and mode II at the edges, ensuring the propagation of the buckle toward the thinner regions. It is finally shown that the film/substrate interfacial toughness can be numerically quantified using the critical thickness of arrest of the buckle as an energetical criterium.

Keywords: Thin film, Coating, Thickness gradient, Buckling, Delamination, Straight-sided buckle, Secondary buckling, Finite element method, Cohesive zone model

Résumé

Les films minces et les revêtements jouent un rôle crucial dans de nombreuses applications technologiques, telles que la micro-fluidique, la microélectronique, les dispositifs optiques et les systèmes de protection thermique. Ces films, souvent produits par dépôt physique en phase vapeur, présentent fréquemment de fortes contraintes intrinsèques, compressives ou tensions, pouvant atteindre plusieurs gigapascals. Ces contraintes peuvent provoquer des dommages réduisant la fonctionnalité des films. Malgré leur aspect indésirable, les flambages peuvent fournir des informations précieuses sur les propriétés mécaniques, telles que les modules d'Young film/substrat, les contraintes internes ou la ténacité interfaciale. Cette thèse étudie l'influence d'un gradient d'épaisseur contrôlé sur la morphologie et l'évolution du délaminage induit par flambage dans des films minces de nickel déposés par pulvérisation ionique sur des substrats en polycarbonate, en utilisant ce gradient pour évaluer les propriétés mécaniques. Les films de nickel ont été comprimés extérieurement pour induire principalement des flambages raides droits. Les observations expérimentales montrent que la hauteur des raides droits alignés parallèlement au gradient diminue lorsque l'épaisseur augmente, tandis que les structures orientées perpendiculairement au gradient présentent un profil d'équilibre asymétrique, avec leur maximum déplacé vers la région la plus fine, entraînant des distances inégales entre les bords et le sommet. Après relâchement de la contrainte externe, un flambage secondaire en cloques alignées parallèlement au gradient a été observé, dont les longueurs d'onde et largeurs diminuent avec l'épaisseur locale décroissante. La modélisation par éléments finis a permis d'analyser systématiquement les effets de la contrainte interne, de la largeur délaminée, de la pente du gradient et enfin de la largeur effilée. La transition de l'état plan vers les cloques, en passant par le raide droit, a été pleinement caractérisée, en accord avec les résultats expérimentaux. De plus, les paramètres morphologiques des cloques perpendiculaires au gradient ont été décrits. Les résultats montrent que les asymétries, tant dans le plan qu'en dehors du plan, sont principalement contrôlées par la pente du gradient et non par la contrainte interne ou la largeur du flambage. Une loi d'échelle prédictive a été établie pour quantifier ces asymétries, fournissant un cadre pour analyser le flambage de films minces non uniformes. Enfin, la propagation des raides droits le long du gradient a été exploitée comme critère énergétique pour évaluer la ténacité interfaciale. Expérimentalement, les flambages se propagent depuis les zones épaisses et s'arrêtent dans les zones fines, où l'énergie élastique disponible devient insuffisante. Ce mécanisme d'arrêt est reproduit par des simulations éléments finis intégrant un modèle de zone cohésive. L'analyse de l'angle de mode mixte montre un mode de rupture prédominant I à l'avant du flambage et II aux bords, garantissant la propagation vers les régions fines. La ténacité interfaciale film/substrat peut ainsi être quantifiée numériquement à partir de l'épaisseur critique d'arrêt du flambage.

Mots-clés : Film mince, Revêtement, Gradient d'épaisseur, Flambage, Délaminage, Ride droite, Flambage secondaire, Méthode des éléments finis, Modèle de zone cohésive.